UNIVERSITY OF CAPE TOWN
IYUNIVESITHI YASEKAPA • UNIVERSITEIT VAN KAAPSTAD

BISRU

CSIR

Investigation into the Electromagnetic field generated by explosions

by

Gareth Erfort

Thesis presented in partial fulfillment
for the Degree of Master of Science

Department of Mechanical Engineering
University of Cape Town
3rd December 2009

Acknowledgments

The author wishes to express his gratitude and thanks to those all those who have assisted and guided him though this project over the years, first and foremost the Lord God for his grace and secondly to his family for their never ending support.
Particular mention goes to:

Prof. G. Nurick for his support through the project

Dr Wilkinson for his invaluable support and expertise in the field of signal processing

Dr Frikkie Mostert for his support during testing and guidance both before and after testing

Inus Grobler as mentor and his repository of information

Vernon Davids for dealing with the authors questions and constant presence

Nicklaus Kruger for his support throughout the years of this project

The two groups who made this project possible and became my two homes BISRU and TSO - Stellenbosch

Finally a word of thanks to all those not mentioned but who supported emotionally and where always on hand with a kind word or snack.

Abstract

The electromagnetic pulse (EMP) resulting from the detonation of nuclear explosives is a documented and studied phenomenon. What is less well known and understood is the similar yet considerably less powerful occurrence surrounding the detonation of high explosives. The phenomenon was first noticed by Kolsky in 1954 during his investigation into stress waves using explosive charges. This project was undertaken to identify any discernible field or wave in the low frequency EM spectrum, focusing particularly on the magnetic field. The work published by Soloviev in 2002 and Adushkin in 2004 served as guidelines on test procedure and setup. Testing of this nature was not found in the literature to have been previously conducted in South Africa and is multi-disciplinary, involving the fields of detonics and signal processing.

The test procedure implemented proved valid as signals were detected and sufficient data were gathered to perform basic pattern recognition and spectral frequency analysis. The analysis allowed for comments to be made on the relationship between the signal and other characteristics surrounding the event.

Inside the frequency band investigated there appeared to be two bands of activity in the kHz range, which is consistent with previously published works. The repeatability of the waveforms shape for identical blasts was good but with the limited sample size a proper database could not be developed. Provisionally it can be said that such events do have characteristic shapes. Testing revolved around small charges and was conducted in the near field. This removed the possibility of commenting on orientation factors.

The testing was a success in terms of recording magnetic field signals from the detonation of high explosives.

Declaration

1. I hereby grant the University of Cape Town free license to reproduce for the purpose of research either the whole or any portion of the contents in any manner whatsoever of this dissertation.

2. I know the meaning of plagiarism and declare that all of the work in this document, save for that which is properly acknowledged, is my own.

3. This thesis or any part of this thesis has not been submitted in past, or is being, or to be submitted in this or any other form for a degree at the University of Cape town or any other University.

Contents

List of Figures

List of Tables

Glossary

Exothermic reaction:	Reaction where energy is released, usually in the form of heat
Oxidation reaction:	Traditionally described as a chemical reaction in which oxygen combines with another element to form an oxide, or a reaction in which one or more free electrons is released[15]
Homogeneous:	Mixtures that contain one or more pure substances in a single phase
Heterogeneous:	Materials or mixtures that have one or more pure substances in more than one phase
CHNO Explosives:	Explosives whose chemical make up is a combination of Carbon, Hydrogen, Nitrogen and Oxygen molecules in different ratios
Chemical kinetics:	Study of the rates of chemical reactions
Shock wave:	A discontinuity as part of the flow, that is an abrupt change in a material's characteristics, propagating through a medium
Deflagration:	The burning of an explosive along its surface at a rapid rate
Gibbs phenomenon:	States that calculations carried out on a truncated series will result in oscillatory behavior on either side of a discontinuity
Windowing:	In spectrum analysis it is the application of a function (window) to a signal so that it reduces the signal gradually and terminates smoothly instead of the abrupt removal of unwanted data
Autocorrelation:	The correlation of a data set with itself
Endfire:	Perpendicular to the normal of the aperture
Broadside:	Inline with the normal of the aperture

Acronyms

ADC:	analog to digital converter
csv:	Comma separated values
BISRU:	Blast Impact and Survivability Research Unit
CJ:	Chapman-Jouguet theory of detonation
DSD:	Detonation Shock dynamics theory developed by Lawrence Livermore National Laboratories
EET:	Electronic Engineering technology
EM:	Electromagnetic
EMC:	Electronic and Magnetic radiation compliance laws
EMF:	Electromagnetic Field
EMI:	Electromagnetic interference
EMP:	Electromagnetic pulse
FFT:	Fast Fourier Transform
OB:	Oxygen Balance
PCI:	Peripheral component interconnect
RH:	Rankine-Hugoniot
SOD:	Stand off distance

TNT: Trinitrotoluene

VOD: Velocity of Detonation

ZVD: Zel'dovitch, Von Neumann and Doring theory of detonation

Symbols

Literature

ρ:	Density
u:	Velocity
ϑ:	Specific volume
C_0:	Speed of sound
s:	Entropy of the gas
P:	Pressure
e:	Energy
U_{esc}:	Escape velocity
γ:	gamma, ratio of specific heats at constant pressure and volume
V_d:	Detonation velocity
T_a:	Arrival time
r_c:	Charge radius
R:	Stand off distance
p^o:	Over pressure
P_a:	Ambient pressure
Z:	Scaled distance
W:	Charge mass
∇:	Gradient function
E:	Electric field vector
$\mathscr{B}$	Magnetic flux density
H:	Magnetic field density
$\mathscr{J}$:	Current density
$\mathscr{D}$:	Electric flux density
q_{ev}:	Electric charge density
q:	Electric charge
$\hat{r_{o1}}$:	Distance between charges
k_e:	Coulombs constant
F:	Force

Loop antennas

l_e: Effective length

k_b: Boltzman constant

d: Diameter

μ_e: Effective permeability

λ: Wavelength

c: Speed of light

f: Frequency

ω: angular frequency

U: Radiation intensity

W_av: Average power density

k: Wave number

I_0: Current

η: Intrinsic impedance

E_Φ: Far-zone electric field component of an antenna

D_0: Directivity

P_{rad}: Power radiated

f_c: Cut off frequency

R: Resistance

C: Capacitance

G: Gain

Signal processing

j: $\sqrt{-1}$

ω_o: Natural frequency

f_p: Periodic waveform

T_0: Period

P: Power

E: Energy

v: Voltage

f_k: non-periodic waveform

E: Expected value operator

C_{xy}: Cross correlation value

C_c: Cross correlation value

x: Vector

$\bar{x}$: Mean value of vector

Analysis procedure

h: Step size

e: Electro motive force

$\vec{S}$: Unit normal of area vector

N: Number of turns

A: Area

1 Introduction

Scientists are aware of the electromagnetic pulse (EMP) resulting from a high altitude detonation of a nuclear bomb. This short burst of electro-magnetic energy travels ahead of the blast at the speed of light. The EMP is responsible for disrupting electronics before the shock wave arrives and can sometimes affect a larger area. What is less well known, and at times disputed, is the observation that the detonation of high explosives generates an electromagnetic field (EMF) that is detectable.
Kolsky[16] first detected such signals when investigating the propagation of stress waves through solids with the aid of small explosives. Kolsky placed stub antennas behind perspex screen to investigate certain aspects of this phenomenon, such as initiation method and type of explosive. Later studies revealed that there are many factors affecting the EMF generated by detonation. These include -

- Surrounding material[17]
- Addition of impurities[18]
- Packaging[19]
- Explosive type[16]
- Initiation method[20]

All of these factors are part of the explosive device itself and affect the signal strength and shape. However there are other factors that affect the measurement of this phenomenon, such as the electric seismic effect: the disturbance of a conductive layer beneath the surface caused by a shock wave that generates an EMP and the dust cloud effect where the dust generated by the explosive has charged particles which forms a dipole that can also be detected. The phenomenon in general is not well understood. Certain aspects of the phenomenon's nature have been investigated and in some studies, developed an empirical relationships based on these investigations.

This project focused on frequencies in the kHz range and aimed to investigate the possibility that the recorded waveform was repeatable in shape and nature, while also looking at the effect of orientation with respect to the initiation cord. The waveform from a charge at particular stand off distance (SOD) is similar but not identical to the waveform from the same setup (mass and SOD) being fired directly after. This is because the factors affecting the shape are too numerous to control. Even so, while testing may keep some

factors constant, the very nature of explosives is to vary in energy output within a certain range.
The study was limited to magnetic fields only, one type of explosive and only the mathematical removal of certain aspects (blast waves). These limitations were a result of the testing ground's location and limited test time. The work provides a starting point from which further studies can progress into a field that is at the moment still very unexplored.

The layout of this thesis is written up for readers in two fields. The nature of the work covered is a combination of electrical and mechanical engineering.

Chapter **2** is the literature review which aims to provide the basic knowledge of explosives to electrical engineers while introducing the simple ideas behind electromagnetism to mechanical engineers. The last section in the literature review is a summary of important information gleaned from articles published in this field. It contains the reasons for previous work, the test setup followed and the equipment used.
Chapters **3** and **4.1** following the review provide the reader with the test setup. These chapters give information on the procedure followed and equipment used in both the preliminary and primary testing stages. Schematics of the test setup and pictures of the equipment aid with the visualization of how the tests were conducted.
Chapter **6** gives a more in-depth look into the techniques used in signal processing, provides the reader with a mathematical background into the Fourier transform and discusses the additional techniques used when analyzing signals.
After having explained which techniques will be used, chapter **7** details where and why each method was employed. This chapter shows the progression from raw data to processed signals and explains the reason behind each step.
Thereafter follow the results and observations, chapters **8** and **9** respectively, discussing the different points of interest found during testing.
Chapter **10** is where conclusions and recommendations are given. These include ideas for further testing and alterations that can be made to improve the test setup.
The appendices include all information gathered during this thesis as well as more in-depth discussion on certain aspects of the analysis procedure.

2 Literature Review

2.1 Introduction

The literature review is structured in three parts. The first section provides an introduction to explosives, the theory behind the detonation process and other topics concerning explosives. The second section gives an introduction to electromagnetic fields and some basic equations governing electric fields and charge distributions. The final section is the history of studies undertaken concerning this phenomenon, including motivation, equipment used and conclusions drawn. A final section is a summation of the findings made during the literature review.

2.2 Explosives

2.2.1 Chemistry of Explosives

Explosives are defined as materials (chemical or nuclear) that can be initiated to undergo very rapid, self-propagating decomposition. The result is the formation of a more stable product and the liberation of heat. This excess heat usually creates a sudden pressure effect through the action of heat on produced or adjacent gases. This type of reaction is called an exothermic process and in chemical explosives the reaction is usually of the oxidation type. Chemical explosives are split into two categories, heterogeneous and homogeneous. To be self-propagating the material needs to contain all the parts for a reaction. The explosive substance therefore requires oxidizer and fuel in a single molecule, which decomposes during the reaction and reforms in its oxidized products. For the purposes of this review explosives with the general chemical formula of CHNO are considered.

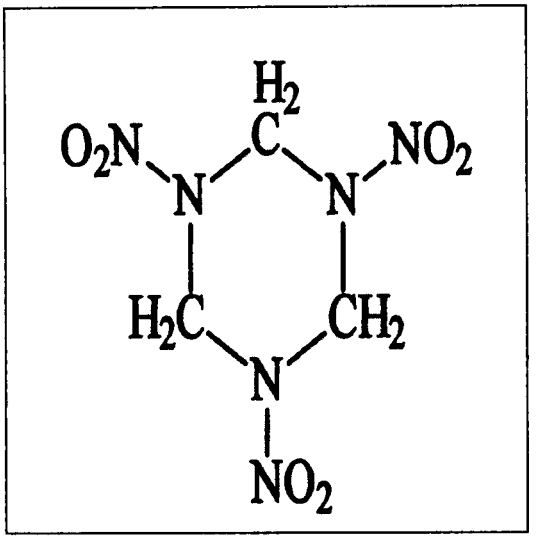

Figure 2.1. Underoxidised RDX chain[1]

The amount of oxygen present plays an important role in detonation. Fuel rich reactions have more fuel present than is required for the reaction (TNT). If there is a higher proportion of oxygen than is required for complete oxidation the explosive is termed fuel lean (nitroglycerin). If the explosive is exactly balanced, with just enough oxygen to completely oxidize, the explosive produces the maximum energy output. The excess/deficiency of fuel can be quantified by calculating the oxygen balance (OB) or by merely knowing the chemical formula of the material and the products of the reaction allow for the determination of a rich/lean fuel explosive.

Some of the more common products formed by an explosion are Nitrogen (N_2), water (H_2O), carbon monoxide (CO) and carbon dioxide (CO_2). Depending on the chemical composition of the explosive other products can also be formed, aluminum oxide (Al_2O_3) and sulfur dioxide (SO_2) for example. To help determine which products will be formed a set of rules were developed in World War 2. Three rule sets are given in table 2.1: the original Kistiakowsky-Wilson (K-W) rules, applicable for moderately oxygen deficient explosives*; the modified K-W rules that apply to explosives with a greater oxygen deficiency; and lastly the Springall Roberts rules †.

*moderately oxygen deficient explosives have an OB % $\geq$ -40

†The Springall Roberts rule set is made up of the K-W rules and an additional two rules

Table 2.1. Original, Modified and Springall Roberts versions of K-W rules[2]

Rule No.	Conditions	Rule Set
1	Hydrogen atoms are converted to H_2O	Original KW rules
2	If any oxygen remains the hydrogen is oxidized to H_2O	
3	If any oxygen remains CO is oxidized to CO_2	
4	All the nitrogen is converted to N2	
1	Carbon atoms are converted to CO	Modified KW rules
2	If any oxygen remains the hydrogen is oxidized to H_2O	
3	If any oxygen remains CO is oxidized to CO_2	
4	All the nitrogen is converted to N_2	
5	$\frac{1}{3}$ of the CO formed is converted to C and CO_2	Springall Roberts
6	$\frac{1}{6}$ of the original CO is converted to C and H_2O	

These rule sets are called the simple hierarchy for CHNO explosives. They are used only as a guide for determining the decomposition products formed.

Detonation is a burning or decomposition reaction whose propagation speed is greater than the speed of sound through the material[2]. For detonation to occur the material must react swiftly and produce gas and energy. Detonation happens much faster than deflagration, at velocities ranging from 1 - 9000ms^{-1}. The detonation process occurs after deflagration only if the conditions are suitable. In deflagration the oxidation proceeds slowly and is usually thermally initiated. In detonation the reaction propagates at a supersonic rate with respect to the unreacted material and is initiated by a shock.
Growth from deflagration to detonation is partially dependent on the intensity of the shock impact. Generally the higher the intensity the quicker the explosive reaches stable detonation. Also when the material is burning in a confined space (casing or shell) the gas produced by the decomposition causes an increase in pressure which in turn causes an increase in burning rate. Secondary explosives can be detonated using a high velocity shock wave. In a typical setup a primary explosive is detonated and produces a shock wave that initiates the secondary explosive. The progression from initiation to detonation occurs over a very short period of time. The process starts when the shock wave enters the explosive

material and compresses the explosive, causing a temperature increase and starting the chemical reaction. Simultaneously the wave imparts a shock and particle velocity to the reacting explosive. Provided the shock wave has a sufficiently high pressure for a long enough time, detonation will occur[2].

2.2.2 Plastic explosives

High explosives are divided into three groups: primary, secondary and tertiary. The distinctions between the groups centers around their ease of detonation, the easiest to detonate being primary and the hardest being tertiary. Secondary explosives do not easily change from deflagration to detonation, they require larger shocks than primary explosives to obtain ignition and electrostatic ignition is difficult.
PE - 4 is the type of military explosive used in South Africa and as a result the explosive used during testing. PE-4 is made up of RDX powder and a plasticizer. The plasticizer is made up of paraffin and Lithium stearate. It has a limited shelf life (approximately 1 year) dependent on such factors as temperature and moisture. The explosive is not a primary explosive unless oil has been leeched out. Also a change in the colour to brown or purple indicates the RDX has undergone decomposition and that batch of PE-4 must be disposed of. The velocity of detonation (VOD) of the PE-4 used in SA is approximately 7500ms^{-1}, with some cases reporting a VOD of 7700ms^{-1}. The variation and decrease in predicted VOD is due to the oil content.

Table 2.2. Composition of PE-4

Components	% ratio
RDX	87 - 89
Plasticizer	9 - 12

2.2.3 Detonation Theories

By 1890 it was well established that detonations were shock waves supported by the chemical energy release.[2] The Chapman-Jouguet (CJ) theory is based on gas dynamics and thermodynamics and assumes a very fast chemical reaction. In contrast the Zel'dovitch, von Neumann and Doring (ZND) theory introduces finite chemistry. Even with a lack of detailed chemistry the CJ detonation predications are sufficiently accurate while ZND accuracy is dependent on the accuracy of the chemical reaction schemes used. CJ theory was first proposed in the early 1900s and is based on the conservation of mass, momentum and energy. The theory was a one dimensional model, with an infinitely thin reaction zone (ideal detonation), that assumes the equilibrium of all detonation products is reached in-

stantaneously and that all explosive material is consumed during detonation. This theory can be used to calculate properties such as velocity and pressure of detonations for non-ideal or slow detonation processes.
In the early 1940s the ZND theory was proposed - which assumed the shock wave was separated from the reaction zone. This theory was developed to study the chemical and physical processes before and after the exothermic chemical reaction. The ZND theory assumes the following:

- Flow is one dimensional
- The wave front is a jump discontinuity
- The reaction zone length is zero
- The product gases leaving the detonation front are in chemical and thermodynamic equilibrium
- The chemical reaction is completed
- The gas reaction products after leaving the front are further affected by the surrounding system or boundary conditions

and predicts similar velocities and pressures to those predicted by CJ theory. The drawback is that ZND theory relies on the integration of detailed chemical kinetic schemes. In addition to pressure and velocity this theory also can be used to calculate the detonation limits, initiation energy, critical pipe diameter and the thickness of the reaction zone. The accuracy of these values depends on the accuracy of the coefficients and reactions used in the kinetic scheme.

A third detonation theory, developed by Lawrence Livermore National Laboratories, is called detonation shock dynamics (DSD). Where previous detonation models have assumed the detonation shock wave to propagate normal to itself at the CJ velocity, DSD assumes the radius of curvature of the shock front is large when compared to the reaction zone length that supports the detonation. DSD uses hydrodynamic flow theory to correct a near planar detonation flow normal to the shock. The theory takes into account changes due to shock curvature and other unsteady effects, and is used to make refined predictions of the detonation process for desired applications. DSD theory combines a hydrodynamic and thermo-chemical codes to fully model the physical and chemical processes of a high explosive detonation.

2.2.4 Shock Theory

Shock behavior and effects are only observed along one axis. Upon the application of force to a material, the material will undergo a change in shape and/or volume. Stress resulting

from the force applied causes further distortions to the material, in the form of strain. Strain presents itself in three forms - simple shear, pure dilation and uniaxial stretching. Material undergoing low stress suffers from a strain that is reversible, so that when the stress is removed the material returns to its original shape and size. The range of stresses for which this is true is called the elastic region. On the other end of the scale large stresses applied to a material cause permanent strain; this region is called the plastic region. In the elastic region at low stresses only sound waves exist, in the plastic region at high stresses only shock waves can exist but in the elastic-plastic region both waves exist and travel at different speeds. In the plastic region, solid material can behave like a fluid. The shock pressures experienced by an explosive material may stress the material well beyond the elastic limit, resulting in the permanent deformation of the material once the stress has been released. As the shock wave passes through the material, motion is imparted to particles in front of the wave by particles behind the front bumping into those ahead. The transition is very sudden and is commonly referred to as a "jump" in state. These statements led to the formation of the Rankine-Hugoniot Jump equations (RH):

$$\frac{\rho_1}{\rho_0} = \frac{U-u_0}{U-u_1} = \frac{\vartheta_0}{\vartheta_1} \tag{2.1}$$

$$P_1 - P_0 = \vartheta_0(u_1-u_0)(U-u_0) \tag{2.2}$$

$$e_1 - e_0 = \frac{P_1u_1 - P_0u_0}{\rho_0(U-u_0)} - \frac{1}{2}(u_1^2 - u_0^2) \tag{2.3}$$

which describe the shock process[‡] where ρ, U, u, ϑ, P and e represents the density, surrounding velocity, material velocity, specific volume, pressure and energy. After taking the conservation equations and a few simplifying assumptions into account the detonation can be viewed as a shock wave passing through an explosive. The shock wave compresses and heats up the material. This initiates the exothermic chemical reaction. While the shock wave is driven through the material by the energy liberated, the gaseous products behind the wave are expanding. As a result a rarefaction wave moves toward the shock front. Theoretically the shock front, rarefaction front and chemical reaction are all in equilibrium and as such all travel at the same speed, so the shock front does not change shape (since the pressure does not change) with time and neither does the detonation velocity. In practice however the reaction is not ideal and as a result the detonation velocity does decrease.

[‡]the subscripts 0 and 1 denote before and after the shock front

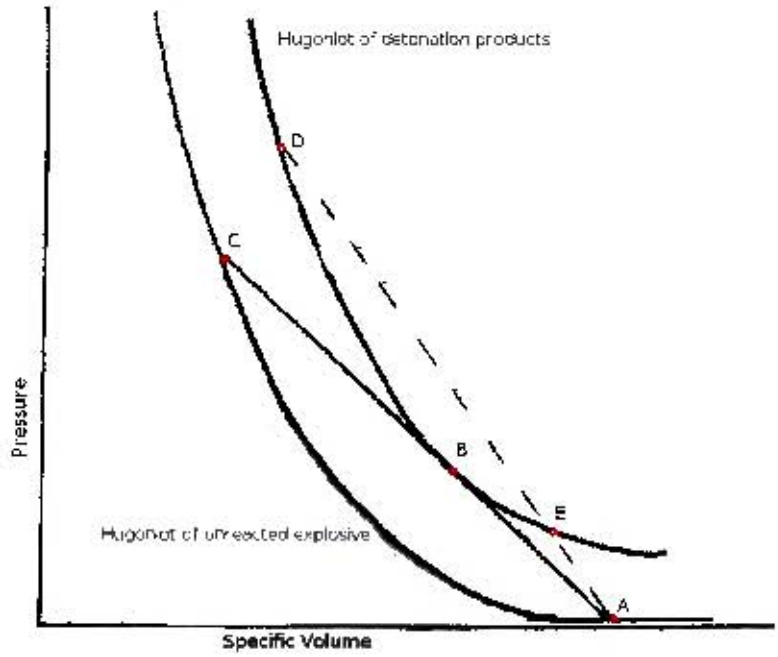

Figure 2.2. A PV diagram of different states for an explosion[2]

The hugoniot[§] of unreacted explosives shown in figure 2.2 is made by considering the RH equations in a specific plane. The plane identified above is the $P-\rho$ plane, using equation (2.2) and the $U-u$ hugoniot while letting $P_0 = 0$ and $u_0 = 0$ an expression for $P = f(v)$ is obtained where C_0 is the speed of sound and s represents the entropy of the gas:

$$P = C_0^2(\vartheta_0 - \vartheta)[\vartheta_0 - s(\vartheta_0 - \vartheta)]^2 \tag{2.4}$$

The curve shown in figure 2.2 represents the locus of all possible equilibrium states for that material. Point A shows the initial state, point C is the fully shocked but as yet unreacted explosive called the Von Neumann spike and is the point that initiates detonation. On such a diagram the line joining the A and C is called a Raleigh line and represents the jump condition. The CJ state is marked by the point where the Raleigh line is tangent to the hugoniot of the detonation products, point B. The slope of the hugoniot curve is given as U^2/V^2. There is a steeper slope from A to D. At point D the reaction zone and rarefaction wave would overtake the shock front, violating the condition that all these velocities were the same. At point E the rarefaction wave velocity is slower than the detonation front, meaning the reaction zone would continually spread in time, again violating the equilibrium constraints. The only place where the Raleigh line and the detonation products hugoniot have the same slope is at the CJ state. The Taylor wave is the rarefaction wave that brings the gases from the CJ state back to ambient pressure. The shape of the Taylor wave is

[§]These curves differ from ordinary isentropic adiabatic's in that the the latter is a single parameter family of curves while the hugoniot is a family of curves with two parameters

determined by factors such as the charge size, degree of confinement and the isentrope of the detonation gases. In normal shock wave events rarefaction waves merge with shock waves and reduce the wave amplitude and speed. This process is halted in detonation as the reaction's products help maintain the pressure behind the front and prevents the rarefaction wave reaching it. A steady state detonation, shock wave with constant velocity, is achieved while there is explosive material available; when all the material is consumed there is no more chemical reaction to add energy to the wave.

2.2.5 Explosion timeline

To better understand the physical result of an explosion, understanding the different stages of the blast and when they occur in time is very important. As previously stated that detonation is seen as a shock wave moving through a charge with a certain velocity (VOD). As the wave passes through the material expansion does occur at one end, the effect however is very small and can be considered negligible. The process is therefore described by assuming the shock wave travels the entire length of the charge before expansion occurs. The particles are released at a speed approximately given by the escape velocity

$$U_{esc} = \frac{3\gamma - 1}{\gamma^2 - 1} V_d \tag{2.5}$$

which is related to the VOD (V_d) of the material and the constant gamma (γ) from the ideal gas relationships. In reality the particles are slowed down by the air pressure encountered. This expansion lasts until the products have reached a distance of 1 unit R, the charge radius. After the 1st stage of expansion the blast wave forms and the explosive products travel in conjunction with the blast wave for the fireball period. This stage lasts till said products have traveled another 50 times the original radius. The equations provided by Graham and Kinney[21], which relate: the time of arrival of a blast wave (T_a) to SOD (R) ,overpressure (p^o), ambient pressure (P_a) and the speed of sound (a_x)

$$T_a = \frac{1}{a_x} \int_{r_c}^{R} \left[\frac{1}{1 + \frac{6p^o}{7P_a}} \right]^{1/2} \mathrm{d}r \tag{2.6}$$

are used once the shock wave is present. This integral is evaluated between the charge radius r_c and R from the blast. The only variable that changes with respect to r is the ratio of $\frac{p^o}{P_a}$:

$$\frac{p^o}{P_a} = \frac{808\left[1 + (\frac{Z}{4.5})^2\right]}{\sqrt{1 + (\frac{Z}{0.048})^2}\sqrt{1 + (\frac{Z}{0.32})^2}\sqrt{1 + (\frac{Z}{1.35})^2}} \tag{2.7}$$

The ratio is based on the scaled distance variable (Z) as defined in Hopkinson's scaling law, which is related to charge mass (W) and R:

$$Z = \frac{R}{W^{1/3}} \tag{2.8}$$

The result is a time versus distance curve as seen in figure 2.3. This is a conservative portrayal of the progression of both the detonation products and blast wave speed. Two separate portions are visible if figure 2.4, the constant velocity portion determined from equation (2.5) and then the deceleration section inferred from equation (2.6).

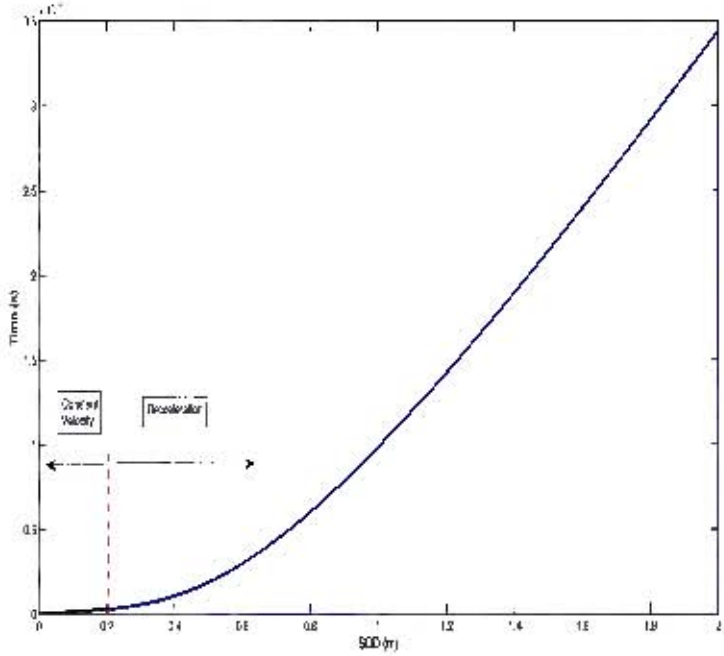

Figure 2.3. Expansion of shock wave from 20g over 2m

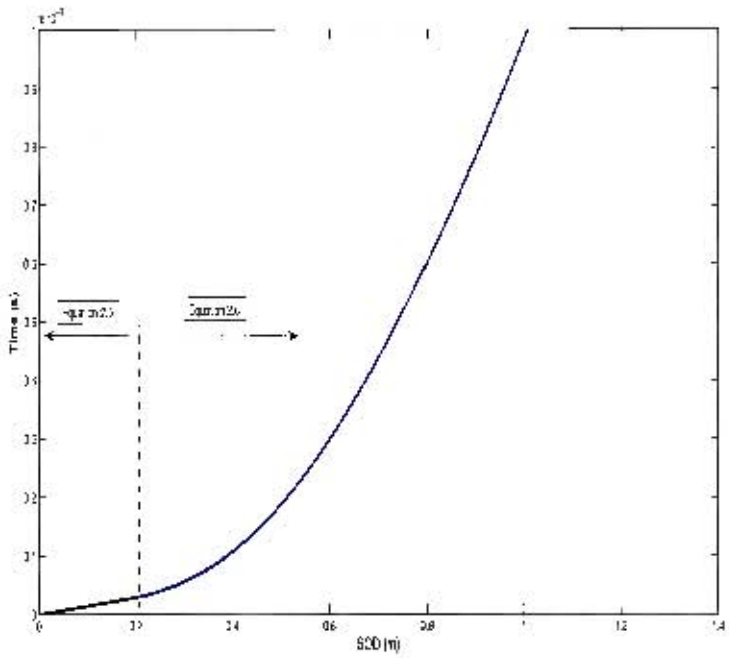

Figure 2.4. 0 - 1ms focus for the expansion of a 20g explosive

2.3 Electromagnetic Fields

2.3.1 Introduction

Balanis[22] provides a simple and clear description of electromagnetic field theory: "a discipline concerned with the study of charges, at rest and in motion, that produce currents and electric-magnetic fields".

Prior to Maxwell's dynamical electromagnetic field theory, so named because it deals with the space or area surrounding the electric or magnetic bodies (field theory) and assumes there to be matter in motion (dynamic theory), all theories relating to this topic were based on statical electricity, on statical magnetism, on the mechanical action between conductors carrying currents and on the induction of currents. In Maxwell's theory on the electromagnetic field[23] he stated:"In these theories the force acting between the two bodies is treated with reference only to the condition of the bodies and their relative position, and without any express consideration of the surrounding medium". Weber developed an almost complete theory of electromagnetic phenomena based on the attraction and repulsion of certain particles. This theory however relied on the relative velocity between the particles and their distance apart. The theory's dependence on velocity encouraged Maxwell to propose his own theory. Maxwell's proposal took a different path and suggested that the observed effects are a result of the surround medium and the excited body's interaction. The manner in which electric and magnetic fields, charges and currents associated with electromagnetic waves change and relate to one another can be described by the physical laws by which they are governed[22]. The four principle equations describing these laws are grouped together and form Maxwell's equations. The differential form of Maxwell's equations:

$$\nabla \times E = -\frac{\delta \mathscr{B}}{\delta t} \tag{2.9}$$

$$\nabla \times H = \mathscr{J} + \frac{\delta \mathscr{D}}{\delta t} \tag{2.10}$$

$$\nabla \cdot \mathscr{D} = q_{ev} \tag{2.11}$$

$$\nabla \cdot \mathscr{B} = 0 \tag{2.12}$$

are used to solve the majority of boundary value problems. Here E, $\mathscr{B}$, H, $\mathscr{J}$, $\mathscr{D}$ and q_{ev} represent electric field intensity, magnetic flux density, magnetic field density, current density, electric flux density, electric charge density. The integral form of these equations are used mainly to solve boundary value problems that have complete symmetry. For these equations to be valid certain assumptions are made; the field vectors are single-valued, bounded and continuous functions of position and time, and they exhibit continuous derivatives.

These equations were developed by different prominent figures in the field; Faraday's Law

of induction (2.9), Ampere's Circuital Law with Maxwell's Correction (2.10), Gauss's law (2.11) and Gauss's law for magnetism (2.12), but it was Maxwell who combined them and used them to develop his field theory.
With these expressions it is possible to describe and relate charge(q), current(i), electric field vector(E) and magnetic field vector(H) at any point in space at any time. This method of describing forces and fields does not replace classical statical electricity but adds further understanding to the field. When it was first proposed and described, many found it tough to explain; it was not based on a purely mechanical model, like previous works, but rather took the mechanical model and introduced a continuous field. Coulombs Law:

$$F = k_e \frac{q_1 q}{r_{o1}^2} \hat{r_{o1}} \tag{2.13}$$

is a cornerstone of statical electricity and describes the force (F) experienced by a charge at a distance (r_{o1}) apart from another charge (q) with the aid of coulombs constant(k_e). After Maxwell, electric and magnetic phenomena have subsequently also been described in terms of fields, for example the force between two electric charges is described as the product of the magnitude of one of the charges and the field of the other;

$$F = q \times E \tag{2.14}$$

Maxwell's theory was expanded upon by Lorentz, through discussions on moving systems.

2.3.2 Charge Distributions

An electric dipole is a very common type of charge distribution, shown in figure 2.5, seen in dielectrics. It consists of two charges of the same magnitude but opposite signs. In dielectrics this indicates the amount of electric energy it can store, similar to the potential energy stored by a spring. A dielectric can be polarized by three different methods[22], dipole, ionic or electronic polarization.

Dipole polarization is the method involved when a material has randomly aligned permanent dipoles but when in the presence of and external field these dipoles align themselves.

Ionic polarization occurs when the positive and negative ions of a material displace themselves when acted on by an electric field

Electronic polarization is the most common and occurs when an external field causes orbiting electric cloud to displace itself relative to the nucleus center of an atom.

Equation (2.15) provides the potential difference (V) between a point infinitely far away and an arbitrary point; a distance r from the center of a dipole, at an angle θ from the

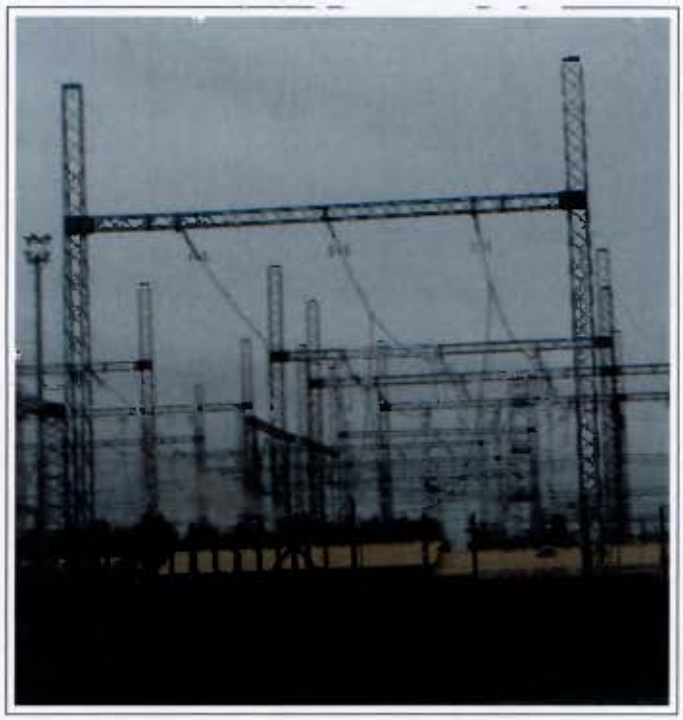

Figure 2.6. Powerlines in suburban area

Burying cables underground reduces the effect of the magnetic field at greater distance, though the field can be stronger than suspended cables at small distances. Buried cables also produce a negligible external electric field.

Figure 2.7. Cellular phones with built in antennas, pictured obtained online[4]

All electronics generate a small field but most of the time the effects are not seen because of shielding, filtering or fields canceling each other out. Cellphones generate a weak EMF(figure 2.7); this has raised health concerns considering the constant exposure to the electric field. The conducting wires between equipment usually have some form of shielding; they can have a layer of aluminum or be twisted pairs to help cancel out the fields, a variety of wires can be seen in figure 2.8.

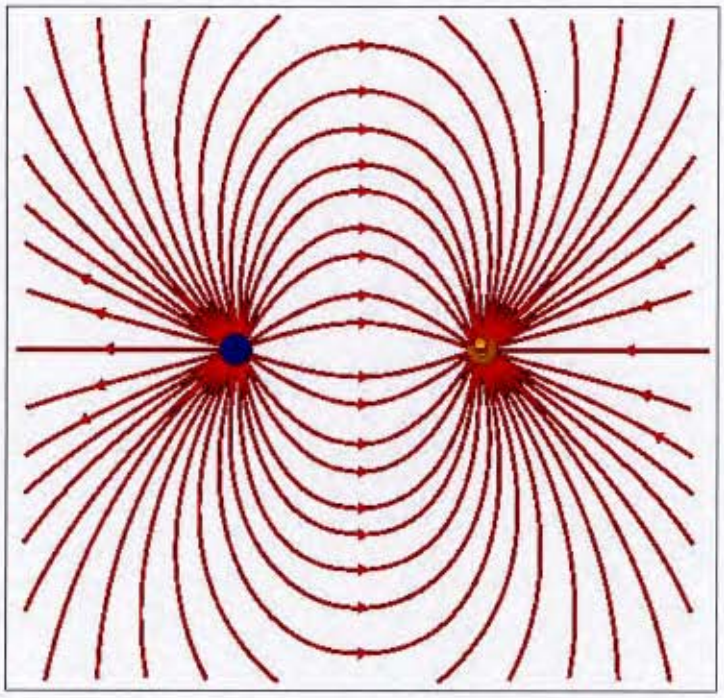

Figure 2.5. A vector image of the electric field lines around an electrostatic dipole[3], picture obtained online

centerline of the dipole, with a charge separated by a distance r_s. This equation holds only for $r_s^3 \ll r^3$

$$V = \frac{qr_s}{4\pi\epsilon_0 r^2}\cos\theta \tag{2.15}$$

2.3.3 Field Occurrences

Any charge has an electric field; a moving charge excites a magnetic field. The word excite is used because even when current is removed the EMF continues to propagate. Hence a current is needed to excite a field but not sustain it[12].

The most widely heard of and talked about EMFs are those surrounding power lines. These large conducting wires carry large voltages as part of electricity distribution networks. The cables are usually suspended above ground (figure 2.6) unless in a densely populated region in which case the cables are buried.

Figure 2.8. Different types of cables used in electronics, pictured obtained online[5]

2.3.4 Detection Methods

Numerous sensors have been developed to measure EMFs. Legislation has been drawn up with regards to the permissible levels of electromagnetic interference (EMI) generated by electronic equipment. These laws, known as electromagnetic compliance (EMC), differ between countries and applications but due to the vast amount of international trade much of the EMC rules are internationally standardized. The military has a stricter set of rules due to the nature of warfare. EMC also stipulates standards for the shielding of such equipment against outside fields.

Figure 2.9. Hand-held sensor, picture obtained online[6]

Figure 2.10. EMI test lab, picture obtained online[7]

Methods for EM detection range from small hand held sensors (figure 2.9) to entire laboratories (figure 2.10) dedicated to determining the EMF generated by electronics. The

small sensors are used for site inspection and independent studies. Different antennas are used to pick up different frequencies depending on their shape and size. Monopole or dipole antennas (figure 2.11) are rather common because they have a wide range of operation (low to high frequency) their ease of construction and predictability. Loop antennas(figure 2.12) are good for very low frequencies and magnetic fields.

Figure 2.11. Dipole antenna, picture obtained online[8]

Figure 2.12. Loop antenna, picture obtained online[9]

2.4 Electromagnetic Fields and Explosions

2.4.1 Brief History of previous studies

The earliest recorded study into the EM fields generated by explosions was published by Kolsky in 1954[16]. While studying the propagation of stress waves through solids he detected a small electrical disturbance. This prompted many other researchers to more closely examine the mechanism of generation for such a field, these include Cook[24], Andersen[18], Gorshunov[20] and Boronin[10,25,26]. Boronin[27] and Adushkin[17,28] also explored the EM field characteristics. Takakura[29] used this phenomenon was also used to validate a theory involving isolated bursts of solar radiation, due to impulsive noises similar to those detected as a result of an explosion. Although not fully explained a vague mechanism of generation was accepted and experiments to determine the source responsible for the EM field were conducted by Cook[24]. Studies relating not only to the mechanism of generation but also to their effects have been produced. investigations conducted by Pechkovskii[19] stated that the magnetic field generated by the explosion causes a quenching of the detonation process and Vel'min[30,31] investigated the passage of radio wave through the region of an explosion. In the majority of previous studies the main sources of information were the oscilloscope records; for this reason a study by Boronin[26] was conducted to take account of discrepancies when interpreting the electrical field pulses observed. Boronin[32] also undertook a concise literature survey to analyze the different methodologies used and mechanisms

proposed. In 2000 Bichenkov[33] conducted a study related to explosive shock waves and magnetic fields. The paper considered the shock wave compression of a magnetic field by waves capable of trapping current and transferring it within the shock front. In 2002 Soloviev[34] provided further insight into the initial stages of the explosion were provided, this work originally appeared contrary to previous publications but actually gave more detail into the time history of the EMF generated. Soloviev[35] more recently published a paper on the effects of physiochemical properties of soils on the EM signals generated by explosions. In 2006 Sorokin[36] modeled the shock wave excited by an explosion in the ionosphere. The model was meant to correspond to exact solutions for strong shock waves, extrapolate to small mach numbers and be in agreement with the experimental data.

2.4.2 Mechanism of EM Generation

In 1990 the mechanism proposed by Boronin[10] was as follows: in the initial moments of time deformation and failure of the metal shell occur. Gaseous and solid explosion products flow out through the cracks, with the gaseous products leading. The electro-kinetic effect and explosion product friction causes charges to build up. Opposite charges are acquired by both the explosion products and the shell fragments. Asymmetrical flight of the explosion products creates an effective dipole. The dipole effect grows as the gaseous and solid particles separate. The gaseous particles lose speed faster as they have less momentum, and thus the solid particles gradually overtake them. A sign change occurs when the solid particles overtake the gaseous particles. Solid matter surrounding the explosive charge is also propelled by the blast wave and is eventually overtakes the explosion products. It was suggested that the solid material overtakes the gas particles and then the solid particles. Figure 2.13 is from Boronin's paper and shows the electric field intensity of explosions from cylindrical shaped charges.

The 2nd sign change is explained by way of momentum. As the solid material passes the gaseous products they could potentially pick up their charge, and when the gaseous particles in turn overtake the solid particles, being slowed by their heavier mass, another sign change would occur. There is a competing process however, and that is the relaxation of charges in the conducting region. As the fragments move through the heated air (result of the shock wave), which is highly conductive, they loose their charge causing a reduction in the dipole moment. This theory has not been investigated further and to date the mechanism of generation is still unknown but does amalgamate many previous theories and account for many of the signals characteristics.

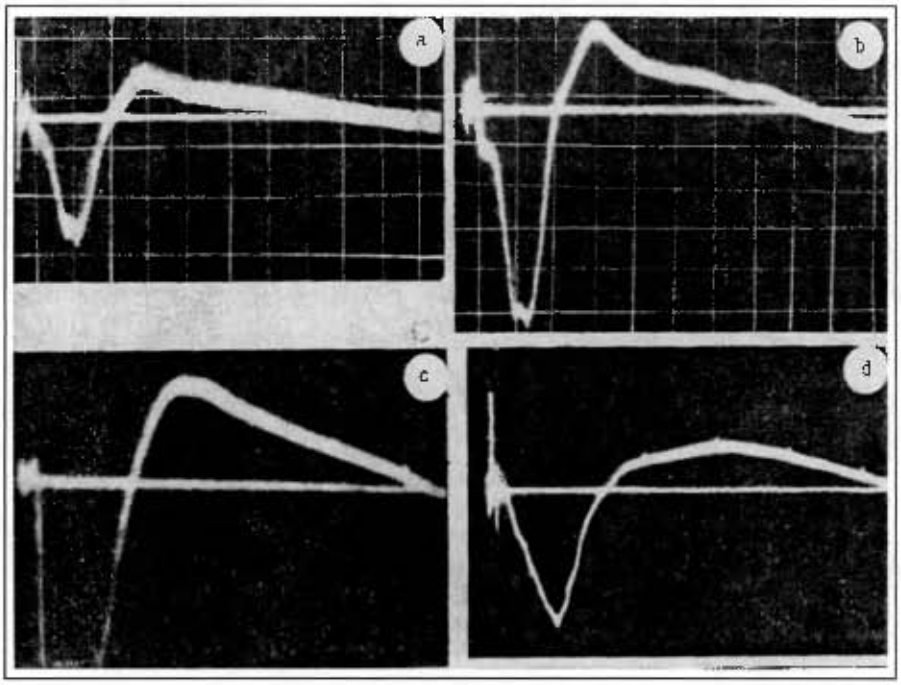

Figure 2.13. Oscillographic records of the field intensity at distances 4.5m (a) and 6,57m (b-d)[10]

Table 2.3. List of factors to be taken into account when looking at EM of explosives

Factors affecting the signals generated
Surrounding material[17]
Addition of impurities[18]
Explosive material[16]
Detonation method[20]
Packaging[19]

These studies conducted highlighted key issues to be faced in such experiments. The accurate measurement of certain phenomena accompanying the blast is a primary concern. The moment of detonation needs to be accurately recorded, so as to help clarify the signals' source. The sensor could pick up the signal from the detonation cord before the blast, causing a pre-triggering. Identifying the blast wave is also important as any motion of the antenna inside a field (the earth's magnetic field) causes a signal to appear. Placement of the antenna is an important point since its location determines which aspect of the EM field it picks up, again if the antenna is placed along the axis of detonation cord the signal obtained might be different.

2.4.3 Testing Methods

The generic testing method adopted by studies relating directly to the EM field generated explosions was to place antenna in the path of the blast wave to register the EM field. The antenna was attached to an oscilloscope which records the signal generated. The first test conducted by Kolsky[16] placed a sheet of Perspex between the explosive and a piece of wire (the wire acting as a stub antenna). The difference in test setups was minimal, for example when Boronin[25] wanted to determine the effect of an external field the explosion had to take place inside a Faraday cage. Some tests have been conducted where explosives have been detonated in the air, on the surface of the ground, Takakura[29] conducted his tests on grounded tables and Soloviev[35] even tested buried charges. These tests have commented on the effect of different detonation methods as well; by using fuse caps, detonating wire and heated fuses as methods of initiation.

2.4.4 Equipment used

Early recording was conducted with a cathode ray oscilloscope and rudimentary stub antenna (with no directional properties). Later, more specialized antennas were used, including the small horned antennas used by Takakura[29], dielectric receiver rods employed by Vel'min[30] and bi conical receiving antenna used by Boronin[26]. The oscilloscopes also developed from cathode rays to digital oscilloscopes. Pressure transducers are at times co-located with the antennas to identify the shock waves time of arrival. To synchronize the recording equipment and the blast event photocells have been used to detect the initiating flash.

2.5 Summary

The explosive being used during testing is well known and its characteristics have been documented. The detonation and shock wave theories contributed to the equations used in the blast wave analysis section(7.2.1). To accurately understand, model and predict any outcome in the field of Electromagnetism requires a solid foundation in its mathematical concepts. However certain methods used in this field of study can be used in the investigation (see chapter 6). The majority of studies conducted on this subject matter occurred between 1960 and 1970 with the topic being revisited again in early 2000. The latter work of Adushkin[17] and Soloviev[34] is of most interest and has provided guidelines for the test equipment and procedure that was followed.

3 Experimental Testing Procedure

3.1 Introduction

This chapter is divided into two main sections, preliminary and primary testing. Each section provides the objectives behind the series of tests and the procedure followed. Lastly a concluding section is provided to discuss the limitations experienced during testing.

3.2 Preliminary testing

3.2.1 Objectives

A set of preliminary tests were conducted to determine the most appropriate testing procedure and to determine what equipment would be required. These tests were conducted at the blast chamber of Blast Impact and Survivability Research Unit (BISRU) and at the military base in Langebaan. The testing at BISRU was performed to gain experience with the equipment and provided necessary insight into the types of signals that arise. The Langebaan testing was the first opportunity to test non-electric detonation and refine the test procedure.

3.2.2 Procedure

Detonations conducted at BISRU were initiated electronically*. The blast lab shown in figure 3.1 is comprised of a blast chamber and a control room. The colored boxes inside the blast chamber represent different pieces of equipment that are fixed inside the chamber. The control room is where the firing box is housed and piping underground (the dotted lines between rooms) runs between rooms enabling the detonator wires (and other cables) to be fed through.

*While this was noted in the literature review to be undesirable it was seen as acceptable in the preliminary stages

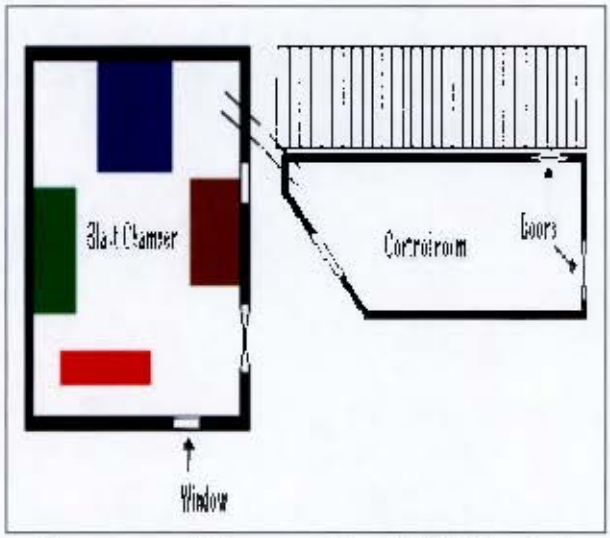

Figure 3.1. Schematic of the BISRU blast lab

The piping carried the coaxial cables for the recording equipment, the cord carrying the detonation signal and any other form of electronic wiring needed in the blast chamber. This situation was again not ideal as the many wires allow for induced signals to travel along their length and interfere with the recorded signal.
The tests were conducted with the lights off in an effort to reduce outside electronic interference. Initially a single inductive loop was placed approximately 1 - 1.5m away from a charge. The antenna was aligned with the normal of its aperture perpendicular to the detonation wires and in some cases at a 45°angle to determine orientation effect, see figure 3.2.

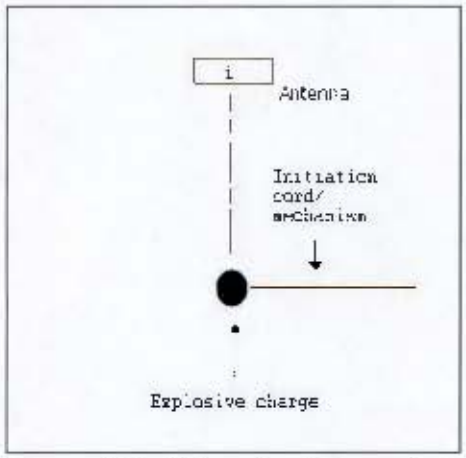

Figure 3.2. Schematic of the preliminary testing setup

Figure 3.3 shows how in the next round of testing a smaller inductive loop was included. This loop was made of copper and placed directly around the explosive, with the charge

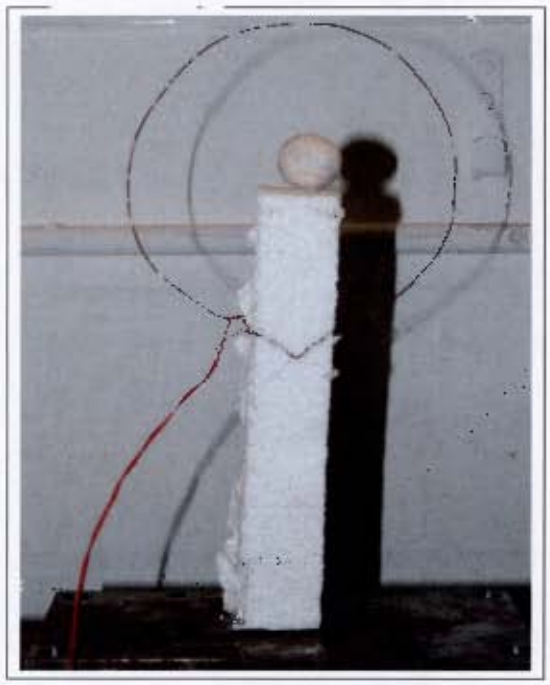

Figure 3.3. Copper loop antenna around explosive on styrafoam pillar

lying approximately 10cm away from its circumference.

In another set of tests a current clamp was included to identify the effect of the detonation wires. The final testing at BISRU involved a whip antenna, see figure 4.5, to identify if another type of antenna could be used to detect the signals. The antennas were placed in various SODs throughout testing but the orientation was for the most part maintained. The final preliminary test series was performed at Langebaan. This was the first opportunity for a mechanical detonation as well as being an environment with a relatively low EM noise floor. In addition to the loop mentioned earlier a commercial antenna was used, the R&S HE300 antenna with the HF module. The explosive was detonated with safety fuse cut to a length resulting in approximately a 30s delay. The antennas were originally placed as depicted in figure 3.4 between 2.5 and 3m away, with their aperture normals at right angles to one another, and later moved to within 1.4m of the charge. A photo of the loop antenna at the Langebaan test range is provided in figure 3.5, which indicates the surroundings to be rocky with a consistent level of ground vegetation.

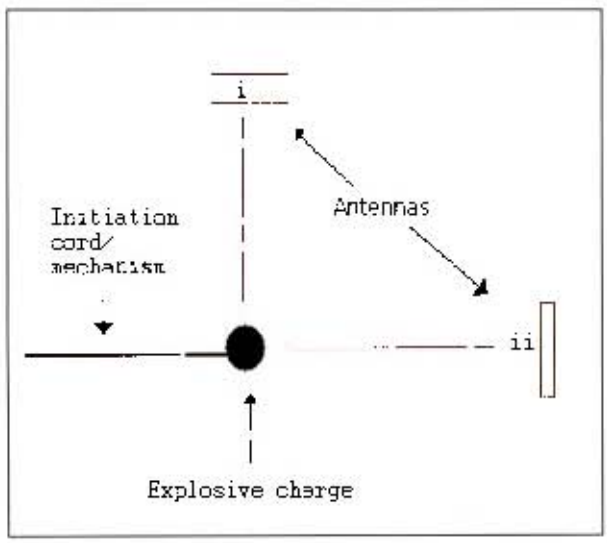

Figure 3.4. Schematic of Langebaan test setup

Figure 3.5. Loop antenna at the Langebaan test range after a blast

3.3 Primary testing

3.3.1 Objectives

For primary testing and an analytical data set, the data had to come from mechanical detonation and have a minimal amount of external interferences. The testing ground was isolated to the extent that external fields were identifiable and could therefore be accounted for.

3.3.2 Procedure

For the testing of EMP generated by high explosives, it was required that the blast event be initiated mechanically. Three antennas were used to accommodate for its radiation pattern, shown if figure 3.6 and discussed in section 5.3, and examine any orientation effects. Each antenna was placed near the charge and rigidly fixed (meaning that it did not move

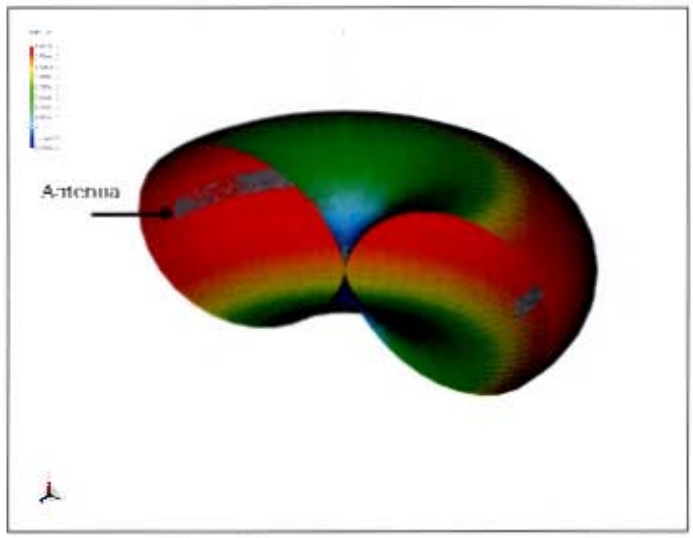

Figure 3.6. Three dimensional radiation pattern based on equation (5.4)

under the pressure from the shock wave). Tests were conducted over a range of charge masses and with varying stand off distances for the antennas. Since surrounding material also plays a part in the recorded signal[28], any loose soil or particles that can be picked up by the blast wave will affect the output; therefore after each test the area was reset as before to maintain similar test conditions and any alterations were noted.

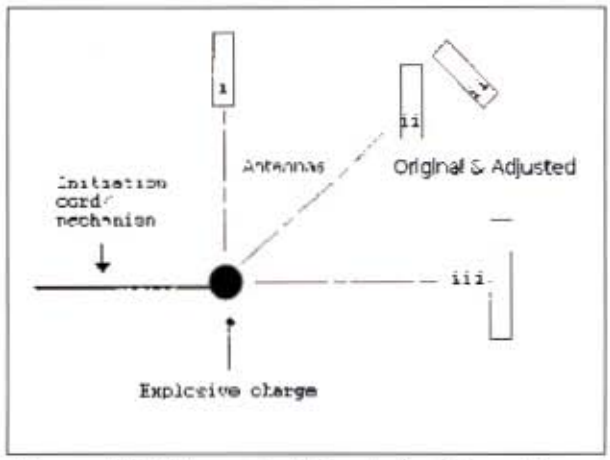

Figure 3.7. Schematic of Paarderfontein test layout

The antennas were arranged as depicted (figure 3.7), with the charge being placed on top of the plastic pillar. A photo of the Paarderfontein setup is given in figure 3.8, this shows the lines drawn in the soil to help line up the antenna and shows the typical surrounds to be sandy and sparsely vegetated. For each charge of explosive the antennas were set at five different SODs. For each SOD and mass two shots were blasted to provide data on the repeatability of the signals. The charges were shaped into balls, the diameters of which were measured for each shot. These charges were then placed on top of plastic tubes of fixed height, held up with a metal stand. The geographical position of the testing was recorded to account for local geographical effects. Distance measurements were taken from the charge to the base of the antenna, as well as to the center of each aperture.

Figure 3.8. Test setup on the day of testing at Paarderfontein

During testing the orange loop was adjusted to help receive signals. The loop was re-orientated, it's aperture at an oblique angle to facing the blast directly, this is the adjusted antenna position seen in figure 3.7.

3.4 Limitations

Potential for human error is present in the form of the charges being rolled by hand as well as the depth of penetration of the detonator into the explosive.
The degree to which the environment was isolated raised concern since the effective removal of outside signals is only possible in a enclosed room.
The lack of experience with this kind of testing technique exposes the chance of unforeseen difficulties.

4 Equipment

4.1 Introduction

The equipment chapter follows the same structure as the previous chapter. It is divided into preliminary and primary testing and describes the equipment available during testing and when each item was used. A concluding section on the limitations is also provided to address certain issues encountered wit the equipment.

4.2 Preliminary testing

Four sets of preliminary tests were conducted at BISRU labs. The tests were set up in a similar fashion with the differences coming in the addition or removal of equipment. This was because of the availability of equipment and in an effort to determine which equipment was best suited for testing.
The first round of tests at BISRU were recorded with a high speed oscilloscope from Tektronix, the TDS 2000 series shown in figure 4.1, and the signals were received by a custom made loop antenna, shown in figure 4.3 and discussed in detail in section 5.

Figure 4.1. Tektronix oscilloscope, picture obtained online[11].

A 20g charge mass was placed on a styrafoam pillar 150cm away from a metal plate. The loop was placed between the charge and the chamber wall. Alongside the loop was a light sensor, figure 4.2, that was used as a trigger. The sensor responded to a certain optical frequency and when the required intensity was reached the sensor generated a pulse. The antenna has 20 turns and was built by ©EET, the oscilloscope was able to record 2500 points and a sampling frequency of 10MHz.

Figure 4.2. Light sensor

Figure 4.3. Loop antenna

For the 2nd test a small copper loop seen in figure 4.4 was placed around the charge. A copper wire was shaped into a ring and connected to wires that were left open and ready to be connected to banana clips at a later stage.

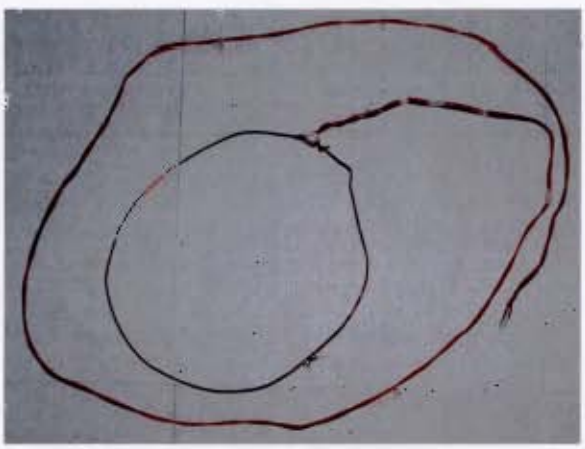

Figure 4.4. Copper loop used in very close proximity to the charge

In conjunction with the oscilloscope a data card was also set to record the event. The card was an Adlink PCI - 9812, a 4 channel 12 bit analog input card, capable of recording at speeds up to 20 MHz (simultaneous sampling) and possessing a -5 to +5 voltage range. The data card was used to confirm the signals seen on the normal oscilloscopes and offered a longer record length than the oscilloscopes.

Figure 4.5. Whip antenna developed by EET

In the 3rd test a current clamp was included and in the 4th series a specially made whip antenna was used. The whip antenna in figure 4.5 was built by EET in conjunction with the loop antennas. The oscilloscope was not available, leaving only the data card to record the event.

The last round of preliminary testing was conducted at Langebaan military base. Three different antennas were taken and used in the testing: a R&S commercial loop (figure 4.6), the custom loop antenna used at BISRU and the small copper loops.

Figure 4.6. R&SHE300 with optional R&SHE300HF RF module for 9 kHz to 20 MHz

The commercial antenna was part of an active directional antenna set purchased from Rhodes and Schwarz. The oscilloscope recording the data was the Agilient 300 series (figure 4.7), powered by a stand-alone power system. The oscilloscope was protected from the blast

by a metal box and the trigger was again the light sensor.

Figure 4.7. Oscilloscope used at langebaan test range

4.3 Primary testing

For the tests conducted at Paarderfontein only one type of antenna was used, the loop antenna designed and built by *EET*. The oscilloscopes supplied at Paarderfontein were the same tektronix oscilloscopes initially used at BISRU and the same light sensor was also used. The light sensor was originally connected to the trigger but light conditions were not conducive to its use, and it was subsequently replaced by a light sensor set to a different wavelength. The replacement light sensor seen in figure 4.8 was also built and developed by EET. After a few test shots it was determined that the light emanating from the shock tube was pre-triggering the oscilloscope. A sheet of metal and sand bags were placed on top of the tube to cover its flash.

Figure 4.8. The replacement light trigger

4.4 Limitations

The antennas had limited range of operation and were identically constructed reducing the frequency range that could be investigated.
The oscilloscope could only have a maximum of 2500 samples - this limited the sampling speed since the duration of the event was unknown. Increasing the sampling speed decreased the record's time length.
A sampling frequency of 2.5MHz was used setting the nyquist frequency at 1.25MHz to allow for as large a band as possible, this was prior to confirming the antenna's frequency band. This sampling frequency gave a record length of 1ms.
The oscilloscopes were capable of being run off a built-in power supply, but due to the expected duration of testing a generator was run to provide power, adding to the ambient noise floor.
While no equipment was present to search exclusively for signals possibly generated by the electro-seismic effect it has been stated that such signals are usually in a lower frequency spectrum, between 0.5 and 10Hz[37]. A small section however has been produced to discuss the possibility of this effect coming into play during testing, see section B.
The effect of the dust cloud on the signals was ignored as it was seen to be outside the scope of this project[17].

5 Loop antenna

5.1 Introduction

The loop antennas, figures 5.1 - 5.3, require detailed mention since they was a key coupponent of the testing. The antennas were built by *EET* and were used from the outset of this project. Originally the antenna was used in a different project for similar purposes and then used in the preliminary testing. Thereafter two more antennas were commissioned for primary testing*. They were of simple construction a plastic ring covered the turns of the loop, which was connected to circuitry inside a metal box attached to the bottom of the loop.

Figure 5.1. Channel 1 loop

Figure 5.2. Channel 2 loop

Figure 5.3. Channel 3 loop

5.2 Physical description

The loop antenna was made from a plastic ring and had wooden support beams. Wire was threaded through the ring to make up 20 turns which was then connected to circuitry housed in a metal box. The wooden beams provided support and rigidity to keep the ring's shape and hold it upright under a blast wave. The loop had a diameter of 0.68m and was attached to the beams with plastic ties. The metal box sat directly below the loop and contained a veriboard construction of the circuit shown in figure 5.7. Two 9V batteries powered the antennas and these too were inside the box.

*The scope of this project did not include antenna design - as a result antenna characterization was delayed until after testing

5.3 Mathematical analysis

The antennas were designed and required to work at low frequencies. The characterizing of antennas at low frequencies is not carried out on a regular basis and requires a specialized testing facility, so a mathematical approach was adopted.

The antenna can be viewed as an electrically small antenna. This in turn can be approximated by an infinitesimal magnetic dipole with an axis perpendicular to the plane of the loop. Electrically small antennas are those whose overall length ($2\pi\times$ circumference) is usually less than 1/10 of a wavelength. The expected range of frequencies in this experiment were to be between the mid-range Hz and low kHz[17]. Using the equation

$$\lambda = \frac{c}{f} \tag{5.1}$$

the range of wavelengths (λ) was calculated by taking the lowest and the highest expected frequency. The lower limit was set as 100Hz and the upper limit set at 100kHz. This provided a range of wavelengths between 3km and 3000km.

Antennas have near and far fields of activity and the region are defined by the relationship between λ and SOD (r). If

$$\frac{2\pi r}{\lambda} \ll 1 \tag{5.2}$$

data is collected in the near field and conversely of the value is greater than 1 the tests would be in the far field. The lower wavelength value was used to identify the region testing was conducted in as the near field as well as confirm the earlier assumption of an electrically small antenna.

The antennas gain pattern was investigated to determine the best configuration for testing. In the near field the difference between the magnetic and electric field is not definitive and most antennas have their gain patterns specified in the far field. In determining the far field gain pattern Balanis[12] first obtains the average power density (in Watts/m^2)

$$W_{av} = \frac{1}{2} Re(E \times H^*) \tag{5.3}$$

by taking the real part of the cross product of the electric and magnetic fields respectively. This is then uses it to work out the radiation intensity (in Watts/steradian)

$$U = r^2 W_{av} = \frac{r^2}{2\eta} |E_\Phi(r, \theta, \Phi)|^2 \tag{5.4}$$

which turns out to be solely dependent on a component of the electric field (E_Φ), the intrinsic impedance (η) and the SOD.

A simulation carried out by a student for a similar shaped and sized antenna performed with ©FEKO predicted the radiation pattern for the loop. The results of the simulation are seen in figure 5.4, where the normal of the loops aperture faces up and the colour differences

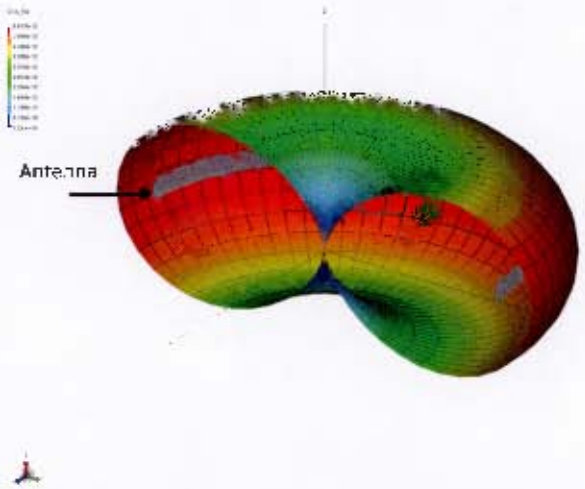

Figure 5.4. Three dimensional radiation pattern based on equation (5.4), for an electrically small antenna

illustrate the intensity variations. This pattern is true for a certain frequency where the overall circumference length multiplied by the number of turns is less than the wavelength. As the frequency increases the wavelength decreases (equation (5.1)) and this increases the effective length of the antenna. The change in length effects the effective circumference which results in a change of shape for the radiation pattern. As the circumference passes the wavelength there is the formation of multi-lobes as seen in figure 5.5.

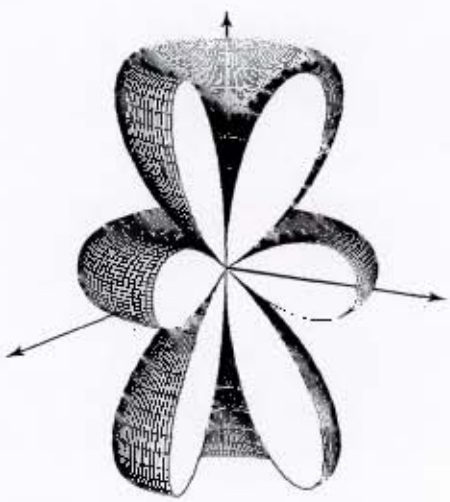

Figure 5.5. Amplitude pattern for a circular loop with constant current distribution[12], for size comparable to wavelength

These patterns are for far field classification but provide a better picture as to how the

antenna functions. Analysis of the antenna showed that the best orientation for receiving signals was either perpendicular (broadside) or in the plane of the loop (endfire) depending on the electrical length given in λ of the antenna at a specific frequency. The two configurations are both sensitive to different types of filed lines. Broadside would detect radially directed lines while endfire detects lines circulating the radiator.

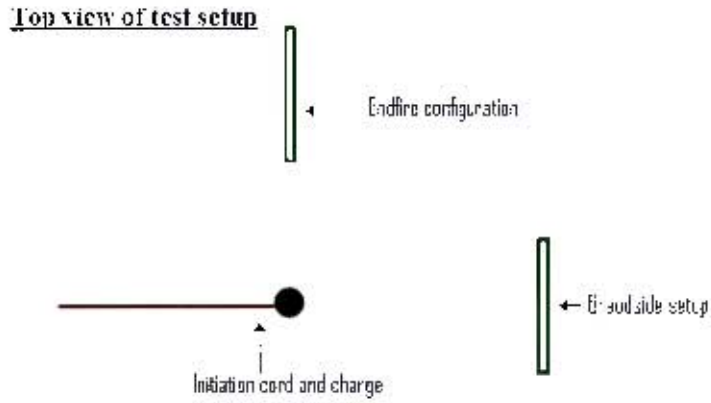

Figure 5.6. Illustration of how antenna were setup for receiving signals

Three antennas were used, the first faced the blast with the aperture, the third faced the blast side on and the remaining antenna was adjusted in orientation during the experiment for better signal detection. The setup is illustrated in figure 5.6.

5.4 Loop antenna as a field probe

When taking measurements that are recored by an oscilloscope, the loop antenna provides an open terminal voltage $V(t)$, as a function of time, which is proportional to the rate of change of the magnetic field (normal component) $\frac{dB}{dt}$ as seen by the loop. For a loop with N turns and area A,

$$V(t) = N \times A \times \frac{dB}{dt} \tag{5.5}$$

If B were sinusoidal with and angular frequency ω

$$B(t) = B_0 sin(\omega t) \tag{5.6}$$

then

$$\frac{dB}{dt} = \omega B_0 cos(\omega t) \tag{5.7}$$

$$V(t) = NA\omega B cos(\omega t) \tag{5.8}$$

Equation (5.8) shows that the voltage seen at the terminals is therefore proportional to angular frequency and the magnetic field, demonstrating how the recorded signals relate to the magnetic field being investigated.

5.5 Circuit analysis

The circuit used in this project as built by *EET*, after specifying a high gain wide band low frequency antenna. The request was for an antenna to operate in the kHz range, from around ten up to the hundreds, while offering as much gain as possible. The details of construction and testing were left in the hands of the designer. Investigation into this circuit showed it to be flawed and resulted in digital manipulation of signals so as to correct for the error.

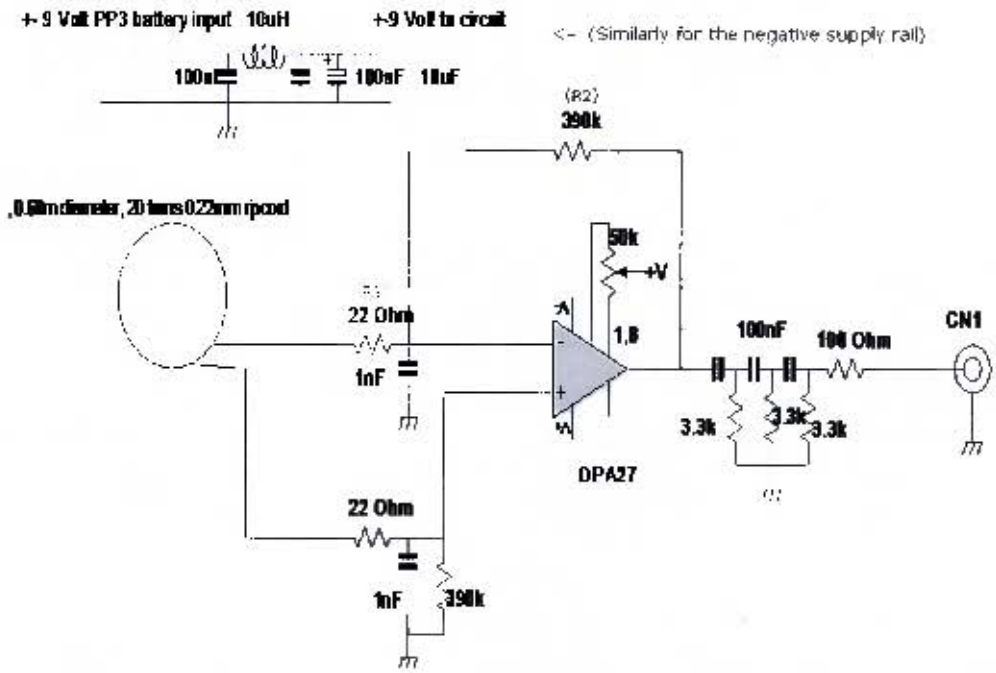

Figure 5.7. Circuit diagram of the bandpass amplifier attached to the loop antenna

The circuit diagram shown in figure 5.7 represents the circuit inside the metal box at the base of the antenna. The OPA27 is configured as a differential amplifier set up with an offset voltage trim controlled by the 50k potentiometer. The circuit can be separated into two stages, amplification and filtering. The amplification was a process of the OPA27 low noise high precision operational amplifier. It has an open loop gain of approximately 800000 (118dB). The closed loop gain

$$G = \frac{R_2}{R_1} \tag{5.9}$$

was worked out by dividing the feedback resistor by the input resistor and turned out to be 18000 (85dB), which is within the amplifier's capability. For the gain to be effective G as calculated above should be 10 times less than the open loop gain. The specified open loop gain of 118dB is valid up until 10Hz, which is roughly the 3dB point, after which it has the characteristic roll off of 20dB/decade as seen in figure 5.8. This graph was plotted in MATLAB after taking information from the data sheets.

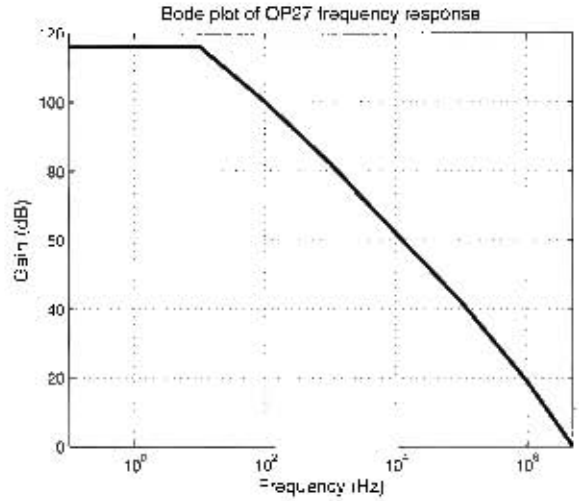

Figure 5.8. Bode plot of OPA27

The output of the opamp is connected to a 3rd order RC high pass filter whose cut off frequency is defined as

$$f_c = \frac{1}{2\pi RC} \times k \tag{5.10}$$

This equation showed the cut off frequency for the 3rd order filter to be some constant k times the cut off frequency of a 1st order system. A normal 1st order system with the resistor and capacitor values used in this circuit yields a cut off frequency of 482.3Hz, through simulation (figure 5.9) the estimated $-3dB$ point for the 3rd order system was found to be 2.84kHz. The high gain asked of the opamp resulted in an effective low pass filter which followed the opamps run off portion. the high pass filters cut off point also narrowed the bandwidth of the circuit.

The total response was modeled with ©MICROCAP simulator, the student version and is shown in figure 5.10.

Model predictions were important in understanding the effect that each component adds to the circuit but for the actual response a physical test was carried out. The loop was disconnected from the main circuit and the end of wire connected to a signal generator. The input signal from the signal generator was at its lowest value, between 100 and 120mV, but clipping was still present at the output of the opamp. A voltage divider consisting of 1 Ω and 1 kΩ resistor provided a further 1000-fold reduction in amplitude. A sine wave was then fed into the system and swept through the different frequencies to determine its response in terms of both magnitude and phase. The measurements taken during circuit testing are shown in figure 5.11 and 5.12.

The two parts, phase and magnitude, form a single transfer function for the circuit. The complex function represent the changes applied to the incoming signal, see Appendix A. Since not all frequencies were tested the missing values were interpolated using a cubic

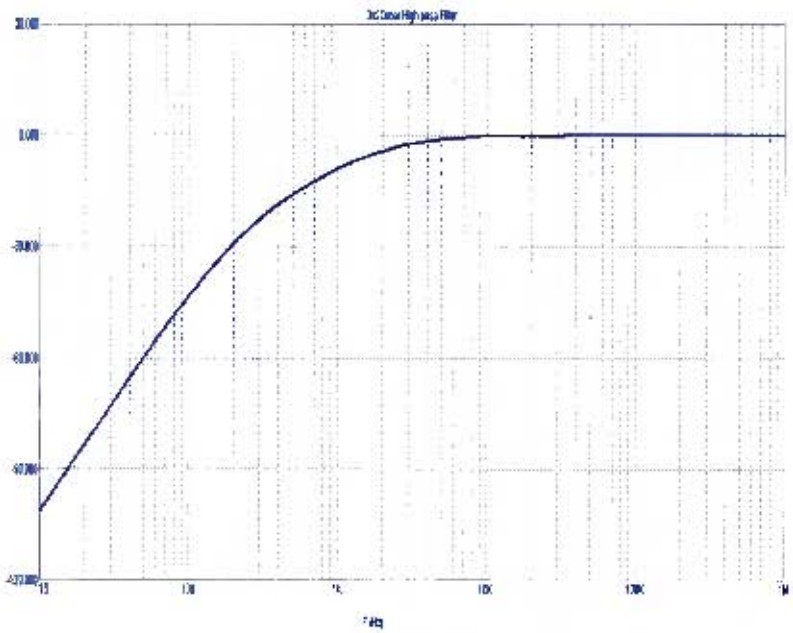

Figure 5.9. High pass filter response of circuit

interpolator function. The results of the interpolation (figures 5.13 and 5.14) were then averaged to create a general response function of the circuit.

To see the true waveform over the desired band the influences of the circuit (phase and magnitude distortion) had to be removed. This was achieved by inverting the transfer function and applying it to the Fourier transformed waves in the frequency domain. The function however was not applied over the entire frequency spectrum as only a portion of the spectrum was tested and provided valid data in creating the function. The inverse function was applied between 300 Hz and 500 kHz. This removed the effect the circuitry had on the waveform's shape and magnitude.

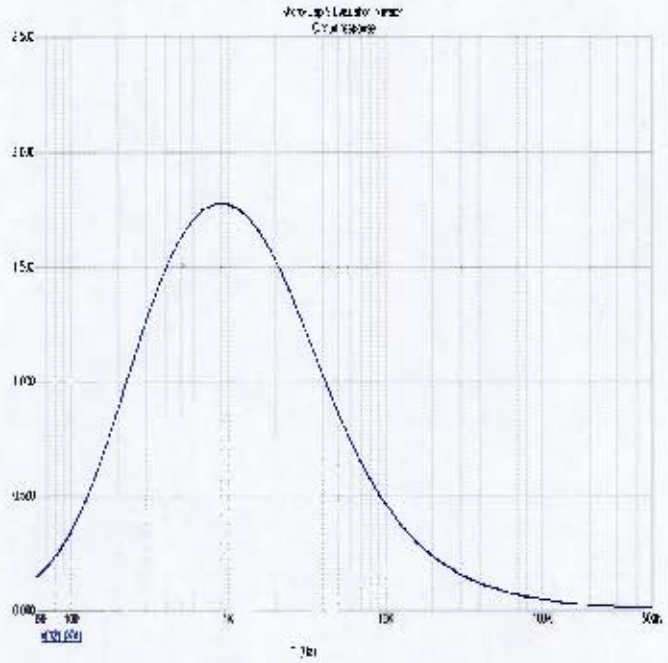

Figure 5.10. Predicted overall response of circuit

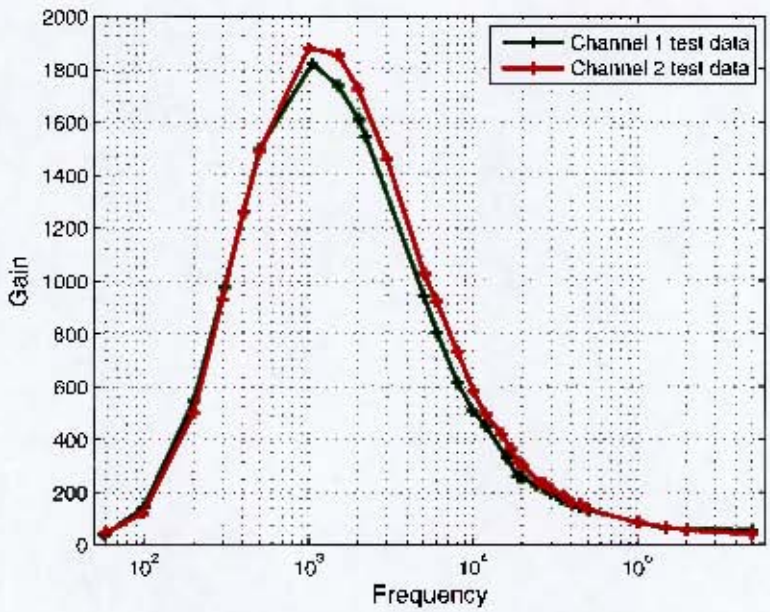

Figure 5.11. Measured gain response of the circuit

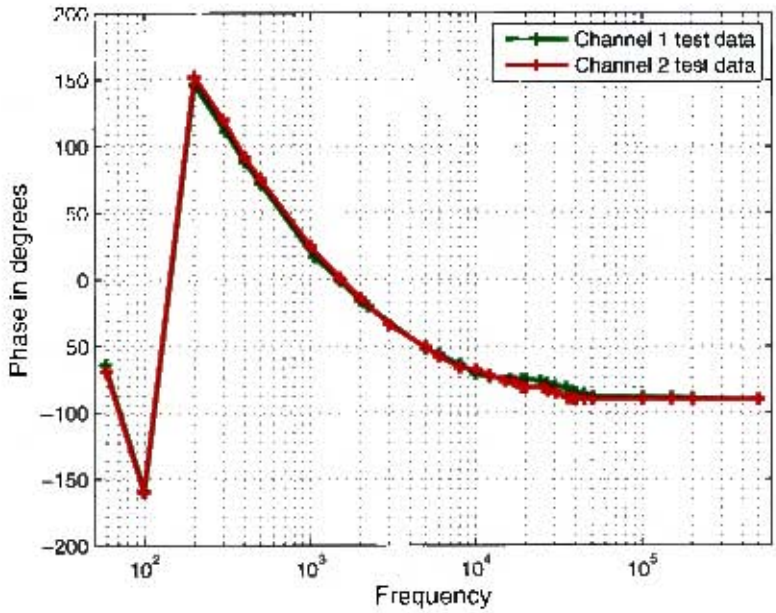

Figure 5.12. Measured phase response of the circuit

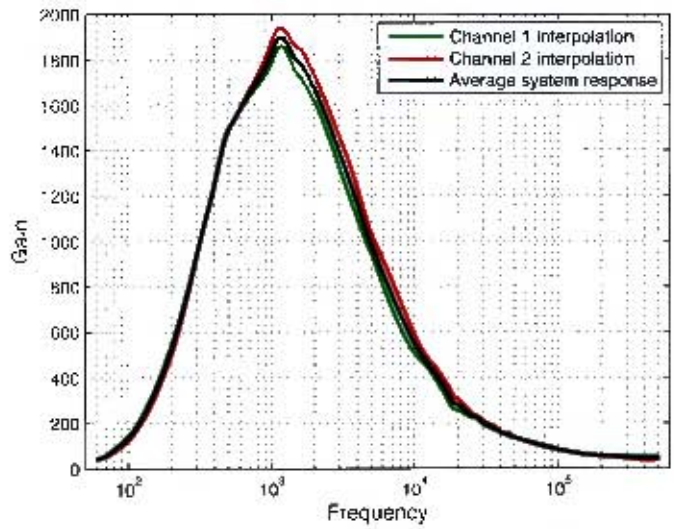

Figure 5.13. Interpolated gain response of the circuit

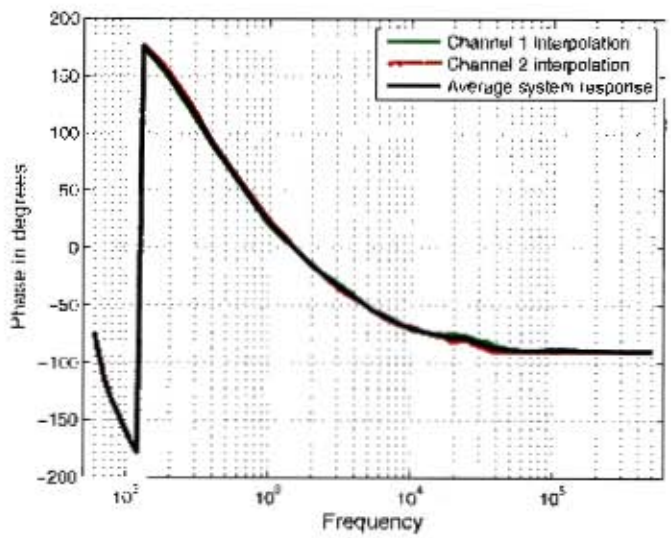

Figure 5.14. Interpolated phase response of the circuit

6 Signal processing and Spectrum analysis

6.1 Introduction

When thinking of a spectrum the first idea that usually comes to mind is that of light and the rainbow. This image is easily the most recognizable display for showing the different wavelengths of light. There are many kinds of spectra and each is analyzed for different purposes. These applications range from cardiograms, providing information on a patients health to a radiation spectrum revealing scientific insights into an object's internal structure and makeup.

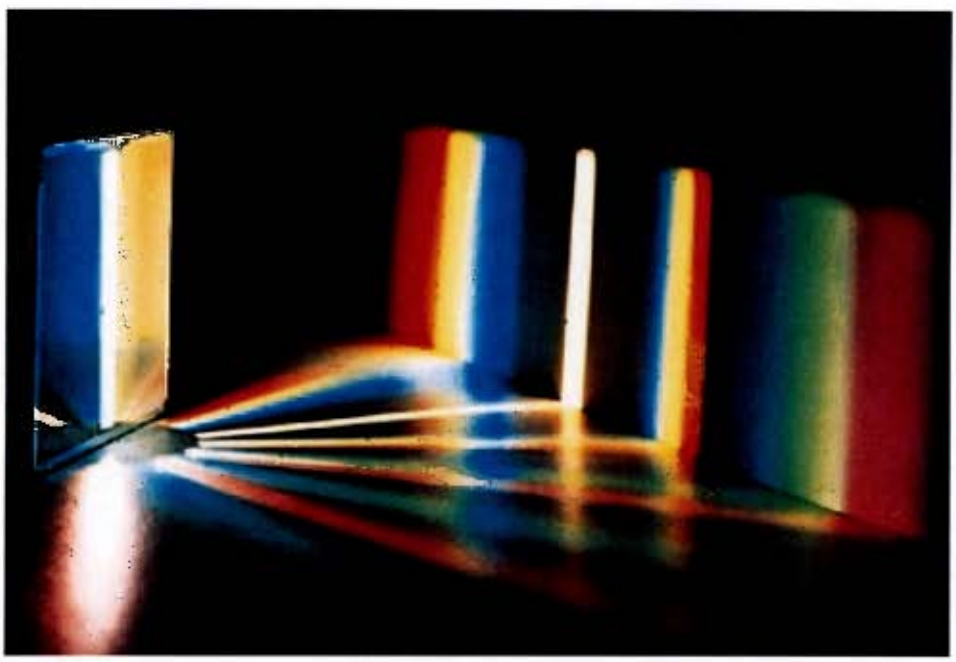

Figure 6.1. Prism with a beam of light split into different wavelengths, picture obtained online[13]

The spectrum analysis employed for this project is mainly used by electrical engineers and deals with the conversion of a signal between the time and frequency domain.

6.2 Fourier analysis

Fourier analysis[38] is a very important tool in spectral analysis - some of its central ideas and those most pertinent to this study revolve around: time vs frequency domain, the representation of waveforms in terms of complex exponentials and magnitude and phase spectra. The method of Fourier analysis came from work carried out by Fourier on heat transfer, and by Laplace with his work in mathematical probability[39,40]. The analysis is based on the idea of a set of mutually orthogonal vectors. For example let U and V be vectors of equal length then

$$U \cdot V = 0 \tag{6.1}$$

means

$$\sum_{i=1}^{n} u_i v_i = 0 \tag{6.2}$$

where u_i and v_i are the components of the vectors U and V. With these and similar vectors a vector space $S = u_1, u_2, u_3...$ can be created which has an orthogonal basis. When the idea of orthogonality is extended to a set of functions $S = f_1(t), f_2(t), f_3(t)...$ it can then be said that the members of S form an orthogonal set over the interval $a < t < b$ if

$$\int_a^b f_n(t) f_m(t) \mathrm{d}t = 0 \qquad \text{when} \qquad n \neq m \tag{6.3}$$

Further defining the natural frequency as

$$\omega_o = \frac{2\pi}{b-a} \tag{6.4}$$

it can be proved that

$$S = ..., e^{-j3\omega_o t}, e^{-j2\omega_o t}, e^{-j\omega_o t}, 1, , e^{j\omega_o t}, e^{j2\omega_o t}, e^{j3\omega_o t}, ..., e^{jn\omega_o t}... \tag{6.5}$$

forms such an orthogonal set . The discrete Fourier transform is the tool used in computers when performing Fourier analysis. The discrete transform pair is defined by Morrison[38] as

$$f_k = \frac{1}{N} \sum_{k=0}^{N-1} F_n e^{j2\pi nk/N} \qquad (0 \leq k \leq N-1) \tag{6.6}$$

$$F(n) = \sum_{k=0}^{N-1} f_k e^{-j2\pi nk/N} \qquad (0 \leq n \leq N-1) \tag{6.7}$$

where k and N are the sample numbers in the time and frequency domain respectively. These equations are called the synthesis and analysis equations respectively. The synthesis equation allows us to express the discrete function f_k as a linear combination of a set of continuous complex exponentials. When implemented by a computer the most common algorithm used is the Fast Fourier Transform (FFT), developed by Cooley and Turkey[38].

This algorithm is a very fast method and reduces the number of operations considerably; a direct transform of N points takes N^2 calculations while a FFT takes $\frac{1}{2}nLOG_2(n)$. The increase in speed is only effective when the sample size of the signal is a power of 2 (1024, 2048, etc...). The complex coefficients of (6.7) are usually expressed separately in phase and magnitude to obtain a clearer picture. If the waveform is in volts across a resistor (R) or amperes through a resistor it can then be used to determine the theoretical instantaneous power dissipated from using

$$P = \frac{|f_p(t)|^2}{R} \tag{6.8}$$

where $f_p(t)$ is the voltage or

$$P = |f_p(t)|^2 R \tag{6.9}$$

where $f_p(t)$ is the current periodic waveform. The absolute signs are not necessary for real waveforms but these equations hold for complex signals too. Assuming a 1Ω resistor makes the two equations equal, meaning the power in a signal may be determined by taking the square of a signals modulus.
For a pulse or non-periodic signal it is more correct, however, to talk about the energy content of the signal, since every physically realizable signal of finite length has a finite energy content (E) as worked out from

$$E = \int_{-\infty}^{\infty} p(t)\mathrm{d}t = \int_{-\infty}^{\infty} |v(t)|^2 \mathrm{d}t = \frac{1}{2\pi} \int_{-\infty}^{\infty} |F(\omega)|^2 \mathrm{d}w \tag{6.10}$$

This equation assumes the resistor to be 1Ω and the signal $v(t)$ to have a Fourier transform $F(\omega)$. The energy worked out is referred to as the 1-Ohm energy content of a signal[38]. The FFT gives an approximation of the Fourier transform that can be made as accurate as required. Padding is the increasing of the signal length which has the effect of decreasing the sample spacing in the frequency domain.

6.3 Window functions

Taking a sample of a larger signal usually results in discontinuities at the samples beginning and end. This can be clearly seen in the example shown in figure 6.3 which the truncated version of the signal in figure 6.2. These abrupt ends cause errors in the spectral representation of tech signal. The truncation is equivalent to multiplying by a rectangle window function.

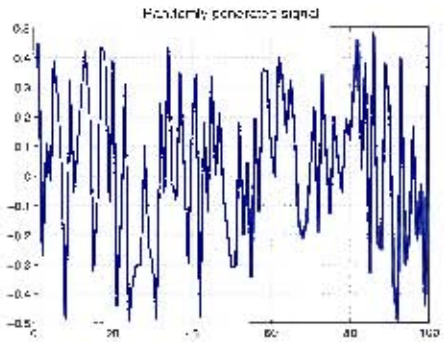

Figure 6.2

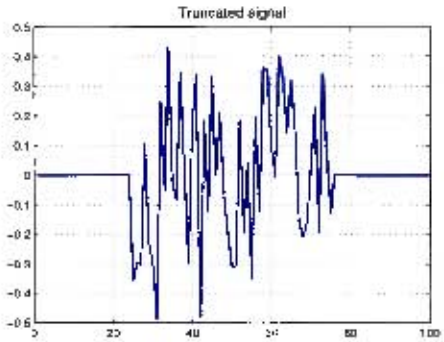

Figure 6.3

A window function is zero valued outside of a certain interval and when applied to a signal gives the result a zero value outside of the same interval. When performing a transform a "window" is inherently present. The problem is the window is not ideal for all purposes. Applying a window function which has smooth ends reduces the errors in the frequency domain. The characteristics of various such functions are described in table 6.1.

Table 6.1. Characteristics of smoothing windows[14]

Smoothing window	-3dB Main lobe width	-6dB Main lobe width	Max side lobe level	Side lobe roll off (dB/decade)
Rectangular(none)	0.88	1.21	-13	20
Hanning	1.44	2	-32	60
Hamming	1.3	1.81	-43	20
Blackman-Harris	1.62	2.27	-71	20
Exact Blackman	1.61	2.25	-67	20
Blackman	1.64	2.3	-58	60
Flat top	2.94	3.56	-44	20

There are standard options for these windows as well as the option of developing a specific window for the task at hand. Two well known and often used windows include the "Hanning" and "Hamming" windows. They are similar in structure since they are based on similar equations. The Hanning window is more useful for analyzing transients whose length is greater than that of the window as it has a smoother decay rate and is less likely to have discontinuities at the ends[14]. The difference in three typical window function is seen in figure 6.4 where a rectangular , Blackman-Harris and Hanning window are plotted on the same graph.

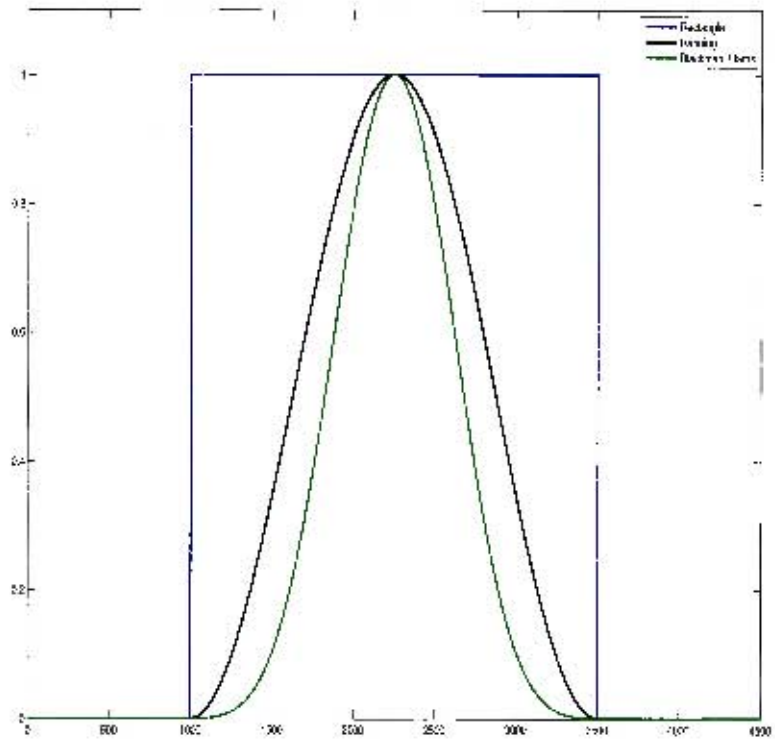

Figure 6.4. Different types of window functions, as generated by MATLAB, over 2500 points

Choosing a window is made simpler when examining their characteristic response, figure 6.5, which illustrates the Fourier transform (for positive frequencies) of a general window function. the window function reduces the spectral leakage. The width of the main lobe limits the frequency resolution of the windowed signal, meaning the ability to identify closely spaced frequencies improves as the lobe width narrows. The choice of which function to apply is a decision based on the trade off between the main lobe width and side lobe levels.

To illustrate this a single 50 Hz sine wave is shown in figure 6.6 and the FFT of this wave is seen along side it in figure 6.7. The FFT was implemented by taking a direct point transformation. The FFT of a step wave is shown in figure 6.9 next to the original wave input (figure 6.8).

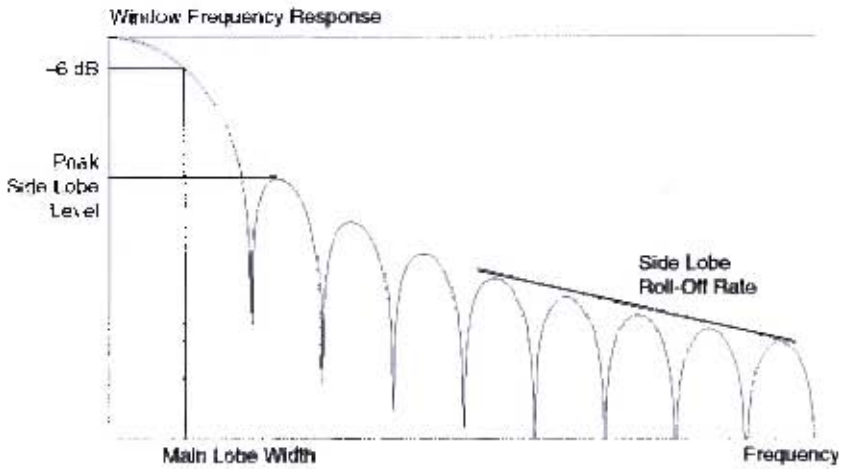

Figure 6.5. Frequency response of a window function highlighting its main characteristics[14]

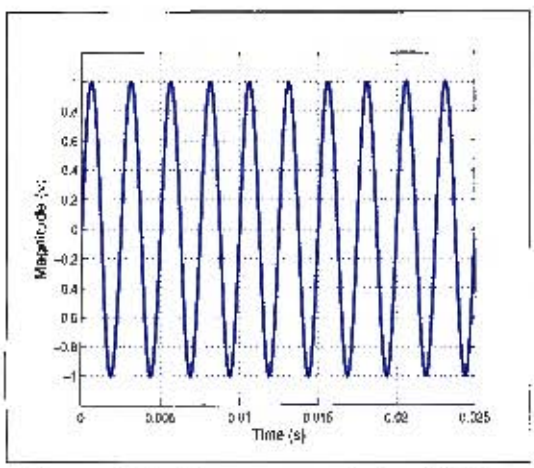

Figure 6.6. Sine wave sampled at 100kHz

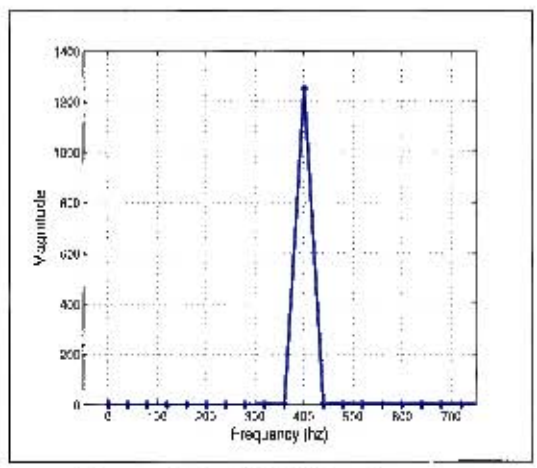

Figure 6.7. FFT of the sine wave

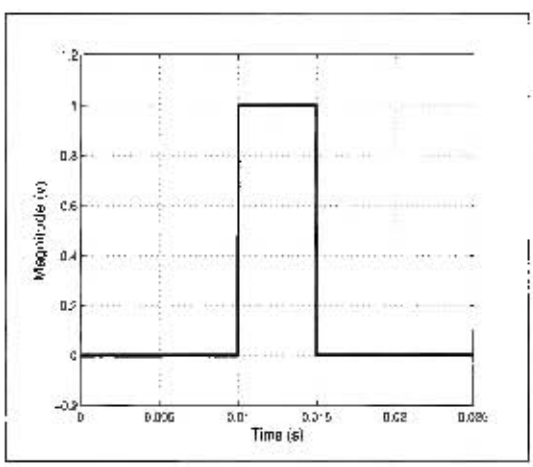

Figure 6.8. Step wave sampled at 1Khz

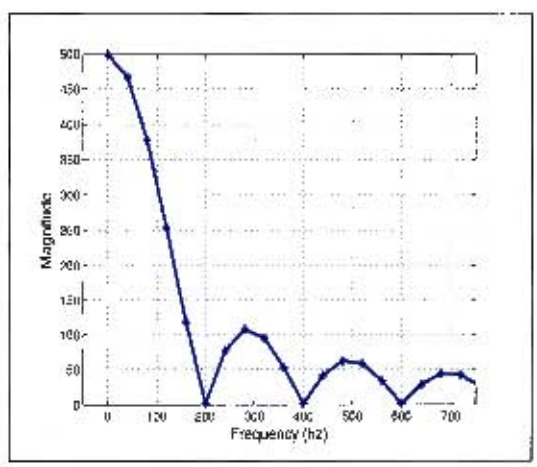

Figure 6.9. FFT of the step wave

The FFT of both of these signals shows the space between points and how a piecewise linear curve is fitted to them. Zero padding the time domain signal is achieved by adding zeros to the end of the signal, after applying the window function, in an effort to increase its length while ensuring that no discontinuity is introduced. Increasing the number of points available to be transformed is beneficial as an FFT transforms N points to N points without increasing the frequency range. So the more points in the time domain the more samples available in the specified frequency range. The results of padding the signal are shown for both the sine wave and the step wave in figures 6.10 and 6.11. Instead of the irregular and unsmooth result, both FFTs reveal a more finely sampled picture of the frequency spectrum.

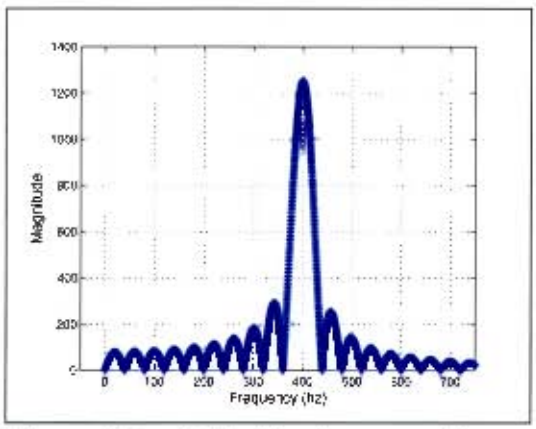

Figure 6.10. FFT of the sine wave with zero padding

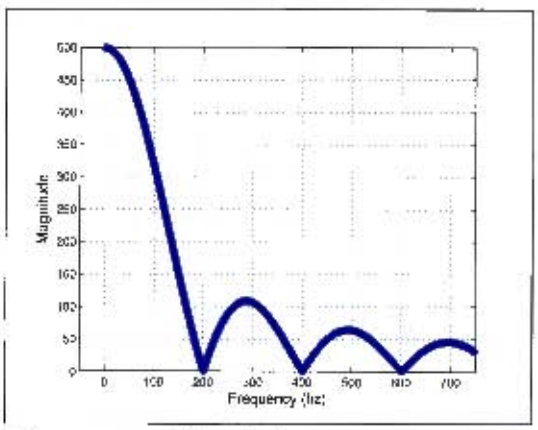

Figure 6.11. FFT of the step wave with zero padding

The application of the window function noticeably reduces the side lobe levels in the sine wave transformation (see figure 6.12). These techniques, window function and padding were used when analyzing the recorded signals.

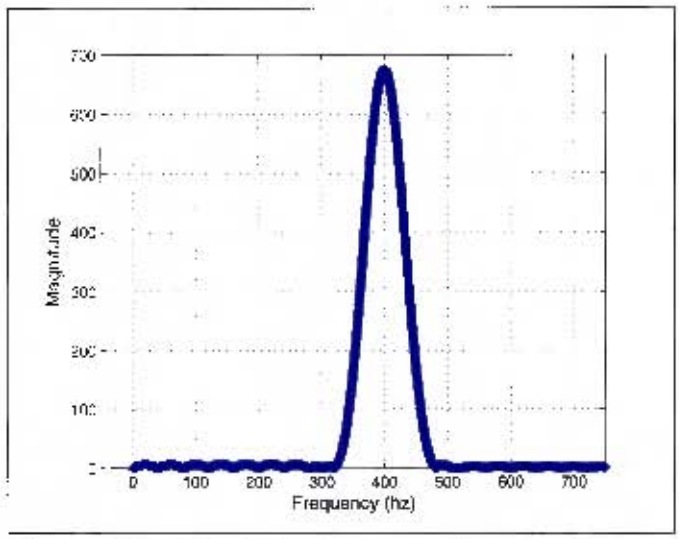

Figure 6.12. FFT of the sine wave with zero padding and a window applied

The output of the FFT had to be adjusted (by an amplitude scaling factor) to account for all the adjustments made to the raw data (windowing and zero-padding).

6.4 Pattern recognition

MATLAB provides a basic function called *xcorr* (cross correlation), which can be used to estimate the normalised cross correlation between two signals, defined as

$$C_{xy} - \frac{E\left\{(x_{n+m} - \bar{x})(y_n^* - \bar{y})\right\}}{\sigma_x \sigma_y} = \frac{E\left\{(x_n - \bar{x})(y_{n-m}^* - \bar{y})\right\}}{\sigma_x \sigma_y} \tag{6.11}$$

where

$$\sigma_x = \sqrt{E\left\{(x - \bar{x})^2\right\}} \qquad \text{similarly for } y \tag{6.12}$$

and E is the expected value operator, x and y are two stationery processes and m a delay. This estimates the cross correlation between two signals by holding one signal stationary and slowly overlapping the other and at each step determines how similar they are at that point. When applied to discrete signals the calculation is

$$C_{xy}(m) = \frac{\sum_i \left[(x(i) - x)(y(i-m) - y)\right]}{\sqrt{\sum_i (x(i) - \bar{x})^2} \sqrt{\sum_i (y(i-m) - \bar{y})^2}} \tag{6.13}$$

where i is the time index and m is the delay. Equation (6.13) resembles convolution except the denominator which is used to normalize the result between -1 and 1. If the value of C_c is 1 the two signals are identical and -1 means they are identical but one is inverted.
In order to rank the degree of correlation presented by two signals the calculated correlation was converted into a percentage and split into deciles between 10 and 100. To appreciate

the meaning of a certain % correlation figures 6.13 - 6.17 are presented. They show different signals at their peak lag position(i.e where $C_{xy}(m)$ is at its maximum), see section 7.3.5 on how the lag affects the correlation value, and their respective correlation percentages.

Another method of characterization calls for stretching the signal horizontally and comparing them. In this study, however, only vertical manipulation was employed to normalize the functions.

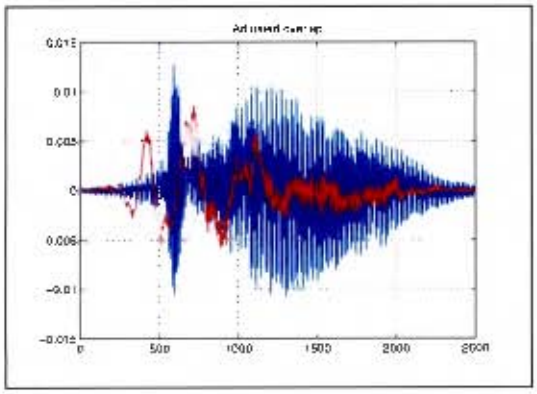

Figure 6.13. Correlation value of 20 %

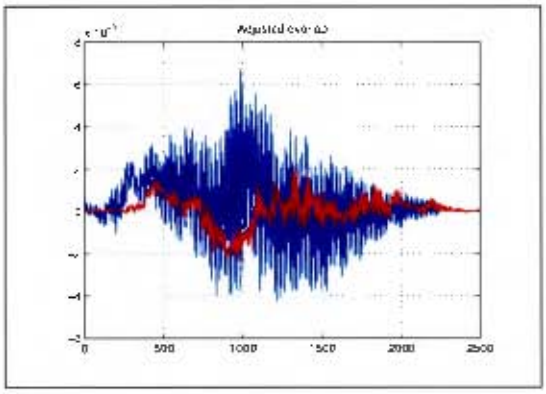

Figure 6.14. Correlation value of 40 %

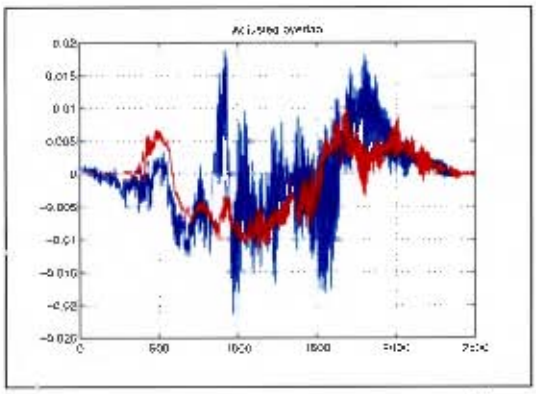

Figure 6.15. Correlation value of 50 %

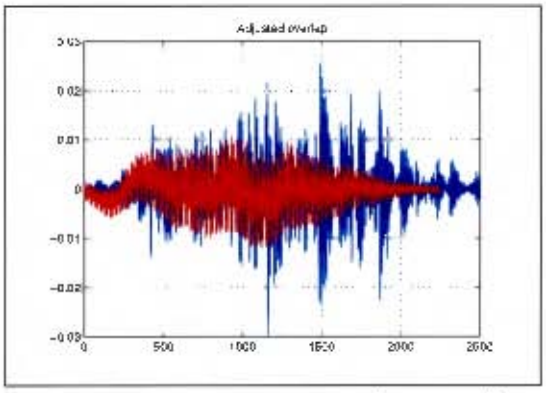

Figure 6.16. Correlation value of 60 %

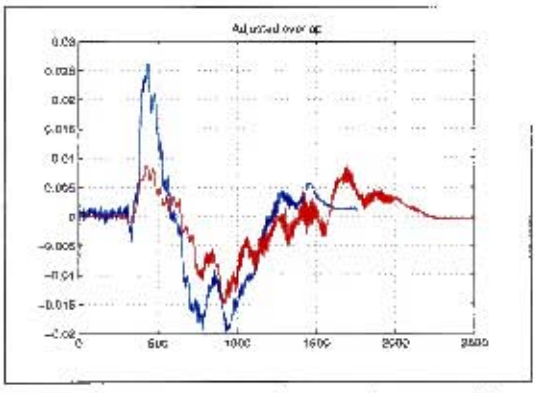

Figure 6.17. Correlation value of 80 %

7 Analysis Procedure

7.1 Introduction

This chapter describes the steps taken during analysis. It is structured to reflect the order in which analysis was carried out and explains the reasoning behind each step. The first section discusses the explosion's blast wave and particle expulsion. The next section is a description of the digital signal processing that took place, going into details about the the filter, and corrective transfer function.

7.2 Blast waves and shocks

7.2.1 Explosion timeline

Using the VOD mentioned in the literature as well as equation (2.5) a timeline for the explosion was modeled to demonstrate the position of the shockwave and particles as a function of time. It also helped clarify which process was being viewed (molecular breakdown, reconstitution, particle expansion, etc)

Table 7.1. Table of measured diameters for each charge mass

Mass (kg)	Diameters (mm)	Average ϕ (mm)
0.02	30, 35	32.5
0.04	40, 40, 40	40
0.06	45, 45, 45, 40	43.75
0.08	50, 50, 50, 45	48.75
0.1	50, 55, 53, 54, 50	52.125

Using the average diameters given in table 7.1 the expansion phase time for different SOD and masses was calculated along with the distance traveled in that time. These values were used to construct table 7.2.

Table 7.2. Particle traveled distance and times

Mass (kg)	SOD (m)	Radius (m)	Time(μs)
0.02	2	0.2059	297.1
0.02	8	0.1413	217.4
0.04	2	0.2594	373.1
0.04	8	0.2594	373
0.06	2	0.2969	424.3
0.06	8	0.2970	424.3
0.08	2	0.3268	467.8
0.08	8	0.3268	467.8
0.1	2	0.3521	503.4
0.1	8	0.3520	503.4

It was initially to be used to determine the time cut off point in the analysis of characteristics involving the primary peaks in the signal. This was to ensure the peaks looked at could be related to certain stages of the blast and dismiss other events (such as particles making contact with the antenna or passing through the loop). In all cases except for the 2m and 20g shot the distance traveled during the fireball phase was less than the SOD. The peaks in the 1st setup did occur before the fireball phase had ended, see table G.1. Using discretion the cut off time for all shots was set to 0.3 ms.

7.2.2 Shock wave arrival time

The possibility of signals picked up by antennas near blasts being attributable to the blast wave moving the antennas is not unreasonable. An antenna moving inside a magnetic field, such as the earth's magnetic field, will result in a signal generated on the oscilloscope. To ensure that this was not the case an algorithm was written to determine the estimated time of arrival for blast waves from different charge masses and SOD. Equations (2.7) and (2.8) were then substituted into equation (2.6). The resultant integral was approximated through numerical quadrature. The quadrature formula used was based on Simpson's rule

$$\int_a^b f(x)\mathrm{d}x \approx \frac{h}{3}\left[f(x_o) + 4f(x_1) + f(x_2)\right] \tag{7.1}$$

and used to implement a composite numerical quadrature algorithm - the results of this integration are seen in the table 7.3.

Table 7.3. Table showing the estimated arrival time for blast waves at defined SODs for a set charge mass

Charge Mass (kg)	SOD (m)	Time (s)	Charge Mass (kg)	SOD (m)	Time (s)
0.02	2	0.0034	0.1	2	0.0023
0.02	4	0.0090	0.1	4	0.0074
0.02	6	0.0148	0.1	6	0.0130
0.02	8	0.0206	0.1	8	0.0187

Only values for the smallest and largest masses were tabulated, and this shows that in the extremes (100g at 2m away) the arrival time is 2.3ms. All records from the testing had a time span of 0.9ms from the detection of the light from the blast. Any signals analysed therefore occurred before the blast wave had time to reach the antenna. Therefore removing the possibility that the antennas moving in the earth's magnetic field was the cause of the signals.

7.3 Processing

The raw data was in the form of a comma separated value (*csv*) file and analyzed in MATLAB. In total four data sets were saved, three from the antennas and one being the light sensor. The oscilloscope was configured to have a certain amount of pre-trigger data and the signal was captured once the light sensor crossed the threshold set before firing. An overlay of a scaled light signal is seen on top of its corresponding waveform.

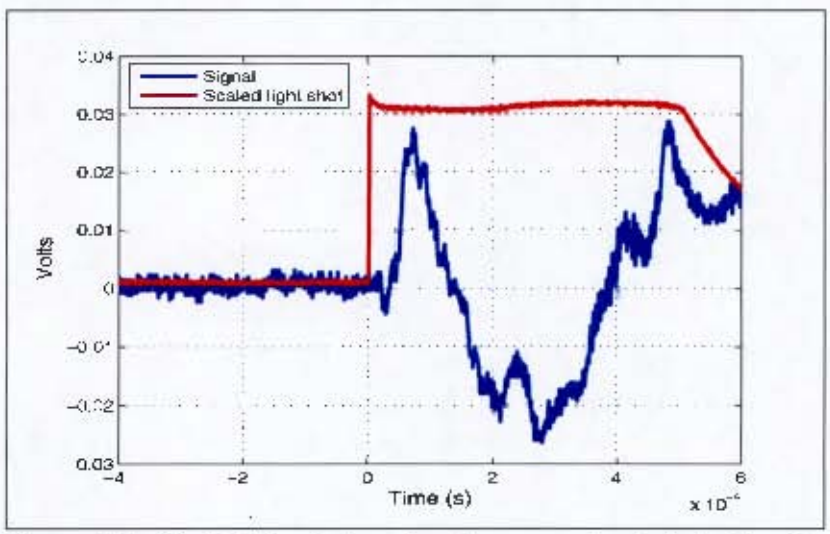

Figure 7.1. Scaled light shot overlayed on a raw signal, indicating the trigger point

Each shot had two columns, one for the time and the other with the voltage readings

from the oscilloscope. Inside MATLAB the raw signals were interrogated to determine various characteristics. Before any actual analysis the raw data was treated, see figure 7.2, with the digitally created inverse transfer function to reduce the circuit's effect and then a filter was applied to band limit the signal and reduce the noise content. At stage 2 of this process the signal was said to be "compensated" and at the stage 3 the signal was "compensated and band-limited".

Figure 7.2. Block diagram for digital treatment of data

The magnitude effect of the digital processing is presented in figures 7.3 - 7.5. Figure 7.3 shows how the magnitude of low kHz frequencies is boosted by the circuitry. Figure 7.4 shows the magnitude of the frequency response of the inverse filter. Figure 7.5 shows the combined frequency response of the circuitry and digital processing. The combined response is a bandpass filter with a flat response from 300Hz to 80kHz.

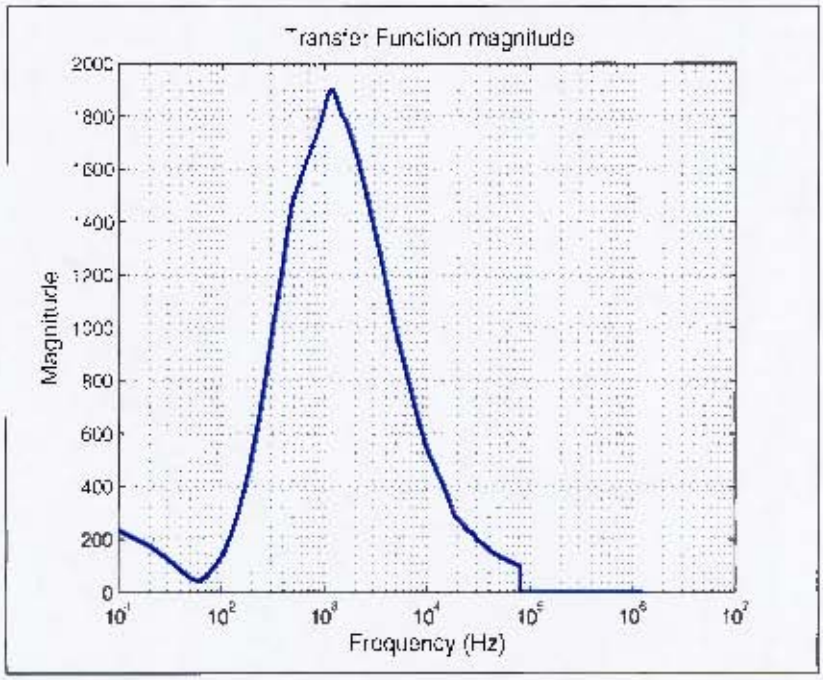

Figure 7.3. Frequency response of the amplifier and filter circuitry

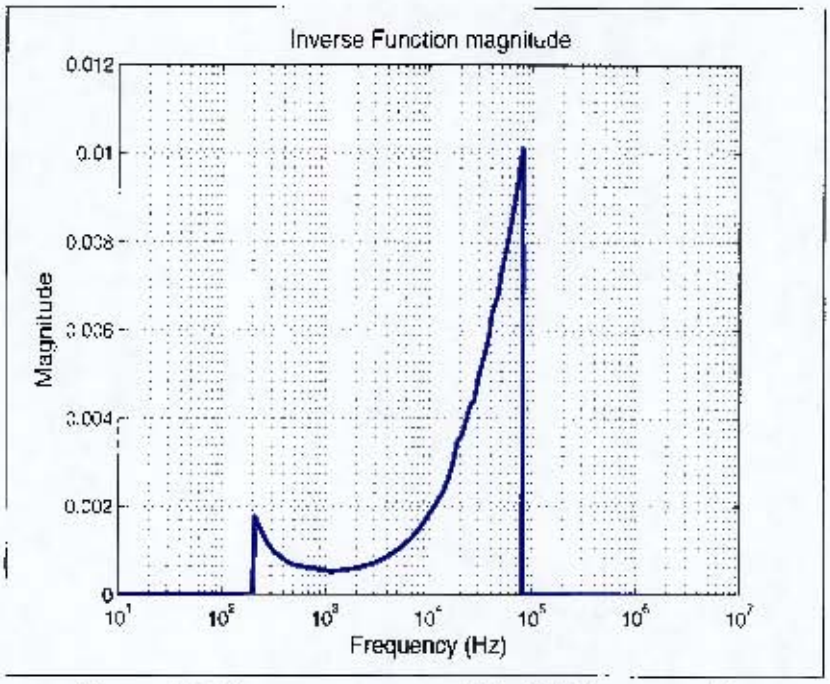

Figure 7.4. Frequency response of the digital compensation

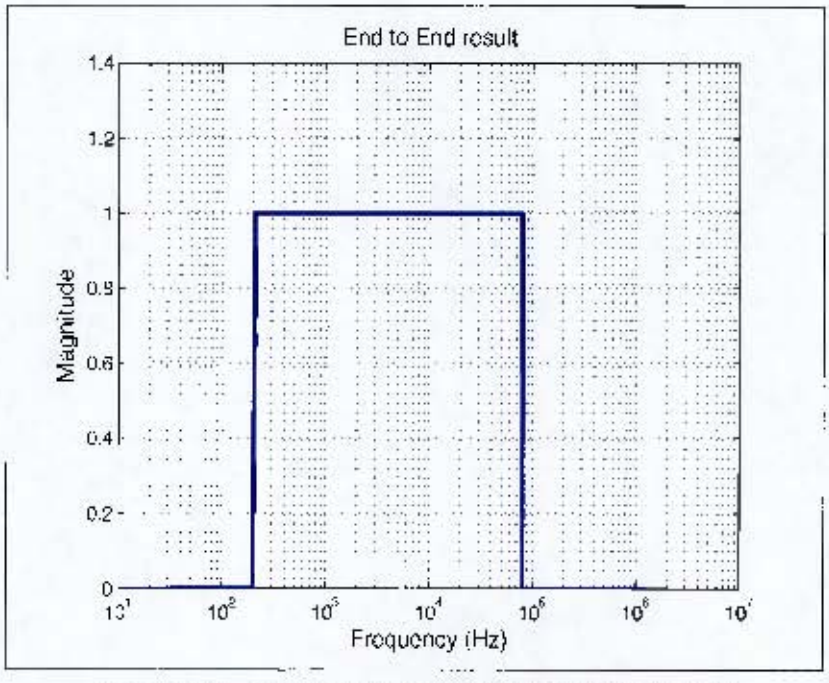

Figure 7.5. Frequency response of the complete process

The final end to end result shows that over the specified band width the signals were multiplied by 1, ensuring they were not altered in shape or magnitude during the digital processing. When taking the signal back into the time domain a band-limited signal shows oscillations based on the bandwidth of the filter. The oscillations usually occur at a frequency equal to the center frequency of the band.

The frequency spectrum was analyzed through an FFT. A pattern recognition function was used in the time domain to inspect signals from identical blasts as well as check for traits in other situations. Using equation (6.10) from signal processing the signal energy* released by each blast was calculated and examined to determine if any relationship was present.

7.3.1 Inverse function

The frequency transfer function resulting from the circuitry is shown in figures 5.13 and 5.14. This function was inverted and applied to the recorded signals. The correction was made between 300Hz and 500kHz. This decreased the magnitude in the low kHz range and boosted both low frequency and high frequency content. Cubic interpolation was performed over a specified range of frequencies, where the data was unreliable the interpolation was no longer valid and the results were seen as an extrapolation. Inverting the result introduced erroneous tails highlighted in figure 7.6. The tails did not affect the processing as on the center portion of the filter was used.

Another component was the phase correction (figure 7.7), which has an effect in the time domain. This changed the overall shape of the signal, which affected all the correlations making this correction imperative to the study. Viewing the signal beneath the noise floor is difficult but a general shape is present and is different from an unfiltered raw signal, an example of an unfiltered raw shot is seen in figure 8.10. Appendix H has all the raw data shots.

*This energy is the energy that was captured by the antenna and only represents a portion of the total EM energy released by the explosion

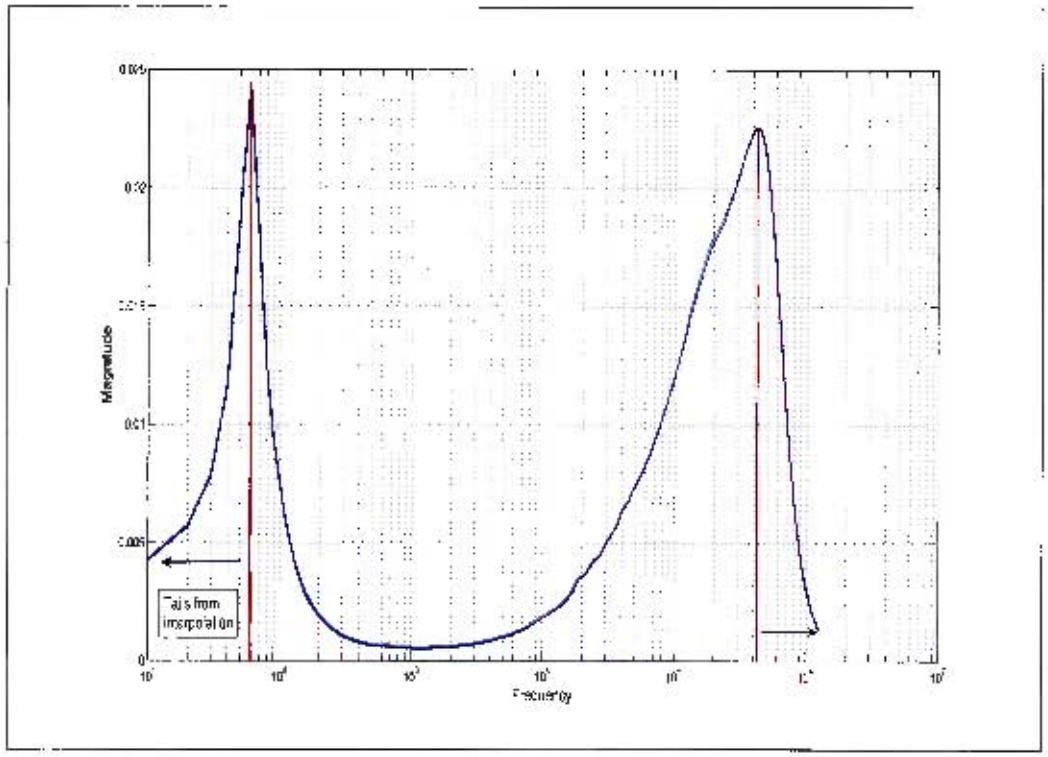

Figure 7.6. Magnitude response of the inverse function

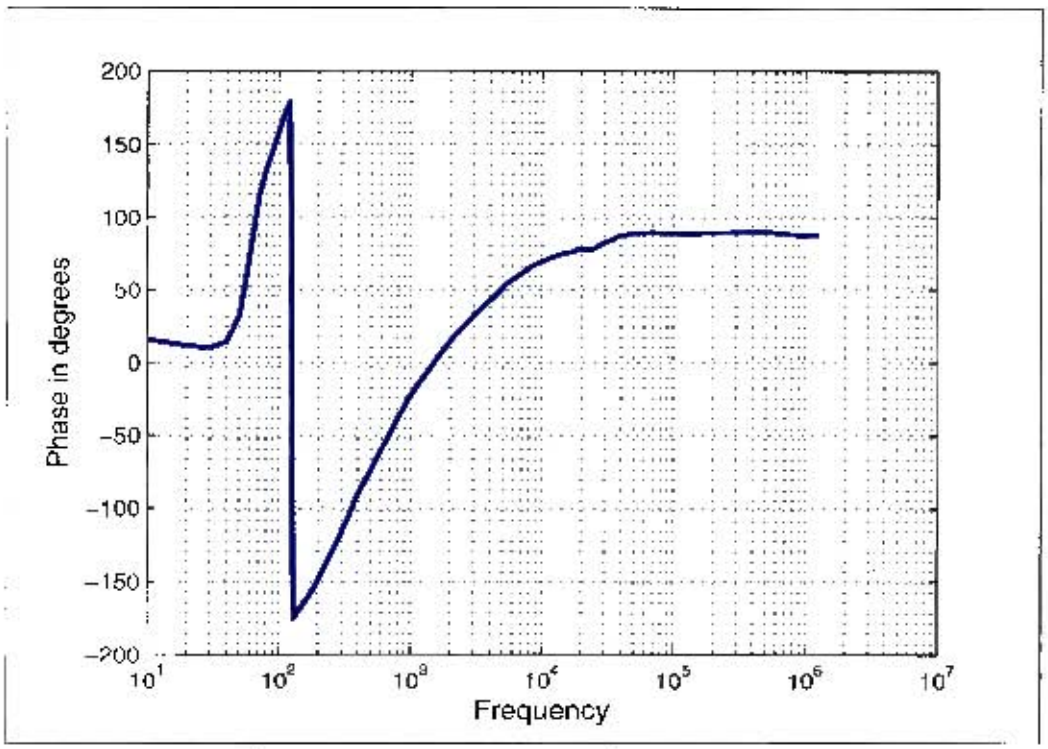

Figure 7.7. Phase response of the inverse function

7.3.2 Filter

An inverse transfer function was applied in the frequency domain and then the signal was transformed back into the time domain using an inverse fast Fourier transform (IFFT). The generation of the inverse function was discussed in section 5.5. Since these test conditions were not exactly the same as those in previous studies there was no predetermined upper cut-off frequency (f_{up}). The initial f_{up} was determined by looking at the pre-trigger data present in all the shots, an example of this data is in figure 7.8. An FFT was performed on just the pre-trigger data, this helped to identify the level of the noise spectrum and possible interfering signals unrelated to the explosion. Figure 7.9 shows the magnitude of the FFT of the pre-trigger data shown in figure 7.8

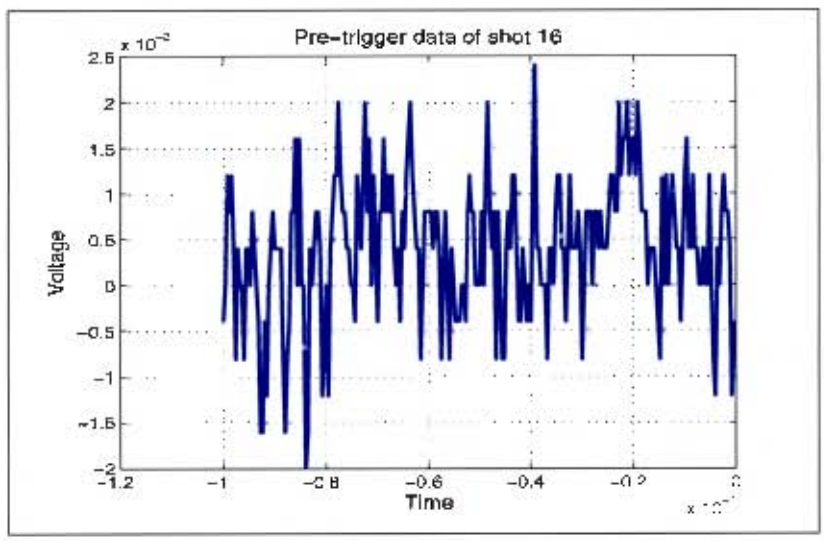

Figure 7.8. Pre-trigger signal

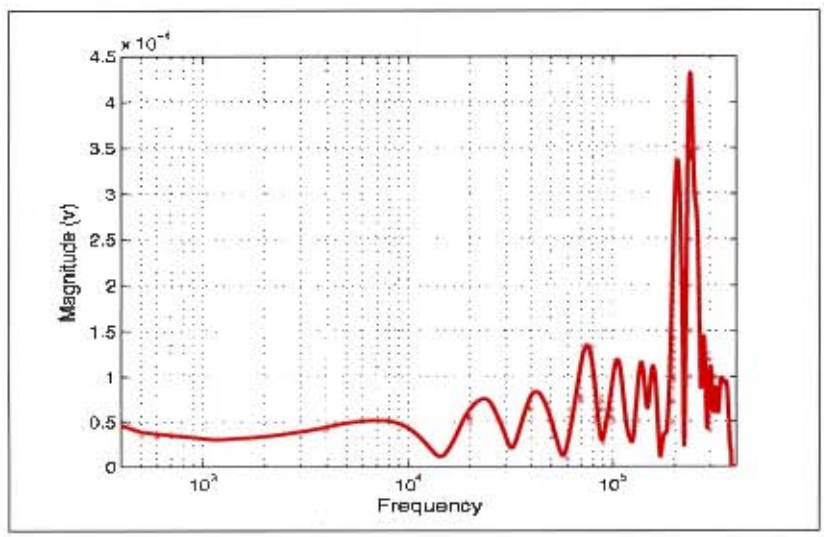

Figure 7.9. FFT of the Pre-trigger signal

There was a consistent spike seen between 250kHz which was attributed to a nearby beacon which seemed to be transmitting. Overlaying this FFT on the raw signal FFT it can be seen that certain high frequency content was a result of the surroundings and not the event.

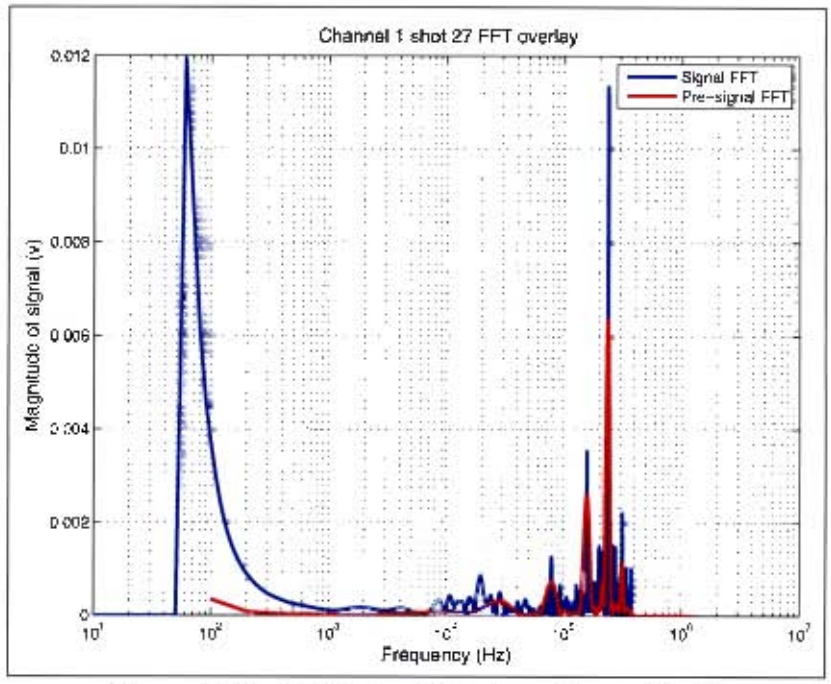

Figure 7.10. ch1s27 signal fft and pre-trigger data fft

Using this knowledge the f_{up} was set just below most of the high frequency noise at 200kHz. Applying the band limiting filter resulted in a vast improvement in the ability to see an underlying signal but some shots still showed a large amount of high frequency content. Personal judgment and trial and error resulted in the f_c being set at 80 kHz. The lower cut-off frequency was a result of the circuits limitations. During circuit testing it was found that below 300Hz the accuracy of measurements was questionable due to the measuring techniques used. The filter was then band limited between 300Hz and 80kHz. This allowed for suitable identification of an event and provided a sizable band of frequencies to investigate. The final function applied to all the data was a combination of the filter and inverse frequency. This magnitude portion of this function is seen in figure 7.11. Taking the band-limited filter into the time domain shows the circuit response to an impulse input and provides a baseline signal with which to compare the recorded data.

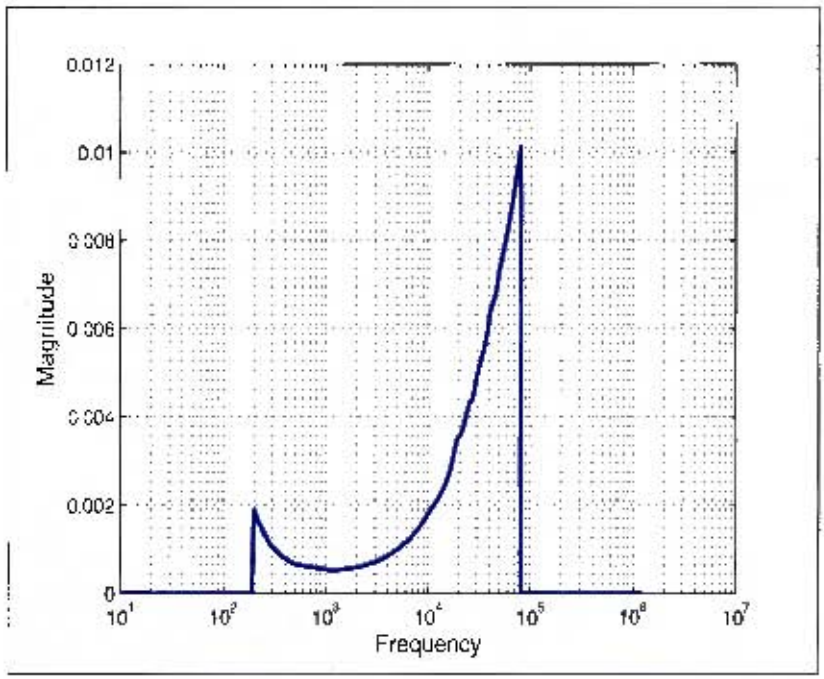

Figure 7.11. The magnitude part of the combination function applied to the raw signals

7.3.3 Time domain analysis

The pressure wave from an explosion is sometimes analysed for pulse width, rise and fall time. This kind of analysis was attempted in this project on the electromagnetic readings. There was a problem with the implementation as the algorithm could not handle the high oscillations in the signal. The oscillations caused calculation errors as they gave false readings in terms of waveform shape, full details are given in Appendix G, and was not used in final analysis. The correct approach when dealing with signals with such a great deal of oscillations is to look at their envelope. Instead of focusing on the smaller oscillations drawing a curve that encapsulates the wave form allows for a more realistic and accurate determination of its characteristics. This method was not employed for the project as it lay outside of the project's scope.

7.3.4 FFT

A discrete Fourier transform was applied to the data to determine the frequencies of interest. The actual technique used was the discrete Fourier transform implemented through a FFT algorithm.
The standard FFT was insufficient to make any judgments because it did not provide a fine enough resolution. To overcome this problem a window function was applied to reduce spectral leakage and the signal was zero padded. The Hamming window applied had a wider main lobe but considerably smaller side lobes. See figure 6.11 and 6.9 for a illustration on the effects of these processing techniques.

7.3.5 Pattern recognition

The correlation function was applied after filtering to determine the presence of a pattern. The purpose of checking for a correlation after filtering is that prior to filtering the correlation value is non-representative because of the noise present. Band limiting provides a smoother and more appropriate view of the event.

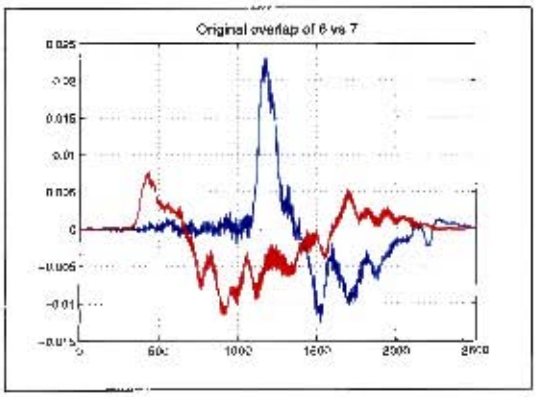

Figure 7.12. Original overlap of raw signals

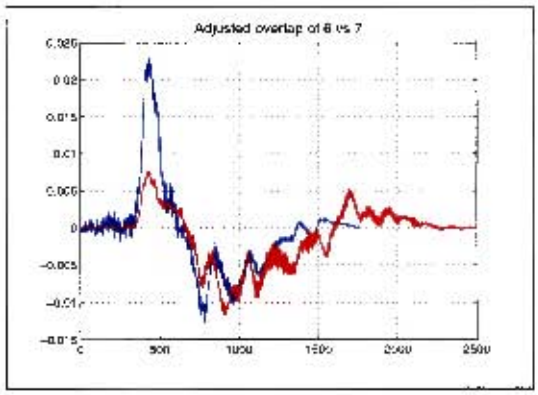

Figure 7.13. Adjusted overlap of raw signals

Figures 7.12 and 7.13 show band-limited signals before and after the lag adjustment and figure 7.14 shows how the correlation coefficient varies with lag position.

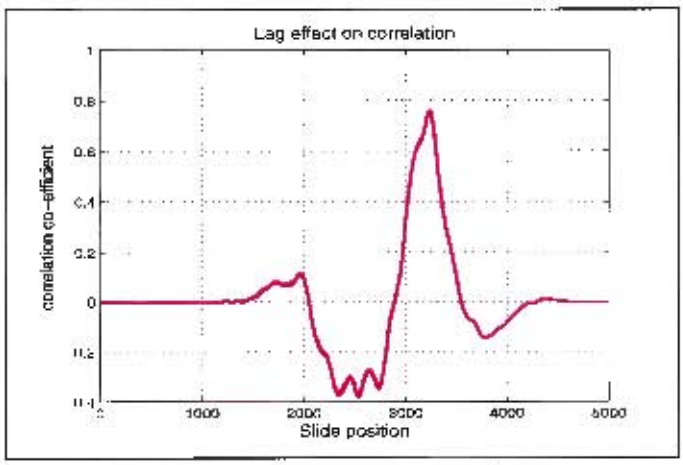

Figure 7.14. Correlation coefficients for different positions of overlap

Since both signals were 2500 points in length the total number of slide positions is doubled. The process involves sliding one signal over another from end to end. Figures 7.15, 7.16 and 7.17 show two randoms signals at the start, during and at the end of the cross correlation. The magenta colored signal is slid from the right to the left.

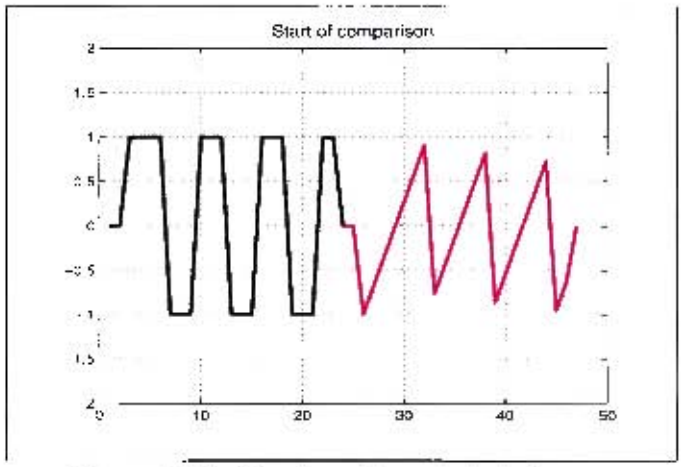

Figure 7.15. Signal positions at start of *xcorr*

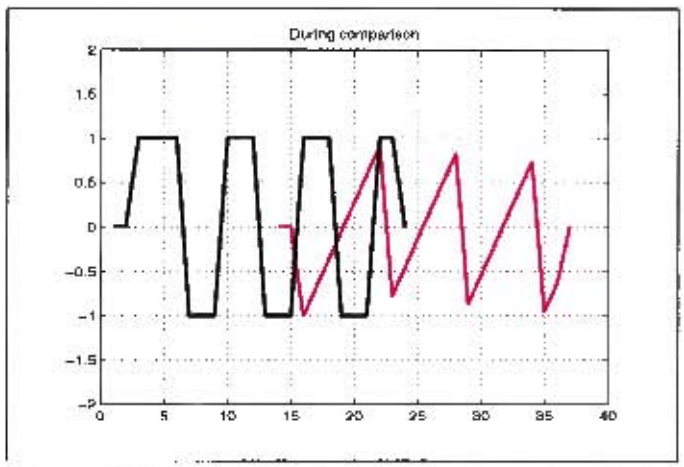

Figure 7.16. Signal positions at a random time during *xcorr*

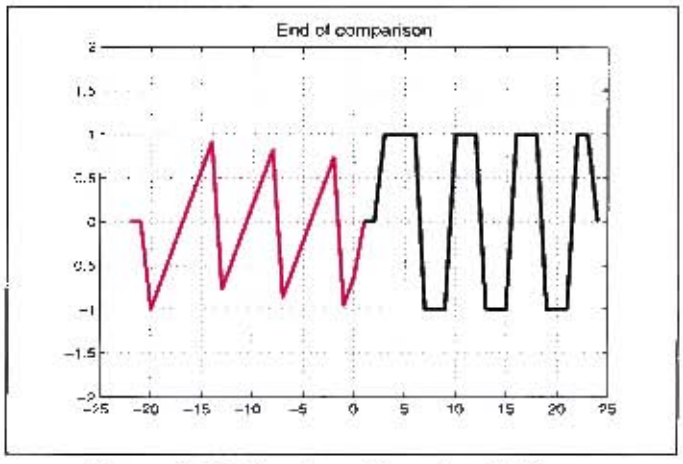

Figure 7.17. Signal positions at end of *xcorr*

This analysis was performed on mechanically similar shots - that is for shots where the same mass and SOD was used. It was also used to compare the pattern from the same event across different channels.

8 Results

8.1 Introduction

The results chapter comprises of two sections, Preliminary and Primary data. The primary data is then further subdivede into: circuit compensation (describing the effect of the digital signal processing), visual inspection (a discussion on the visual traits of particular signals and how they relate to the testing), characteristic frequencies (describing the frequencies containing the majority of the calculated energy), Energy dissipated (illustrates the relationships between the calculated energy and the SOD from the charge) and finally waveform shape (the results of the pattern recognition).

8.2 Preliminary data

The preliminary data were not used to make any comments on the actual waveform characteristics. The data were used to highlight any testing issues as well as provide a testing ground for the analysis procedure. All waveforms captured by the loop and recorded by the oscilloscope are the compensated signals with the complete set of preliminary data is in Appendix C.

8.2.1 February - BISRU

As mentioned in section 4.2 the first round of testing was recorded with an oscilloscope and was conducted in conjunction with another test being conducted at BISRU labs and utilized electrical detonation. The first graph (figure 8.1) shows the raw signal. The secondary pulses were put down to either reflections from the chamber walls, the wave interacting with some other metal content inside the blast room or the shock wave moving the loop. This series of data was band-limited to 100kHz after compensation. The signals were digitally treated then taken back into the time domain. The first millisecond was then selected and transformed back into the frequency domain producing the FFT seen in figure 8.3.

The filter also more clearly demonstrated that the events recorded were starting before the light was detected as the pulse starts before the 0s point. The fact that teh signal starts before the explosion was assumed to be a result of electrical detonation.This was best seen in shot 8, figures 8.2 and 8.3, but the trend was found in all shots recorded that day.

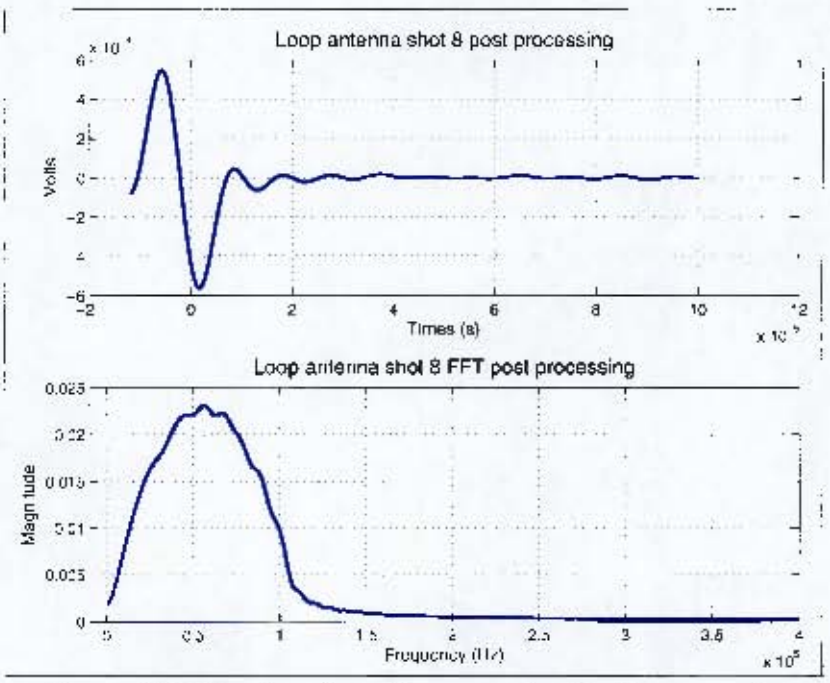

Figure 8.3. Time domain and frequency domain after processing

8.2.2 March - BISRU

The second round of testing was capable of recording for a longer period because of the PCI card being used. The ADC was used in conjunction with the oscilloscope. These recordings had the same peak activity between 200 and 250kHz and is illustrated in figure 8.4.

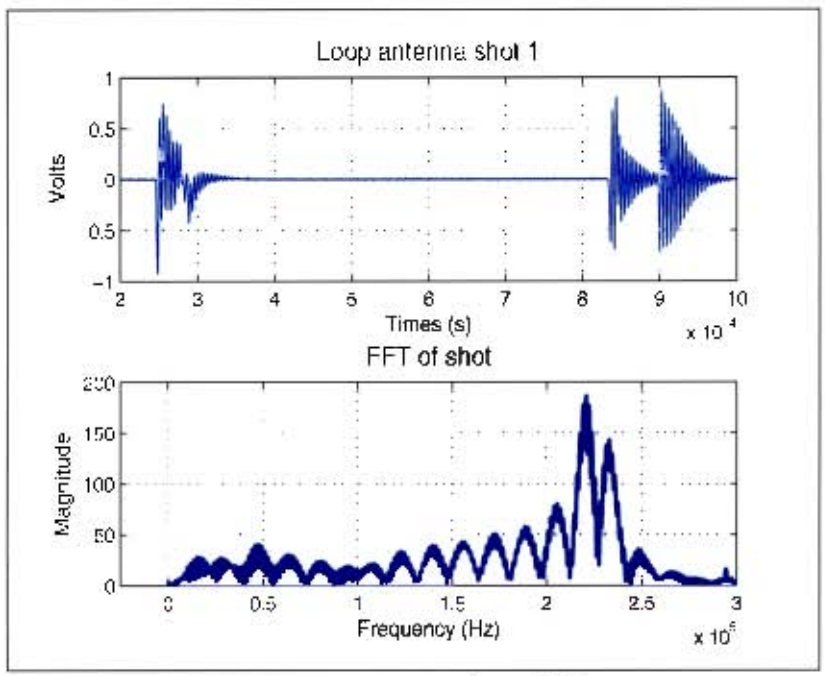

Figure 8.4. Loop shot 1 PCI

For a different series of tests in the same month a current clamp was attached to the detonation wires. This enabled the establishment of a more accurate relationship between the detonation method and signals received. Figures 8.5 and 8.6 show shot two as detected by the loop, as well as the comparison between the current clamp and loop signals. This indicates the ringing seen by the loop corresponds in time with the signals seen by the current clamp on the detonation wires. This helps account for the secondary pulses seen in previous and subsequent tests.

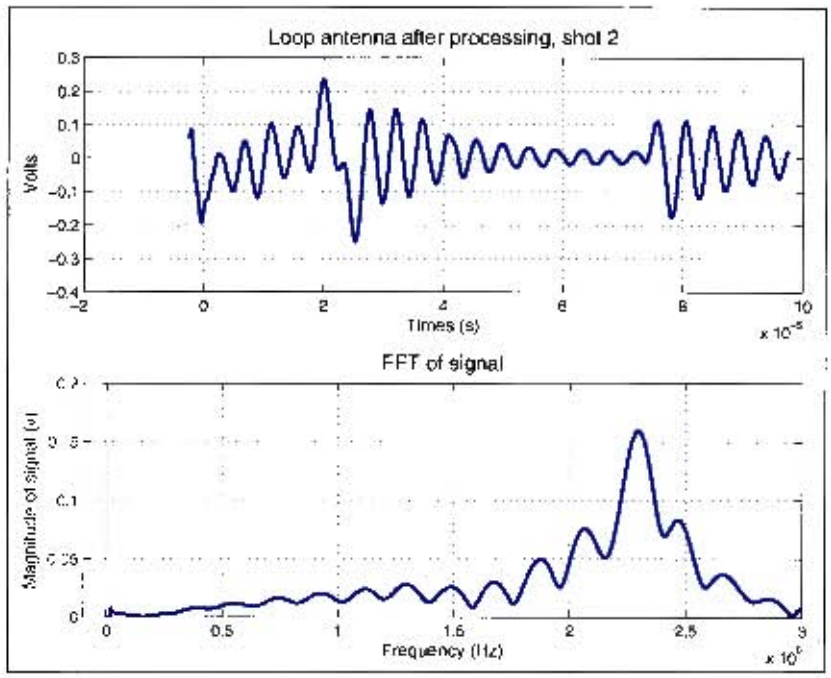

Figure 8.5. Loop shot 2

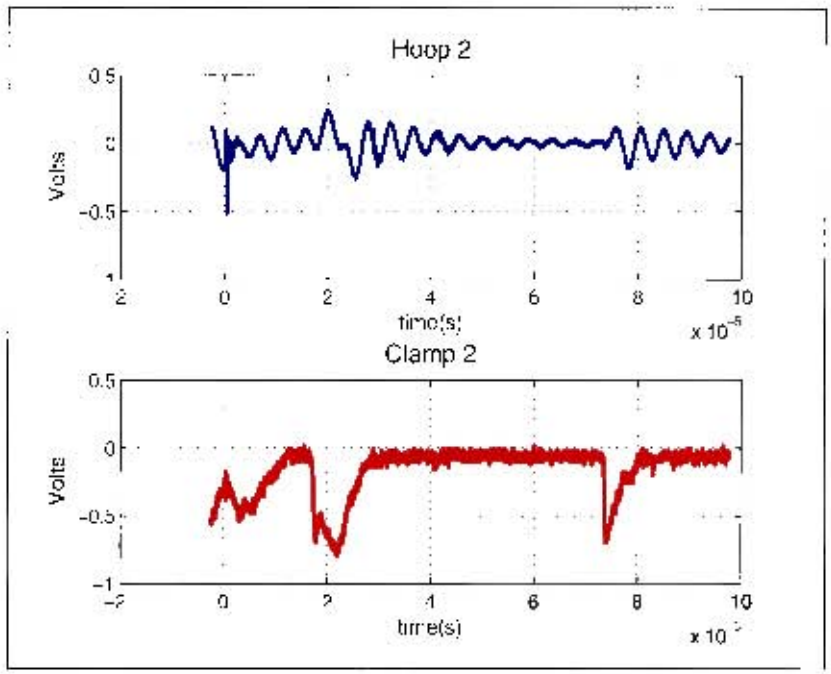

Figure 8.6. Clamp and Shot view

8.2.3 September - Langebaan

The only testing carried out prior to the Paarderfontein series without electrical detonation was conducted at Langebaan military base. Figure 8.7 and 8.8 represents the typical signals received at Langebaan, with the exception of a few shots, illustrated in figure 8.9.

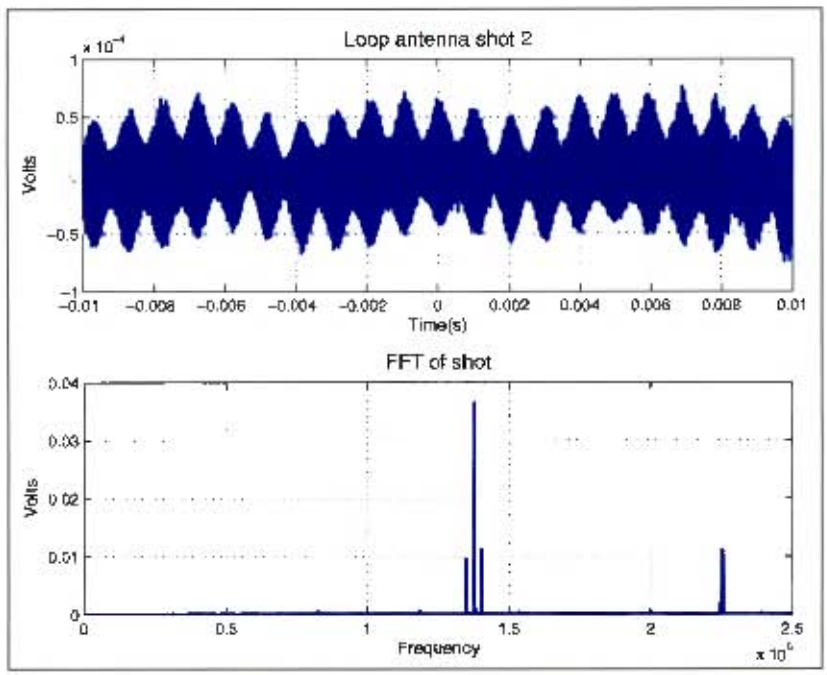

Figure 8.7. Compensated and band-limited signal 2, Loop antenna

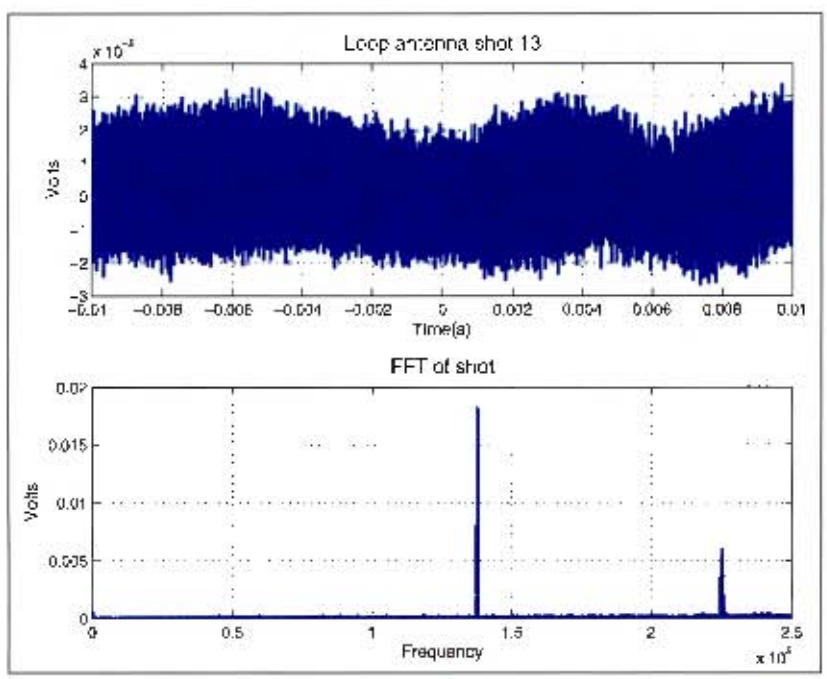

Figure 8.8. Compensated and band-limited signal 13, Loop antenna

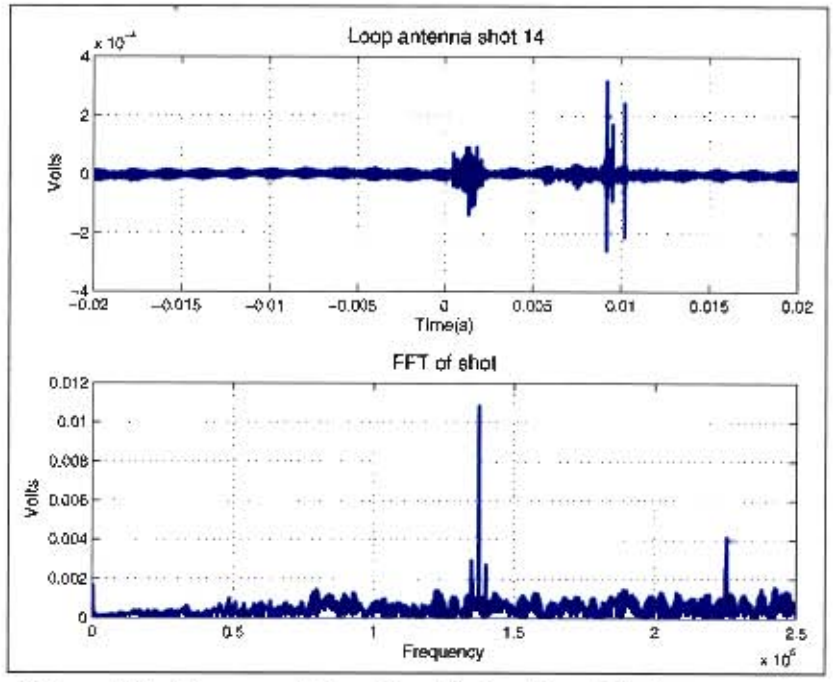

Figure 8.9. Compensated and band-limited signal 14, Loop antenna

Most of the shots were deemed as having not picked up signals as they all showed high frequency content with no differentiation before or after the blast. Those shots that did have a discernible event confirmed that something could be received from a mechanical detonation.

8.3 Primary Data

The data collected at Paaderfontein made up the primary data set. Although all shots were investigated particular shots are presented to better convey the main points in each section. All shots from the analysis are presented in Appendix II.

8.3.1 Effect of Circuit compensation

The inverse function not only affected the magnitude of certain frequencies but also the phase. This meant that the general time domain shape of the signal was altered. The function (see figure 7.6) also increased the high frequency noise, which buried what was perceived to be the signal of interest. The effect of the circuit compensation and band limiting is seen when comparing the raw signal (figure 8.10) to the compensated signal (figure 8.12) to the compensated and band-limited signal in (figure 8.14). All the signals are accompanied by their FFT representations (figure 8.11, figure 8.13 and figure 8.15) ordered accordingly

The application of the filter reduced the ambient noise to acceptable levels and in some

instances was so effective it showed signals buried under a great deal of noise. In shot 33 of channel 1, figures 8.16 and 8.17 the filter helped remove a significant amount of high frequency content after 0.2ms.

The filter also allowed the event to be seen clearly- in some cases the start or end could not be accurately identified but after applying the filter these points became more apparent. Shot 40 originally appeared to have little information, figure 8.18, but when filtered the slight rise in volts and barely visible pattern change is visible just after detonation. This level of clarity was important for determining the energy dissipated by the event.

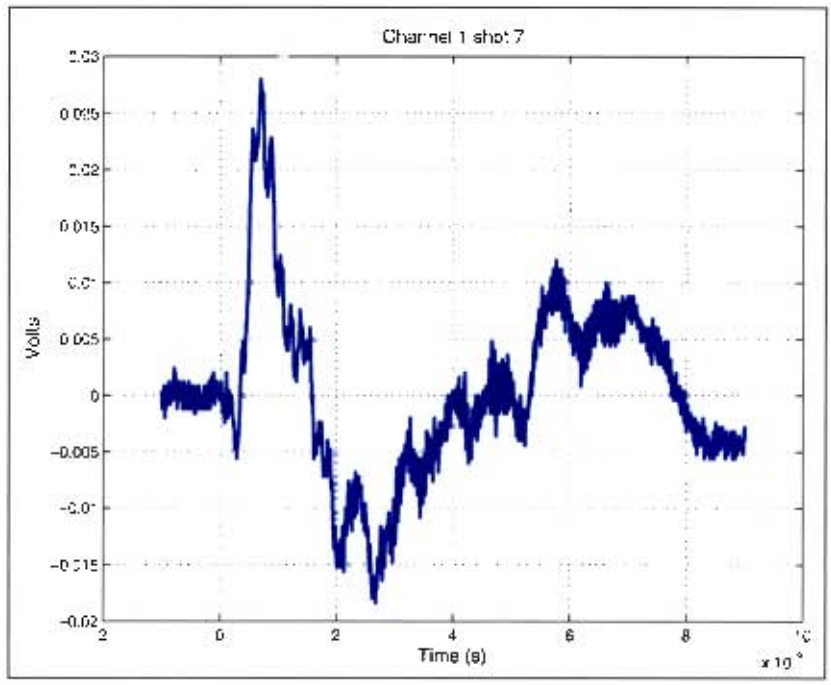

Figure 8.10. Raw untouched signal recorded by oscilloscope

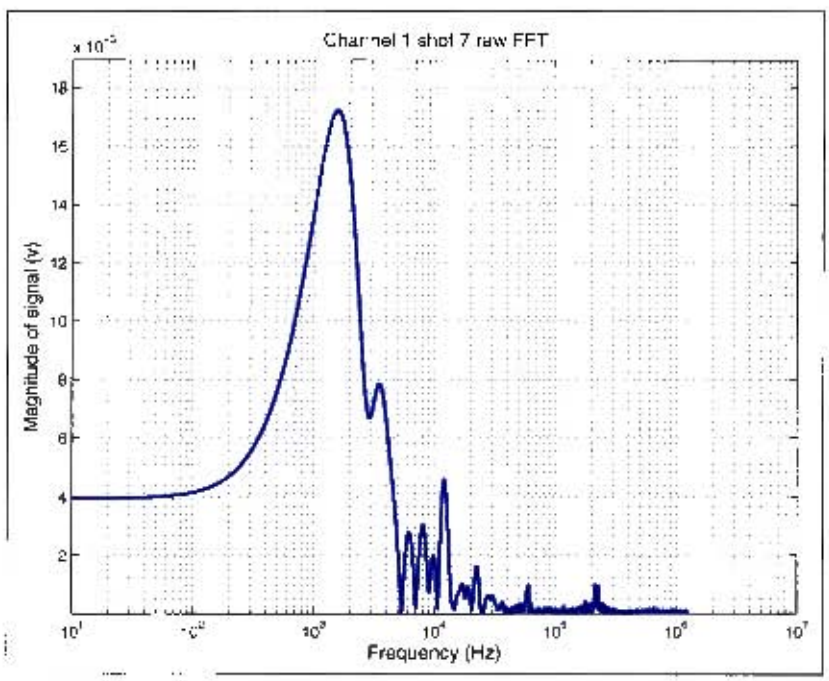

Figure 8.11. FFT of raw signal, padded and windowed

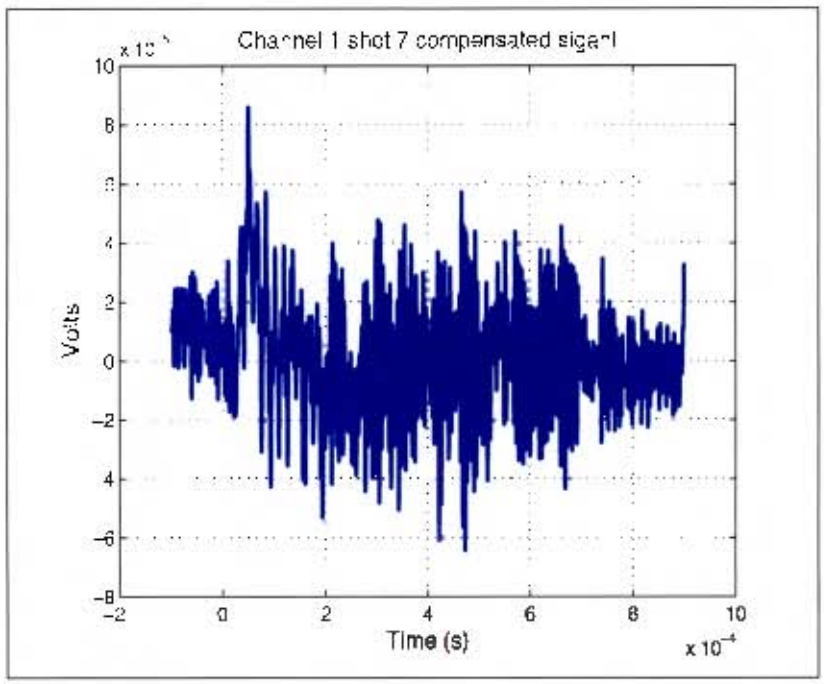

Figure 8.12. Compensated signal, has increased high frequency content

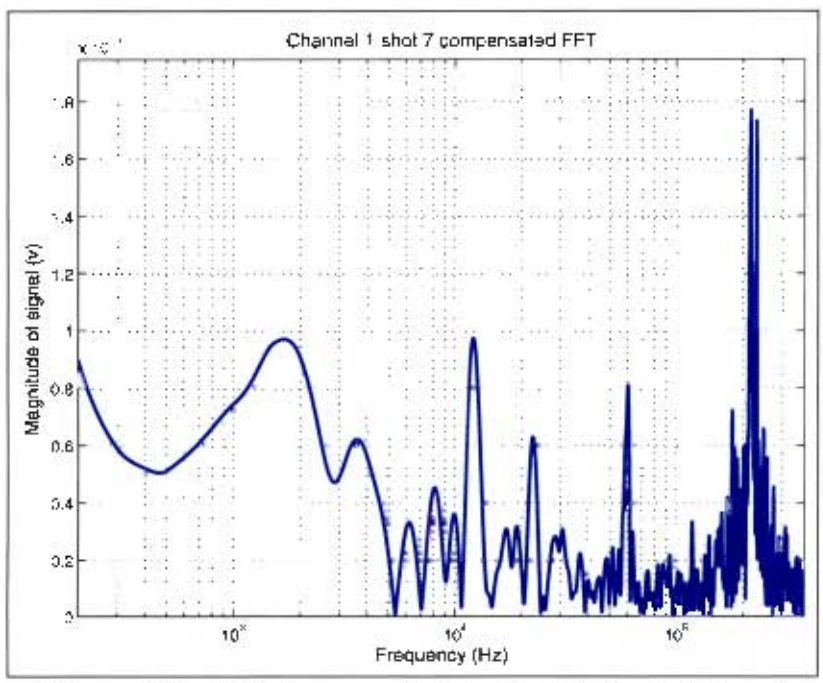

Figure 8.13. FFT of compensated signal, padded and windowed

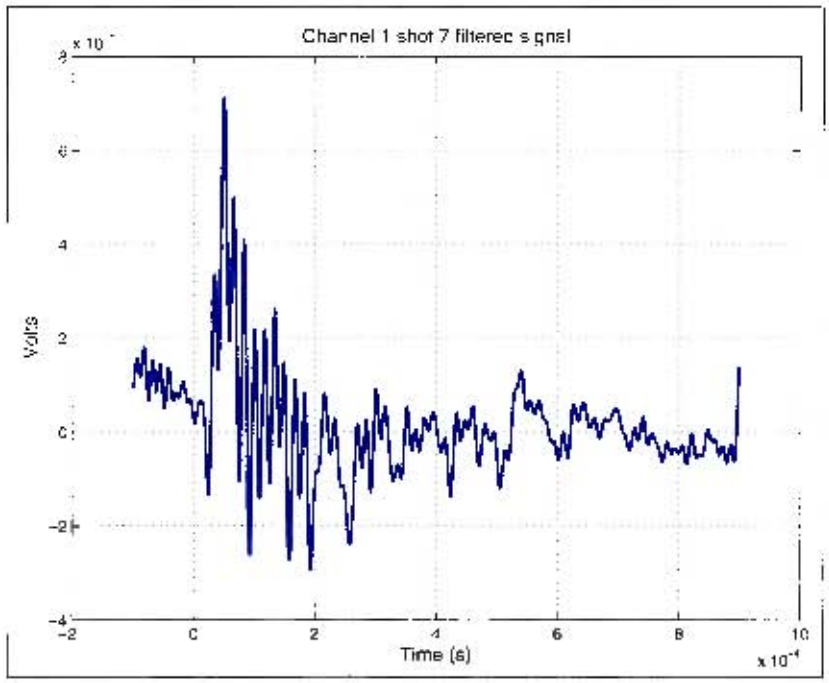

Figure 8.14. Compensated and band-limited signal

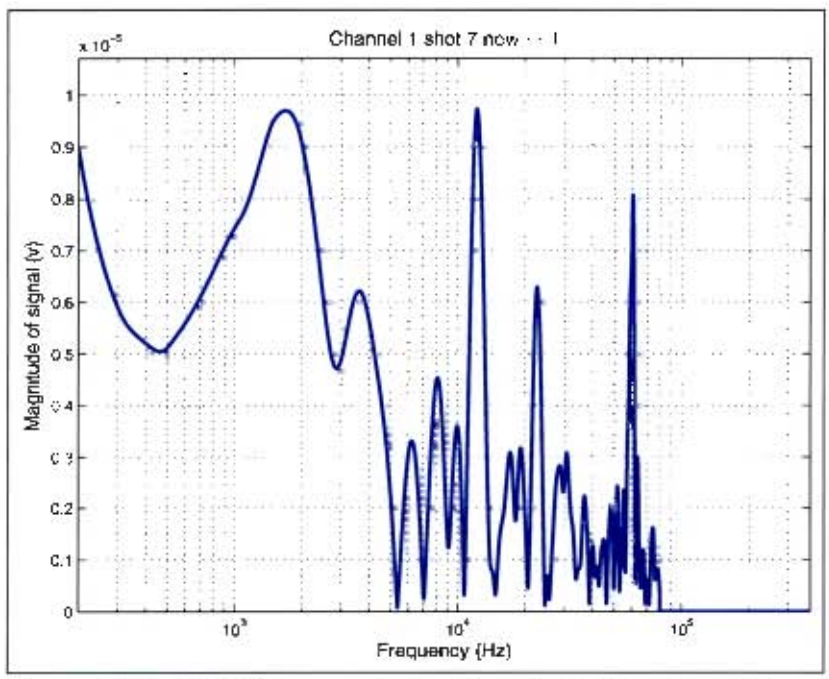

Figure 8.15. FFT of Compensated and band-limited signal, padded and windowed

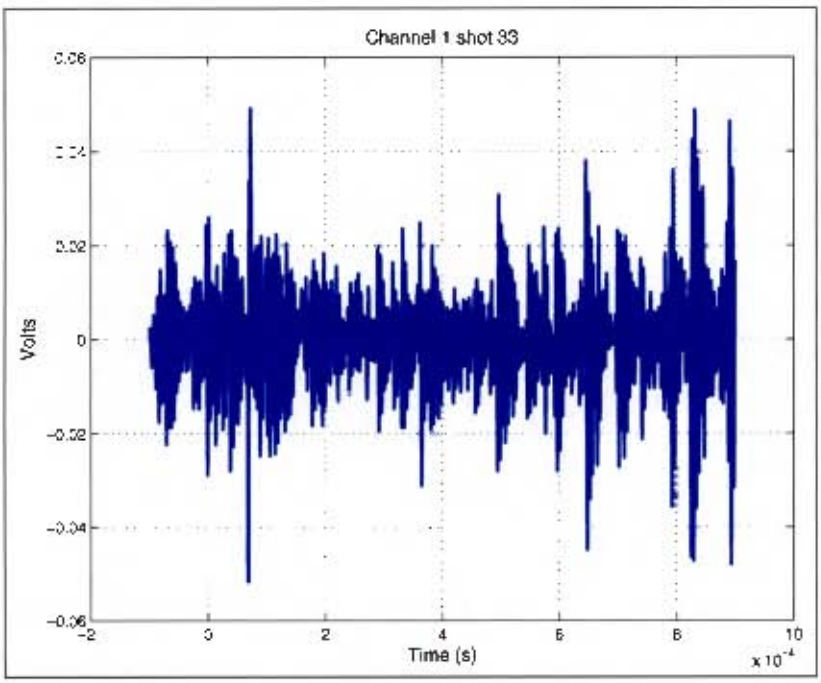

Figure 8.16. Raw signal

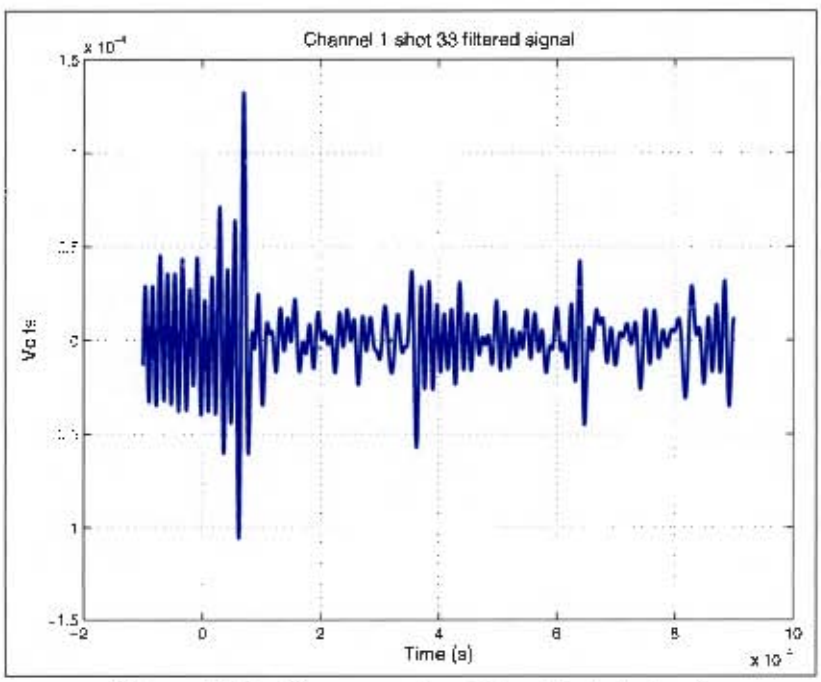

Figure 8.17. Compensated and band-limited signal

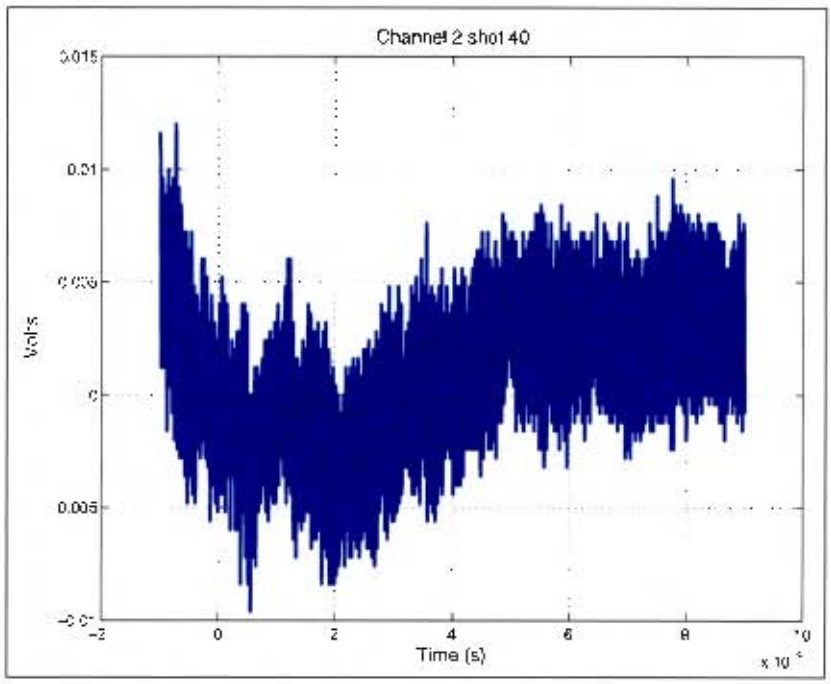

Figure 8.18. Raw signal 40

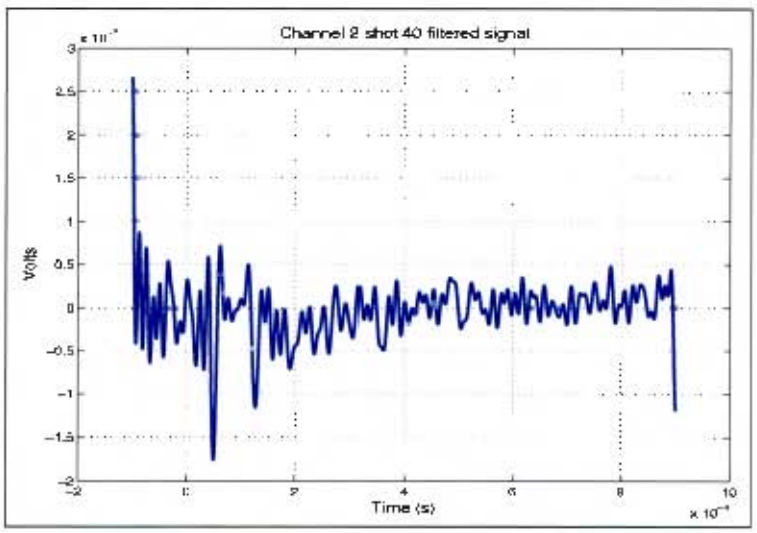

Figure 8.19. Compensated and band-limited signal

8.3.2 Visual inspection

In figure 3.8 the three antennas are shown in their test setup. Channel one is the green loop, two is the orange (which was later re-orientated) and finally channel 3 is the purple loop. In general signals* appeared to be of low magnitude, with a great deal of noise on top of a low frequency disturbance. The impulse response of a filter is determined from the IFFT of the filter function. The benefit of seeing the filter in the time domain (figure 8.20) is that the general effects of the filter can be viewed and compared to the recorded signals.

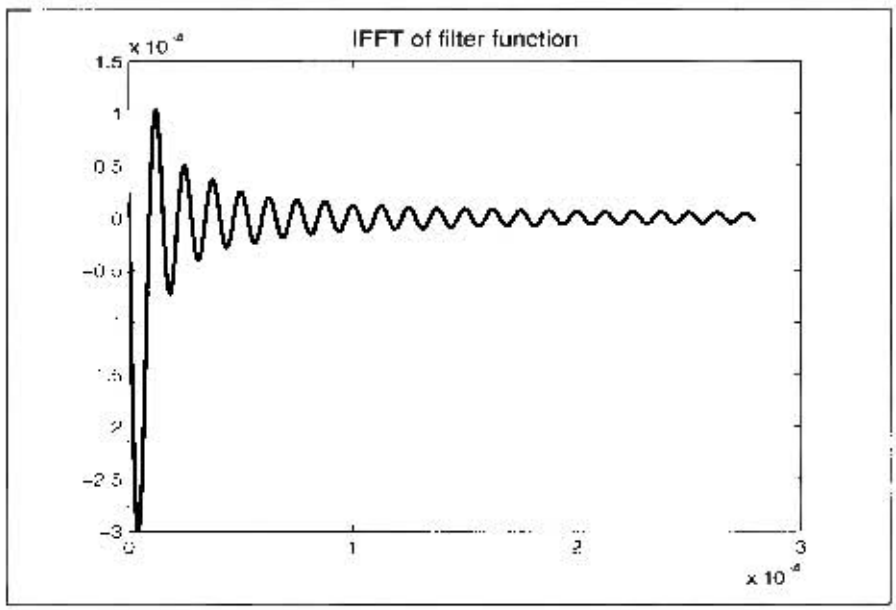

Figure 8.20. IFFT of filter, x-axis is in seconds

There was negligible similarity to the impulse response of the filter, indicating that the event being recorded could not be accurately modeled as an impulse function. A sample of the fill data set are presented in the following figures. Figures 8.21 and 8.22 are some of the first shots recorded at Paarderfontein. After detonation at time 0 a peak or trough is present that tapers off over time.

*All signal viewed were compensated and band-limited

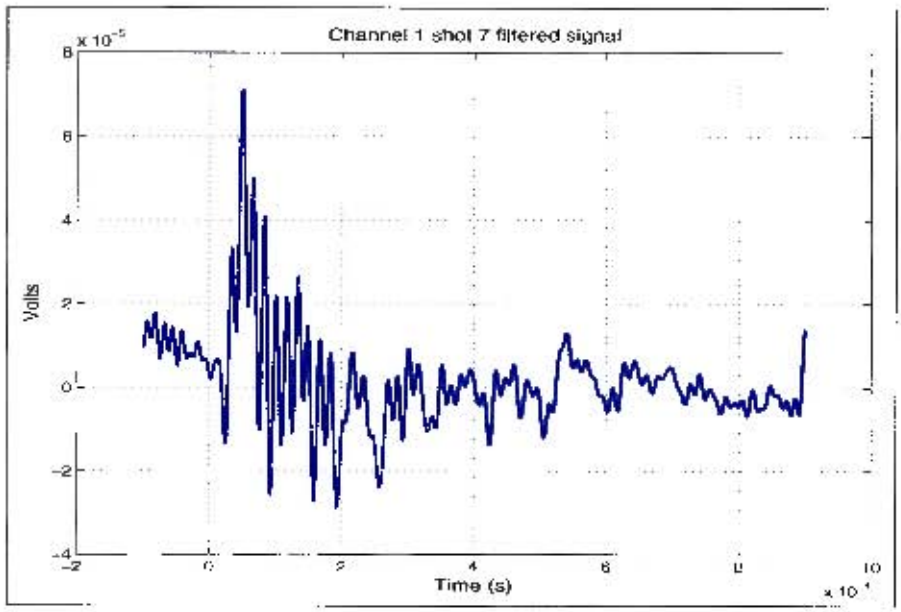

Figure 8.21. Channel 1 shot 7

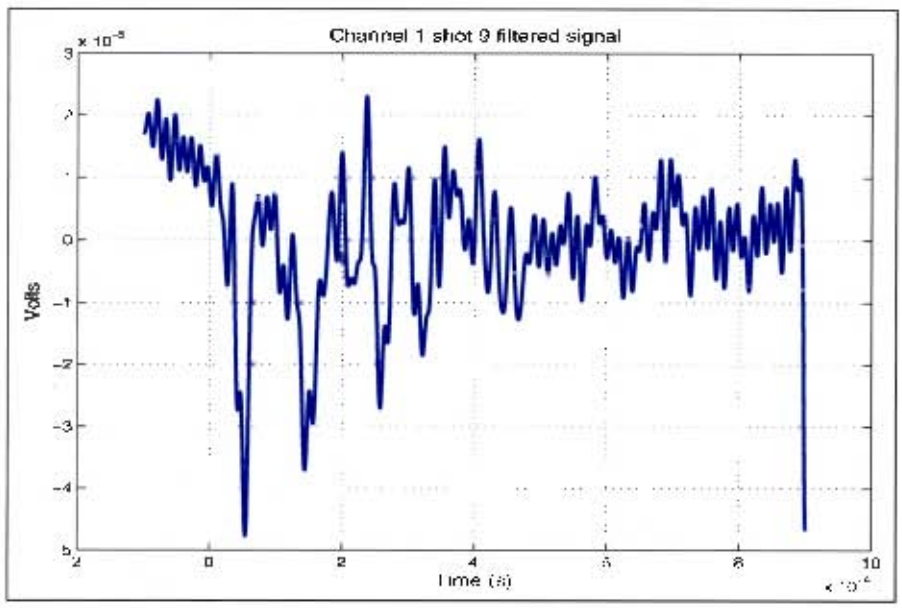

Figure 8.22. Channel 1 shot 9

However not all signals were as easily described. In channel 1, shot 17 seems to start before the blast (figure 8.23), 19 seems to only have picked up ambient noise (figure 8.24) and 25 only registers an event at 0.6ms (figure 8.25). These are only a few of the differences spotted when merely inspecting the signal by eye, the full series of shots can be found in Appendix H.

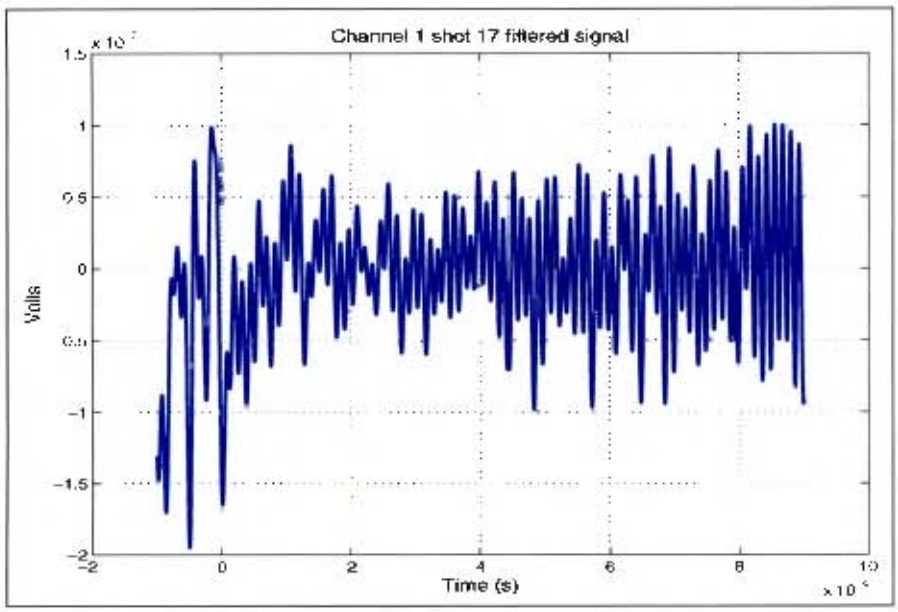

Figure 8.23. Channel 1 shot 17

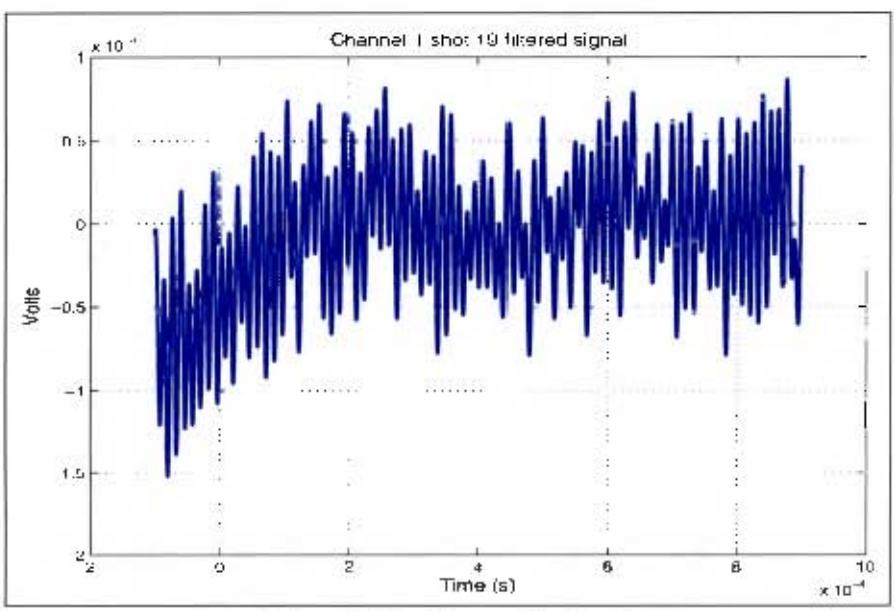

Figure 8.24. Channel 1 shot 19

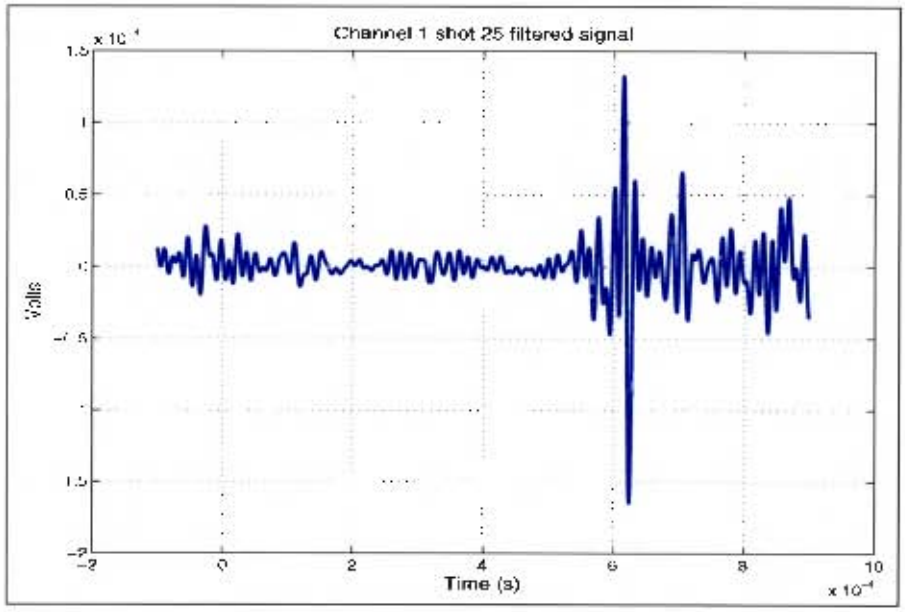

Figure **8.25.** Channel 1 shot 25

In channel 2 a signal was only picked up after shot 12 (figure 8.26), when the adjustment to the antennas orientation was made, discussed in section 3.3. All the shots prior to shot 13 (figure 8.27) looked identical to figure 8.26.

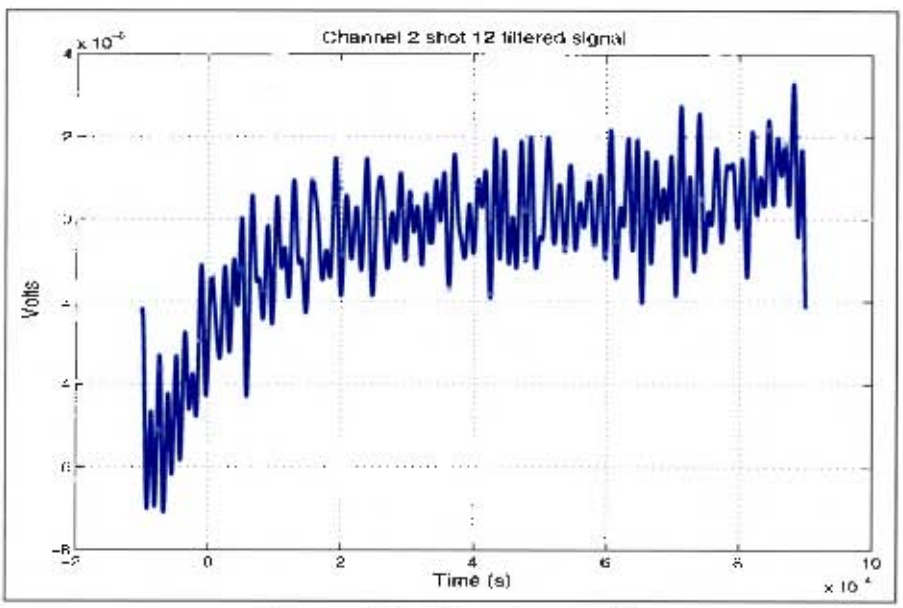

Figure **8.26.** Channel 2 shot 12

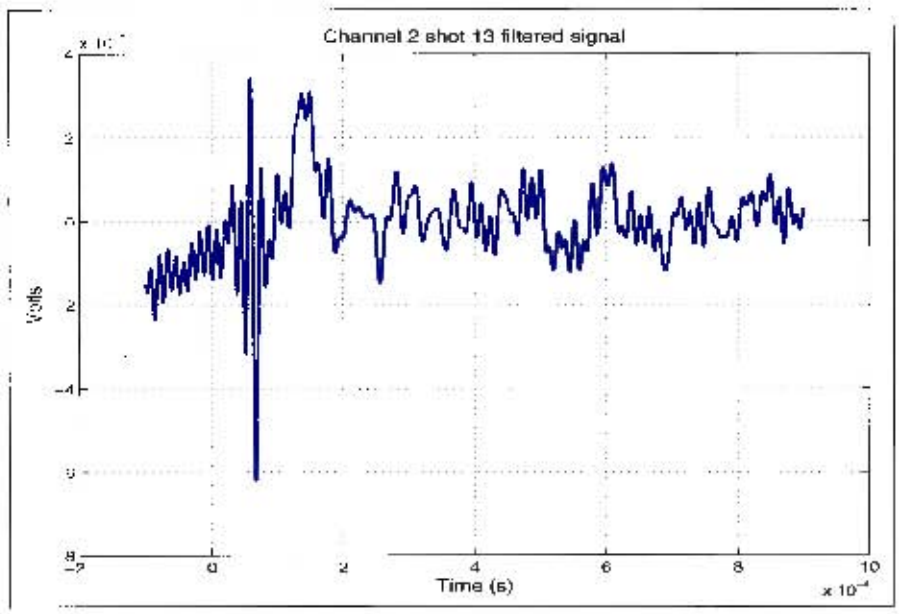

Figure 8.27. Channel 2 shot 13

After looking at the anomalous shots in channel 1 it was expected that for the same shots the other channels might have registered something similar trends. This was not always the case as illustrated from shot 17 (figure 8.28) but again shot 25 (figure 8.29) had a significant delay.

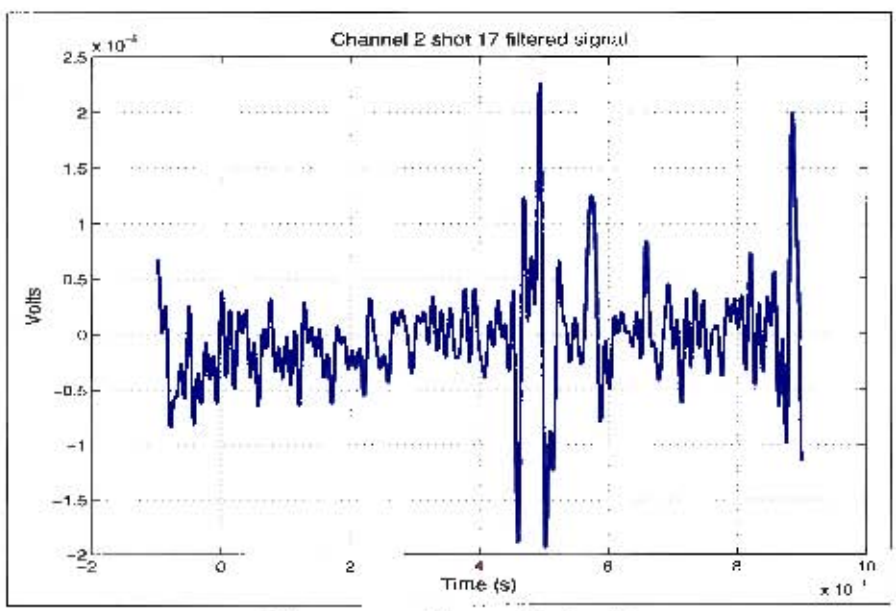

Figure 8.28. Channel 2 shot 17

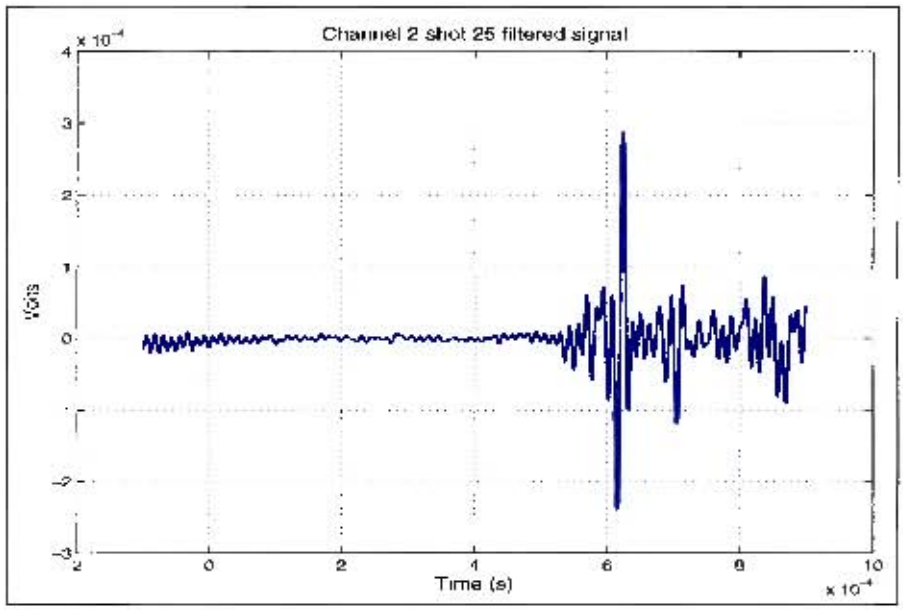

Figure 8.29. Channel 2 shot 25

It is interesting to note that channel 1 and channel 3 picked up almost the same signal pattern in a significant number of shots. This is highlighted in section 8.3.6 but a good example of this can be seen when comparing figures 8.30 and 8.31.

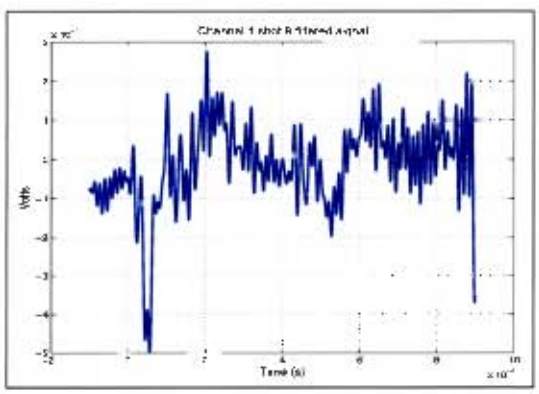

Figure 8.30. Channel 1 shot 8

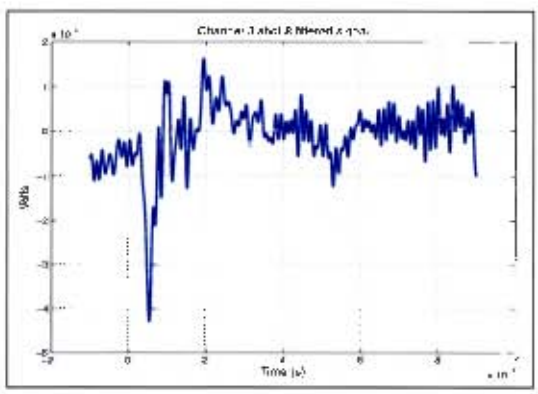

Figure 8.31. Channel 3 shot 8

8.3.3 Characteristic frequencies

A comparison of the signals in the frequency domain led to the conclusion that within the band being viewed the frequencies of interest were in the kHz range, these can be seen in H.295 and H.300 for example. The peaks with the maximum power were singled out and plotted in figure 8.32.

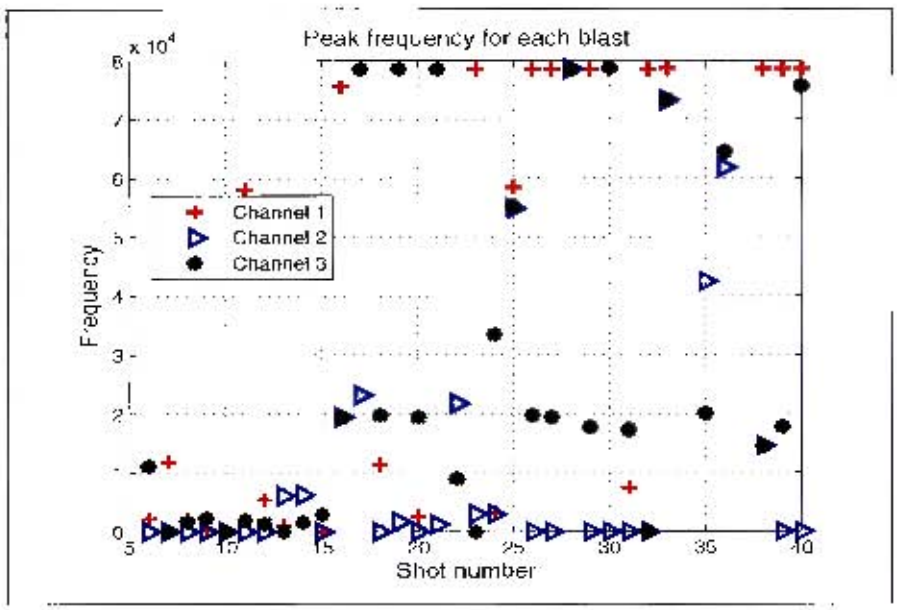

Figure 8.32. Plot of all the peak freq for each channel and shot.

The statistical information of this plot has been tabulated to show the average frequency and the deviation for each channel.

Table 8.1. Data on peak frequencies

Original			Adjusted		
Channel	Average Freq	Stand Dev	Channel	Average Freq	Stand Dev
1	43.5 kHz	36 kHz	1	46.3 kHz	35 kHz
2	12.5 kHz	23 kHz	2	23.8 kHz	24 kHz
3	27.6 kHz	30 kHz	3	32.6 kHz	30 kHz

Th variation in results for each channel is not wholly accounted for but discussed in the observations, Chapter 9. Table 8.1 is separated into two groups. The 1st group was evaluated using all the data points while the 2nd group had any "erroneous" points removed before determining the standard deviation and average values. The erroneous points that were removed from the calculation were in fact the 0-valued peaks.
In some cases the frequency containing the largest amount of power was at 0Hz. This is

characteristic of a step input when transformed (see section 6.3). The dominant shape of the signal received by the antenna may have appeared as a step wave.

8.3.4 Energy relationship

8.3.5 SOD vs Energy

It was observed that as the SOD increases the power received by the antenna decreases. The relationship was assumed to follow a power function curve of the form $\frac{1}{x^2}$ from the power density relationship or the $\frac{1}{x^3}$ relationship from the Hopkinsons scaling law, where x is the distance from the source. The following curves were fitted to the data and evaluated based on how well they approximated the data.

$$y = \frac{a}{x^2} \tag{8.1}$$

and the other

$$y = \frac{a}{x^3} \tag{8.2}$$

In previous work the equation fitted to the power loss over SOD was of the form $log(y) = -a * log(x) + b$. The difference between this and those curves fitted is merely the degree of freedom allowed in the fitting. In Adushkin's article on surface explosions[17] the author had two constants, **a** and **b** whereas the curves being fitted in this thesis had only one. The curves fitted to the 60g and 100g data points in both channels 1 and 3 are presented in figures 8.33 - 8.40, to illustrate how close each curve fitted the data. The full collection of curves fitted are presented in Appendix F.

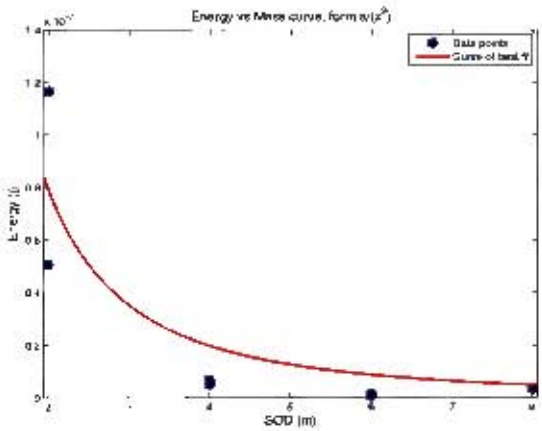

Figure 8.33. Constant mass of 60g, channel 1

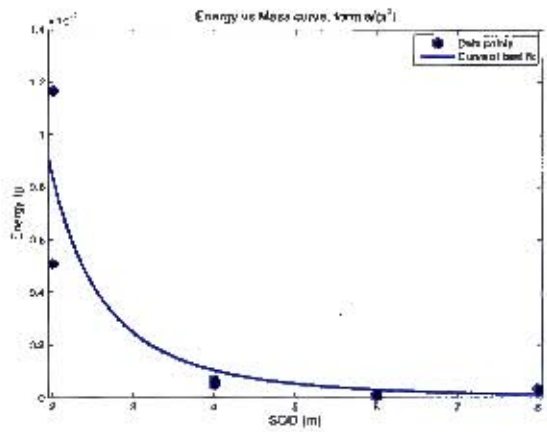

Figure 8.34. Constant mass of 60g, channel 1

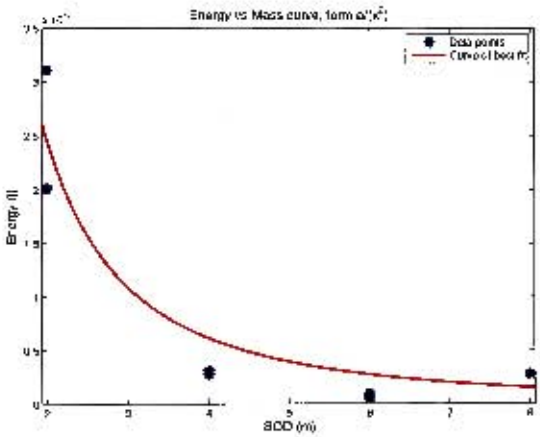

Figure 8.35. Constant mass of 60g, channel 3

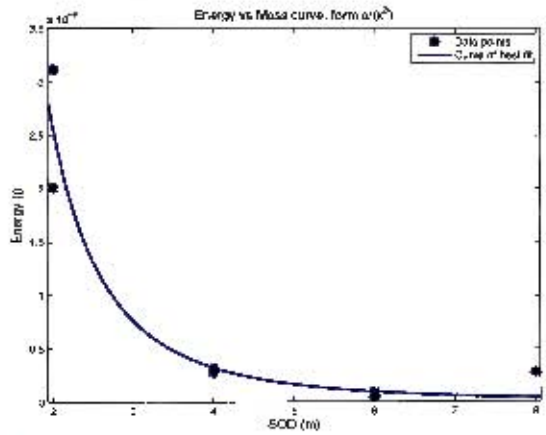

Figure 8.36. Constant mass of 60g, channel 3

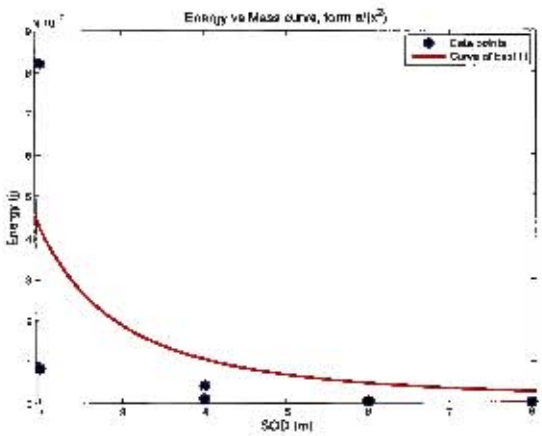

Figure 8.37. Constant mass of 100g, channel 1

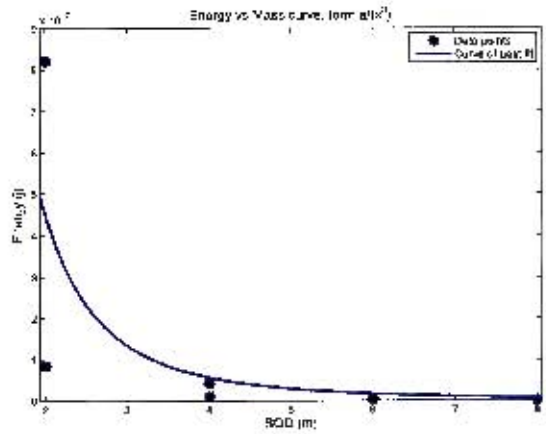

Figure 8.38. Constant mass of 100g, channel 1

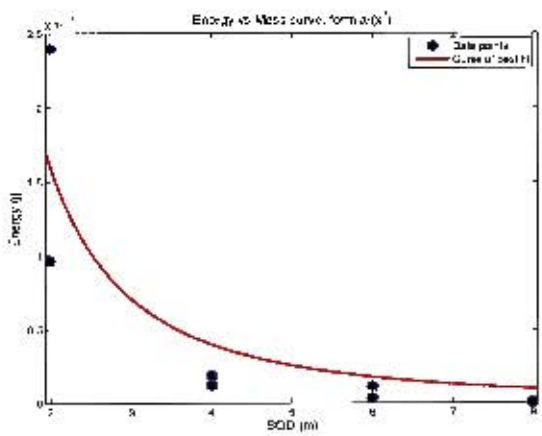

Figure 8.39. Constant mass of 100g, channel 3

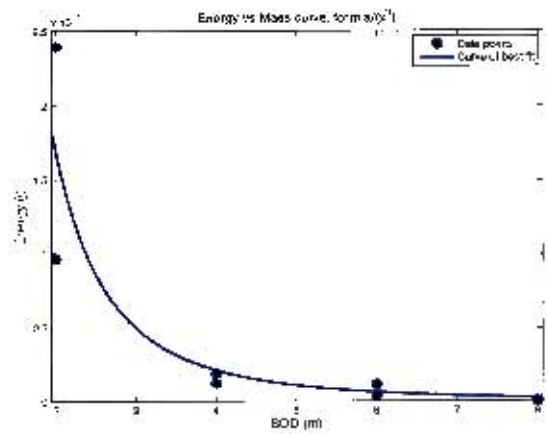

Figure 8.40. Constant mass of 100g, channel 3

The collection of these curves were plotted between 2m and 4m to allow for a better view of the elbow of the curves. By presenting just a small portion of the curves their relationship with each other was more closely analyzed.

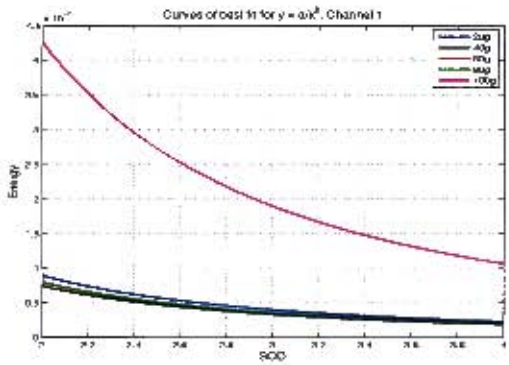

Figure 8.41. Fitted curves for channel 1

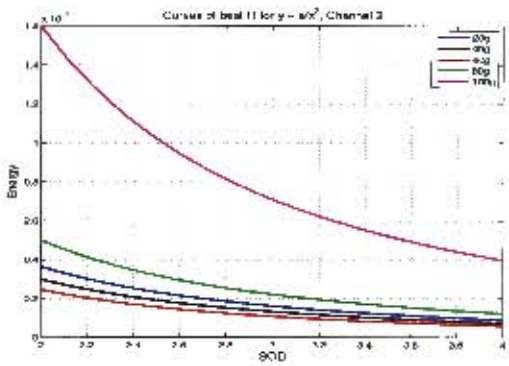

Figure 8.42. Fitted curves for channel 3

Figures 8.41 and 8.42 are the squared relationship curves for both channel 1 and 3. Data from the 20g shots were not fitted because there was insufficient usable data points. The results for curve fitting for channel 2 are not presented as they too were deemed unusable for also having too few data points.

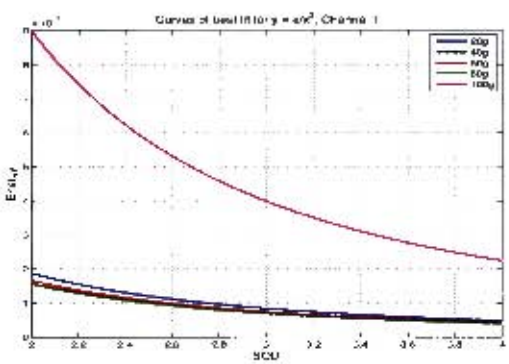

Figure 8.43. Fitted curves to channel 1

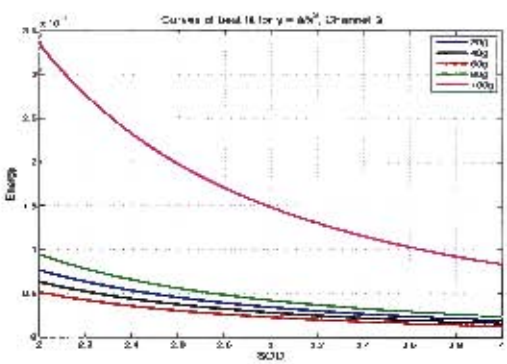

Figure 8.44. Fitted curves to channel 3

Figures 8.43 and 8.44 are the cubic relationship curves for both channel 1 and 3. To properly view the differences between the varying masses the 100g shot was removed and the graph was focused on a SOD between 2 and 4 meters.

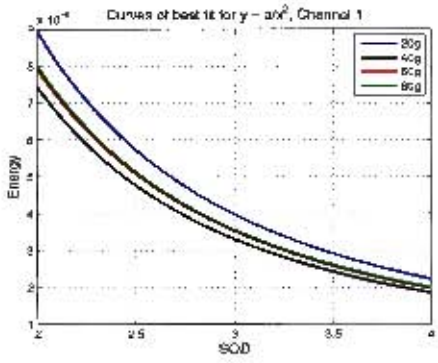

Figure 8.45. Zoom in on 2 - 4m, less 100g curve

Table 8.2. Coefficients and r^2 and sse for channel 1, $y = \frac{a}{x^3}$

Mass	a	r^2	sse
20	3.6e-007	0.67	3.83e-015
40	3e-007	0.89	8.68e-016
60	3.2e-007	0.76	2.72e-015
80	3.2e-007	0.34	5.3e-015
100	1.7e-006	0.49	2.91e-013

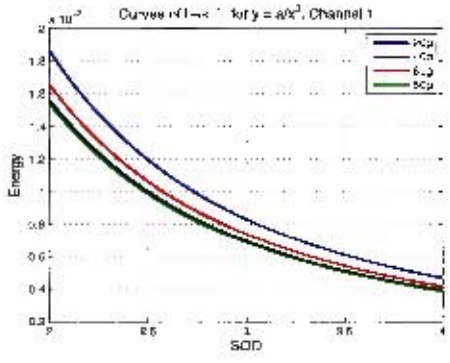

Figure 8.46. Zoom in on 2 - 4m, less 100g curve

Table 8.3. Coefficients and r^2 and sse for channel 1, $y = \frac{a}{x^2}$

Mass	a	r^2	sse
20	7.5e-007	0.73	3.11e-015
40	6.3e-007	0.96	3.3e-016
60	6.6e-007	0.8	2.23e-015
80	6.2e-007	0.13	7.05e-015
100	3.6e-006	0.52	2.74e-013

Table 8.3 and 8.2 show the coefficients used in generating the curves as well as their fit characteristics for both the squared and cubic relationship. The figures along side (8.45 and 8.46) are the best fitting curves for masses between 20g and 80g. The r squared (coefficient of determination) value should be near 1 for a very good fit and 0 for bad, inversely the SSE (sum square of errors) should be near zero when a good fit is present. The very low SSE value should be attributed to the low actual values of the curve. In effect they should all be regarded without their exponential ends.

8.3.6 Waveform shape

A comparison was made between mechanically identical shots from the same antenna to identify if any waveform patterns were present. For every configuration, SOD and charge mass, two shots were fired allowing for only a single comparison for every setup. Taking in to account all mis-fires other errors during testing, there were 16 comparisons available. This comparison was done for each channel and then a comparison between channels was carried out. The bar graphs, figures 8.47 and 8.48, show the total number of shots in each 10% band of correlation. Channels 1 and 3 were the primary source of data since channel 2 had less data points to work with as the antenna was re-orientated during testing for a better siganl detection.

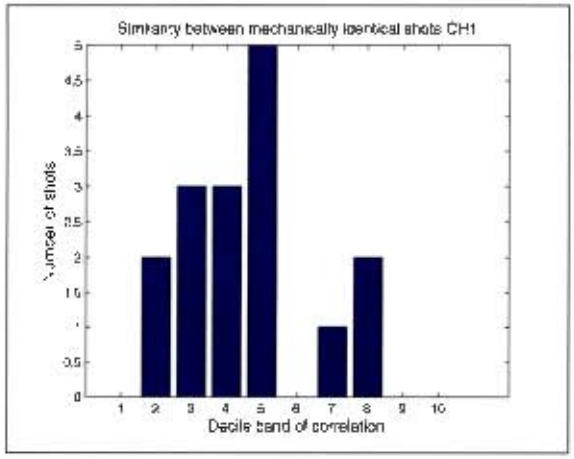

Figure 8.47. Bar graph showing number of similarly correlated shots

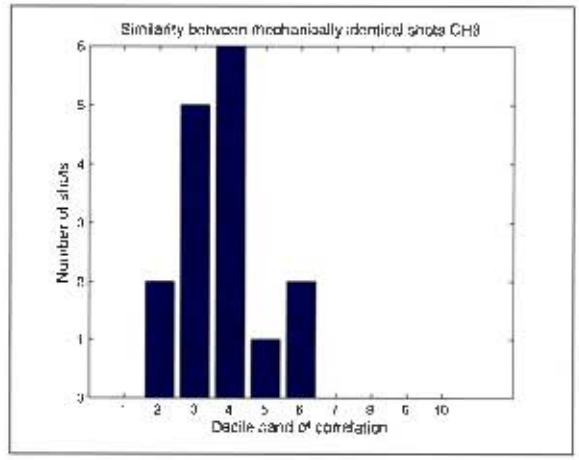

Figure 8.48. Bar graph showing number of similarly correlated shots

Lastly the individual shots from each antenna were compared with their counterpart in another antenna. Figure 8.49 shows how similar channel 1 and channel 3 were.

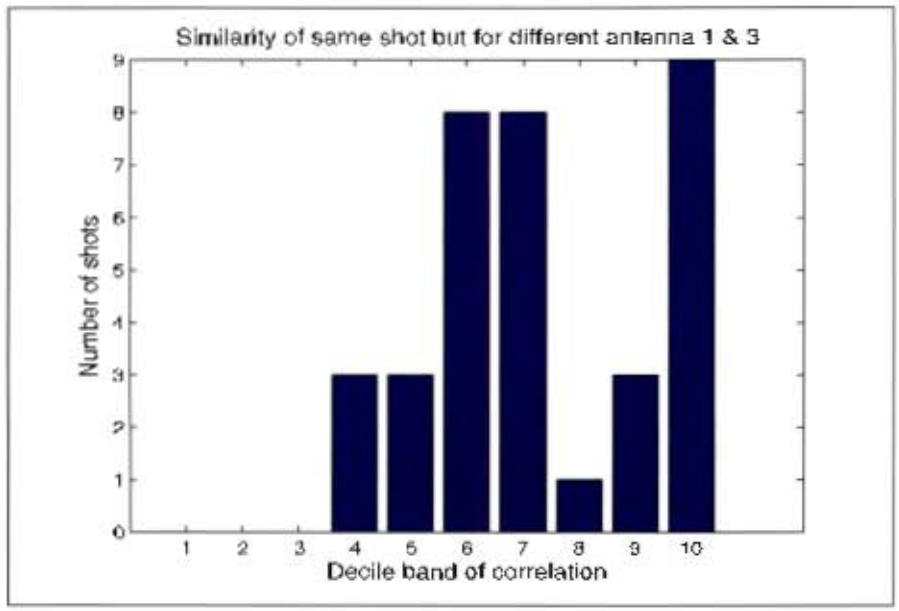

Figure 8.49. Bar graph showing % correlation between individual shots of different antenna

9 Observations

9.1 Visual inspection

Inspecting the signals by eye and comparing the waveform shapes to notes made during testing, some factors can be accounted for. For example, in channel 2 it was very clear that changing the direction in which the antenna faced affected the detection of signals. In shot 24 the metal stand upon which the tubing was placed became so damaged that it was discarded. From shot 25 (the delayed signal) sand was used to prop up the tubing. At the same time an adjustment to the equipment used in recording seemed to have little effect. For the large blasts and at greater SOD an additional coaxial cable had to be used on channel 3 but this made no significant impact on the signal recorded.

9.2 Characteristic frequency

The individual channels picked up different frequencies more regularly than its counterparts. Channel 1 had a tendency to see signals in the 70 - 80kHz range, while channel 3 stayed lower in the 10 - 30kHz range. This is illustrated by comparing figures H.235 and H.301. Channel 2 had too little usable points for any judgment to be made on what kind of frequency it was picking up. The difference in the range of frequencies could be put down to antenna orientation, refer to section 5.3 for a discussion on antenna characteristics. The limited bandwidth studied in this project also impairs the ability to say that the isolated frequencies are the only indicators of and explosion of this type but rather confirm previous studies in that such frequencies could be found in the kHz range.

9.3 Energy relationship

No definitive curve was obtained that could accurately follow the data points. The cubic relationship produced the best fitting coefficients which was not unexpected since a higher order polynomial often has better curve fitting properties. The 60g and 100g curves were the best fitting in both channels with data points being closets to the curve. The energy calculated for mechanically similar shots at times had a wide spread and this is very clear in the spread of the 80g shots in both channels, Appendix F. The variance in energy output could be attributed to the noise levels or variance in explosive energy.

9.4 Waveform shape

For this project a correlation above 50% was deemed "good", correlation criteria were not mentioned in open literature before.
Channel 2 data was not used in the correlation since it had a small usable data set. Channel 1 had only half of its comparisons at 50% or more while channel 3 had only three. Notabley the majority of channel 3 comparisons were in the 40% band. The correlation between mechanically similar shots was therefore deemed to be "unsatisfactory". These statistics appear not to favour the idea that mechanically similar shots produce similar waveforms. However the data from channel 1, with approximately half of the shots being well correlated, is encouraging and with more accurate equipment and/or testing procedures a larger degree of similarity may present itself. The designation of unsatisfactory is a comment on the data set and does not necessarily reflect the expected results for similarly conducted tests at a later stage.

9.5 Orientation

The placement of the antenna made a significant impact only in terms of its own gain pattern. This is seen in channel 2, where the antenna was placed with neither its aperture being side on nor endfire to the blast. This resulted no signal detection until it was re-oriented with the aperture facing the charge head on. This was an antenna characteristic and not a feature of the event. Channel 2 and Channel 1 had the same antenna setup but were at different angles with respect to the the initiation cord - unfortunately there was insufficient data to make any conclusive statements concerning this factor. The correlation between Channel 1 and 3 was very good with only three out of 33 shots being under 50% similar. It appears that the location in the azimuthal plane has little effect on polarization of the signals. Also since the proximity to the source was much less than the wave length observations on the directional properties was not possible.

10 Conclusions and Recommendations

To control the many aspects affecting the results of signals generated by blast waves is a difficult task. But in order to better understand and explain the event it is required that each factor be studied individually. This leads to the following recommendations:

Antenna and circuitry

The antennas used were effective over a small bandwidth and were not specifically designed for this study, while the circuit was custom made. A complete redesign however is needed for the circuit to ensure a flat high gain frequency response over a large band. The loops were used because of their ease of construction and previous experience with them. The use of a purpose built antenna covering a wide band and with a large amount of gain as it seems the signals generated were small, would increase the effectiveness of the study.

Surrounding material

A clean environment would remove the dust cloud effect and help isolate the explosive particle effect. The surrounding area should not have any particles or material that would move under the blast wave action.

Seismic effect

The electric seismic effect was removed as an aspect of consideration but to minimize the effect the best approach would be to suspend the charge. The height above the ground would delay the blast wave interacting with the sub surface water table as the impedance offered by the different material (air and soil) would help slow the blast wave.

Record length

The record length of these tests was not sufficient to record the full event, this is most evident in shot 6 and 7. Recording for a longer time would give a more complete picture and ensure significant data is missed. The ideal length would be when the signal has returned to the starting level and has ceased fluctuating.

Sampling speed

The sampling speed sets the cut-off frequency to which the data can be analyzed. This is the nyquist frequency and it is half the sampling frequency. For this project only data up to 1.25 MHz could be reliably analyzed assuming all other aspects were accounted for. Increasing this limit means a higher range of frequencies can be investigated (MHz) which literature states could contain additional information.

Charge shape

The balls of PE-4 were rolled by hand and although their diameters were fairly consistent, this introduced a human factor. Having moulded charges removes this, allowing for a closer relationship between size and effect to be established.

Antenna type

Identifying which field is more prominent, E or H, is important and determining this means testing various antenna types and again covering a wider range of frequencies. Establishing which type of field holds the most energy also sheds light onto the mechanism of generation.

Directional monitoring

Replacing antenna that pick up the general surroundings with a directional antenna would allow for the identification of a source of the signals received. That is should there be ringing pieces directional antenna could pick this up as one station would get a signal and then another as the piece is moving.

Explosive material

Different types of explosive have been noted to produce different signals. Testing the different compositions of explosives and their relationships to each other chemically could also shed light into the generation mechanism.

Once a clearer picture of the basic event is obtained future studies should introduce real world factors. Placing obstacles in the path of the shock wave, between the charge and the antenna, would show the effects of foreign material on the signal. Subsurface testing would also be interesting as it would more accurately simulate the detonation of land mines.

References

[1] Paul W Cooper. *Explosives engineering.* Wiley-VCH, 1996.

[2] Stacey Order. *Literature Research Report: Detonics.* BISRU, 2002.

[3] Wikipedia. Dipole — wikipedia, the free encyclopedia, 2009. [Online; accessed January-2009].

[4] User Interface Engineering. Galleries: The hardest working page on your site, 2009. [Online; accessed January-2008].

[5] Chennai Cable Corporation. Flexible cables, 2009. [Online; accessed July-2009].

[6] Geek24. Electrosensor, 2009. [Online; accessed July-2008].

[7] The Howland company. About the howland company, 2009. [Online; accessed July-2009].

[8] Fox electronics. Skywave dipole antenna, 2009. [Online; accessed July-2009].

[9] Test equipment connection. New com-power pa-118 - antennas, 2009. [Online; accessed July-2009].

[10] A P Boronin, V N Kapinos, and S A Krenev. Phyisical mechanism of electro magnetic field generation with explosion of condensed explosive charges. results of experimental studies. *Fizika Goreniya i Vzryva*, 26(5):117–123, 1990.

[11] Test equity. Tektronix tds 1000, tds2000 series digital storgae oscilliscopes, 2009. [Online; accessed September-2009].

[12] C Balanis. *Antenna Theory analysis and design.* John Wiley & Sons, 2nd edition, 1994.

[13] Encyclopedia britanica. diffraction grating, 2009. [Online; accessed July-2009].

[14] National Instruments. Characteristics of different smoothing windows, 2009. [Online; accessed 28-January-2009].

[15] UNESCO. Memory of the world safeguarding the documentary heritage, glossary, 2007. [Online; accessed December-2007].

[16] H Kolsky. Electromagnetic waves emitted on detonation of explosives. *Nature*, 173(4393):77, 1954.

[17] V V Adushkin and S P Soloviev. Generation of electric and magnetic fileds by air, surface and underground explosions. *Combustion, Explosions and shock waves*, 40:649 –657, 2004.

[18] W H Andersen and C L Long. Electromagnetic radiation from detonating solid explosives. *Journal of applied Physics*, 36(4):1494–1495, 1965.

[19] V I Pechkovskii and G S Kal'chik. Quenching of detonation by the magnetic field associated with the explosion of cased charges. *Fizika Goreniya i Vzryva*, 6(1):123–126, 1970.

[20] L M Gorshunov, G P Kononeko, and E I Sirotinin. Eelctromagnetic disturbances accompanying explosions. *Journal of experimental and theoretical Physics*, 26(3):500–502, 1968.

[21] GF Kinney and KJ Graham. *Explosive shocks in air*. Springer-Verlag New york, 2nd edition, 1985.

[22] C Balanis. *Advanced Engineering Electromagnetics*. John Wiley & Sons, 1989.

[23] J C Maxwell. A dynamical theory of the electromagnetic field. *Philosophical Transactions of the Royal Society of London*, 155:459–512, 1865.

[24] MA Cook. *Science of High explosives*, chapter 7. Reinhold Publishing, 2 edition, 1958.

[25] A P Boronin, Yu A Medvedev, and B M Stepanov. Explosion in an external electric field. *Journal of experimental and theoretical Physics Letters*, 8(4):169–173, 1968.

[26] A P Boronin, Yu A Medvedev, and B M Stepanov. Generalized electrical pulse and dissapation dynamics of high-explosive-charge explosion products. *Fizika Goreniya i Vzryva*, 9(4):541–551, 1973.

[27] A P Boronin, V A Vel'min, Yu A Medvedev, and B M Stepanov. study of the electro field in the near zone of explosions produced by silid explosives. *Zhurnal Prikladnoi Mekhaniki i Tekhnicheskoi Fiziki*, 9(6):99–103, 1968.

[28] V V Adushkin, S P Soloviev, and V V Sukrov. Electric field arising during ejection explosion. *Fizika Goreniya i Vzryva*, 26(4):117–121, 1990.

[29] T Takakura. radio noise radiated on the detonation of explosive. *Publications of the Astronomical Society of Japan*, 7(4):210–220, 1955.

[30] V A Vel'min, Yu A Medvedev, and B M Stepanov. Passage of radio waves through the region of an explosion. *Fizika Goreniya i Vzryva*, 6(3):410–413, 1970.

[31] V A Vel'min, V F Korets, Yu A Medvedev, and B M Stepanov. Certain effects which take place when a radio wave passes through the region of an explosion. *Zhurnal Prikladnoi Mekhaniki i Tekhnicheskoi Fiziki*, 2:136–139, 1971.

[32] A P Boronin, V N Kapinos, S A Krenev, and V N Mineev. Phyisical mechanism of elecromagnetic field generation during the epxlosion of condensed explosive charges. survey of literature. *Fizika Goreniya i Vzryva*, 26(5):110–116, 1990.

[33] E I Bichenkov. Electrodynamic effects accompanying the propagation of current-carrying shock waves in a transverse magnetic field. *Combustion, Explosions and shock waves*, 36(36):809 – 815, 2000.

[34] S P Soloviev, V V Surkov, and J J Sweeney. Quadropolar electromagnetic field from detonation of high explosive charegs on the ground surface. *Journal of geophysical reasearch*, 107:B6, 2002.

[35] S P Soloviev and J J Sweeney. Generation of electric and magnetic field during detonation of high epxlosive charegs in boreholes. *Journal of geophysical reasearch*, 110:B01312, 2005.

[36] V M Sorokin, I Sergeev, and A K Yaschenko. Electromagnetic field generation by explosion in the ionosphere. *Advances in Space research*, 30:2511 –2515, 2006.

[37] R A Broding, S D Buchanan, and D P Hearn. Field experiments on the electroseismic effect. *IEEE Transactions on Geoscience Electronics*, 1(1):23 – 31, 1963.

[38] Norman Morrison. *Introduction to Fourier analysis.* John Wiley & Sons, 1994.

[39] GM Jenkins and DG Watts. *Spectral Analysis and it's applications.* Holden-Day, 1969.

[40] JN Rayner. *An introduction to spectral analysis.* Pion Limited, 1971.

A Transfer functions

A transfer function is used to describe the change undergone by a signal when passing through a system, in this case a circuit. Assume an input voltage, V_{in}, is a function of frequency (ω) and time (t) written in phasor notation as

$$V_{in} = A_i e^{j\omega t} \tag{A.1}$$

and the output voltage is

$$V_{out} = A_o e^{j(\omega t+\theta)} \tag{A.2}$$

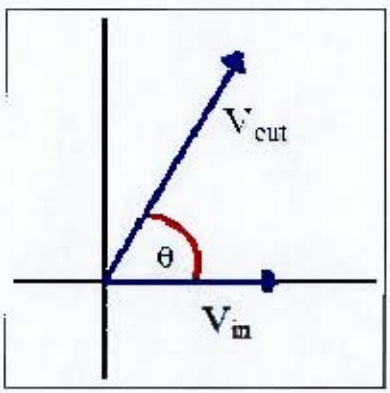

Figure A.1. phasor diagram of transfer function effect

The transfer function can then be viewed as the vector

$$h(\omega) = \frac{A_o}{A_i} e^{j\theta} \quad f \geq 0 \tag{A.3}$$

$$= \frac{A_o}{A_i} e^{-j\theta} \quad f < 0 \tag{A.4}$$

applied to the V_{in} to obtain the V_{out} whose magnitude is

$$H(\omega)_| = \frac{A_o}{A_i} \tag{A.5}$$

and with an directional component of

$$\angle H(\omega) \quad \theta \tag{A.6}$$

B Electric seismic effect

The exact location of the test site was recorded using GPS. These co-ordinates were 25 29 02.8 S and 28 22 52.8 E. An image of this location was obtained from ©Google Earth and is presented in figure B.1.

Figure B.1. Google earth high image of South Africa

The electric seismic effect is the result of P or S waves traveling in through the surface of the earth and when coming into contact with a conductive layer causes a shock wave polarization. this generates a field that can possibly be detected by sensitive equipment. Below is a map of the ground water levels as on record with the department of water affairs and forestry.

Using this map and the satilite image an estimate was made based on the greatest speed possible for shock waves in the earth, calculations were made for the time required for a P wave to potentially hit a body of water and thereby create the EMF .

A P wave can travel between 5 and 7km.s^{-1} through the earths surface, depending on its make up. Given our location a conservative guess can be made, stating the water table to be approximately 10m below the surface. Between the time of detonation and the time taken for a P wave to hit the conductive layer is 1.4ms. This is longer than the record length itself so we can dismiss this effect on our recordings.

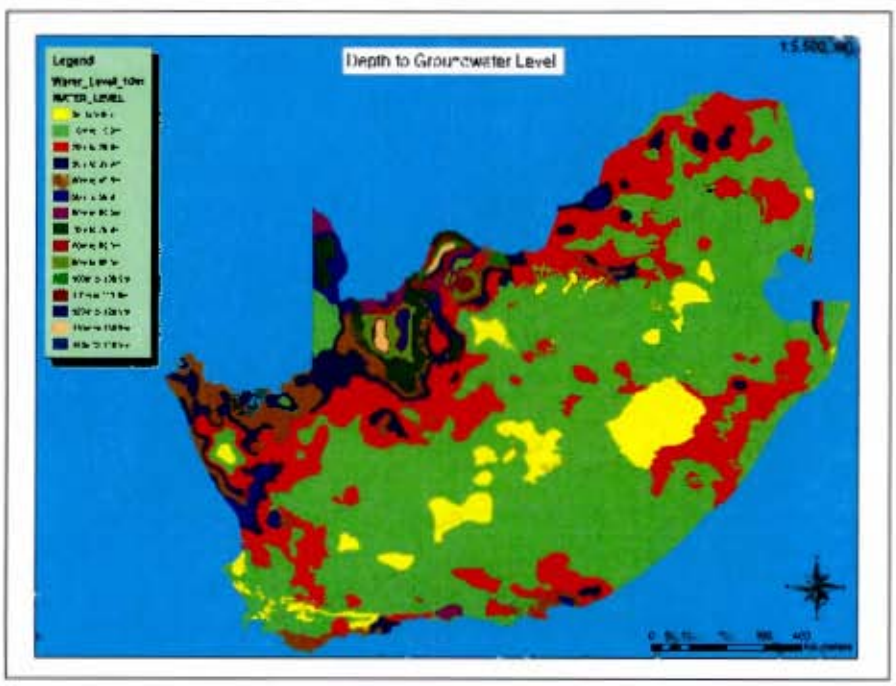

Figure B.2. Water level map obtained from Dept. Water affairs and forestry

C Preliminary Data

The data collected during preliminary testing is presented here in full. The conclusions and insights gained during this test phase have been discussed and mentioned in the body but only a piece of the work was given as evidence. The full collection of data is now shown.

C.1 February

This was the first set of test conducted in this project. The data was collected using the now familiar TDS oscilloscope during the testing of another project. The antenna was placed inside the blast chamber to one side so as to not interfere with the main test.

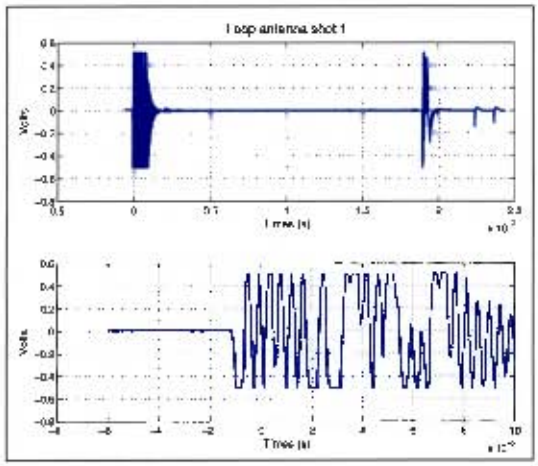

Figure C.1. Loop 1

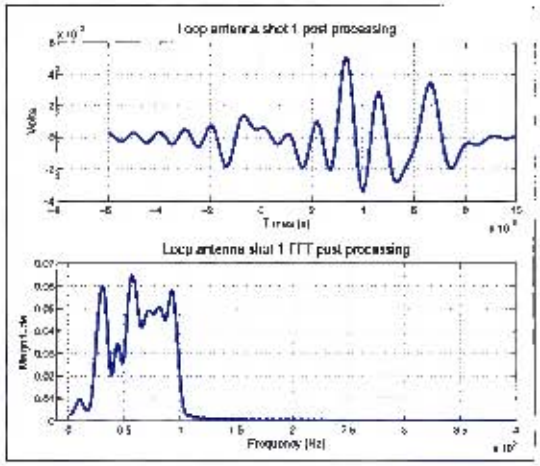

Figure C.2. Loop 1 filtered

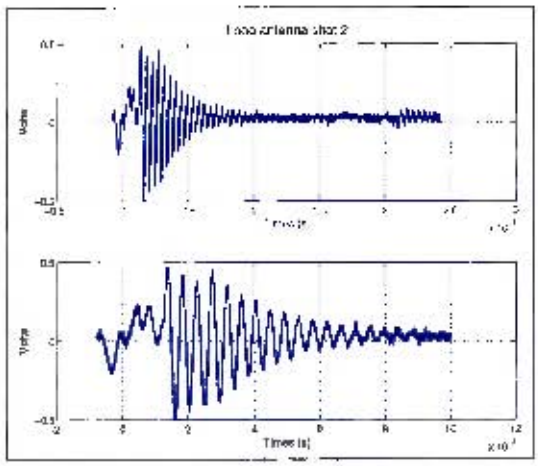

Figure C.3. Loop 2

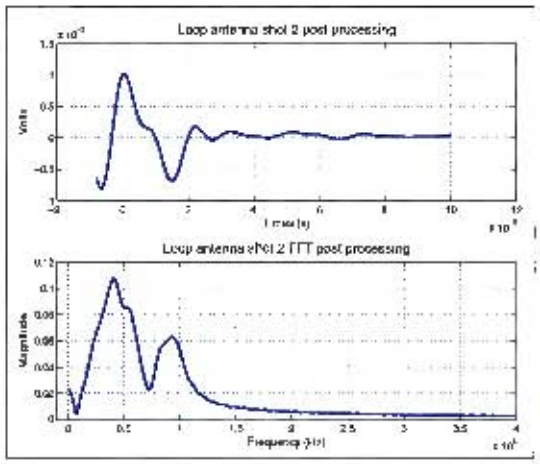

Figure C.4. Loop 2 filtered

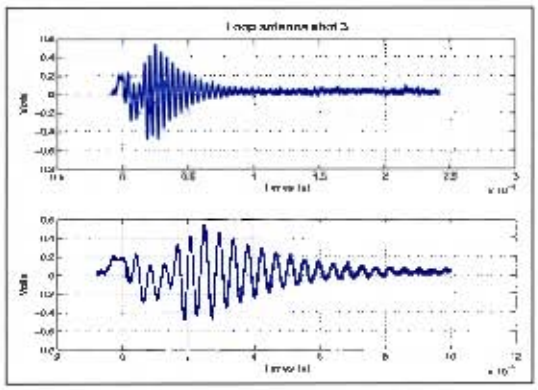

Figure C.5. Loop 3

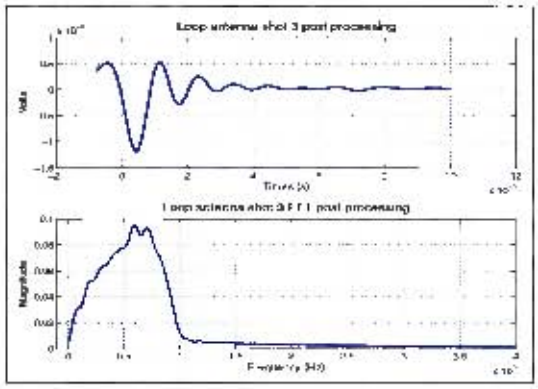

Figure C.6. Loop 3 filtered

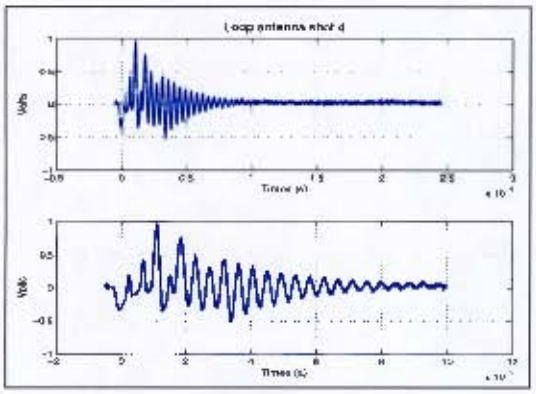

Figure C.7. Loop 4

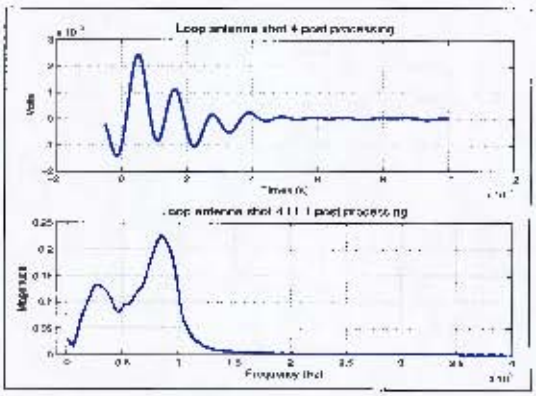

Figure C.8. Loop 4 filtered

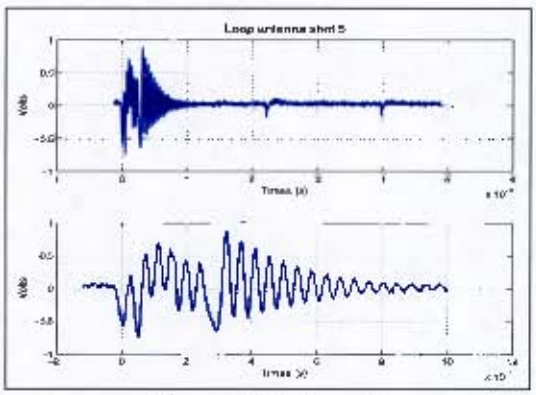

Figure C.9. Loop 5

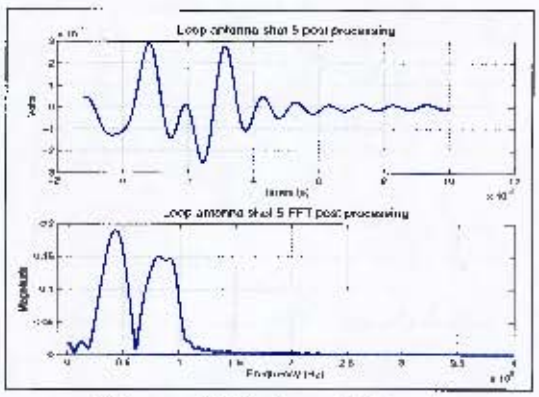

Figure C.10. Loop 5 filtered

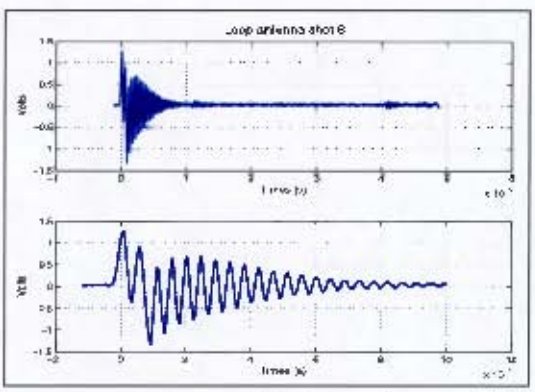

Figure C.11. Loop 6

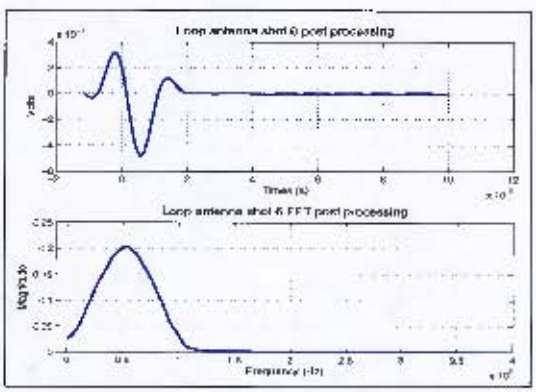

Figure C.12. Loop 6 filtered

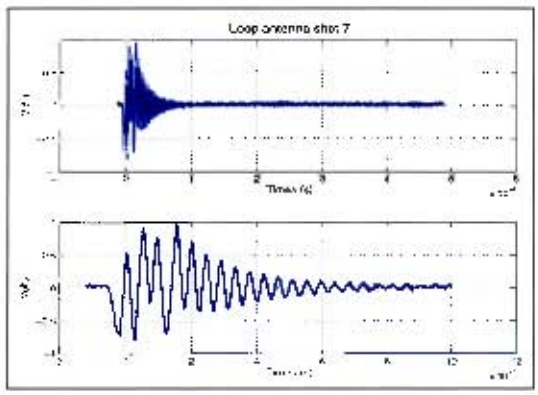

Figure C.13. Loop 7

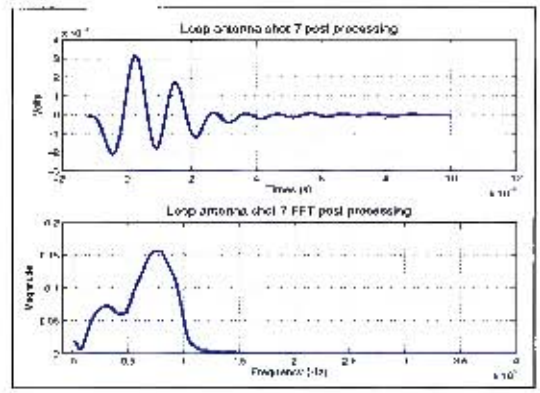

Figure C.14. Loop 7 filtered

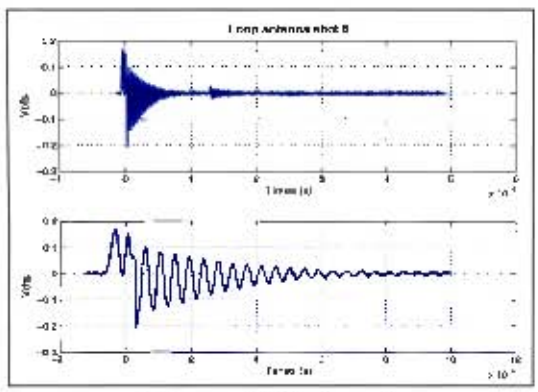

Figure C.15. Loop 8

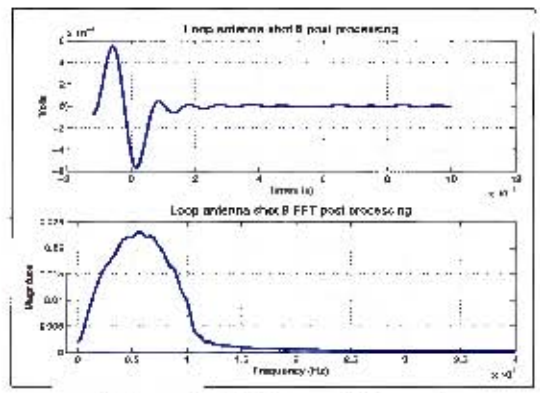

Figure C.16. Loop 8 filtered

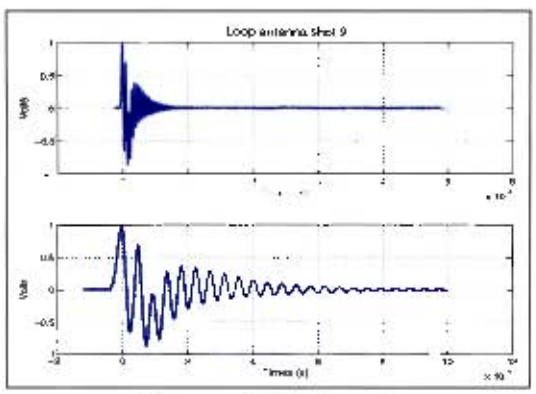

Figure C.17. Loop 9

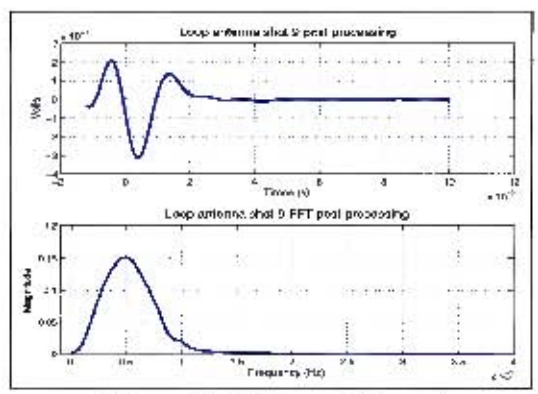

Figure C.18. Loop 9 filtered

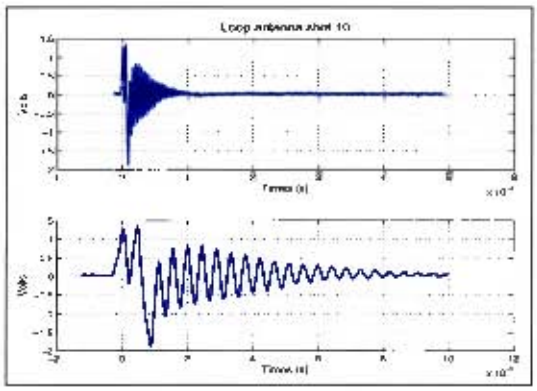

Figure C.19. Loop 10

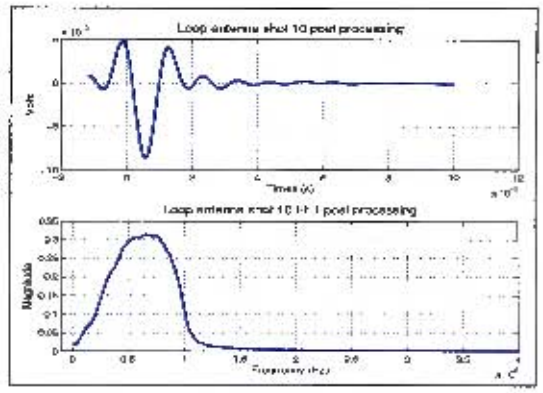

Figure C.20. Loop 10 filtered

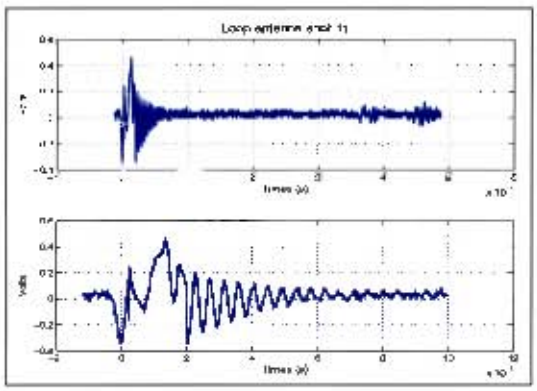

Figure C.21. Loop 11

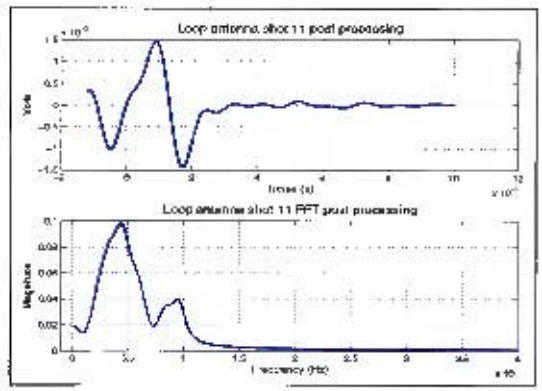

Figure C.22. Loop 11 filtered

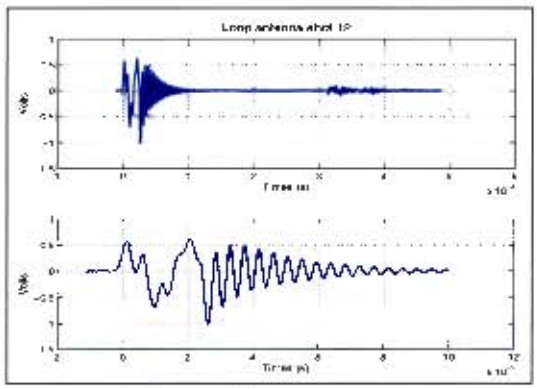

Figure C.23. Loop 12

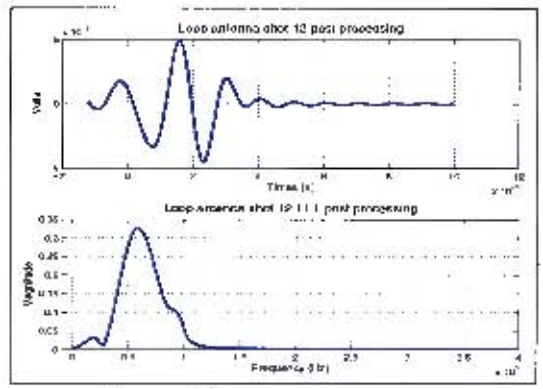

Figure C.24. Loop 12 filtered

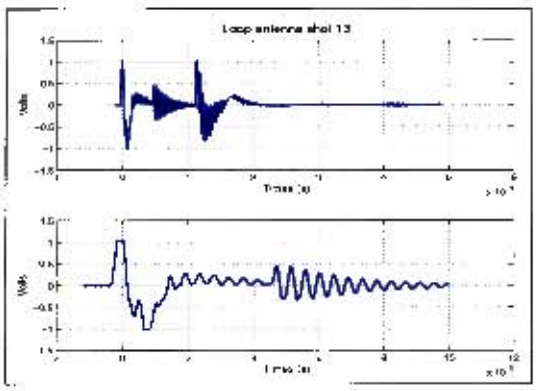

Figure C.25. Loop 13

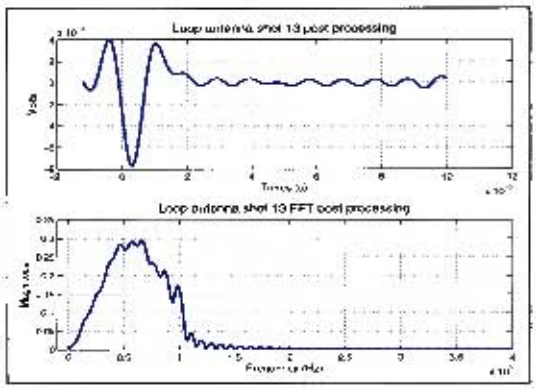

Figure C.26. Loop 13 filtered

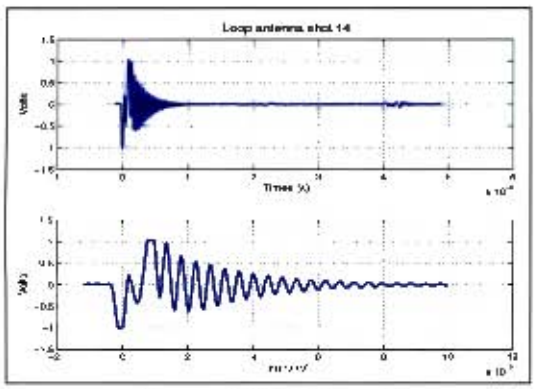

Figure C.27. Loop 14

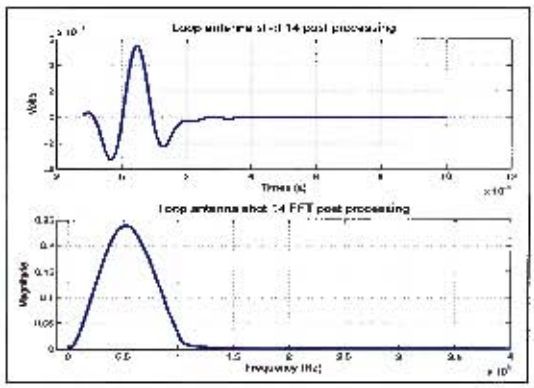

Figure C.28. Loop 14 filtered

C.2 March

C.2.1 series 1

Series one differs since not only was data collected on a oscilloscope but a PCI card was used at the same time. The card was capable of much longer records and provided a back up and as well as more wide vision of the event.

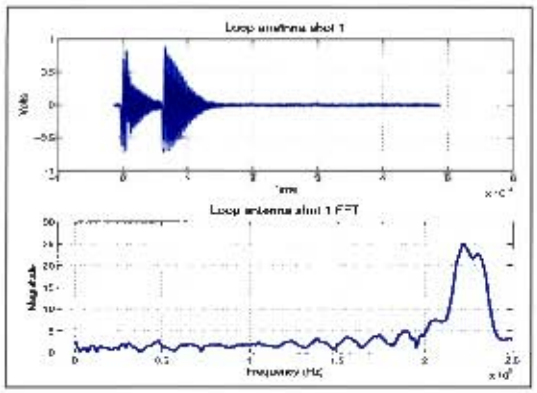

Figure C.29. Loop 1

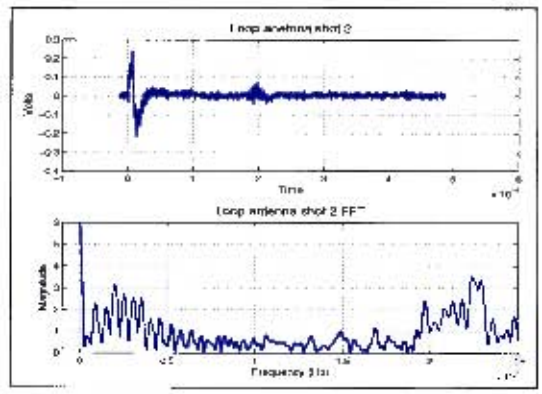

Figure C.30. Loop 2

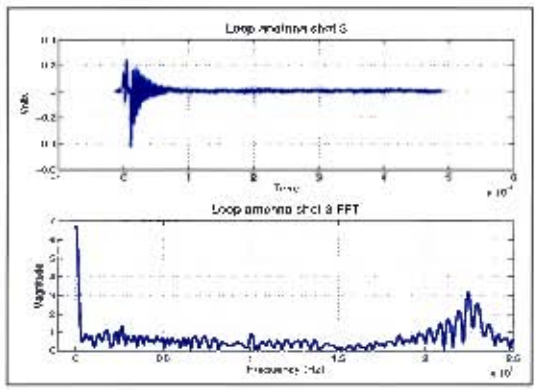

Figure C.31. Loop 3

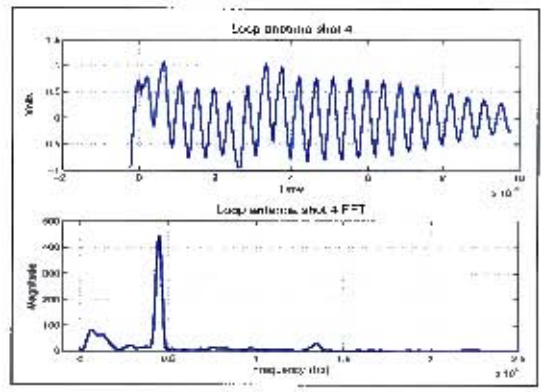

Figure C.32. Loop 4

Figure C.36 is a combination of the original and filtered signal and adjacent to that is the FFT of the filtered version's first 0.2ms.

The data from the PCI card is presented in figures C.38 - C.44

The figures below were obtained with the PCI recording two channels simultaneously, taking data from the Hoop and the small copper ring at the same time.

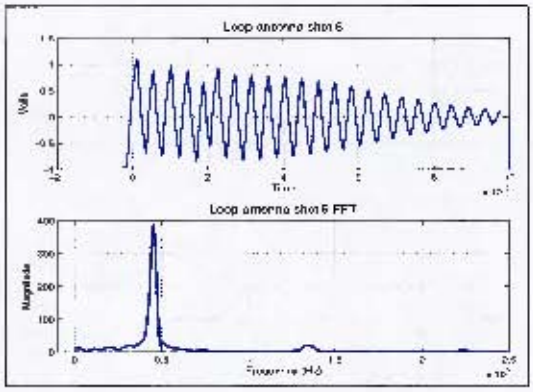

Figure C.33. Loop 5

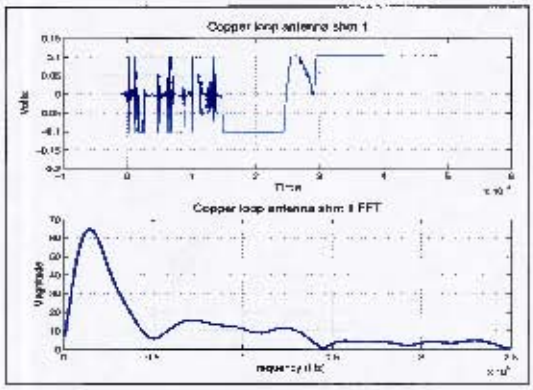

Figure C.34. Copper loop 1

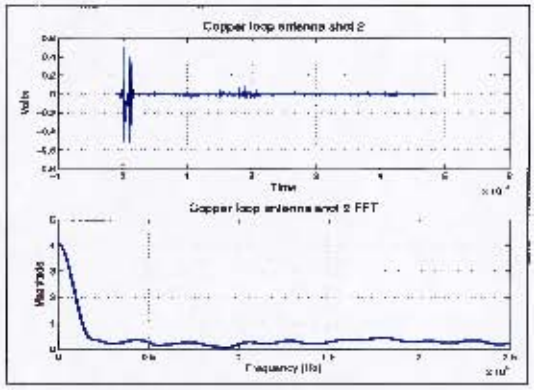

Figure C.35. Copper loop 1

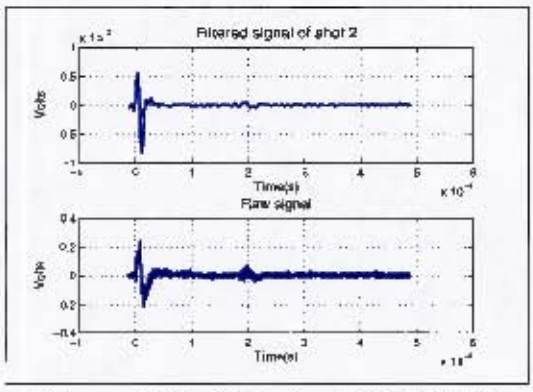

Figure C.36. Original and RAW shot 2

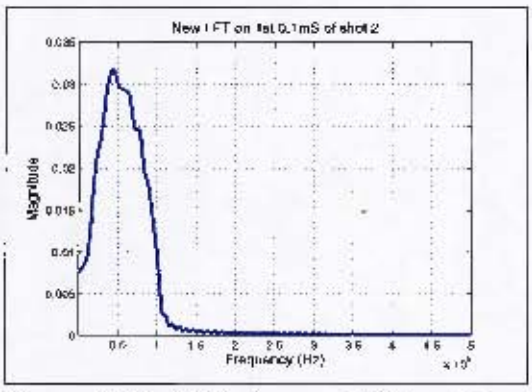

Figure C.37. FFT of truncated filtered signal 2

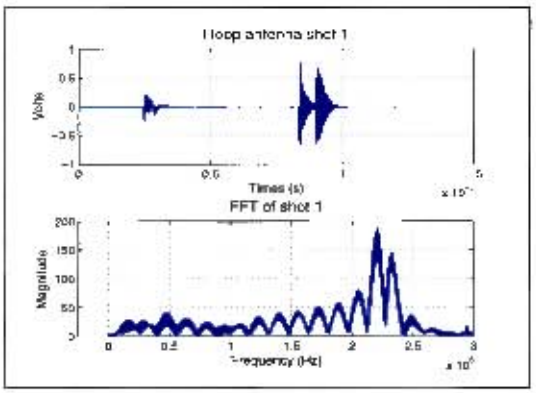

Figure C.38. PCI - Hoop 1

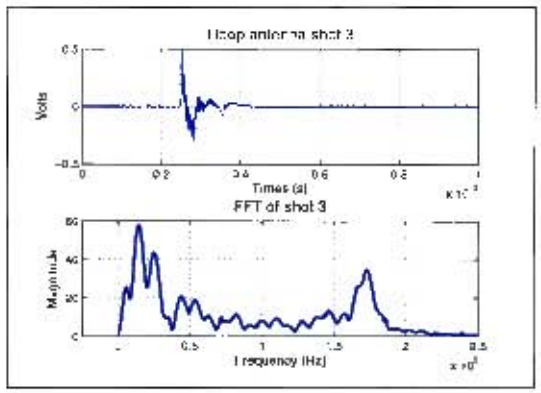

Figure C.39. PCI - Hoop 3

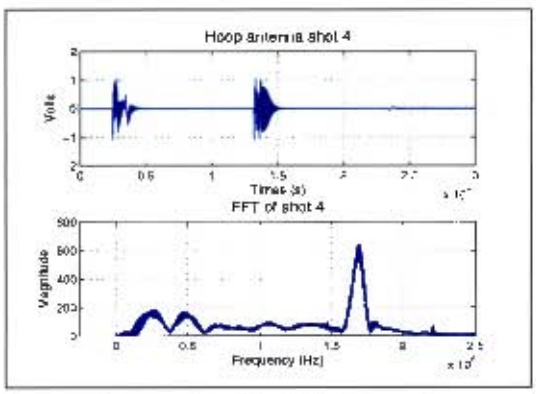

Figure C.40. PCI - Hoop 4

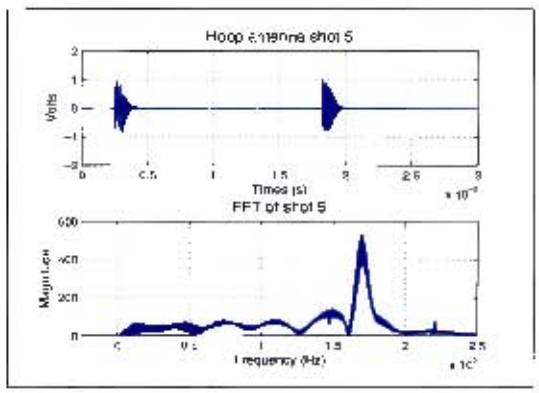

Figure C.41. PCI - Hoop 5

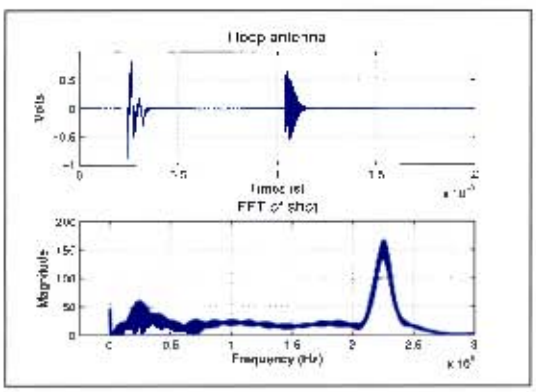

Figure C.42. PCI - Hoop 2

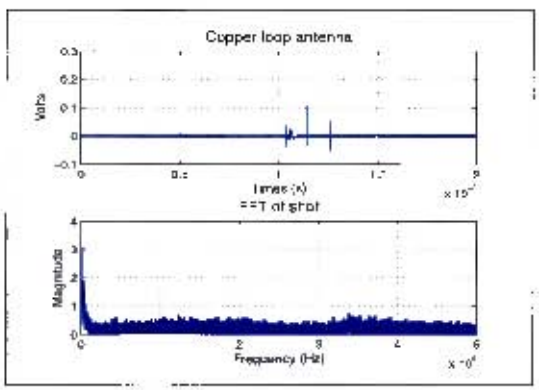

Figure C.43. PCI - Copper hoop 2

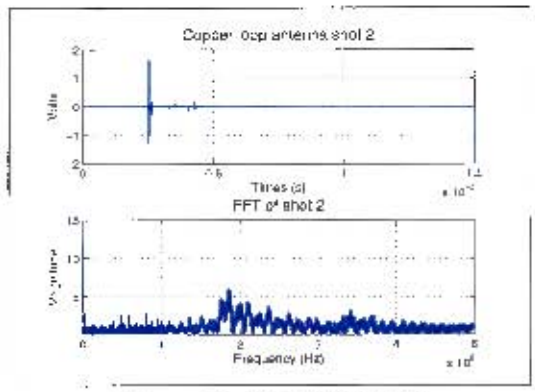

Figure C.44. NOT SURE

C.2.2 series 2

This series was run in the same fashion as the 1st except for the inclusion a current clamp on the detonation wires. The clamps were used to properly identify the effect of the electric detonation method.

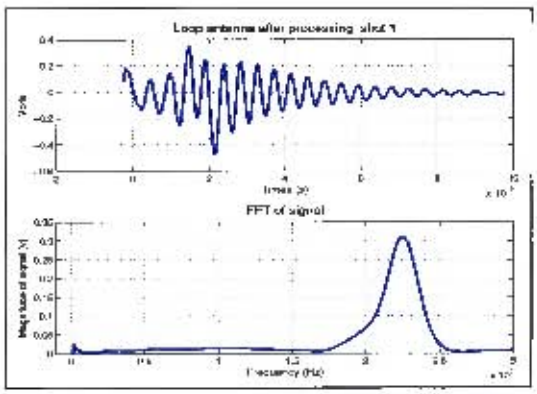

Figure C.45. Loop 1

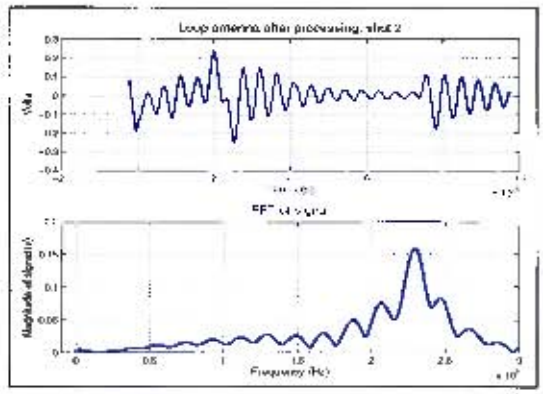

Figure C.46. Loop 2

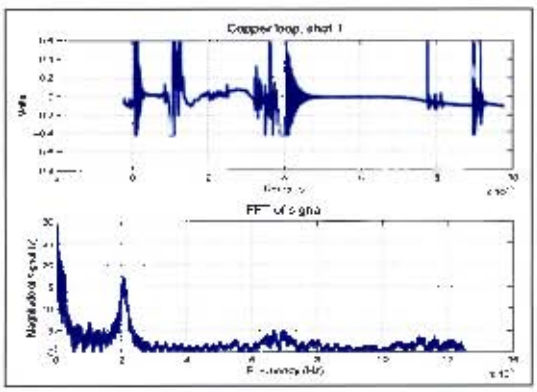

Figure C.47. Copper loop 1

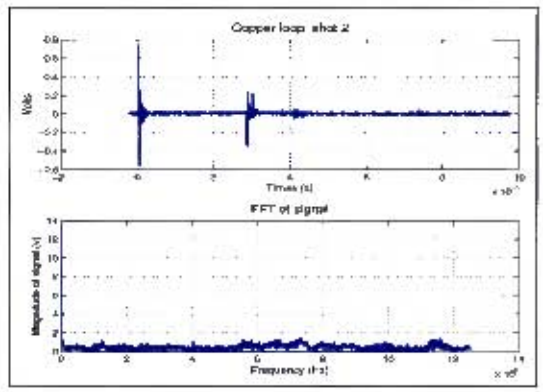

Figure C.48. Copper loop 2

Figures C.54 and C.55 shows how the detonation wires themselves seem to couple with the Hoop.

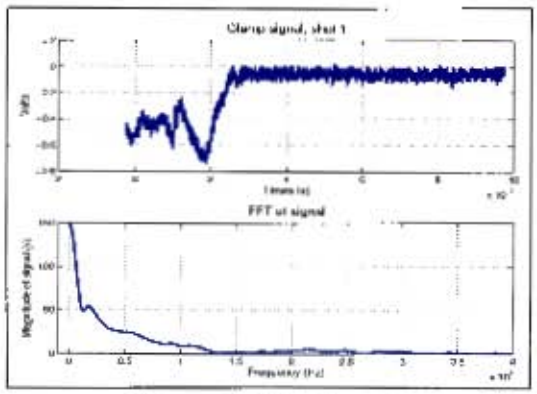

Figure C.49. Clamp 1

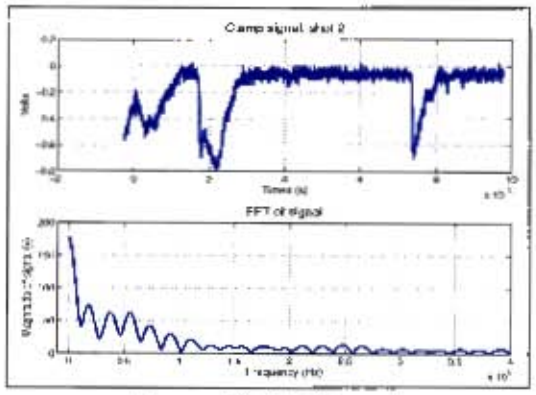

Figure C.50. Clamp 2

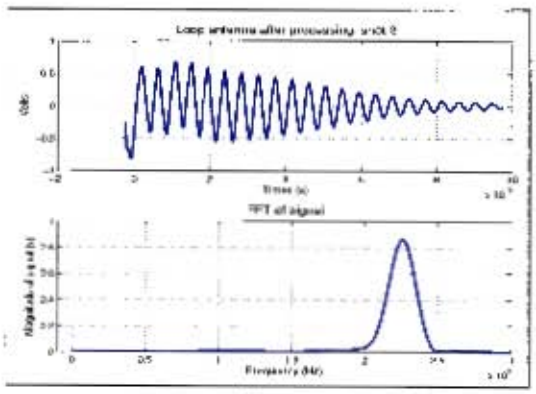

Figure C.51. Loop 3

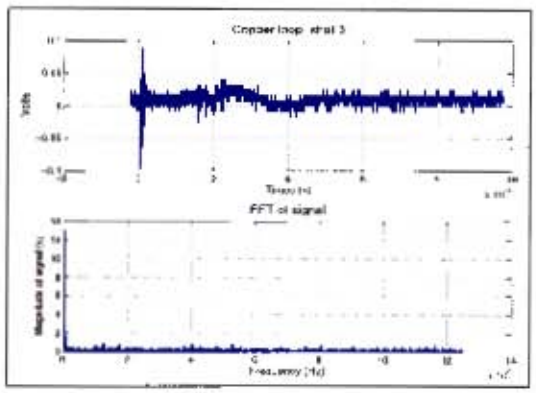

Figure C.52. Copper hoop 3

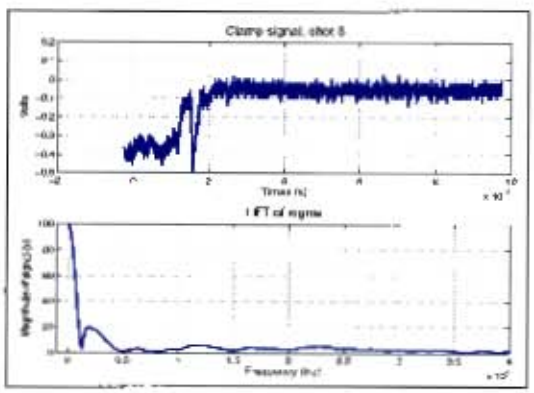

Figure C.53. Clamp 3

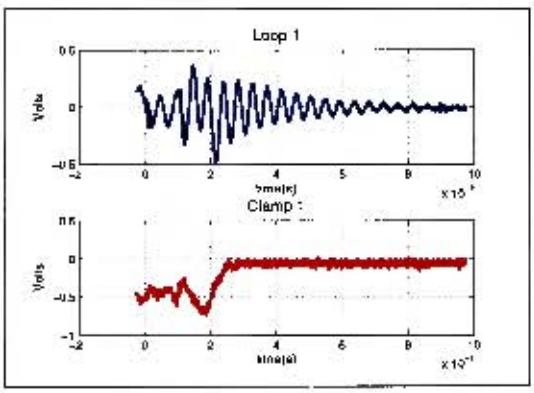

Figure C.54. Loop signal above clamp signal

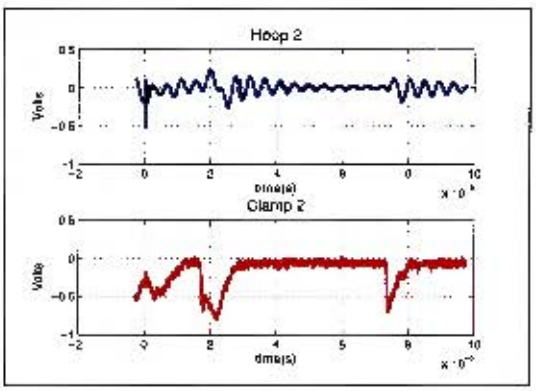

Figure C.55. Loop signal above clamp signal

C.2.3 series 3

This series used a whip antenna to determine if an electric field could be detected. Because of its nature the whip was inherently biased to a higher frequency.

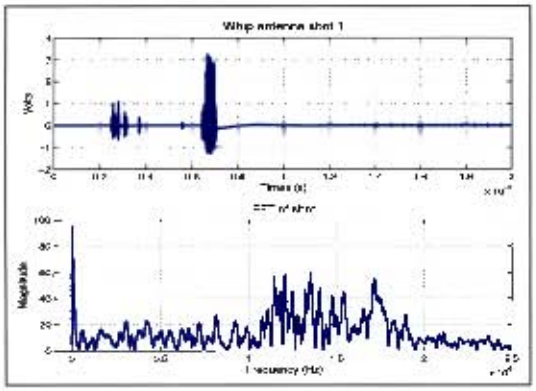

Figure C.56. Whip 1

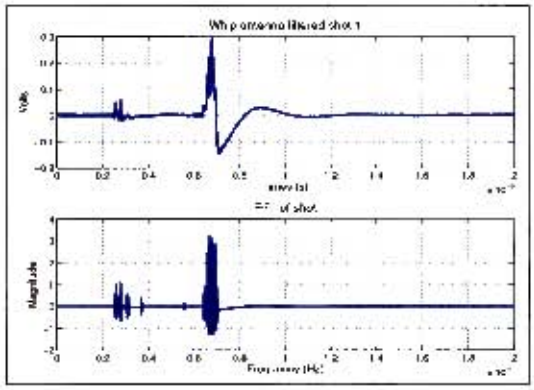

Figure C.57. Whip 1 filtered

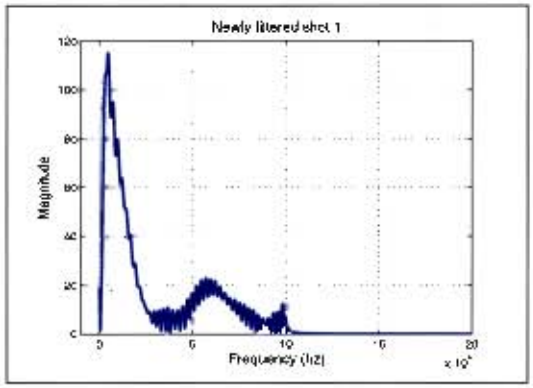

Figure C.58. Filtered shot 1

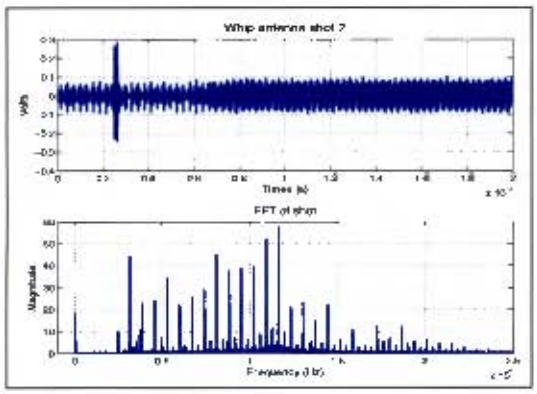

Figure C.59. Whip 2

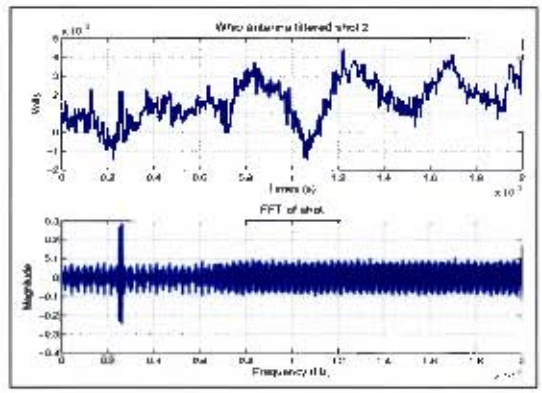

Figure C.60. Whip 2 filtered

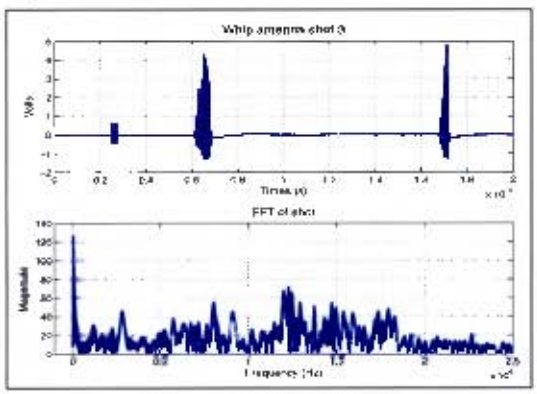

Figure C.61. Whip 3

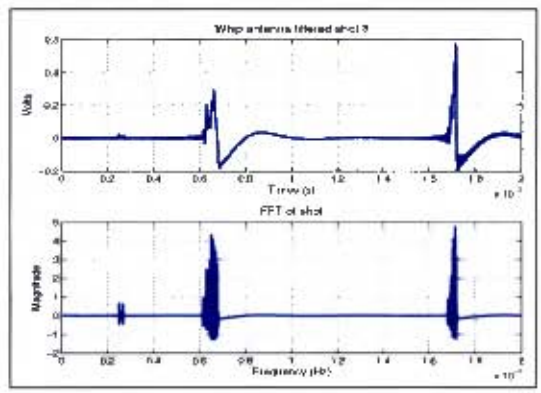

Figure C.62. Whip 3 filtered

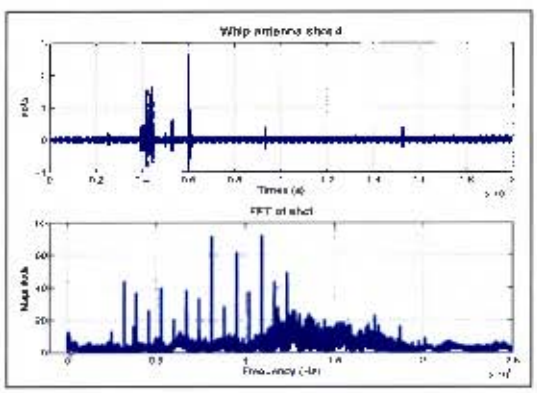

Figure C.63. Whip 4

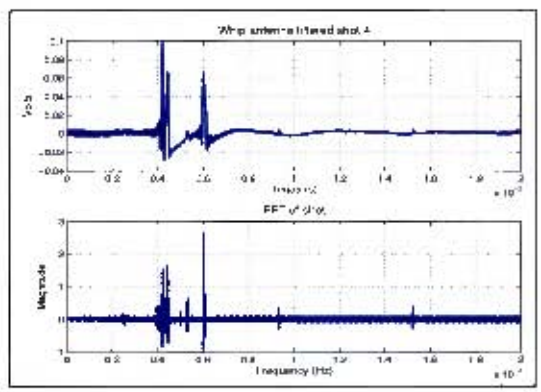

Figure C.64. Whip 4 filtered

C.3 Langebaan

The mechanical detonation carried out at the military base was initiated by safety fuse. The charge was placed on the ground and approximately a 30s delay was implemented using the safety fuse. There were 3 antennas used to receive signals, the *EET* hoop, the small copper hoops and the Rhodes Schwarz.

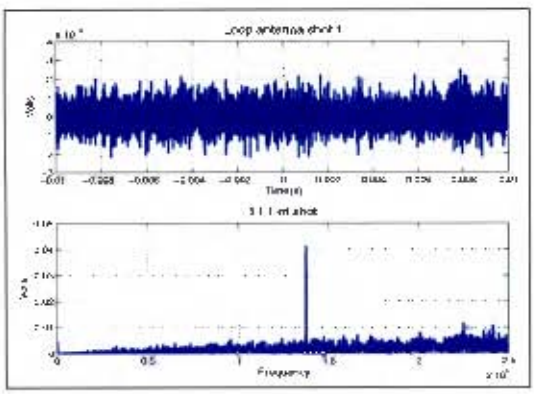

Figure C.65. Loop 1

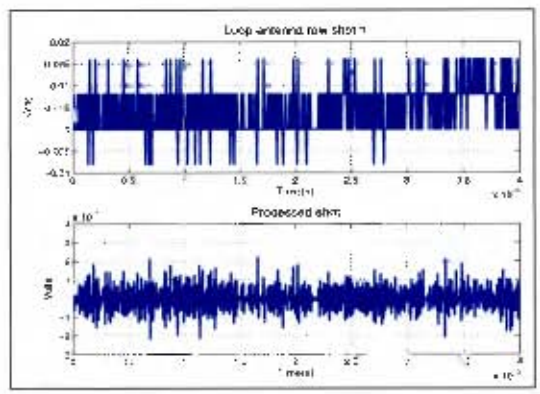

Figure C.66. Loop 1 pre-trigger data

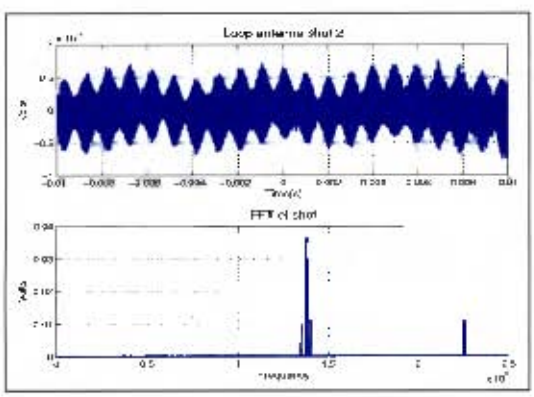

Figure C.67. Loop 2

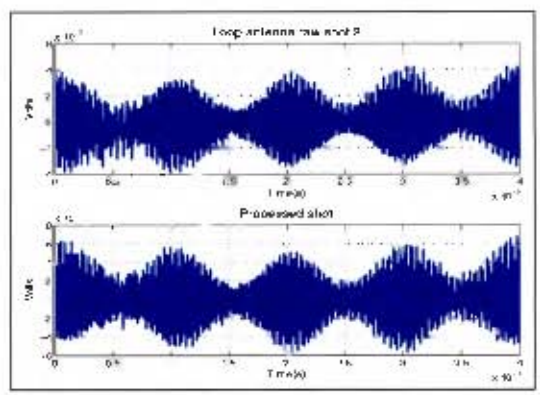

Figure C.68. Loop 2 pre-trigger data

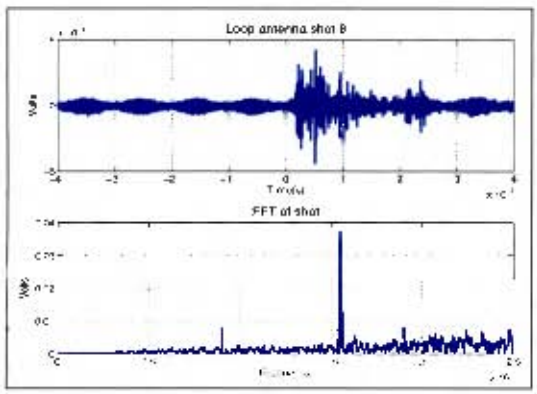

Figure C.69. Loop 8

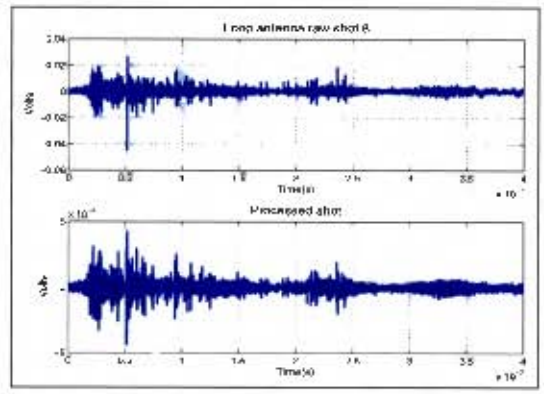

Figure C.70. Loop 8 pre-trigger data

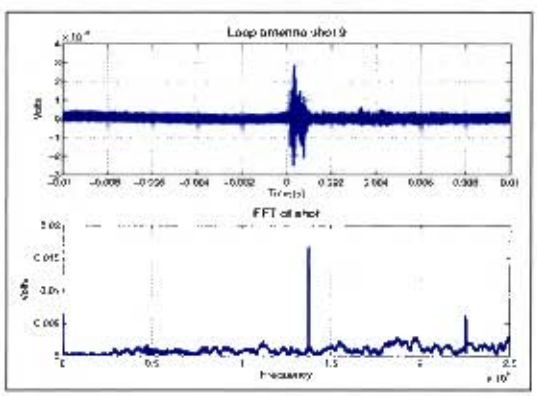

Figure C.71. Loop 9

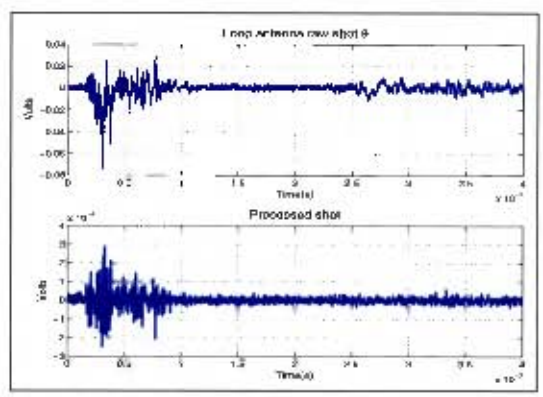

Figure C.72. Loop 9 pre-trigger data

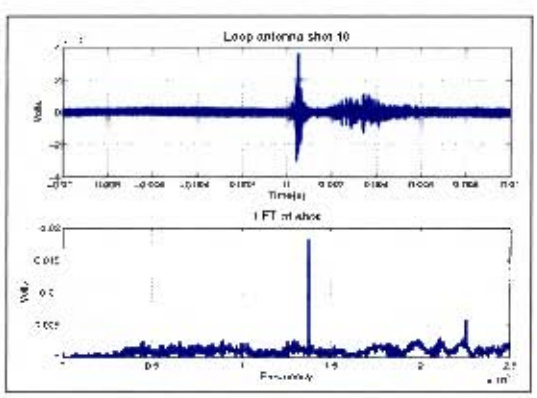

Figure C.73. Loop 10

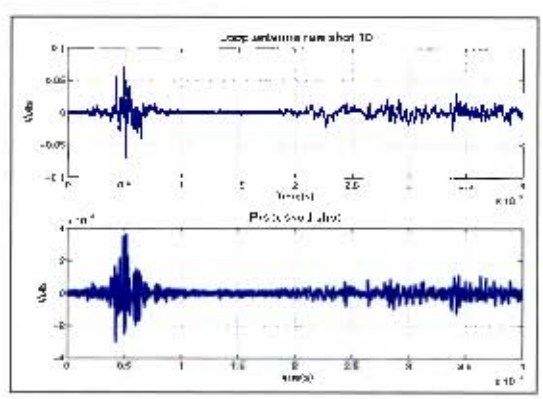

Figure C.74. Loop 10 pre-trigger data

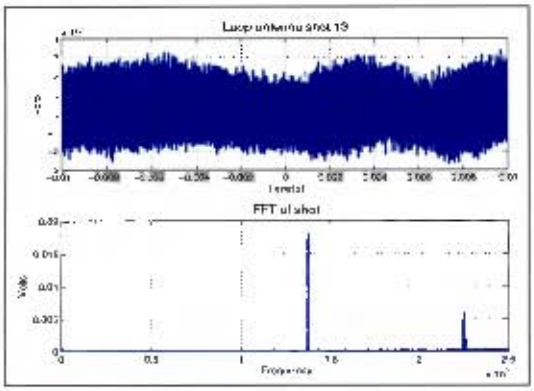

Figure C.75. Loop 13

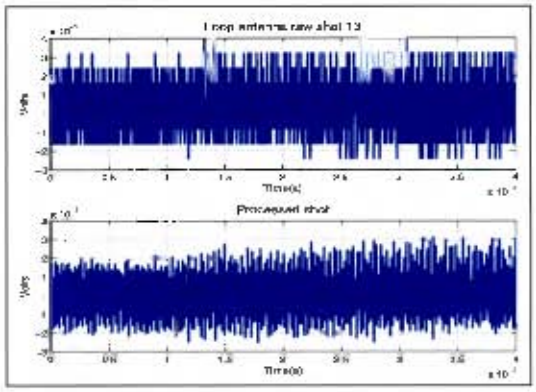

Figure C.76. Loop 13 pre-trigger data

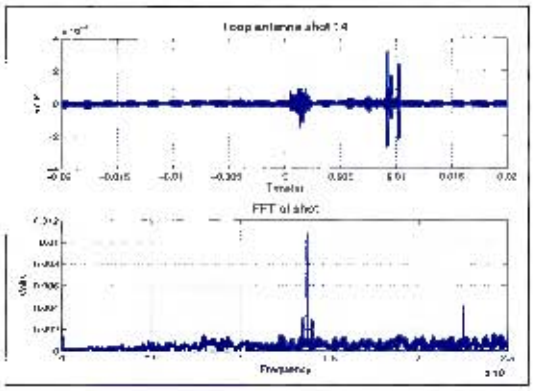

Figure C.77. Loop 14

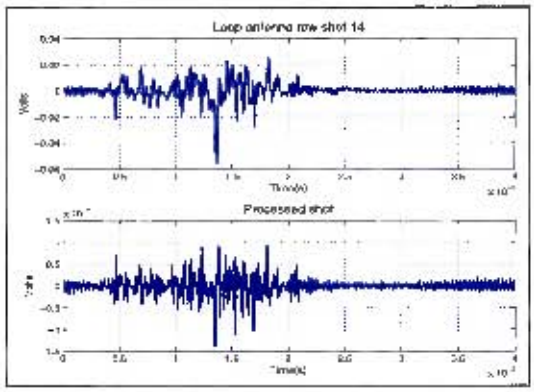

Figure C.78. Loop 14 pre-trigger data

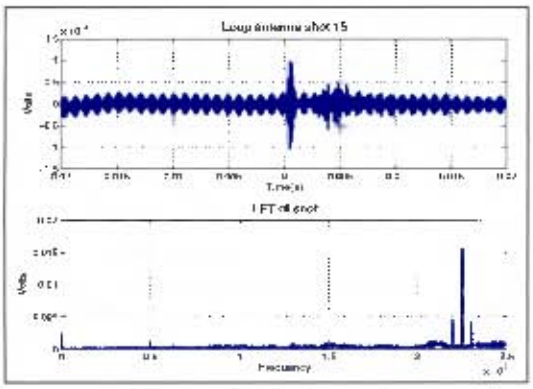

Figure C.79. Loop 15

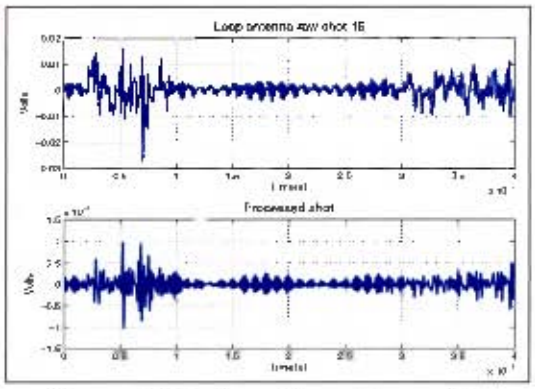

Figure C.80. Loop 15 pre-trigger data

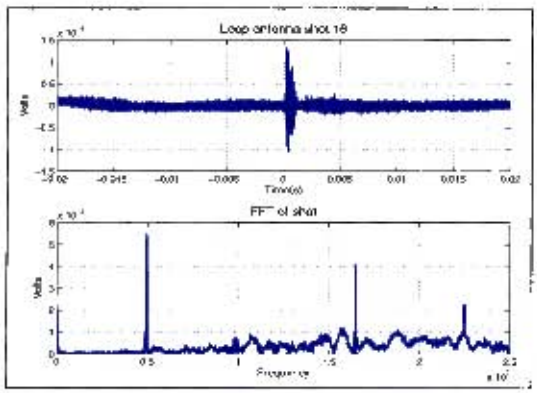

Figure C.81. Loop 16

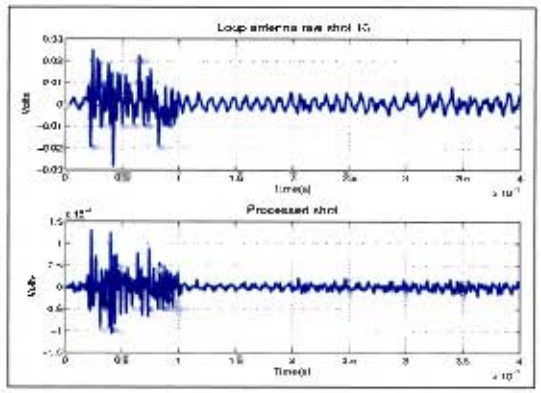

Figure C.82. Loop 16 pre-trigger data

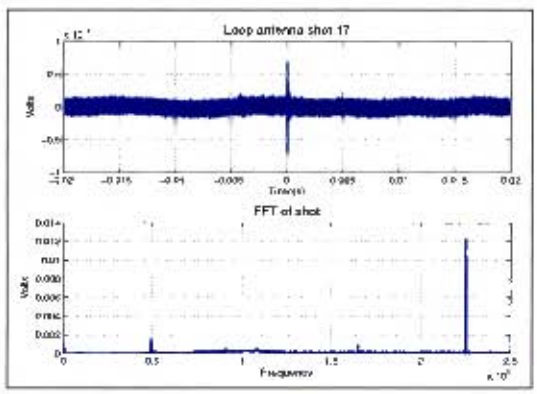

Figure C.83. Loop 17

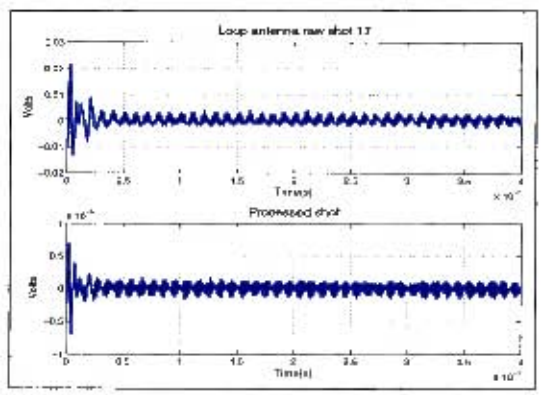

Figure C.84. Loop 17 pre-trigger data

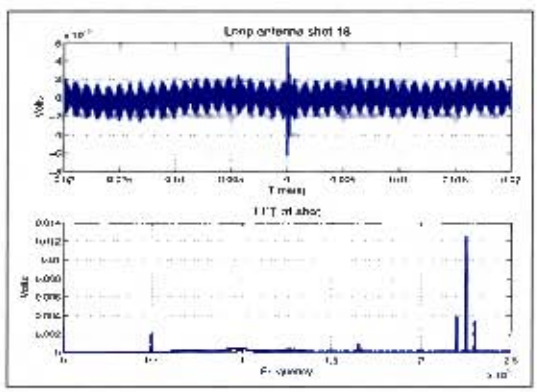

Figure C.85. Loop 18

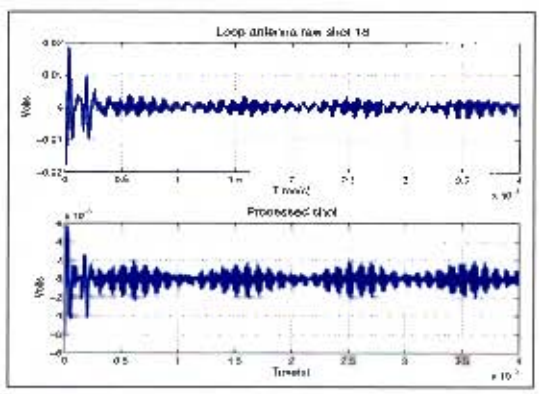

Figure C.86. Loop 18 pre-trigger data

The small copper loops were only used in 3 shots, the results have been presented below

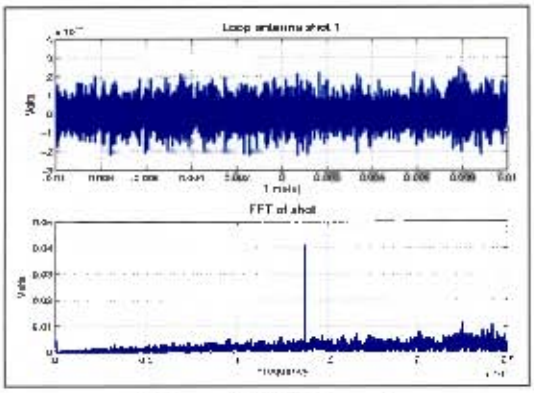

Figure C.87. Loop 1

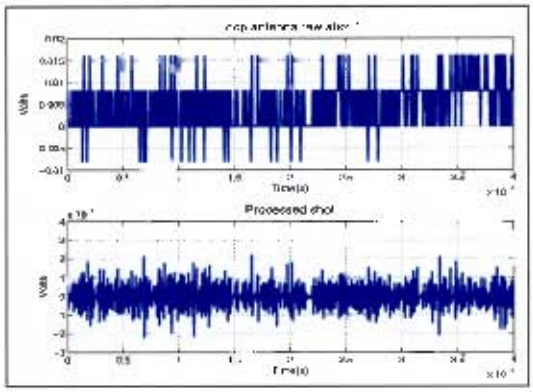

Figure C.88. Loop 1 pre-trigger data

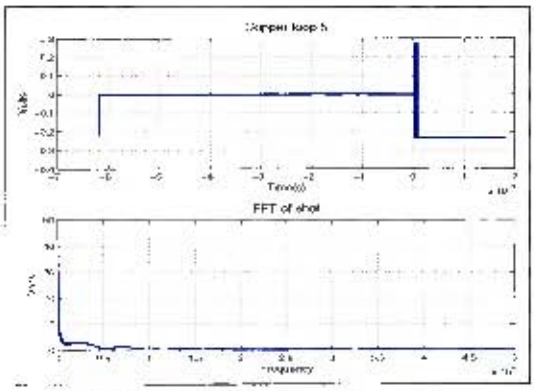

Figure C.89. Copper hoop 5

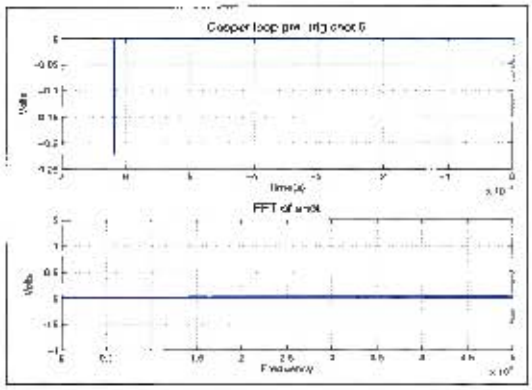

Figure C.90. Copper hoop 5 pre-trigger

In conclusion the RS commercial antenna data are presented.

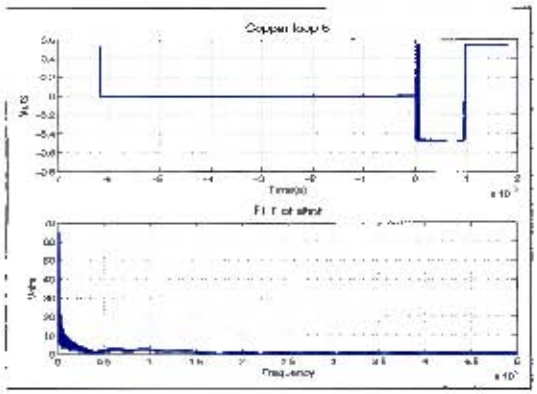

Figure C.91. Copper hoop 6

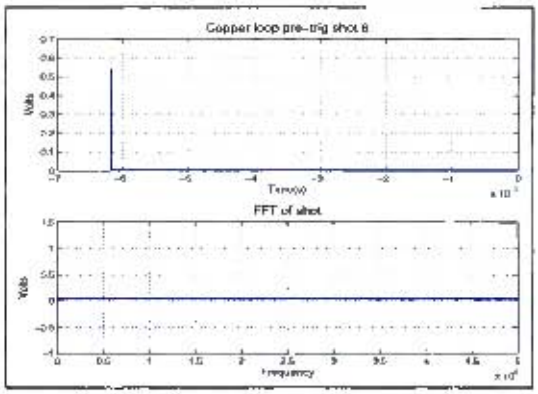

Figure C.92. Copper hoop 6 pre-trigger

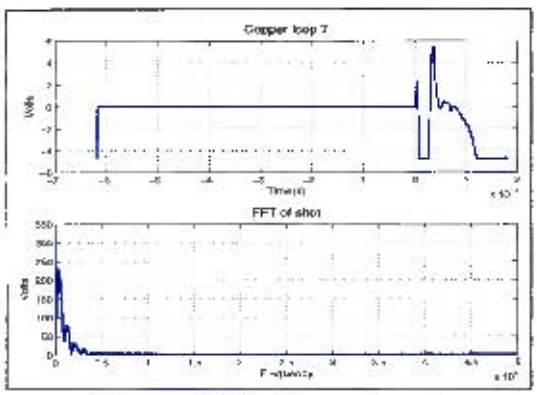

Figure C.93. Copper hoop 7

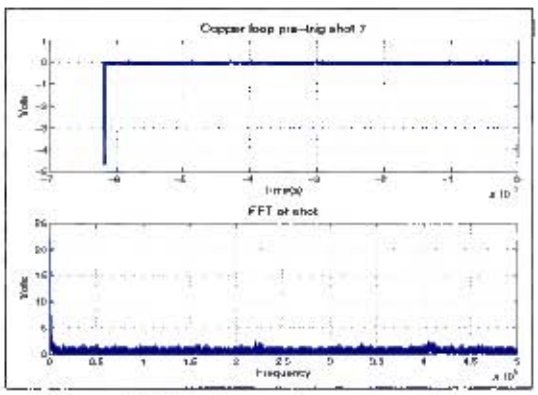

Figure C.94. Copper hoop 7 pre-trigger

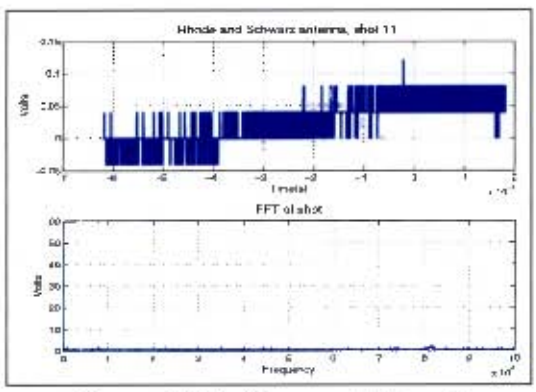

Figure C.95. Commercial Loop 3

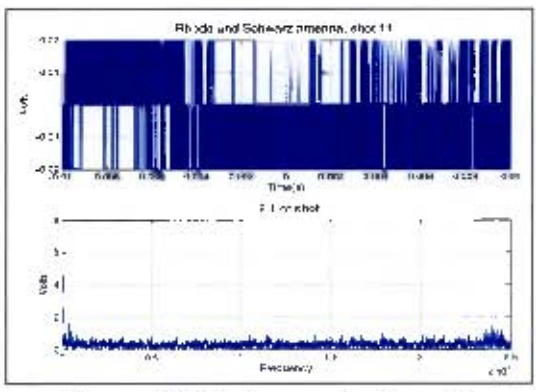

Figure C.96. Commercial Loop 11

D Blast wave tables

The entire table of expansion times for the fireball period, initial particle expansion, over various SOD and charge masses. This is based on equation (2.5).

Table D.1. Particle traveled distance and times

Mass (Kg)	SOD (m)	Radius (m)	Time(μS)
0.02	2	0.2059	297.1
0.02	4	0.2059	297.1
0.02	6	0.1413	217.5
0.02	8	0.1413	217.4
0.04	2	0.2594	373.1
0.04	4	0.1780	272.7
0.04	6	0.2594	373.1
0.04	8	0.2594	373
0.06	2	0.2969	424.3
0.06	4	0.2038	309.5
0.06	6	0.2969	424.2
0.06	8	0.2970	424.3
0.08	2	0.3268	467.8
0.08	4	0.3268	467.8
0.08	6	0.2243	341.5
0.08	8	0.3268	467.8
0.1	2	0.3521	503.4
0.1	4	0.3521	503.4
0.1	6	0.3520	503.3
0.1	8	0.3520	503.4

Table D.1 contains the data from the time line code written in MATLAB. The last column shows the time at which the shock wave starts to overtake the escape particles and the radius at which that occurs. Table D.2 shows the arrival time of the shock wave itself to the location of the antenna. This data was also obtained from a simulation MATLAB and is based on equation (2.6).

Table D.2. Arrival time of shcok wave to antenna location

SOD (m)	Mass (kg)	Arrival Time(s)
0.02	2	0.003418
0.02	4	0.008984
0.02	6	0.01475
0.02	8	0.02059
0.04	2	0.002955
0.04	4	0.008374
0.04	6	0.01407
0.04	8	0.01987
0.06	2	0.002665
0.06	4	0.007969
0.06	6	0.01362
0.06	8	0.01938
0.08	2	0.002453
0.08	4	0.00766
0.08	6	0.01327
0.08	8	0.019
0.1	2	0.002287
0.1	4	0.007406
0.1	6	0.01298
0.1	8	0.01869

Graphically this data is presented in the following graphs:

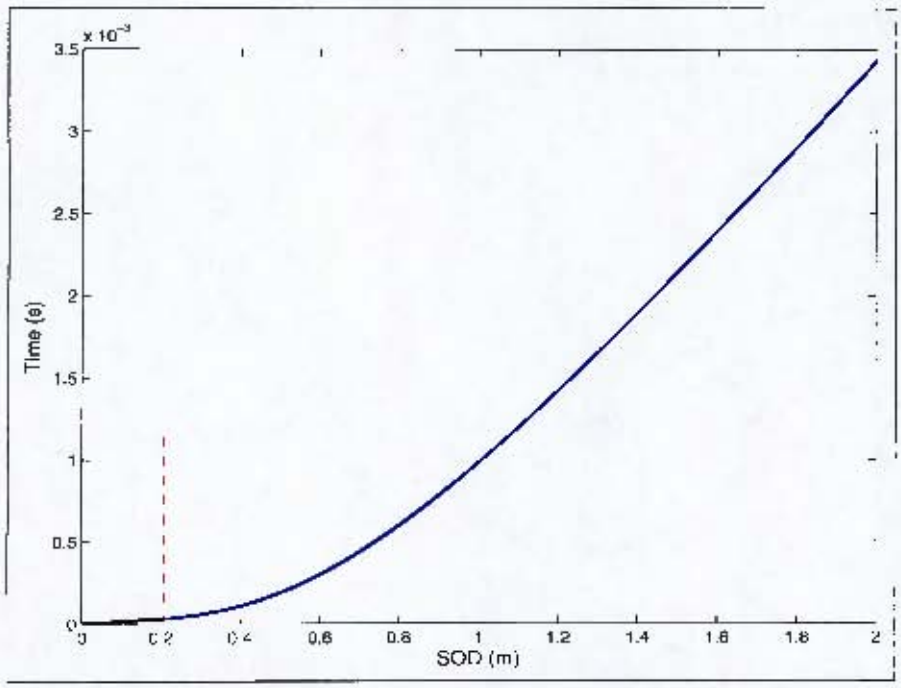

Figure D.1. Timeline for an explosion of 20g and 2m away

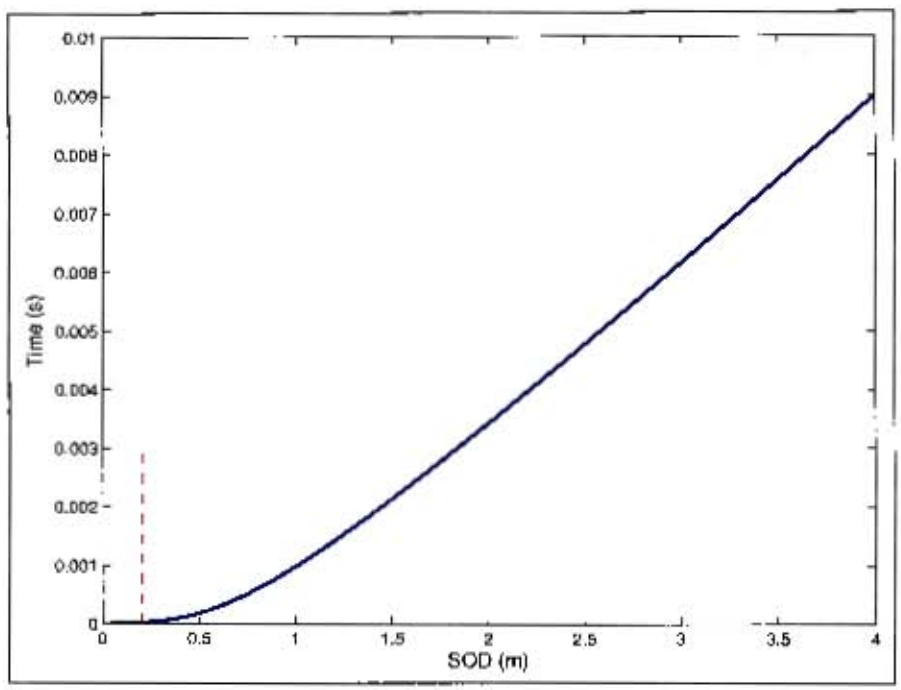

Figure D.2. Timeline for an explosion of 20g and 4m away

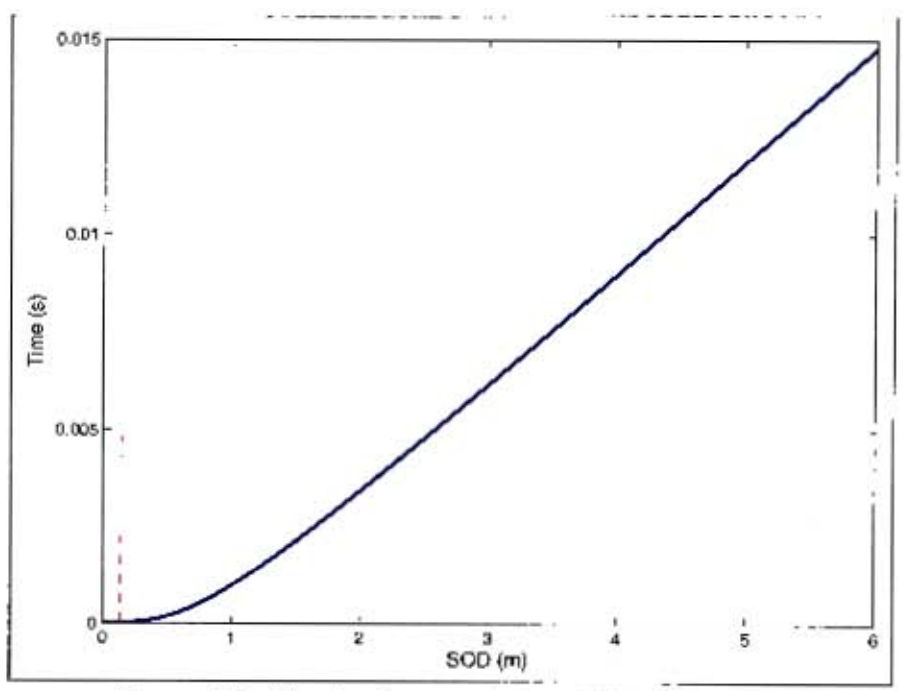

Figure D.3. Timeline for an explosion of 20g and 6m away

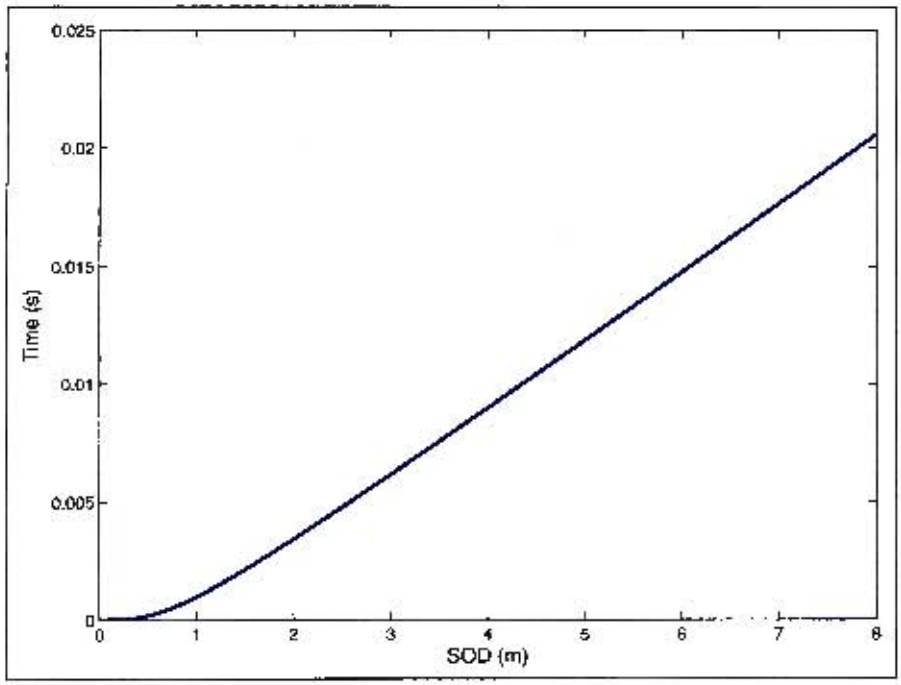

Figure D.4. Timeline for an explosion of 20g and 8m away

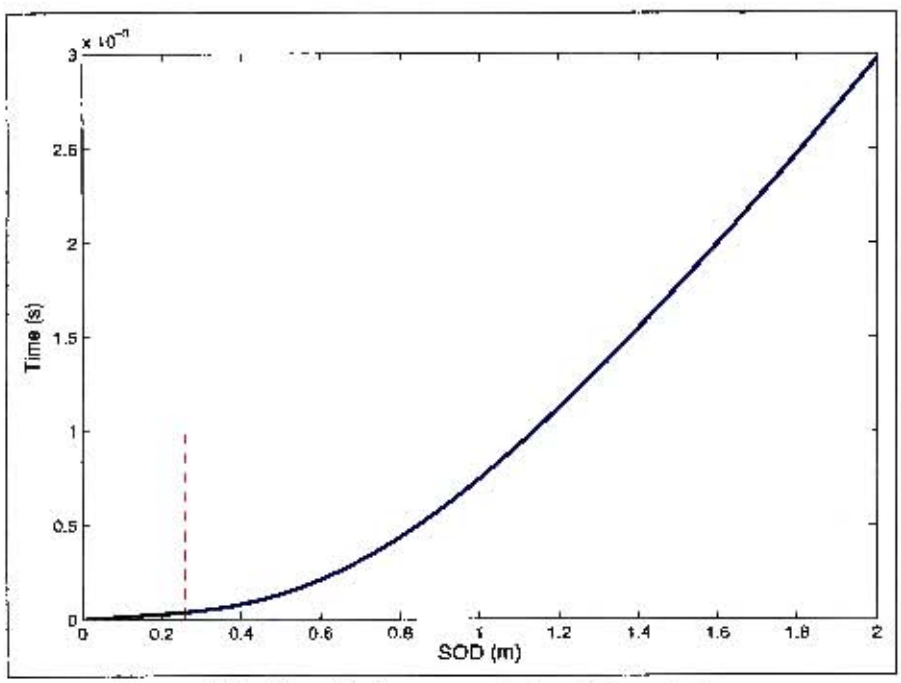

Figure D.5. Timeline for an explosion of 40g and 2m away

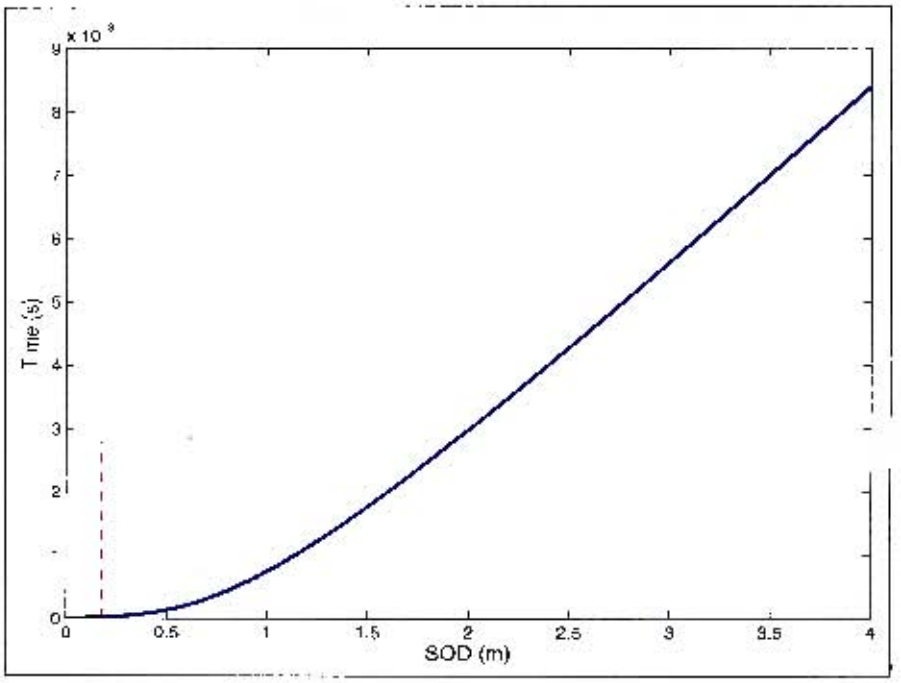

Figure D.6. Timeline for an explosion of 40g and 4m away

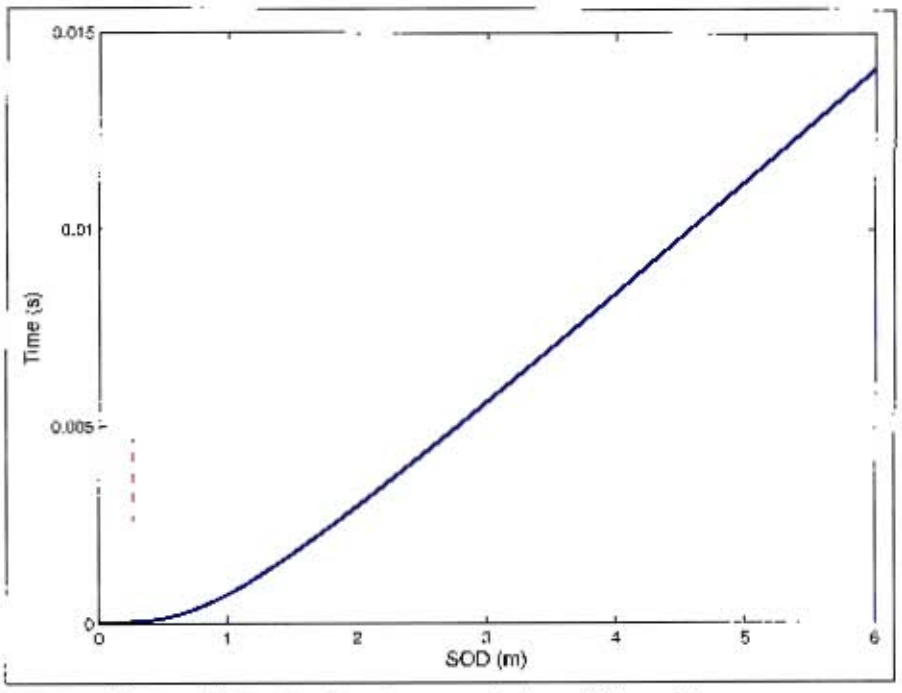

Figure D.7. Timeline for an explosion of 40g and 6m away

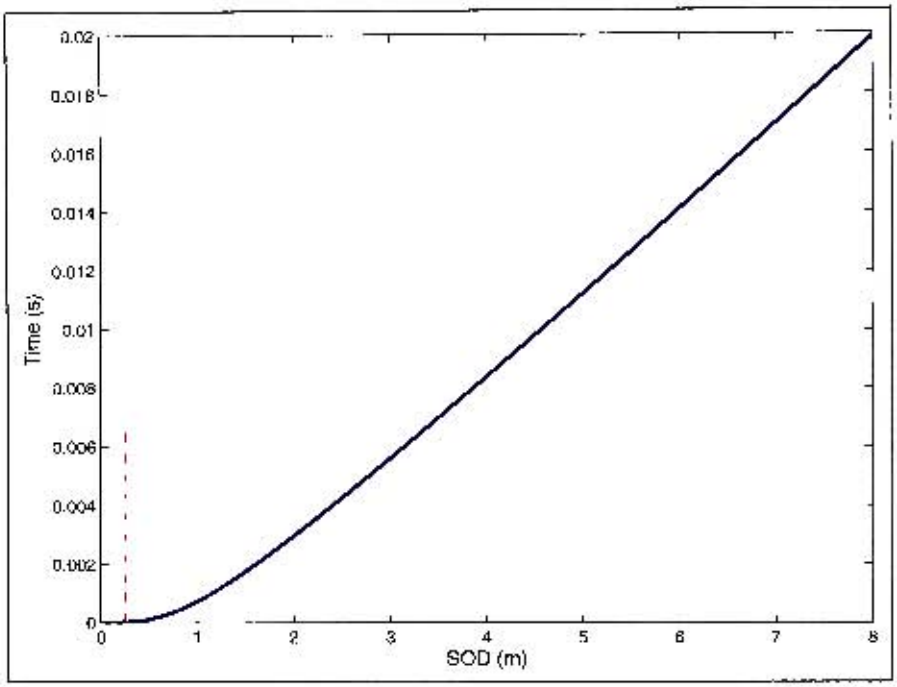

Figure D.8. Timeline for an explosion of 40g and 8m away

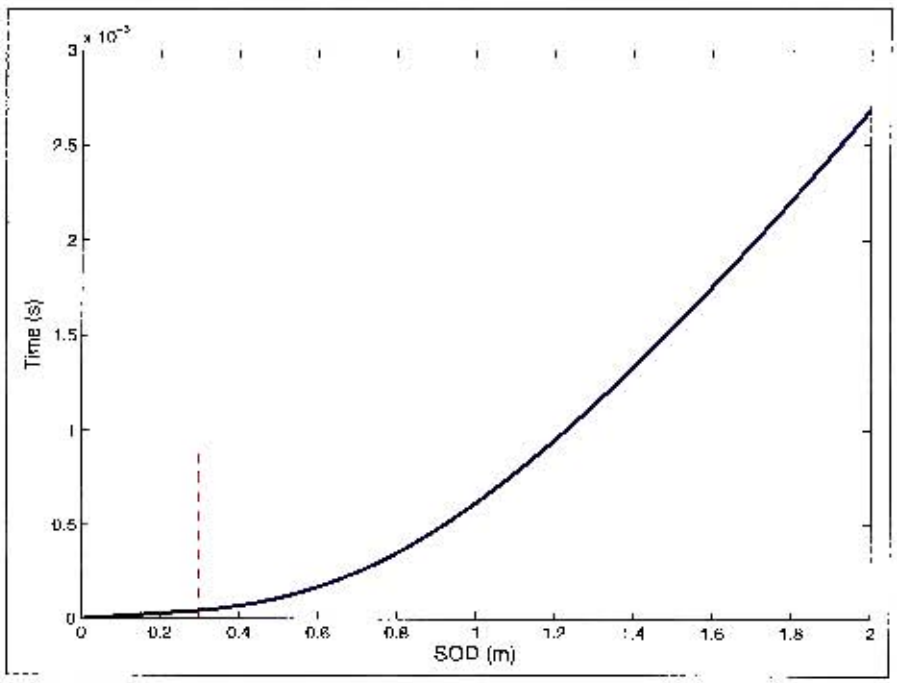

Figure D.9. Timeline for an explosion of 60g and 2m away

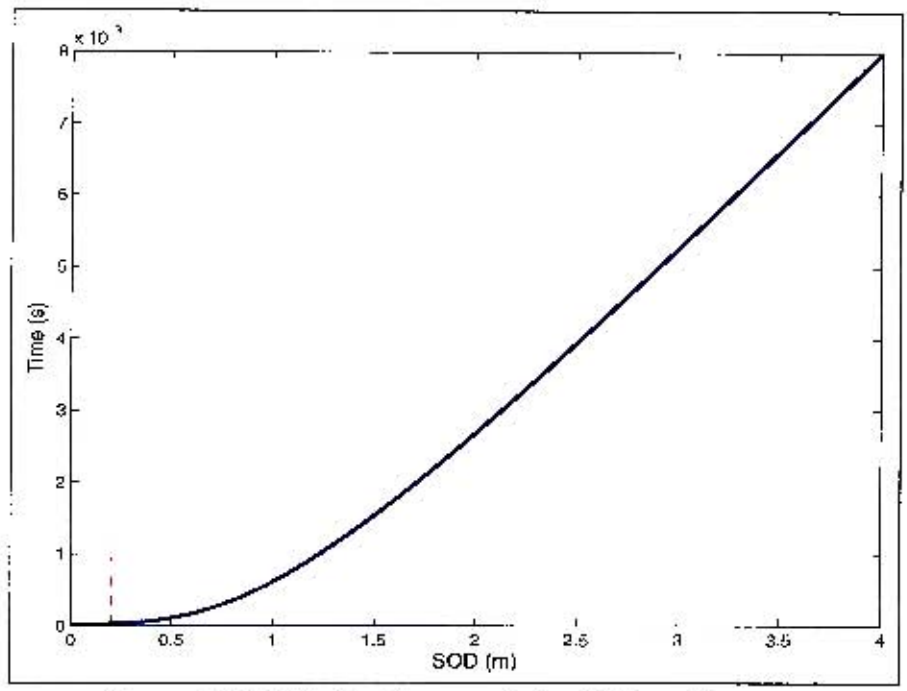

Figure D.10. Timeline for an explosion of 60g and 4m away

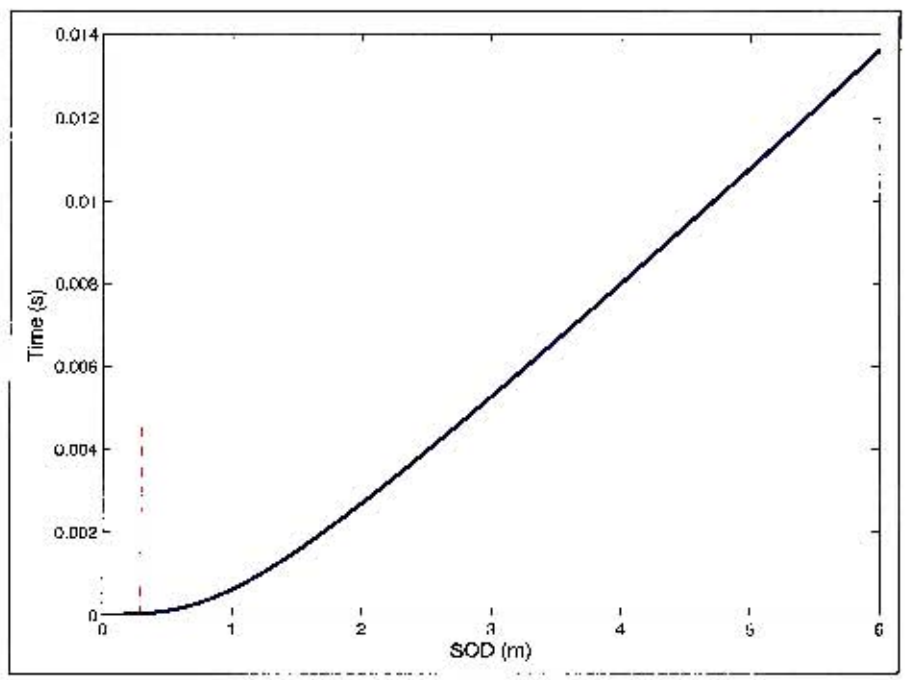

Figure D.11. Timeline for an explosion of 60g and 6m away

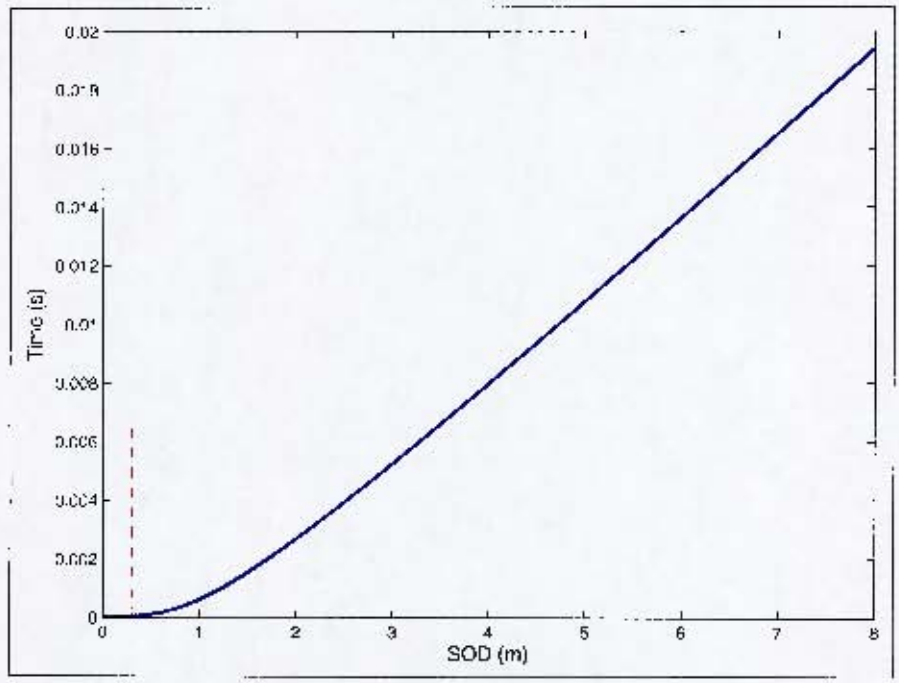

Figure D.12. Timeline for an explosion of 60g and 8m away

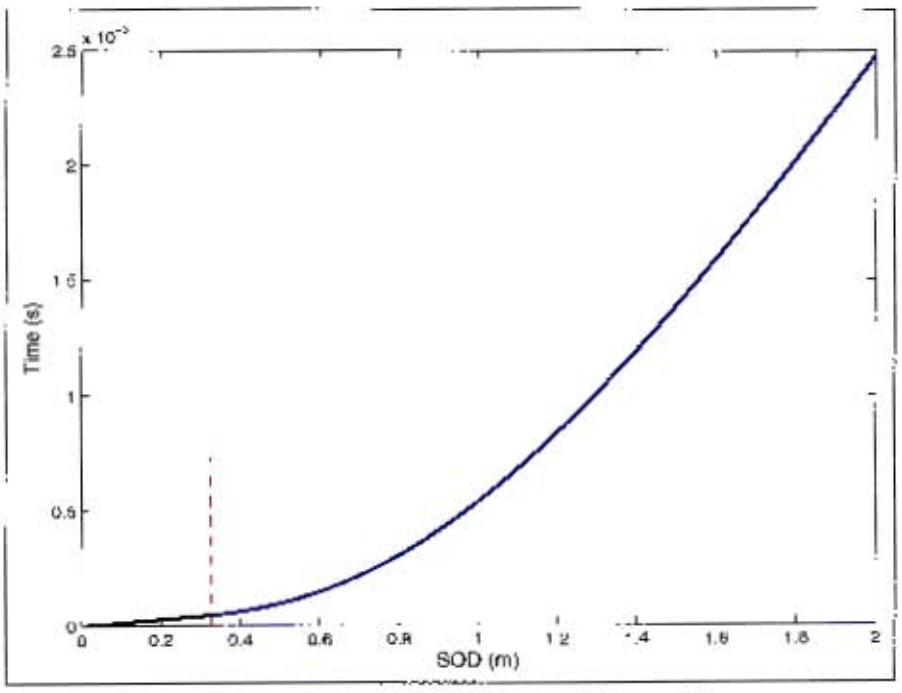

Figure D.13. Timeline for an explosion of 80g and 2m away

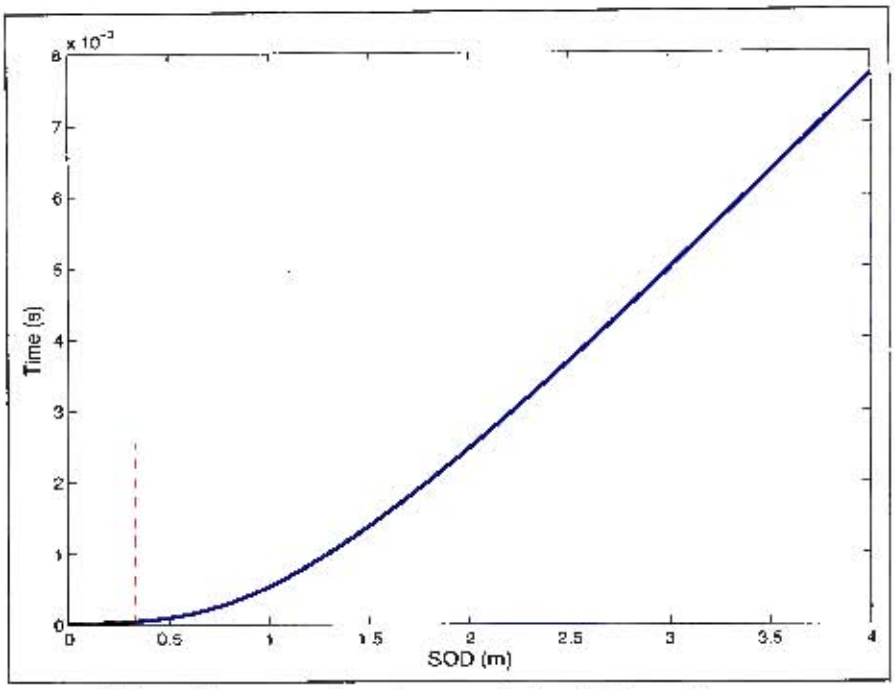

Figure D.14. Timeline for an explosion of 80g and 4m away

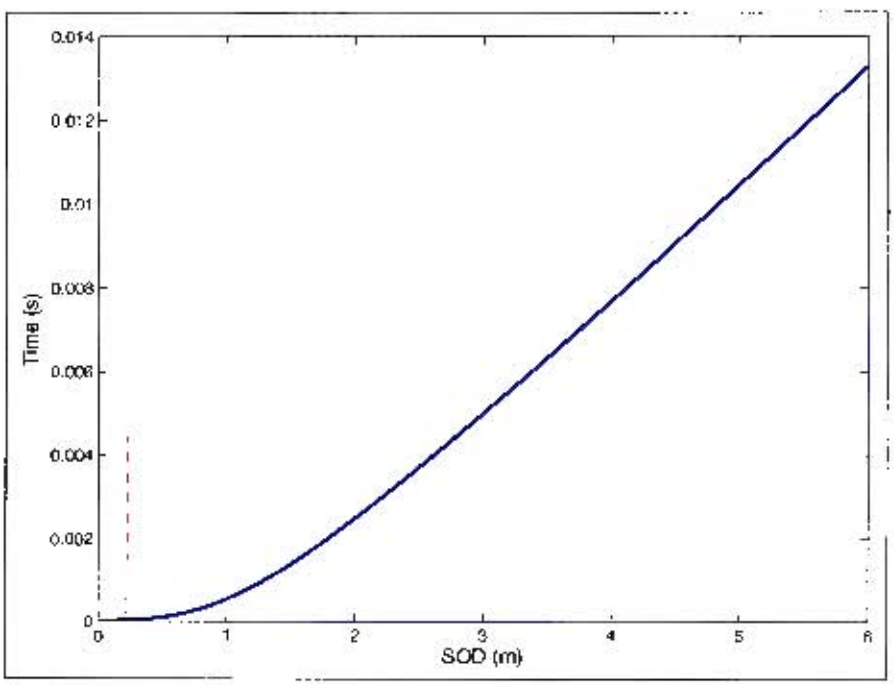

Figure D.15. Timeline for an explosion of 80g and 6m away

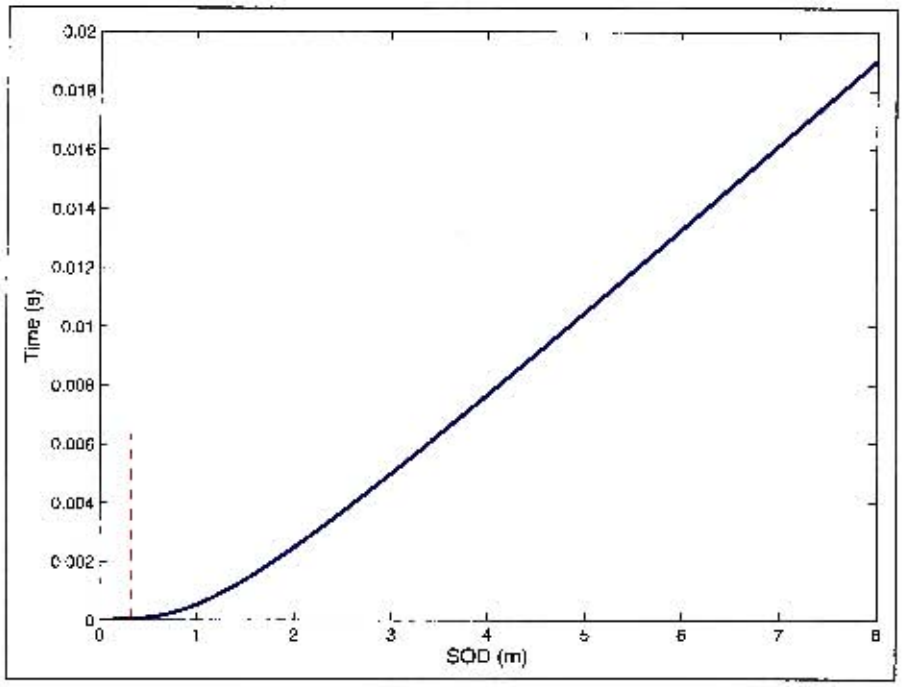

Figure D.16. Timeline for an explosion of 80g and 8m away

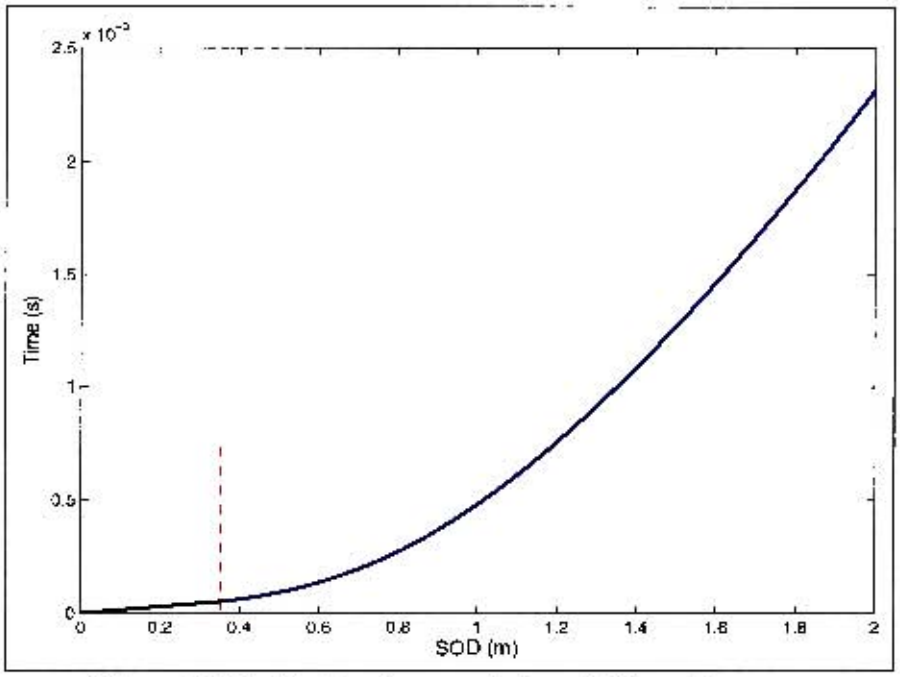

Figure D.17. Timeline for an explosion of 100g and 2m away

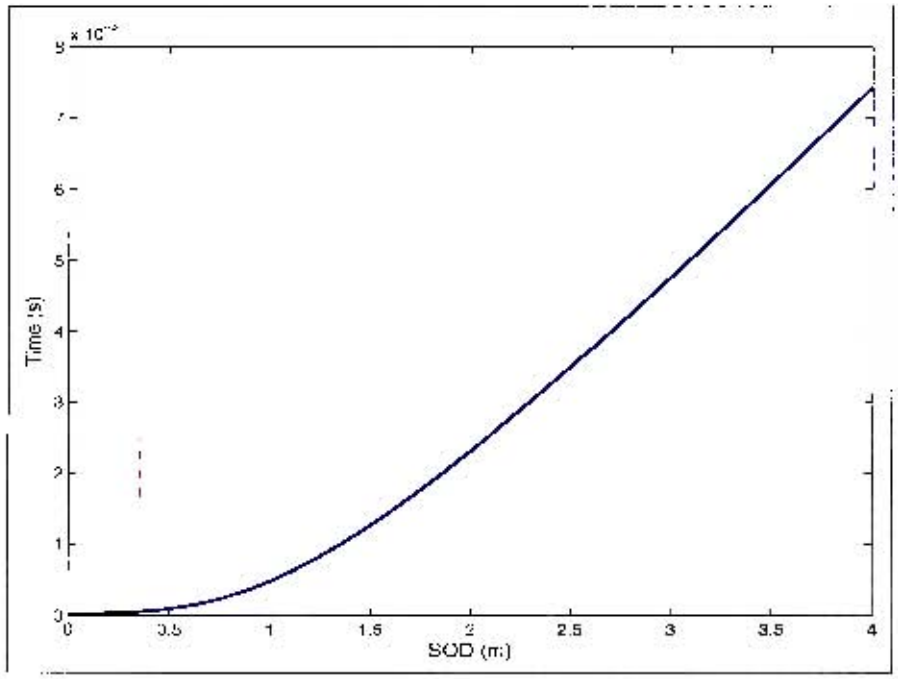

Figure D.18. Timeline for an explosion of 100g and 4m away

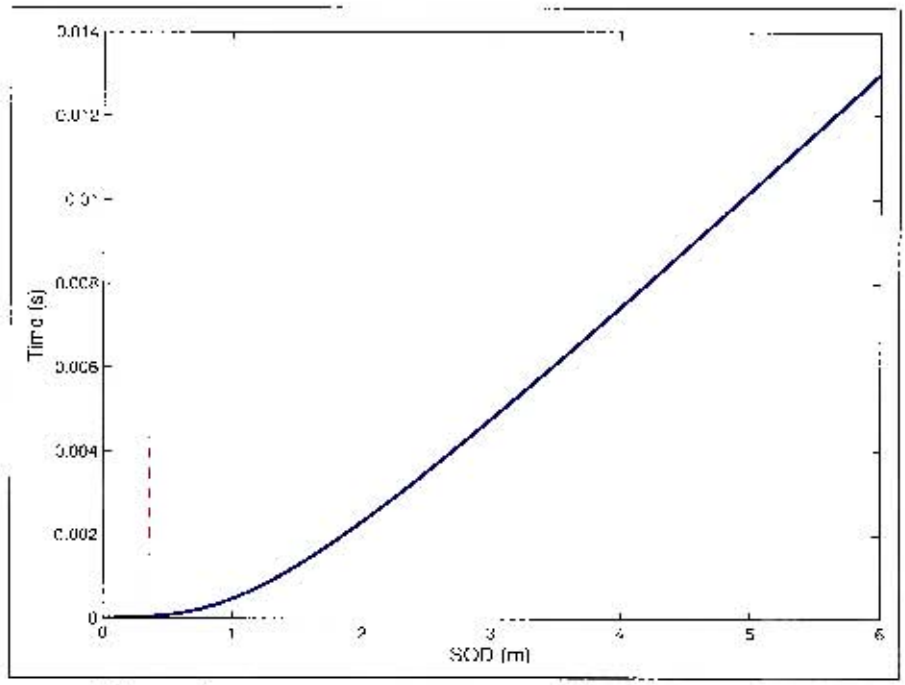

Figure D.19. Timeline for an explosion of 100g and 6m away

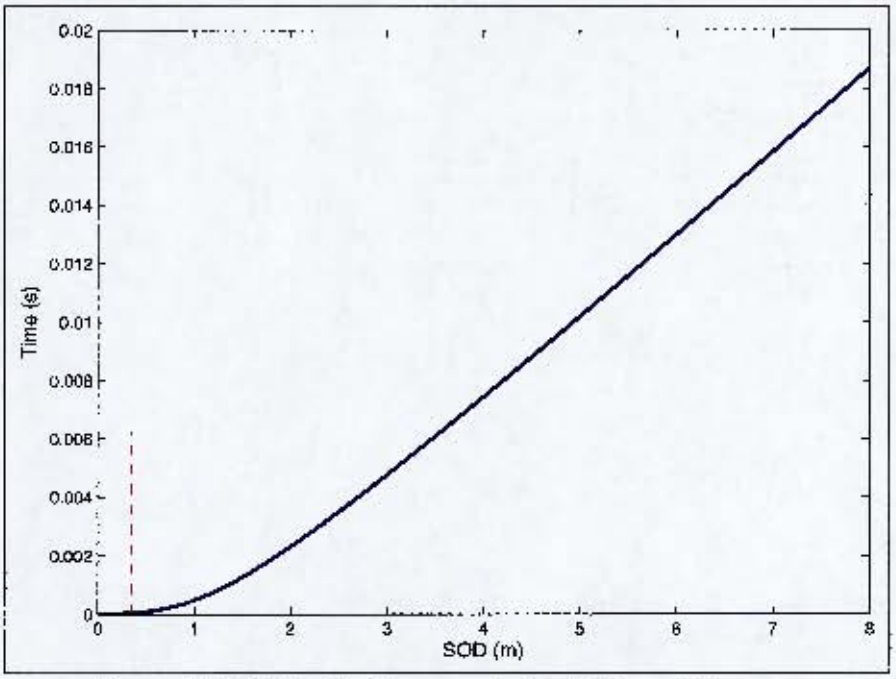

Figure D.20. Timeline for an explosion of 100g and 8m away

E Key frequencies

Then identifying the frequencies containing the most power the FFT of each signal was in through an algorithm which found the frequency with the greatest 1 ω energy content. he original results of this algorithm are in figure E.1.

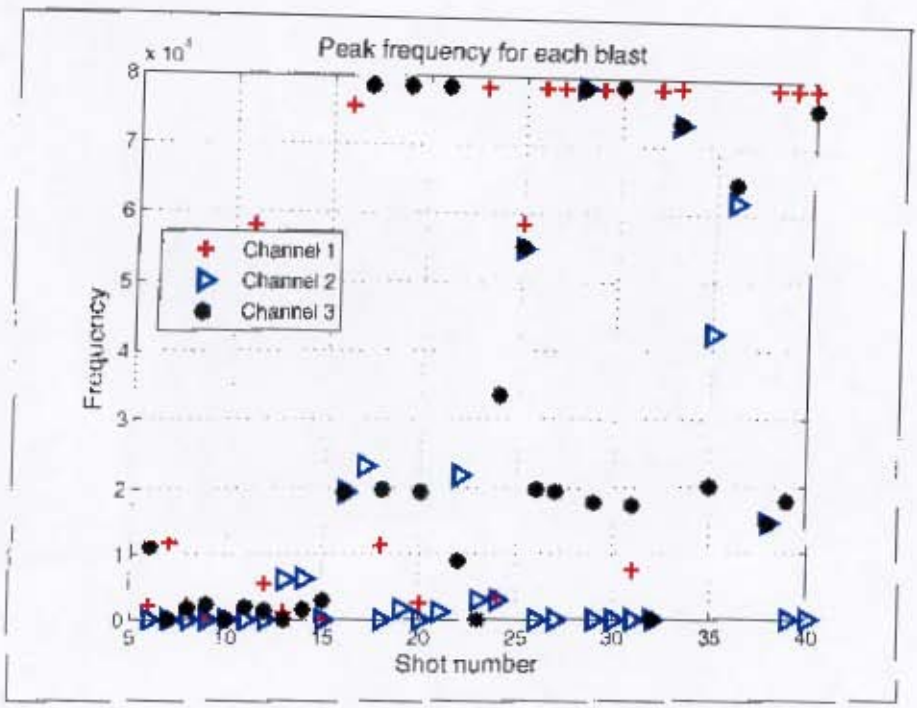

Figure E.1. 120 kHz filter

After the 40 kHz filter was applied the plot for all the channels were more closely spaced. he average value for channel 1 through 3 was 3.123 kHz, 1.095 kHz and 4.34 kHz respecvely. Their standard deviation was determined to be 4.44 kHz, 2.121 kHz and 5.7 kHz. owever when the zero valued frequency points were removed, shown in figure E.3 the ew averages for channel 1 - 3 were 3.557 kHz, 2.12 kHz and 4.77 kHz respectively with a eviation of 4.58 kHz, 2.58 kHz and 5.8 kHz.

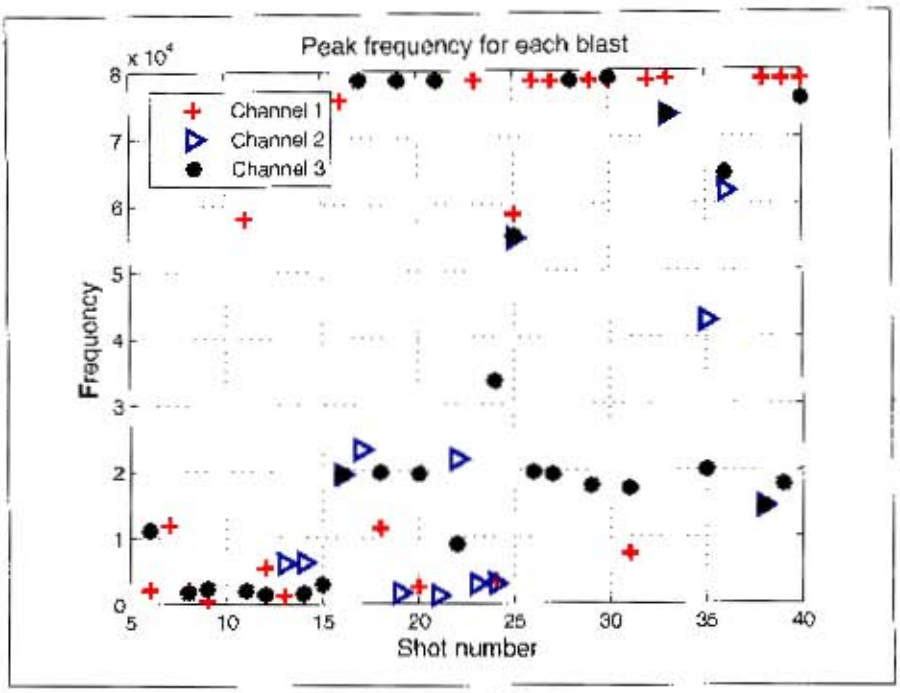

Figure E.2. 40 kHz filter

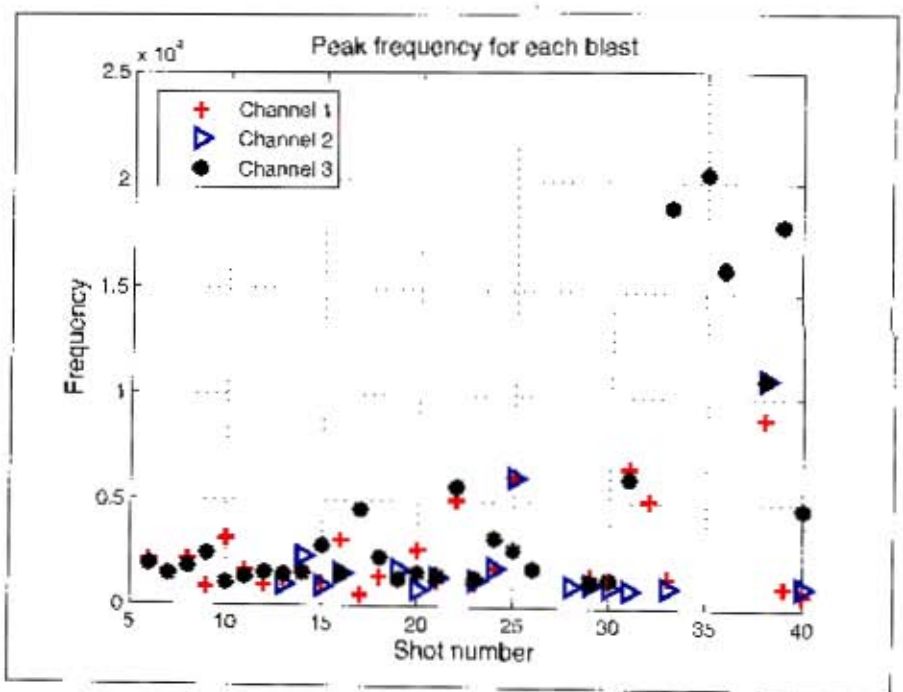

Figure E.3. No zero point frequencies

Table E.1. Times for different peaks, channel 1

channel 1	channel 2	channel 3
2180	0	11090
11840	0	0
2030	0	1680
470	0	2270
0	0	0
58000	0	1930
5430	0	1400
1140	6080	0
1530	6240	1510
0	0	2890
75610	19460	19460
78700	23210	78560
11360	0	19780
78550	1620	78630
2540	0	19450
78590	1190	78550
8930	21800	8930
78520	2950	0
3300	2960	33470
58500	54880	55190
78540	0	19760
78460	0	19450
78580	78600	78480
78460	0	17740
78460	0	78820
7500	0	17310
78540	0	0
78690	73320	73370
20150	42490	20090
64510	61810	64480
78600	14580	14500
78560	0	17790
78550	0	75690

Table E.2. channel 1

Shot number	Frequency
6	2180
7	11840
8	2030
9	470
11	58000
12	5430
13	1140
14	1530
16	75610
17	78700
18	11360
19	78550
20	2540
21	78590
22	8930
23	78520
24	3300
25	58500
26	78540
27	78460
28	78580
29	78460
30	78460
31	7500
32	78540
33	78690
35	20150
36	64510
38	78600
39	78560
40	78550

Table E.3. channel 2

Shot number	Frequency
13	6080
14	6240
16	19460
17	23210
19	1620
21	1190
22	21800
23	2950
24	2960
25	54880
33	73320
35	42490
36	61810
38	14580

Table E.4. channel 3

Shot number	Frequency
6	11090
8	1680
9	2270
11	1930
12	1400
14	1510
15	2890
16	19460
17	78560
18	19780
19	78630
20	19450
21	78550
22	8930
24	33470
25	55190
26	19760
27	19450
28	78480
29	17740
30	78820
31	17310
33	73370
35	20090
36	64480
38	14500
39	17790
40	75690

F Energy Relationships

F.1 E vs SOD

Following the literature, it was assumed that the relationship between the E out and the charge mass was linear. Two forms of linear curves were tested to determine the best fit. Each line has a r^2 value - the coefficient of multiple determination is a statistic measures how successful the fit is in explaining the variation of the data. Another measure of the curves' valididity is the sse - the sum of squares due to error. This statistic measures the deviation of the responses from the fitted values of the responses. The equations used to fit the lines were of the form $y = ax$ and $y = ax + b$. The latter had lines that were very close together but at the same time showed trends that went against predictions.

F.1.1 Channel 1

Channel 1 coefficients are listed below, the a values need to multiplied by 10^-5 for a and sse by 10^-12. The reason for this low value is a reflection of the low magnitude in the data points.

Table F.1. Coefficients and r^2 and sse for channel 1, $y = \frac{a}{x^2}$

Mass	a	r^2	sse
20	3.6e-007	0.67	3.83e-015
40	3e-007	0.89	8.68e-016
60	3.2e-007	0.76	2.72e-015
80	3.2e-007	0.34	5.3e-015
100	1.7e-006	0.49	2.91e-013

Table F.2. Coefficients and r^2 and sse for channel 1, $y = \frac{a}{x^3}$

Mass	a	r^3	sse
20	7.5e-007	0.73	3.11e-015
40	6.3e-007	0.96	3.3e-016
60	6.6e-007	0.8	2.23e-015
80	6.2e-007	0.13	7.05e-015
100	3.6e-006	0.52	2.74e-013

The following figures show the actual curves fitted to various points.

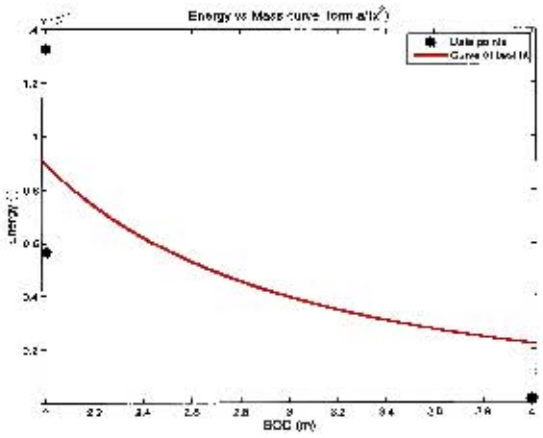

Figure F.1. Constant mass of 20g

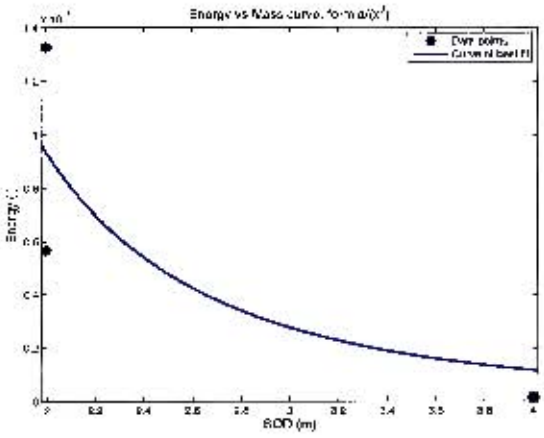

Figure F.2. Constant mass of 20g

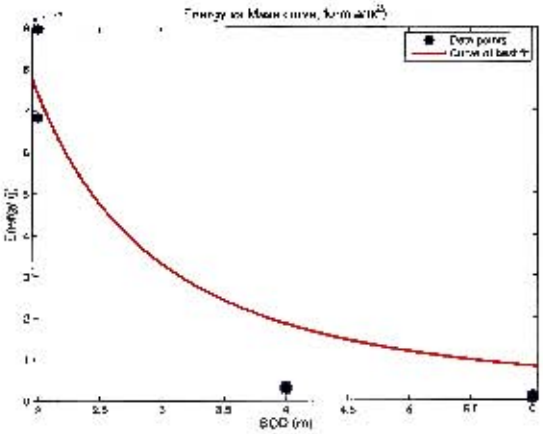

Figure F.3. Constant mass of 40g

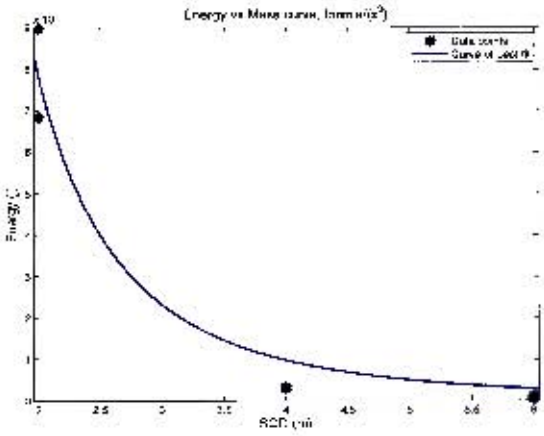

Figure F.4. Constant mass of 40g

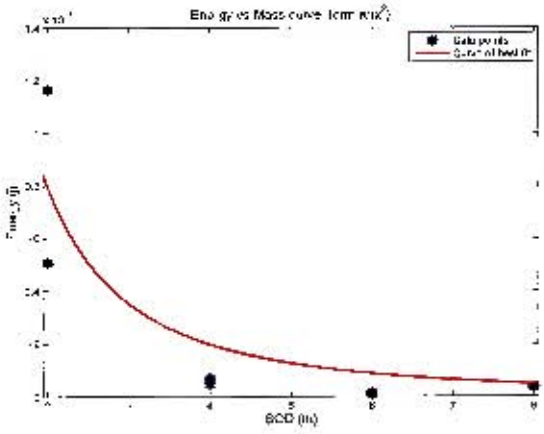

Figure F.5. Constant mass of 60g

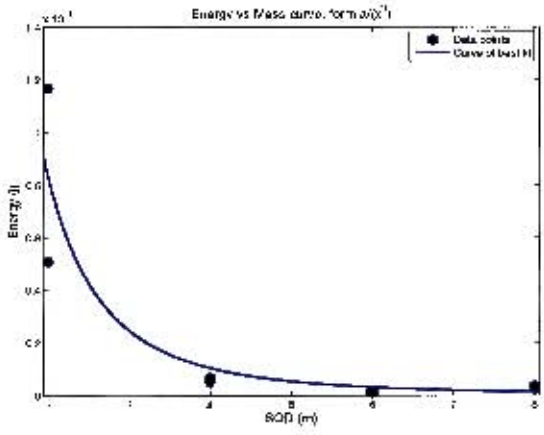

Figure F.6. Constant mass of 60g

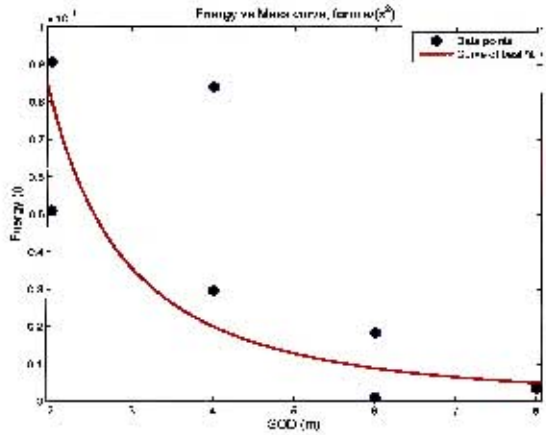

Figure F.7. Constant mass of 80g

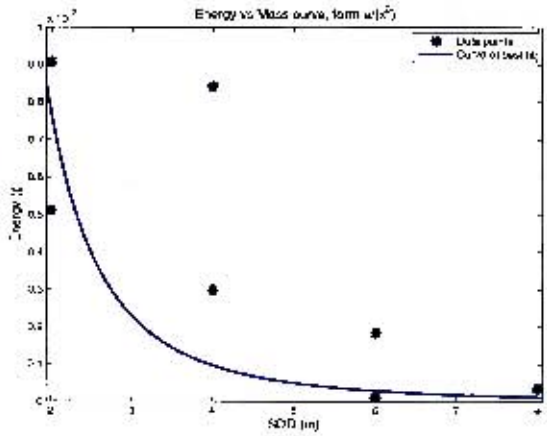

Figure F.8. Constant mass of 80g

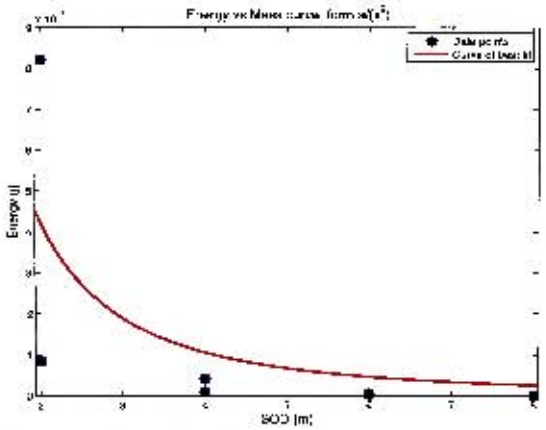

Figure F.9. Constant mass of 100g

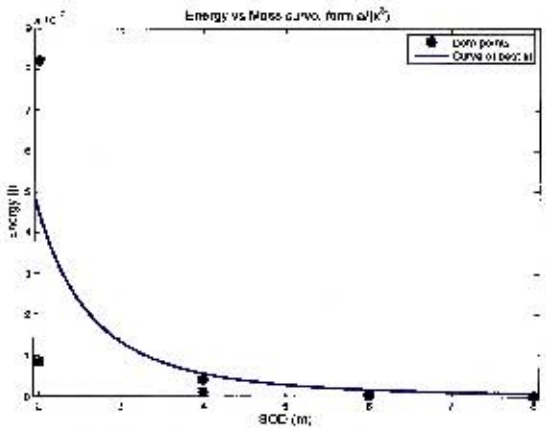

Figure F.10. Constant mass of 100g

F.1.2 Channel 2

Channel 2 coefficients are listed below. the a values need to multiplied by $10^{-}5$for a and sse by $10^{-}12$.

Table F.3. Coefficients and r^2 and sse for channel 2, $y = \frac{a}{x^2}$

Mass	a	r^2	sse
20	3.6e-009	-0.97	3.67e-018
40	9.3e-008	0.61	1.16e-017
60	3.4e-007	0.84	7.62e-017
80	2e-007	-0.31	1.01e-015
100	2.3e-006	0.43	6.34e-013

Table F.4. Coefficients and r^2 and sse for channel 2, $y = \frac{a}{x^3}$

Mass	a	r^3	sse
20	6.2e-009	-1.2	4.12e-018
40	4e-007	0.67	9.78e-018
60	1.5e-006	0.96	2.17e-017
80	3.6e-007	-1.2	1.68e-015
100	4.8e-006	0.45	6.17e-013

The following figures show the actual curves fitted to various points.

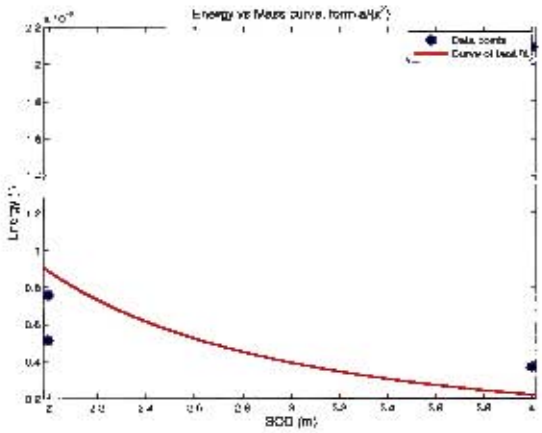

Figure F.11. Constant mass of 20g

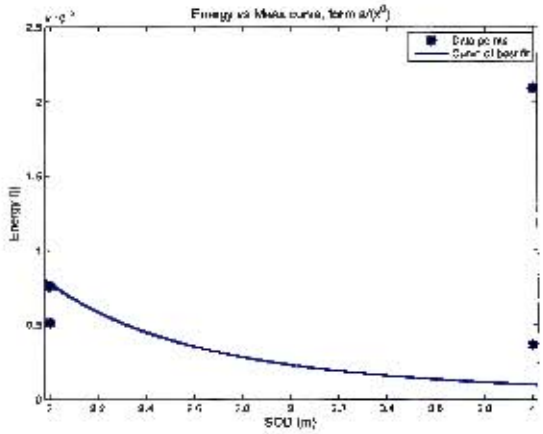

Figure F.12. Constant mass of 20g

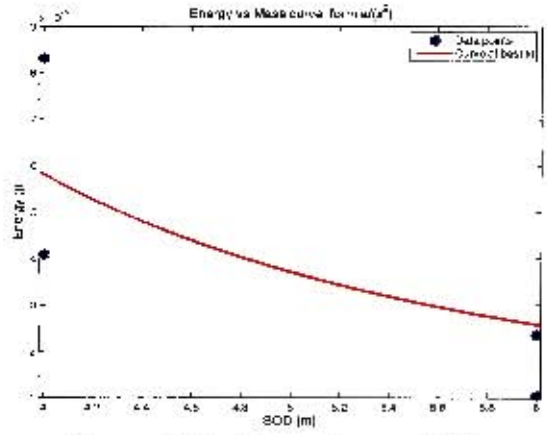

Figure F.13. Constant mass of 40g

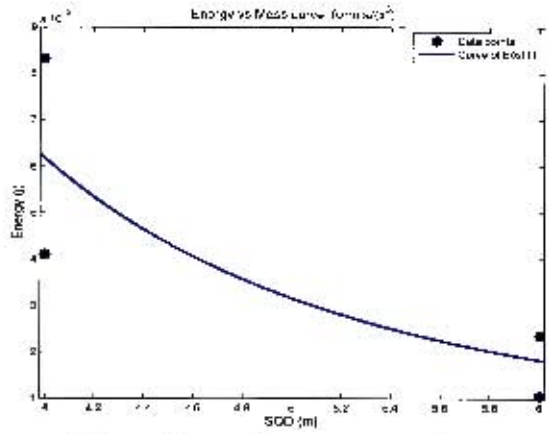

Figure F.14. Constant mass of 40g

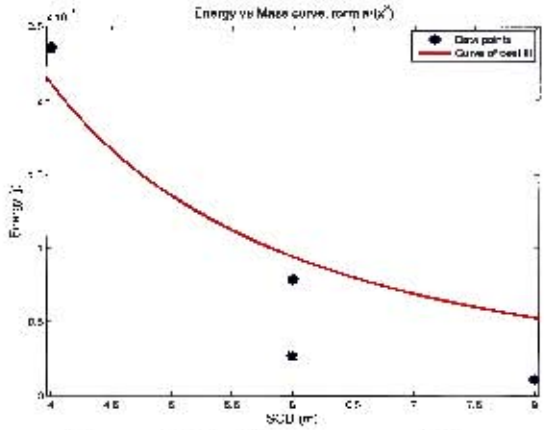

Figure F.15. Constant mass of 60g

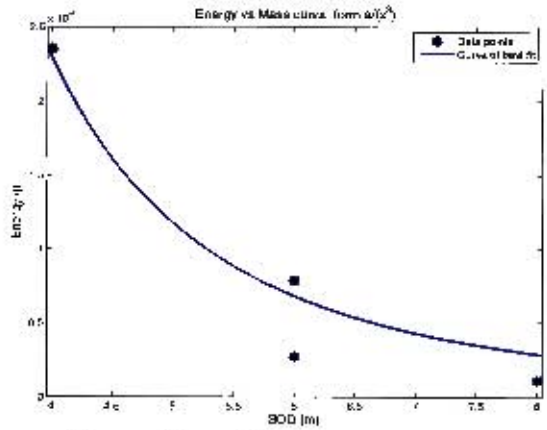

Figure F.16. Constant mass of 60g

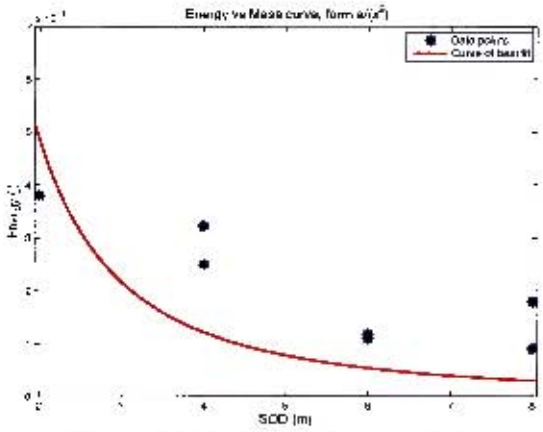

Figure F.17. Constant mass of 80g

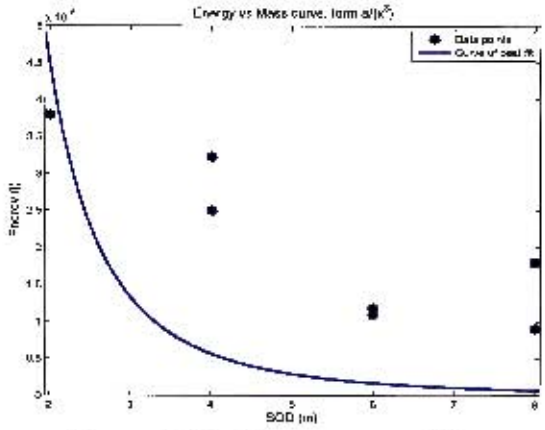

Figure F.18. Constant mass of 80g

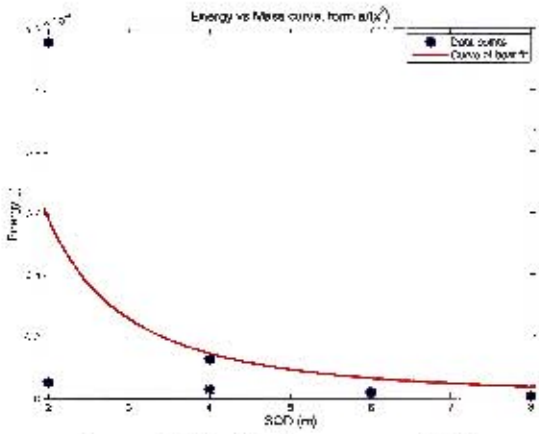

Figure F.19. Constant mass of 100g

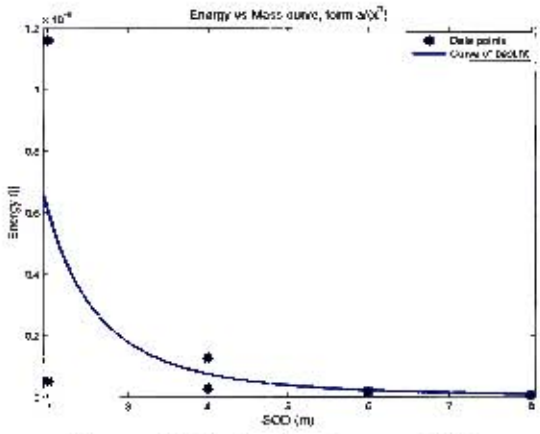

Figure F.20. Constant mass of 100g

F.1.3 Channel 3

Channel 3 coefficients are listed below, the a values need to multiplied by $10^{-}6$ for a in table 1 and $10^{-}5$ in table 2 and sse by $10^{-}13$.

Table F.5. Coefficients and r^2 and sse for channel 2, $y = \frac{a}{x^2}$

Mass	a	r^2	sse
20	1.5e-007	0.89	1.68e-016
40	1.2e-007	0.92	1.03e-016
60	9.9e-008	0.89	9.37e-017
80	2e-007	-0.009	3.64e-015
100	6.4e-007	0.75	1.2e-014

Table F.6. Coefficients and r^2 and sse for channel 2, $y = \frac{a}{x^3}$

Mass	a	r^3	sse
20	3.1e-007	0.97	4.75e-017
40	2.5e-007	0.98	2.27e-017
60	2e-007	0.92	6.7e-017
80	3.8e-007	-0.26	4.53e-015
100	1.3e-006	0.79	1.03e-014

The following figures show the actual curves fitted to various points.

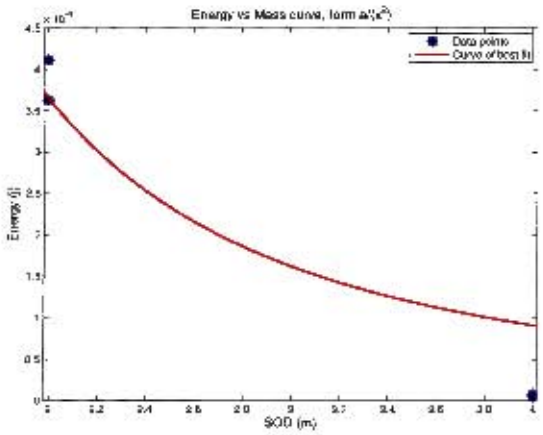

Figure F.21. Constant mass of 20g

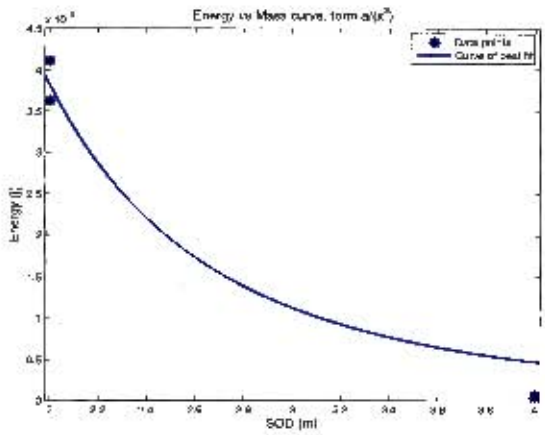

Figure F.22. Constant mass of 20g

The combination of the curves for the squared relationship is shown in figures F.31 - F.34 .

The combination of the curves for the cubic relationship is shown in figures F.35 and F.37 .

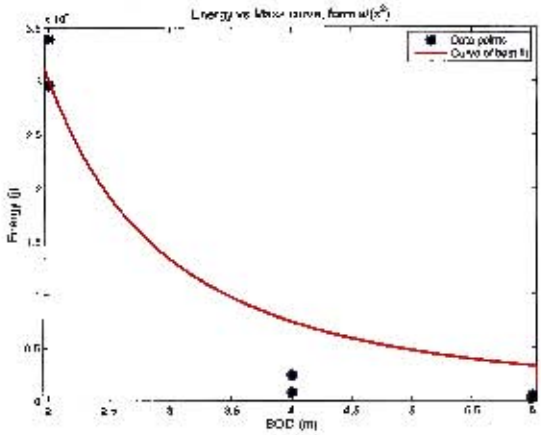

Figure F.23. Constant mass of 40g

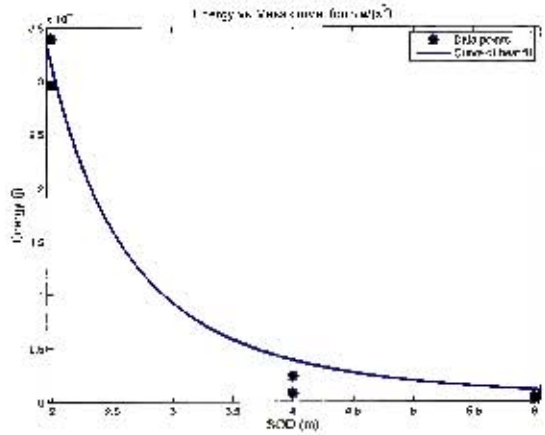

Figure F.24. Constant mass of 40g

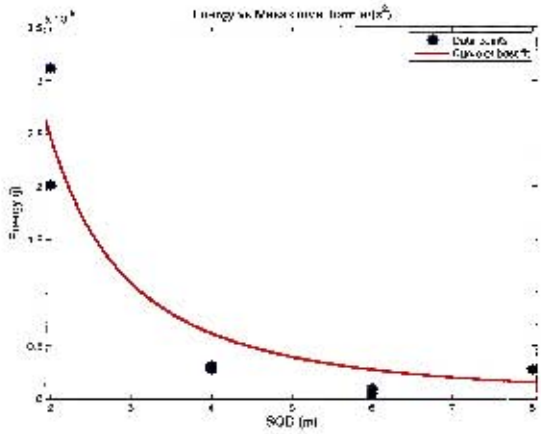

Figure F.25. Constant mass of 60g

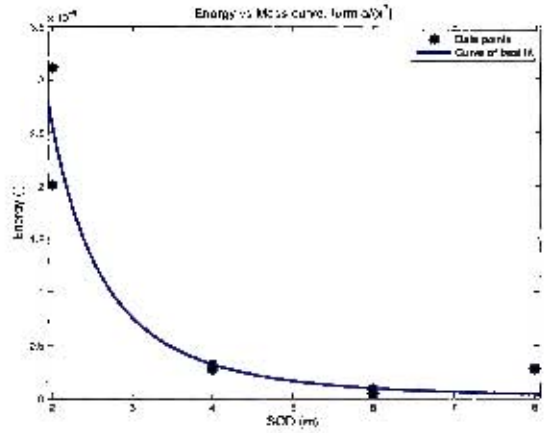

Figure F.26. Constant mass of 60g

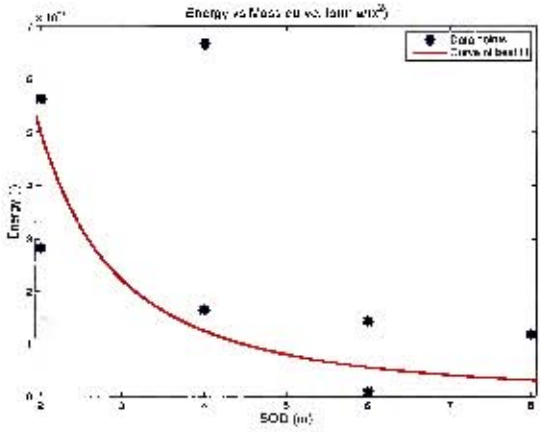

Figure F.27. Constant mass of 80g

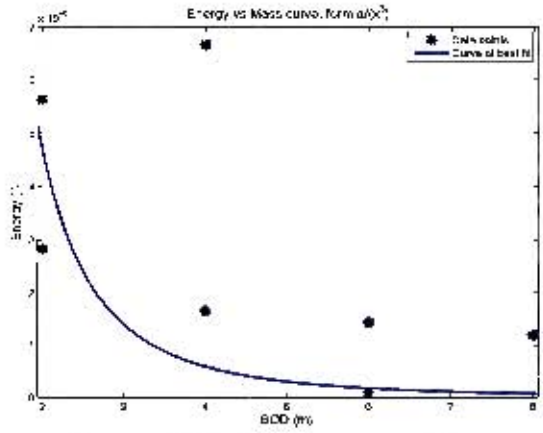

Figure F.28. Constant mass of 80g

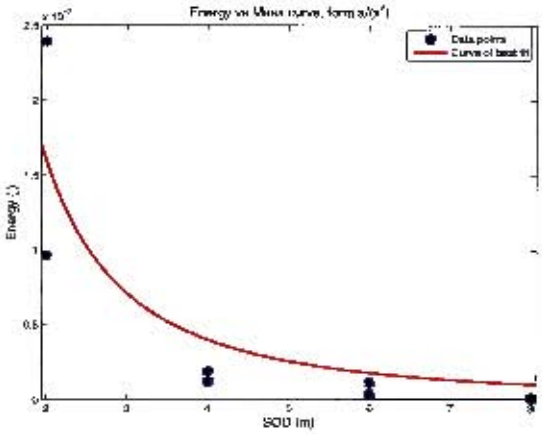

Figure F.29. Constant mass of 100g

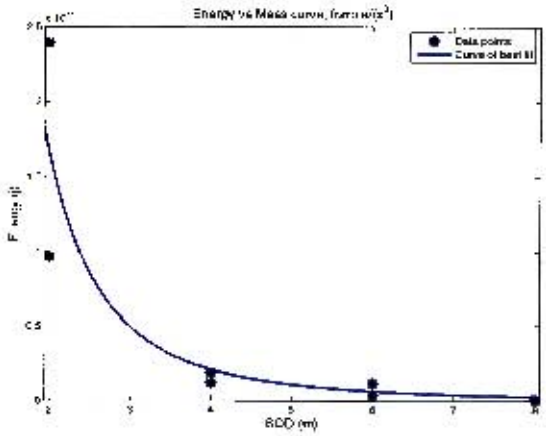

Figure F.30. Constant mass of 100g

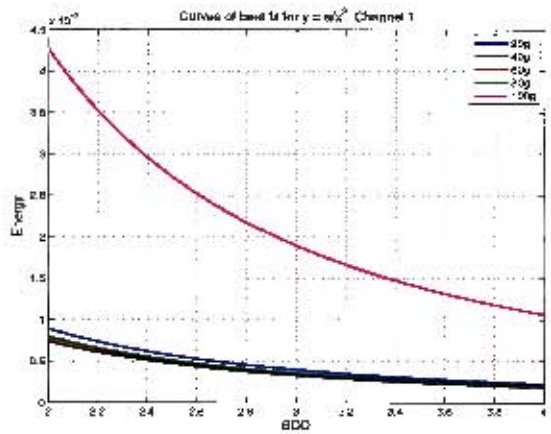

Figure F.31. Curves for masses between 20 and 100g, channel 1

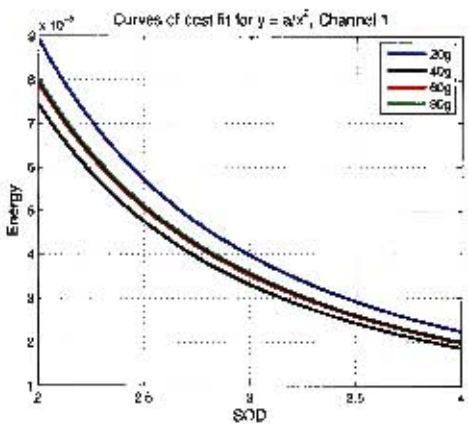

Figure F.32. Curves for masses between 20 and 100g, channel 1

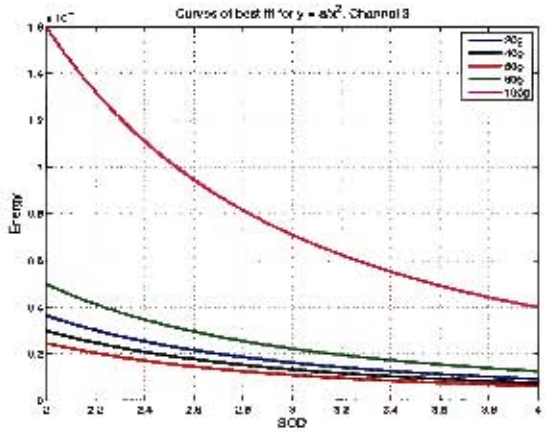

Figure F.33. Curves for masses between 20 and 100g, channel 3

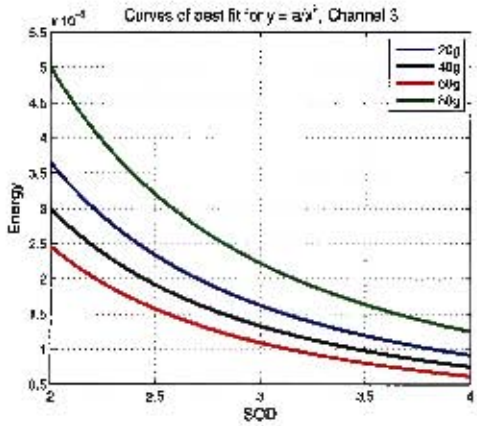

Figure F.34. Curves for masses between 20 and 100g, channel 3

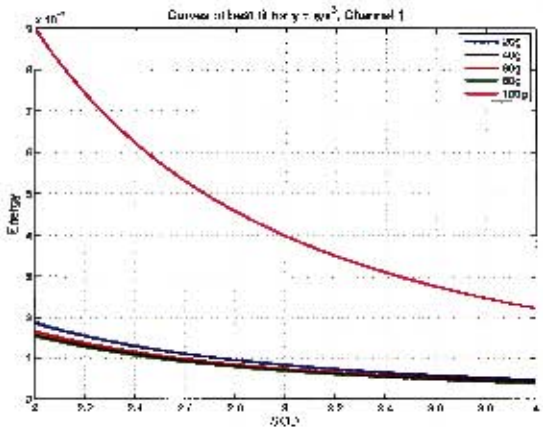

Figure F.35. Curves for masses between 20 and 100g, channel 1

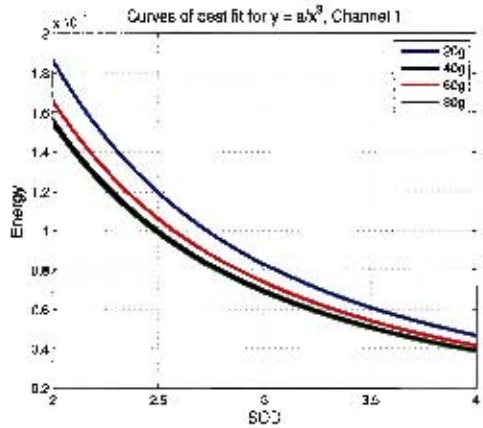

Figure F.36. Curves for masses between 20 and 100g, channel 1

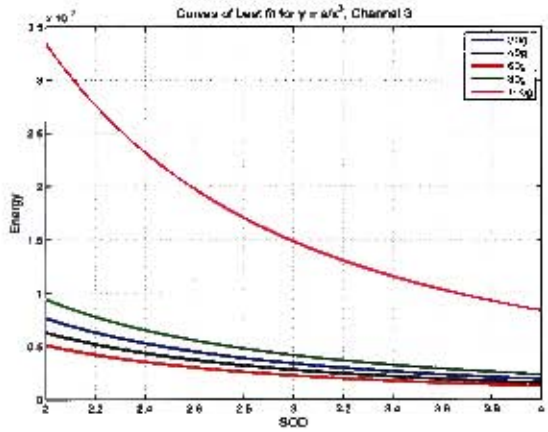

Figure F.37. Curves for masses between 20 and 100g, channel 3

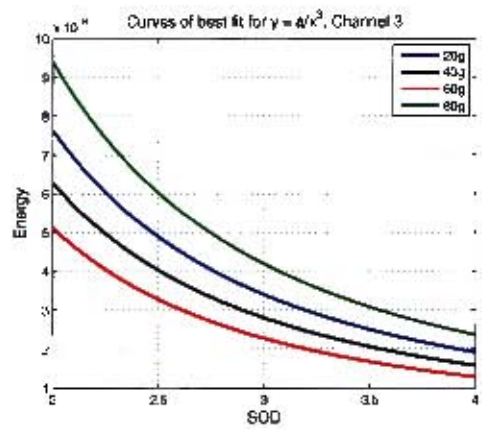

Figure F.38. Curves for masses between 20 and 100g, channel 3

G Main spike activity

After filtering the high frequency content there was a clearer picture of the event, and using the timeline discussed in section 7.2.1 focus was directed at the 2nd - 3rd stage of the explosion, escaping particles and shock wave formation. So in the first 0.3ms peaks or dips that would indicate the generation of a dipole were examined. The arrival time of this peak as well as its width, time to reach 1/2 of its maximum, was evaluated and compared to SOD and mass variances.

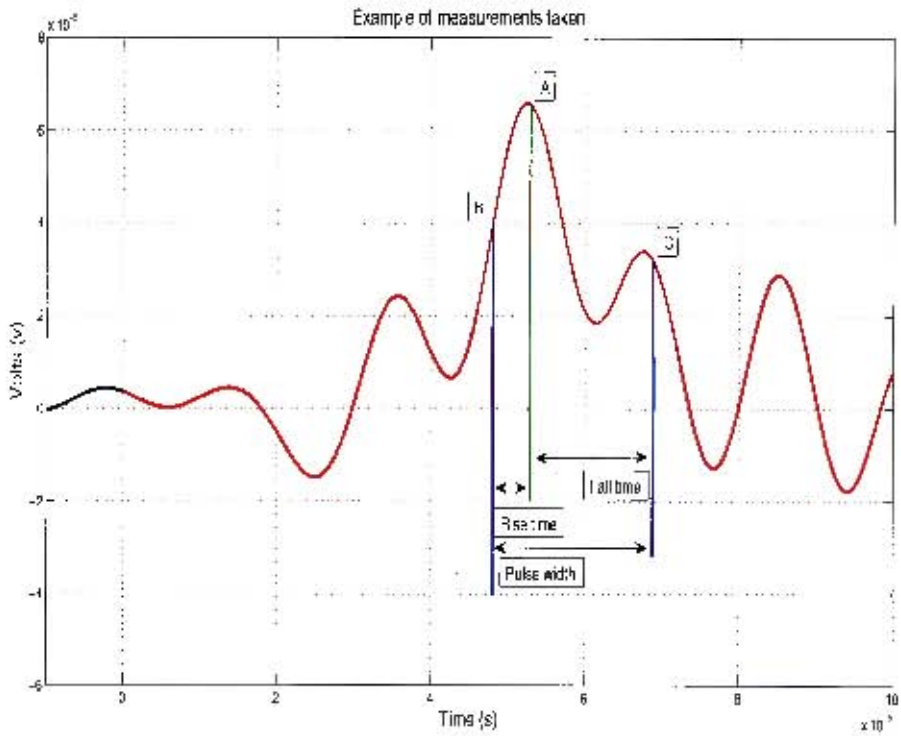

Figure G.1. Sample signal with points used to make calculations

The rise time and pulse width were measured based on the peak value. Point A was defined as the peak, B and C were set as half the value of A on either side. The time between B and C was defined as the pulse width and the the time between B and A was defined as the rise time. The fall time was not evaluated as on occasion the peak had not completed its cycle by the cut off time set. Due to clipping shot 15 was discredited from this section of analysis. It seems that any trend present was hard to detect. the width of the pulse and the peak values as well as the rise time itself held very little trend. The relationship at best can be said to be linear but further comments are not possible.

G.1 Waveform peaks

As with the pressure analysis on signals from blast waves the signals were examined for arrival time, rise time and overall width of the largest initial peak. The expectation was:

- *Arrival time* should be delayed with an increase in mass and SOD since the larger charge takes longer to fully detonate and at a further SOD the effect would register later

- *Rise time* would show a dependence on mass assuming the amount of charge affects the dipole formation

- *Peak value* should also be dependent on mass since more explosive could mean more dipoles formed

- *Pulse width* may show a dependence on SOD, if the further away the antenna is could result in picking up dipoles that have formed later. A dependence on mass is expected similarly to the reasoning in *Peak value*

The rise time and pulse width was highly dependent on number of samples in the time domain. The algorithm looked for a certain value associated with the peak time. It then scanned for the sample closest to that number and may at times have exaggerated both the width and rise time of the pulses, examples of this are shown in figures G.2 and G.3. All of these graphs are derived from channel 3 as it had the greatest number of signals with identifiable content.

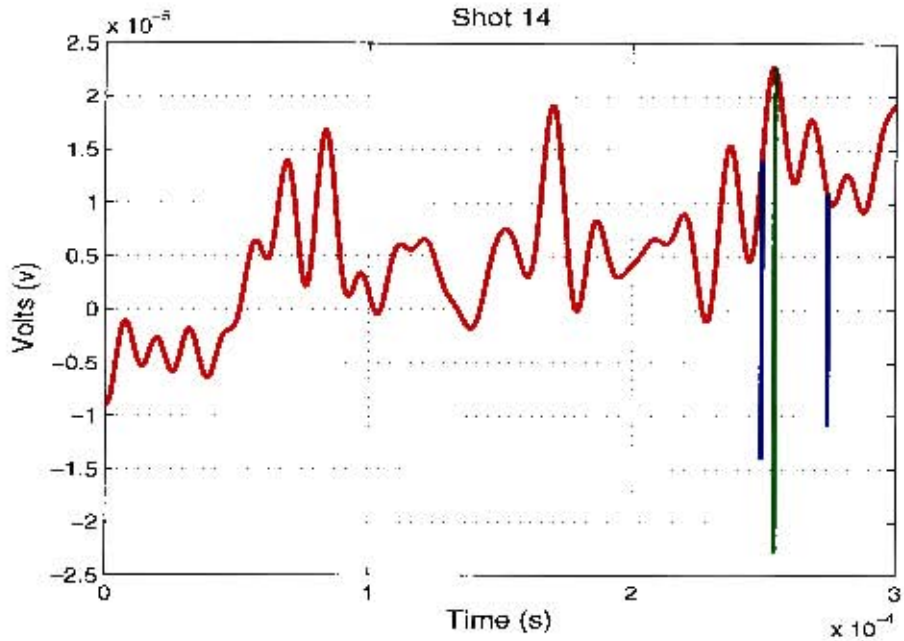

Figure G.2. Blown up portion of shot 14 with lines indicating reference points used in calculations

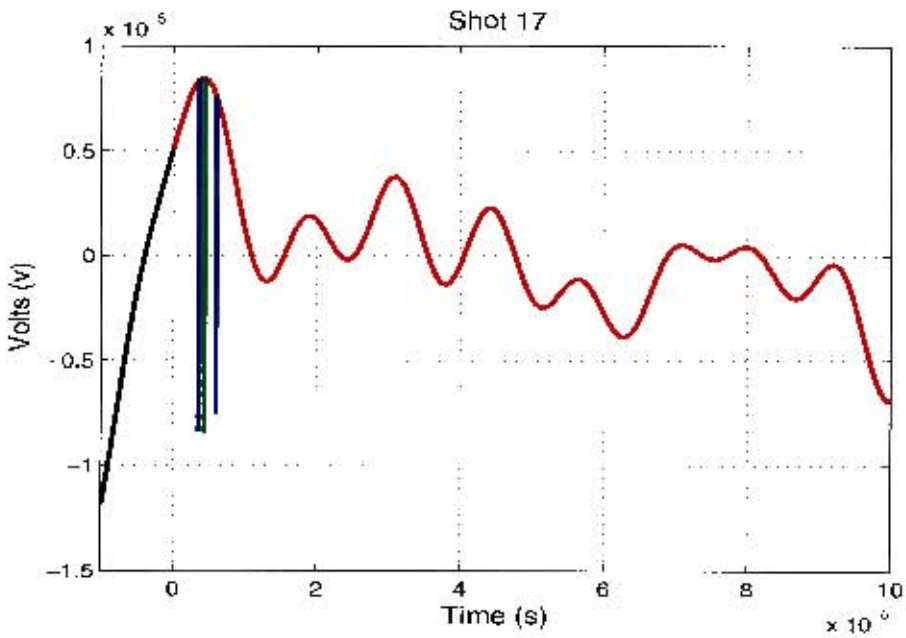

Figure G.3. Blown up portion of shot 17 with lines indicating reference points used in calculations

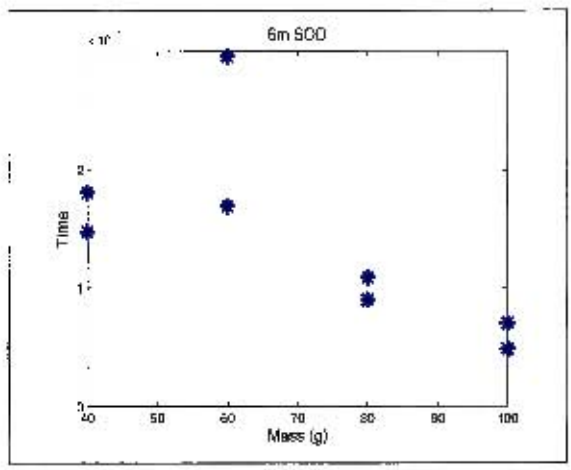

Figure G.6. Mass vs Time

G.1.1 Arrival time

For a constant mass of 100g (figure G.4) a weak trend of decreasing time of arrival as SOD increases can be seen. This is not true for the same channel and using 80g mass (figure G.5).

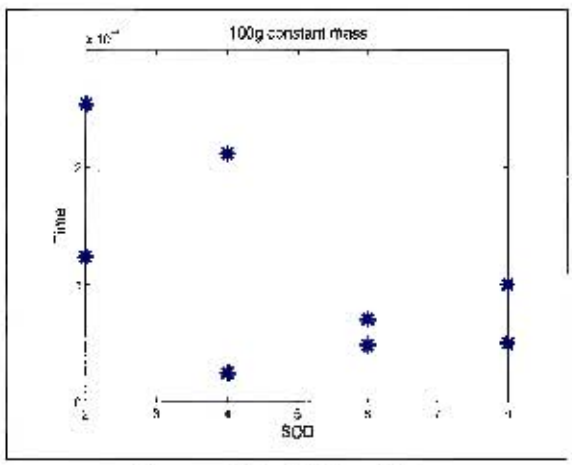

Figure G.4. SOD vs Time

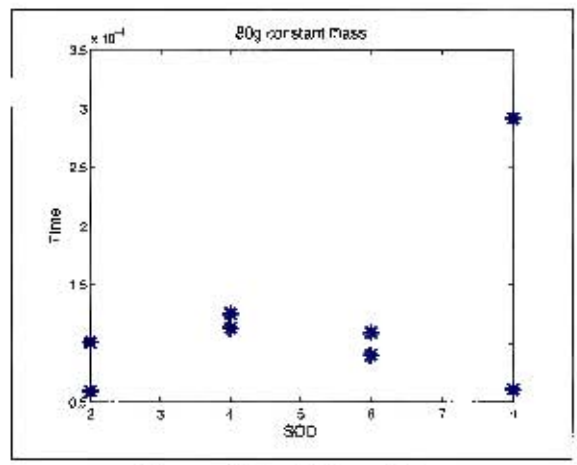

Figure G.5. SOD vs Time

The values over a constant SOD of 6m (figure G.6) seem to contradict the idea of a delay in arrival time as mass increases since the points show less time taken with a larger mass.

G.1.2 Rise time

The rise time is expected to be more dependent on mass than SOD. All constant SOD graphs, for example figures G.7 and G.8, have a slight trend showing a decrease in time except for the 2m(figure G.9) graph.

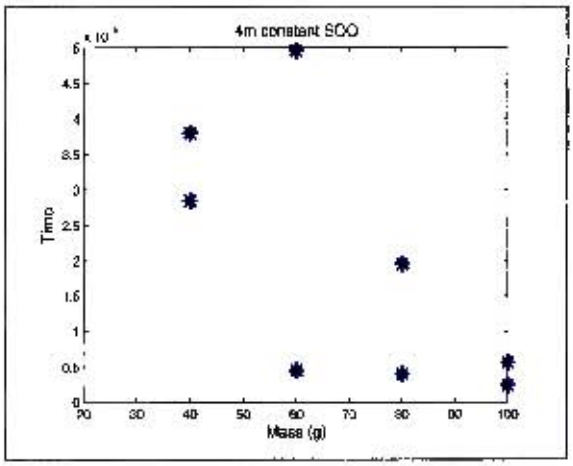

Figure G.7. SOD vs Time

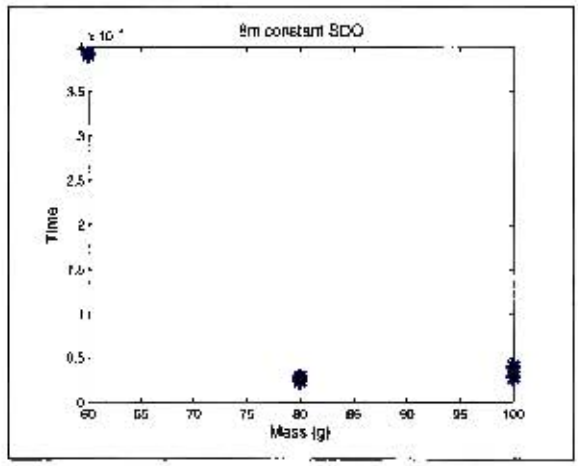

Figure G.8. SOD vs Time

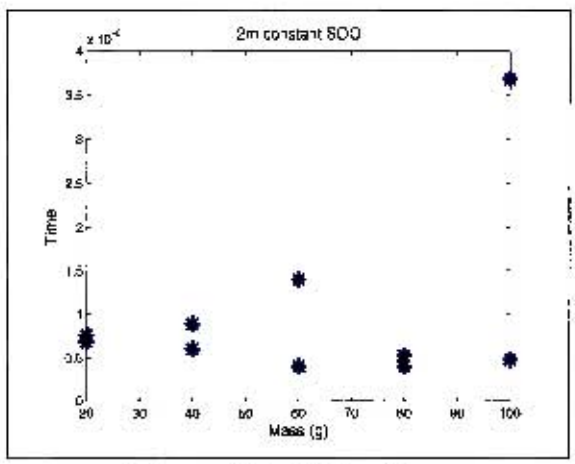

Figure G.9. SOD vs Time

The graphs with constant mass and varying SOD (figures G.10 and G.11) show no definitive trend

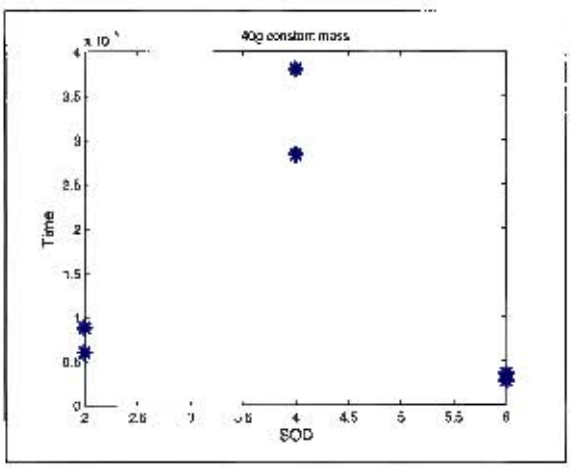

Figure G.10. Mass vs Time

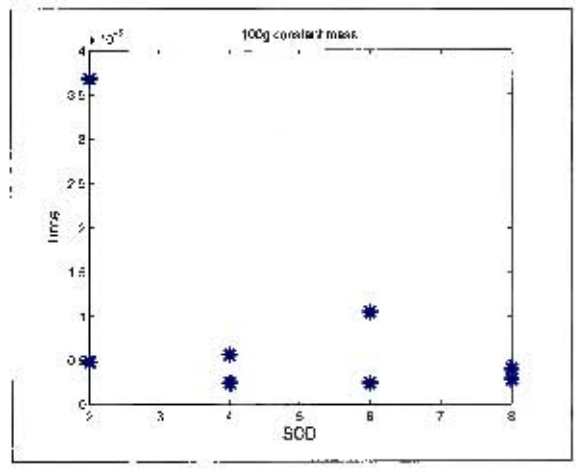

Figure G.11. Mass vs Time

G.1.3 Peak values

The signals also presented a negative peak at times so the absolute values were taken to take these into account. As previously mentioned the expectation is for a dependency on mass to appear. The constant SODs of 2m (figure G.12) and 6m (figure G.13) showed a data set that was more constant over the range of masses.

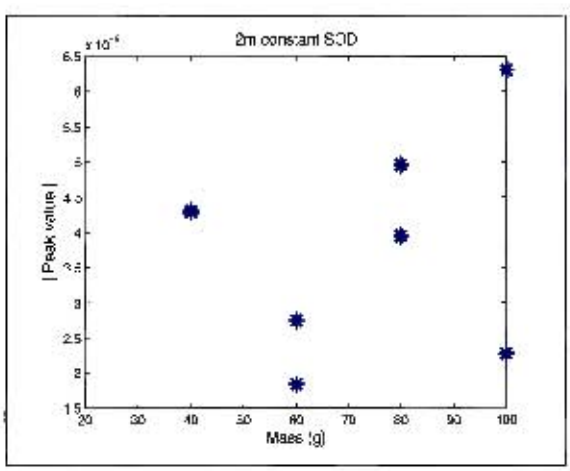

Figure G.12. Mass vs Absolute voltage

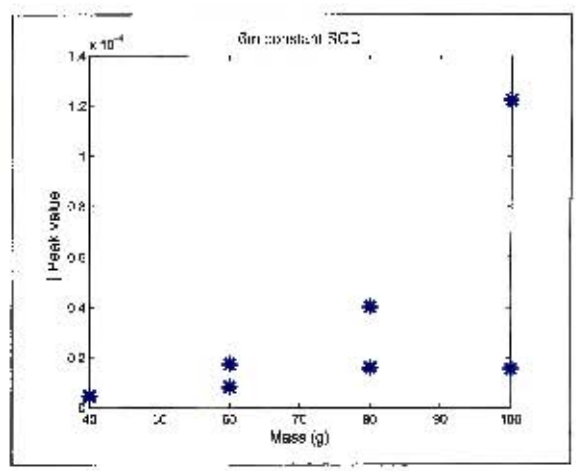

Figure G.13. Mass vs Absolute voltage

The graphs for constant masses all showed no discernible trend and were similar to the 60g(figure G.14) view shown below.

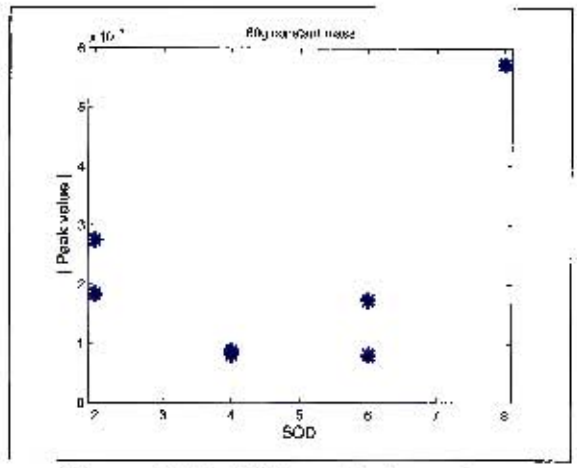

Figure G.14. SOD vs Absolute voltage

G.1.4 Pulse width

The dependence on mass is not definitive since the 2m and 6m graphs show different trends, the first increasing (figure G.15) and the later decreasing (figure G.16).

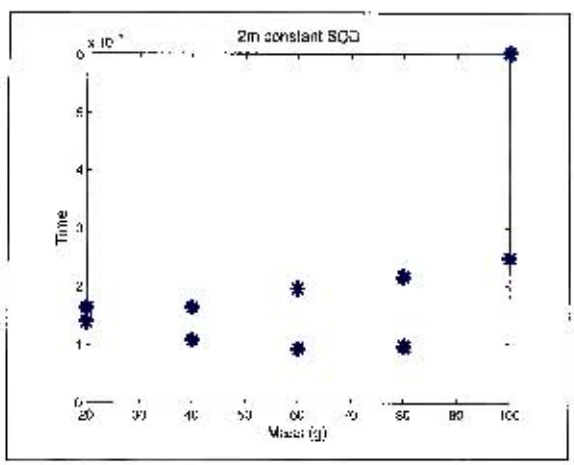

Figure G.15. Mass vs Duration

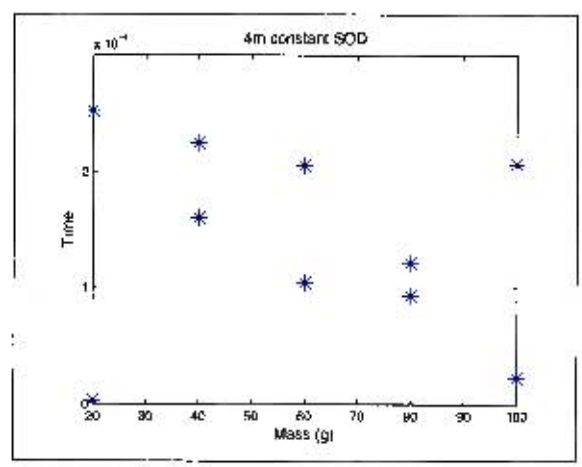

Figure G.16. Mass vs Duration

The 80g, figure G.17, graph showed no trend and is indicative of all the constant mass graphs evaluated.

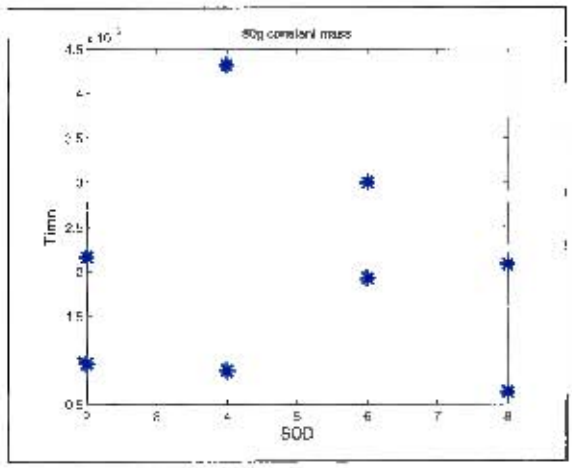

Figure G.17. SOD vs Duration

Table G.1. Times for different peaks, channel 1

Mass (Kg)	SOD (m)	Shot number	arrival time	pulse width	Max value	rise time
20	2	6	5.3e-005	2.1e-005	6.6e-005	4.8e-006
20	2	7	5.1e-005	1e-005	7.1e-005	5.2e-006
40	2	8	5.8e-005	2.3e-005	-5e-005	1.7e-005
40	2	9	5.4e-005	1.8e-005	-4.8e-005	1.3e-005
60	2	10	0.00024	2.4e-005	-4.1e-005	5.6e-006
60	2	11	6.1e-005	2.2e-005	-3.5e-005	1.7e-005
80	2	12	0.00029	1.4e-005	3.7e-005	3.2e-006
80	2	13	6.8e-005	3.7e-005	5.6e-005	1.7e-005
100	2	14	0.00026	3e-005	3.3e-005	1.8e-005
100	2	15	7e-005	3.4e-005	0.00011	1.7e-005
20	4	16	5.4e-005	1.6e-005	8.8e-006	4.4e-006
20	4	17	2e-006	8e-007	-1.6e-005	0
40	4	18	0.0001	8.8e-006	1.2e-005	4.4e-006
40	4	19	2.2e-005	6e-006	-9.6e-006	2.8e-006
60	4	20	0.0002	1.2e-005	7.8e-006	5.6e-006
60	4	21	5.2e-005	2.5e-005	1.5e-005	1e-005
80	4	22	8.9e-005	6.8e-006	0.00017	3.2e-006
80	4	23	0.00026	3.2e-005	-1.6e-005	2.2e-005
100	4	24	0.00016	4.6e-005	-1.7e-005	1.4e-005
100	4	25	2.4e-005	5.6e-006	2.2e-005	2.4e-006
40	6	26	3.1e-005	5.6e-006	-4.6e-006	2.4e-006
40	6	27	4.4e-006	2.4e-006	-7.1e-006	8e-007
60	6	28	1.7e-005	4e-006	1.8e-005	1.6e-006
60	6	29	0.00029	4.4e-006	-1.1e-005	2e-006
80	6	30	0.00015	7.8e-005	-1.6e-005	4e-005
80	6	31	8.9e-005	1.8e-005	-4.6e-005	1.2e-005
100	6	32	1.7e-005	4.8e-006	-2.2e-005	2e-006
100	6	33	7e-005	5.6e-006	0.00013	2.4e-006
60	8	35	0.00015	4.9e-005	-6.6e-005	4.4e-005
80	8	36	0.00029	6e-006	-0.00028	2.8e-006
80	8	38	6e-005	1.4e-005	1.8e-005	2e-006
100	8	39	0.0001	5.6e-006	1.3e-005	2.8e-006
100	8	40	2.6e-005	4.8e-006	-1.8e-005	2.4e-006

Table G.2. Times for different peaks, channel 2

Mass (Kg)	SOD (m)	Shot number	arrival time	pulse width	Max value	rise time
20	2	6	0.00025	5.7e-005	2.6e-006	5.3e-005
20	2	7	7e-005	2.6e-005	-3.5e-006	1.4e-005
40	2	8	1.1e-005	6.4e-006	-3.1e-006	2.8e-006
40	2	9	1.2e-005	6.4e-006	-4.5e-006	2.8e-006
60	2	10	4e-007	0	-3.2e-006	-4e-007
60	2	11	5.2e-006	2.4e-006	-4.3e-006	8e-007
80	2	12	5.8e-005	1.7e-005	-4.3e-006	1.4e-005
80	2	13	6.8e-005	1.8e-005	-6.1e-005	1.5e-005
100	2	14	0.00027	4.7e-005	-3.2e-005	4.4e-005
100	2	15	7.1e-005	1.6e-005	-0.00015	6.8e-006
20	4	16	0.00026	1.3e-005	-3.8e-006	9.6e-006
20	4	17	5.8e-005	1.7e-005	-6.3e-006	1.4e-005
40	4	18	7.1e-005	1.8e-005	-8.5e-006	5.6e-006
40	4	19	0.00013	5e-005	-7.5e-006	1.3e-005
60	4	20	0.00017	6.1e-005	-1.4e-005	2.3e-005
60	4	21	5e-005	1.9e-005	-1.6e-005	8.8e-006
80	4	22	0.00012	8e-006	-4.6e-005	3.6e-006
80	4	23	0.00021	6.2e-005	1.7e-005	1.7e-005
100	4	24	0.00013	3.6e-005	3.5e-005	2.6e-005
100	4	25	4e-007	0	-1.1e-005	-4e-007
40	6	26	0.0003	5.5e-005	4.3e-006	5.2e-005
40	6	27	2.9e-005	1.6e-005	-5.5e-006	7.2e-006
60	6	28	1.8e-005	4.8e-006	-8e-006	2e-006
60	6	29	0.00017	4.9e-005	-2.3e-005	4.5e-005
80	6	30	0.00014	3.6e-005	-1.5e-005	2.2e-005
80	6	31	6.2e-005	1.5e-005	-1.7e-005	8e-006
100	6	32	0.00012	5.8e-005	-1.8e-005	3e-005
100	6	33	7.1e-005	6e-006	-5.6e-005	2.8e-006
60	8	35	0.00015	4.6e-005	-8.7e-006	4e-005
80	8	36	0.00029	5.6e-006	-0.00015	2.4e-006
80	8	38	7.6e-005	1.5e-005	-1.5e-005	1.1e-005
100	8	39	9.9e-005	8.4e-006	-1.2e-005	3.6e-006
100	8	40	5.1e-005	8.4e-006	-1.8e-005	3.6e-006

Table G.3. Times for different peaks, channel 3

Mass (Kg)	SOD (m)	Shot number	arrival time	pulse width	Max value	rise time
20	2	6	5.5e-005	1.4e-005	4.5e-005	6.8e-006
20	2	7	5.3e-005	1.6e-005	5.3e-005	7.6e-006
40	2	8	5.4e-005	1.6e-005	-4.3e-005	8.8e-006
40	2	9	5.3e-005	1.1e-005	-4.3e-005	6e-006
60	2	10	0.00027	9.2e-006	-2.8e-005	4e-006
60	2	11	6.1e-005	2e-005	-1.8e-005	1.4e-005
80	2	12	0.0001	9.6e-006	4e-005	5.2e-006
80	2	13	5.9e-005	2.2e-005	5e-005	4e-006
100	2	14	0.00025	2.5e-005	2.3e-005	4.8e-006
100	2	15	0.00012	6e-005	-6.3e-005	3.7e-005
20	4	16	0.00026	1.3e-005	-3.8e-006	9.6e-006
20	4	17	4.4e-006	2.4e-006	8.5e-006	8e-007
40	4	18	0.00025	3.2e-005	-8e-006	2.8e-005
40	4	19	0.0002	9.1e-005	-8.5e-006	3.8e-005
60	4	20	0.00011	9.6e-006	-8.2e-006	4.4e-006
60	4	21	0.00025	6.1e-005	8.8e-006	5e-005
80	4	22	0.00013	8.8e-006	0.00016	4e-006
80	4	23	0.00011	4.3e-005	1.5e-005	2e-005
100	4	24	0.00021	9.6e-006	1.2e-005	5.6e-006
100	4	25	2.5e-005	5.6e-006	-1.8e-005	2.4e-006
40	6	26	0.00015	4.3e-005	4.3e-006	3.6e-006
40	6	27	0.00018	4.5e-005	-4.5e-006	2.8e-006
60	6	28	0.0003	4e-005	8e-006	3.7e-005
60	6	29	0.00017	4.5e-005	-1.7e-005	4.2e-005
80	6	30	0.00011	3e-005	1.6e-005	2e-006
80	6	31	9e-005	1.9e-005	4e-005	1.4e-005
100	6	32	4.8e-005	1.4e-005	1.5e-005	1e-005
100	6	33	7e-005	5.6e-006	-0.00012	2.4e-006
60	8	35	0.00015	4.4e-005	5.7e-005	3.9e-005
80	8	36	0.00029	6.4e-006	0.0002	2.8e-006
80	8	38	6.1e-005	2.1e-005	-1.4e-005	2.4e-006
100	8	39	0.0001	6e-006	-1.1e-005	2.8e-006
100	8	40	5e-005	8.8e-006	-2.5e-005	4e-006

H Test data

The entire collection of signals recored during testing at Paarderfontein have been presented here. They are divided into different sections; Raw and filtered signals, FFT of signals and the overlay of pre-trigger and signal FFTs . The raw data is direct from the scope while the filtered section shows the digitally processed results. In these sections the data is once again split into different channels.

H.1 Raw and filtered Signals

H.1.1 Channel 1

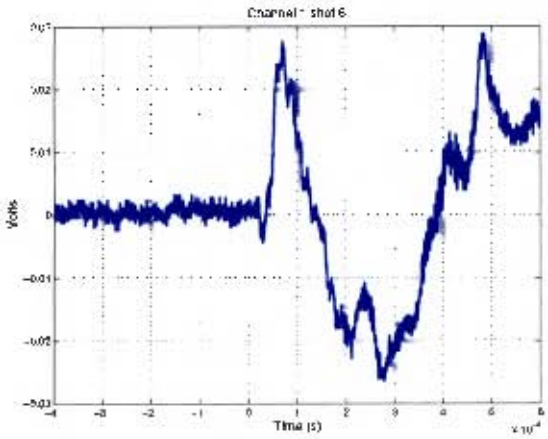

Figure H.1. Channel 1 20g at 2m

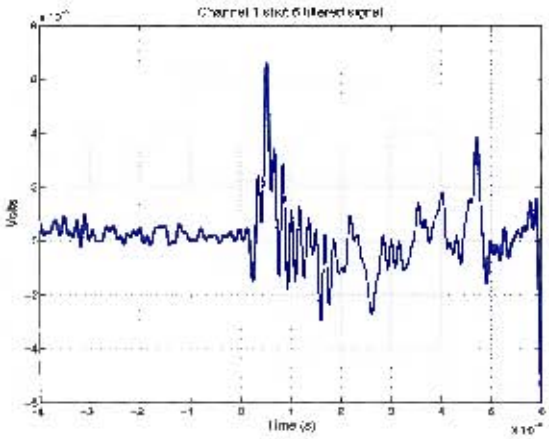

Figure H.2. Channel 1 20g at 2m filtered

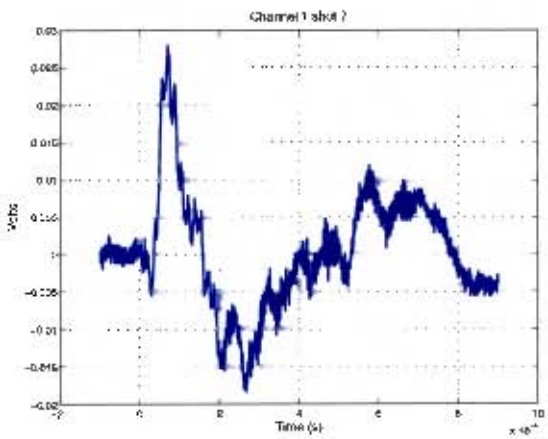

Figure H.3. Channel 1 20g at 2m

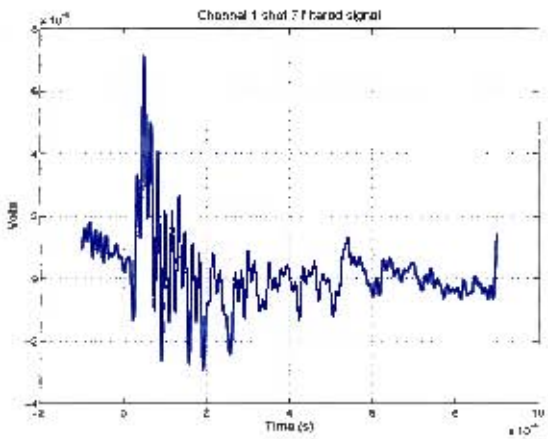

Figure H.4. Channel 1 20g at 2m filtered

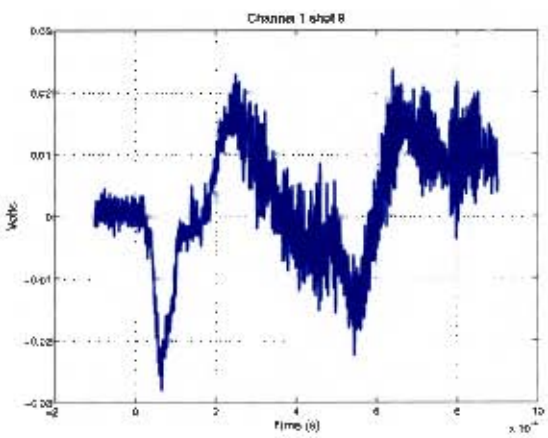

Figure H.5. Channel 1 40g at 2m

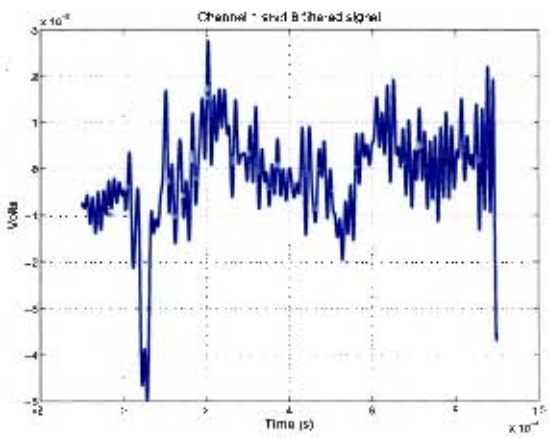

Figure H.6. Channel 1 40g at 2m filtered

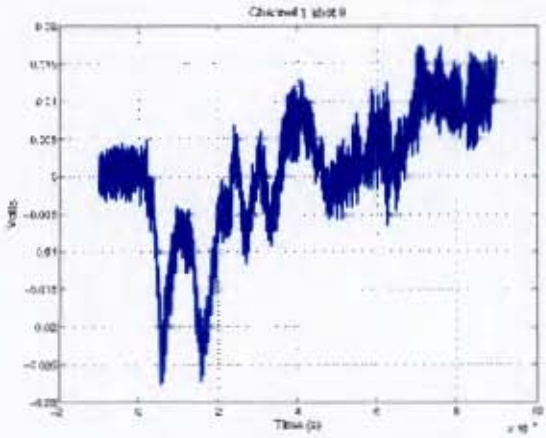

Figure H.7. Channel 1 40g at 2m

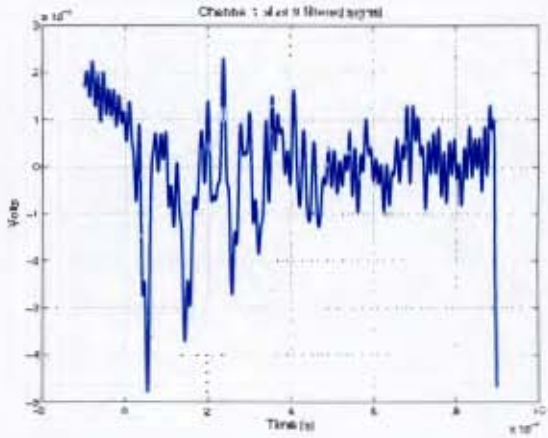

Figure H.8. Channel 1 40g at 2m filtered

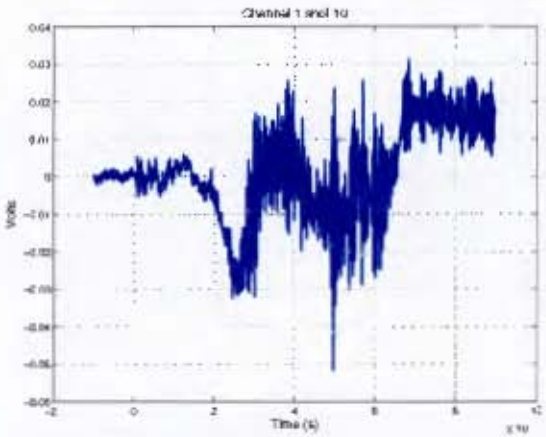

Figure H.9. Channel 1 60g at 2m

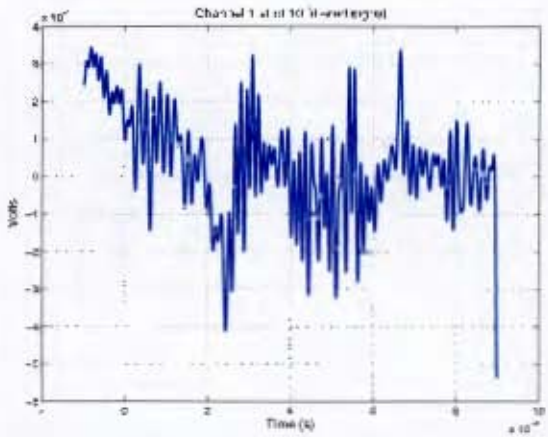

Figure H.10. Channel 1 60g at 2m filtered

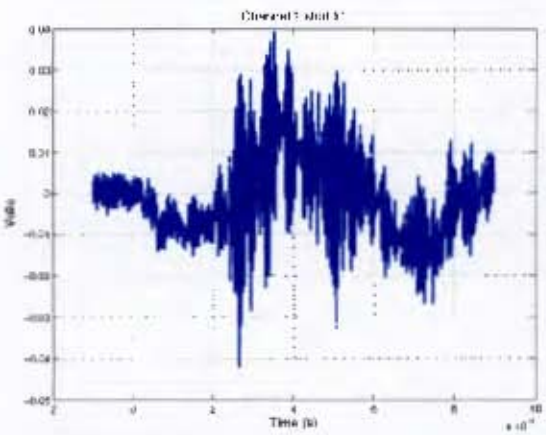

Figure H.11. Channel 1 60g at 2m

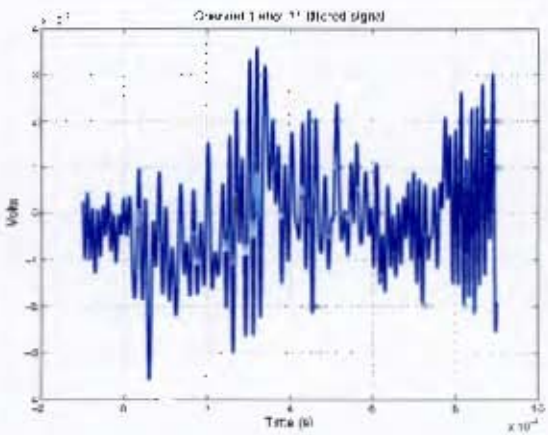

Figure H.12. Channel 1 60g at 2m filtered

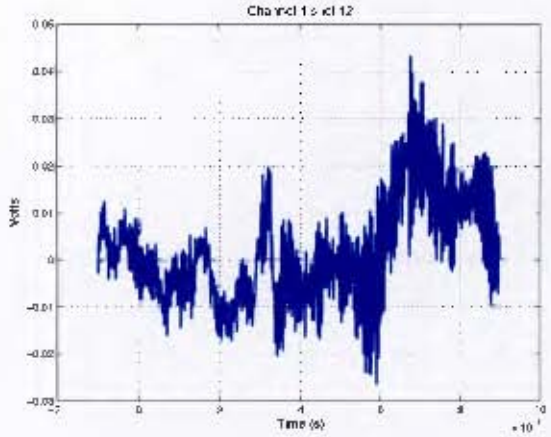

Figure H.13. Channel 1 80g at 2m

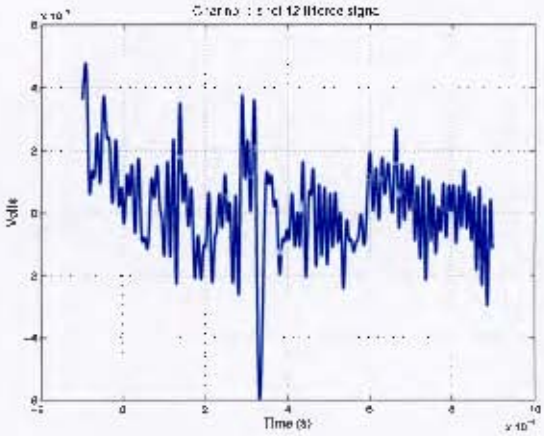

Figure H.14. Channel 1 80g at 2m filtered

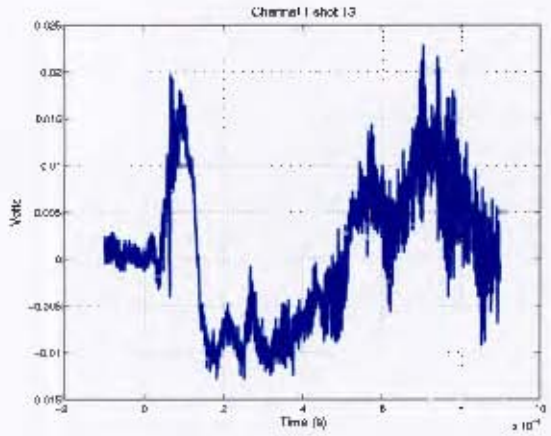

Figure H.15. Channel 1 80g at 2m

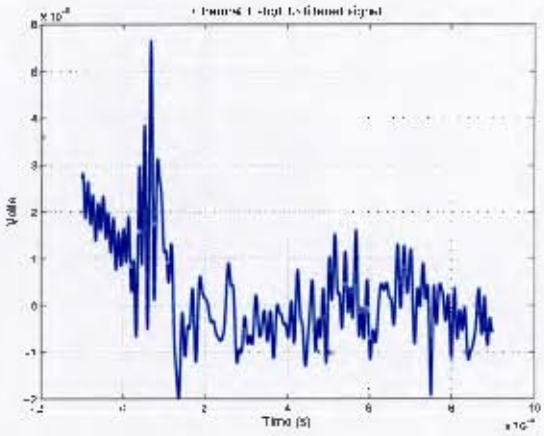

Figure H.16. Channel 1 80g at 2m filtered

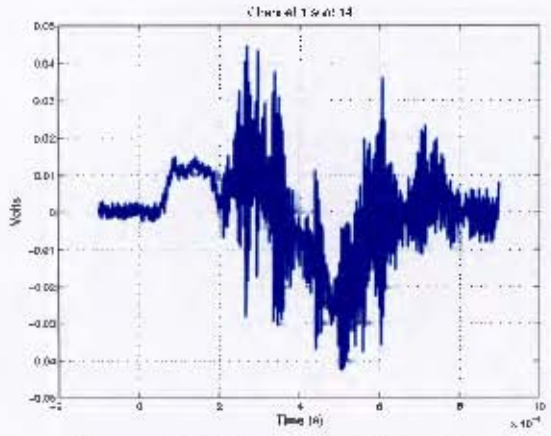

Figure H.17. Channel 1 100g at 2m

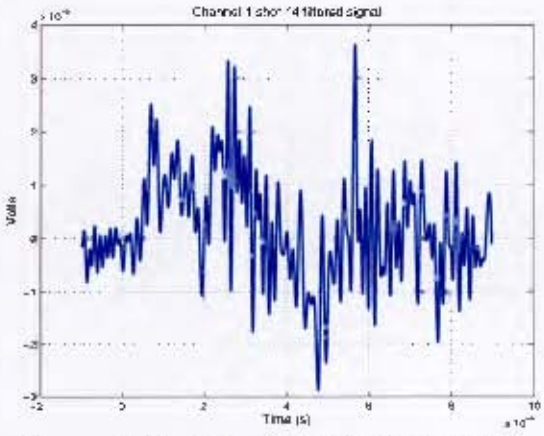

Figure H.18. Channel 1 100g at 2m filtered

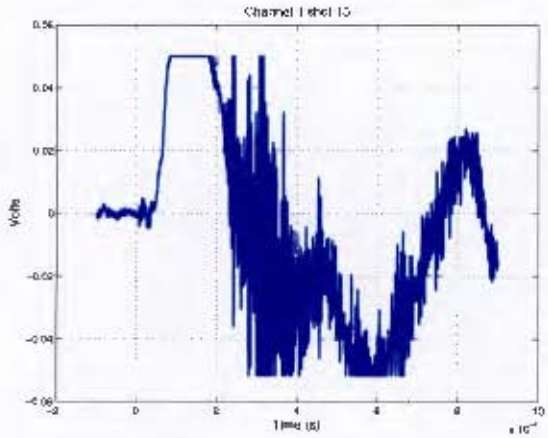

Figure H.19. Channel 1 100g at 2m

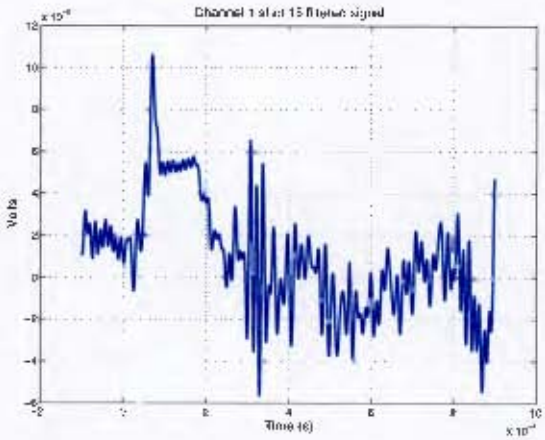

Figure H.20. Channel 1 100g at 2m filtered

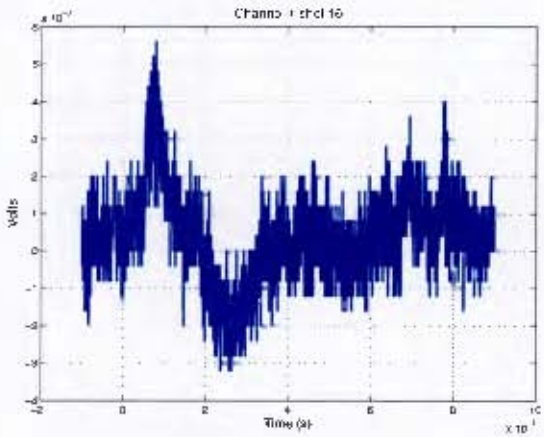

Figure H.21. Channel 1 20g at 4m

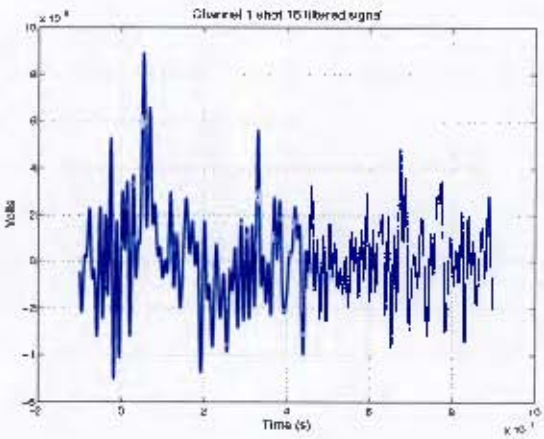

Figure H.22. Channel 1 20g at 4m filtered

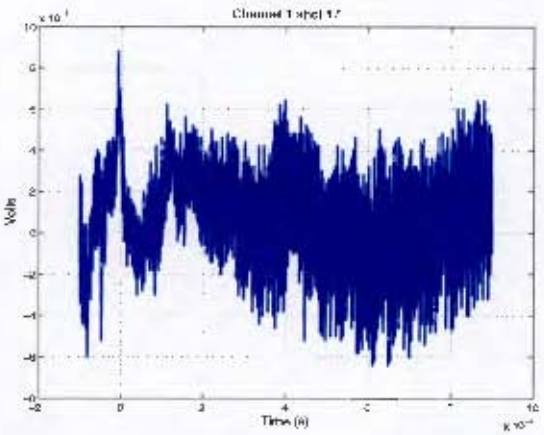

Figure H.23. Channel 1 20g at 4m

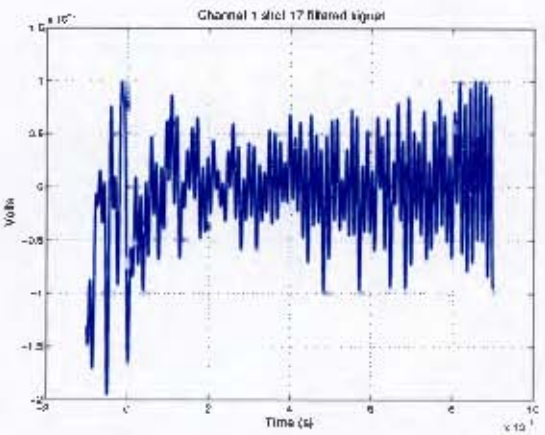

Figure H.24. Channel 1 20g at 4m filtered

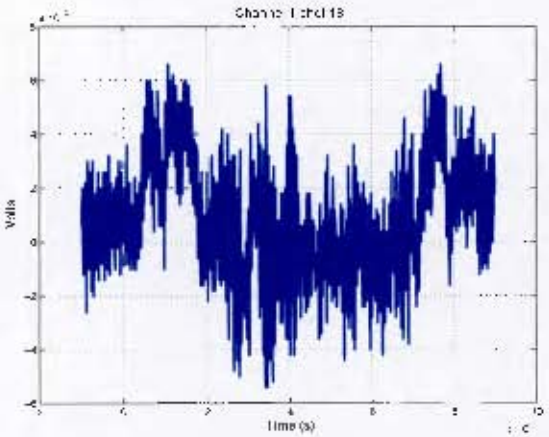

Figure H.25. Channel 1 40g at 4m

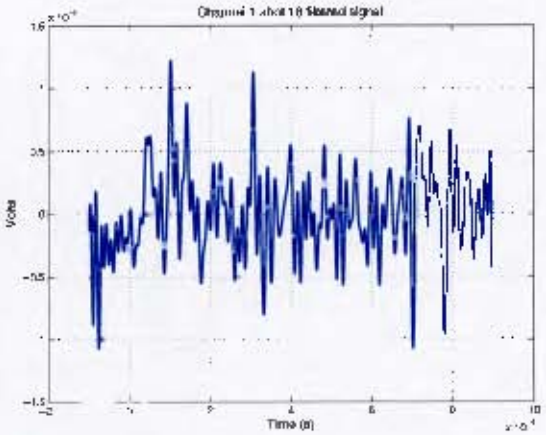

Figure H.26. Channel 1 40g at 4m filtered

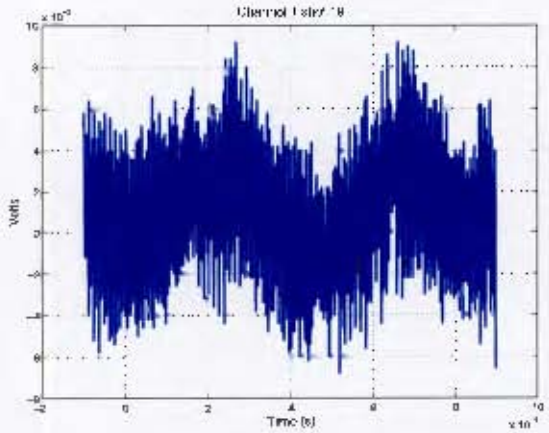

Figure H.27. Channel 1 40g at 4m

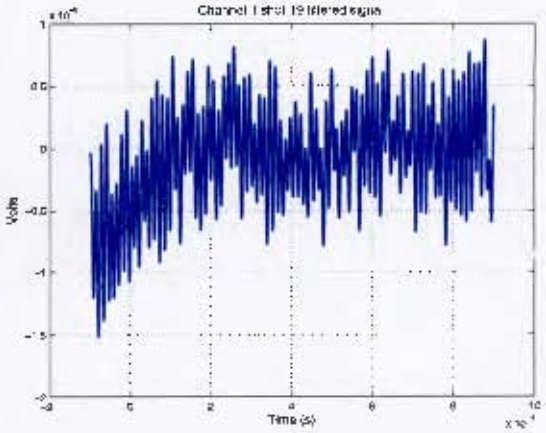

Figure H.28. Channel 1 40g at 4m filtered

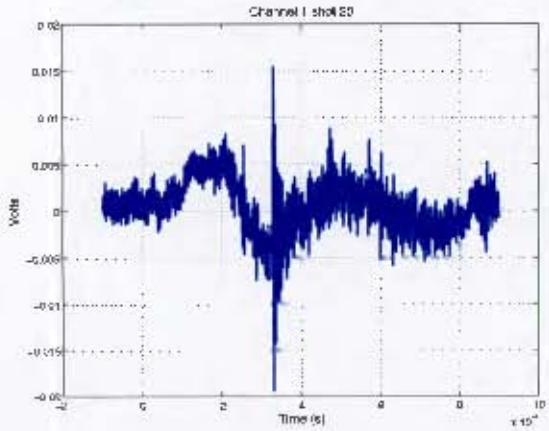

Figure H.29. Channel 1 60g at 4m

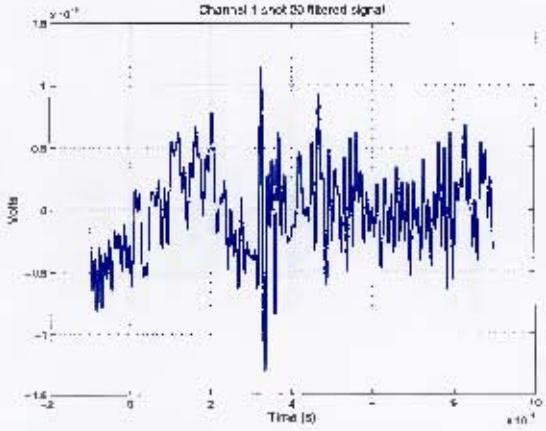

Figure H.30. Channel 1 60g at 4m filtered

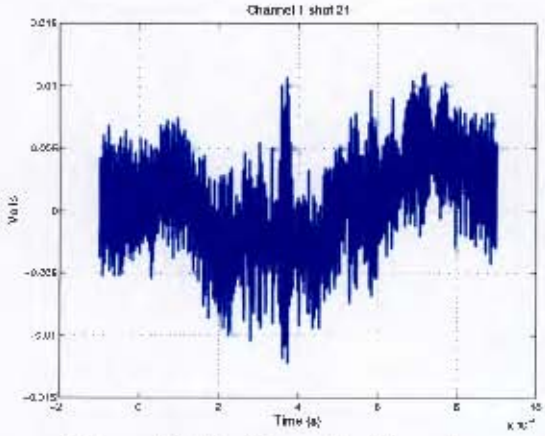

Figure H.31. Channel 1 60g at 4m

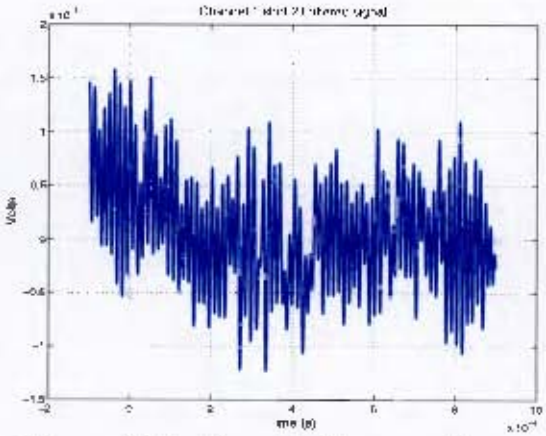

Figure H.32. Channel 1 60g at 4m filtered

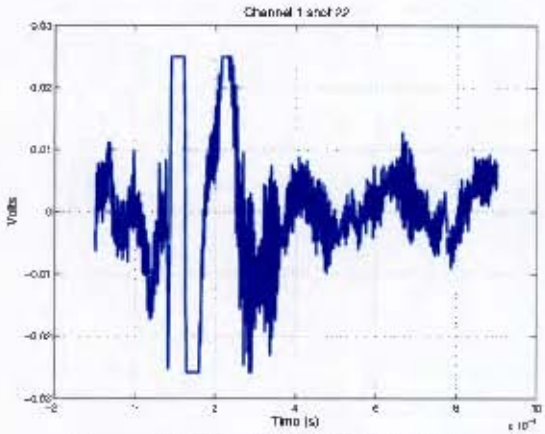

Figure H.33. Channel 1 80g at 4m

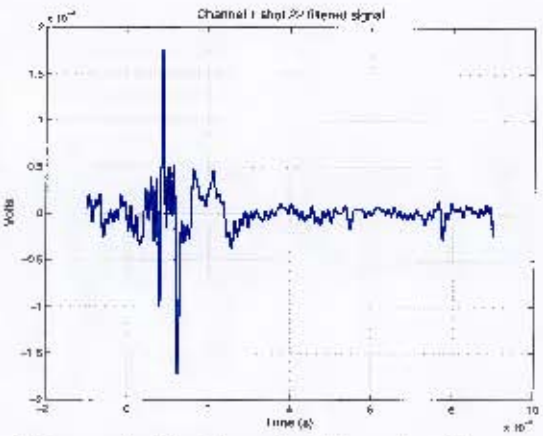

Figure H.34. Channel 1 80g at 4m filtered

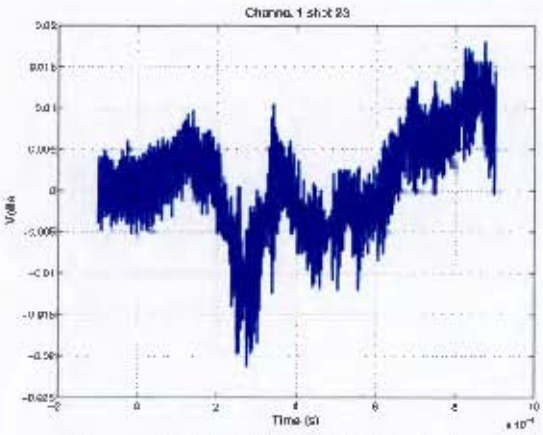

Figure H.35. Channel 1 80g at 4m

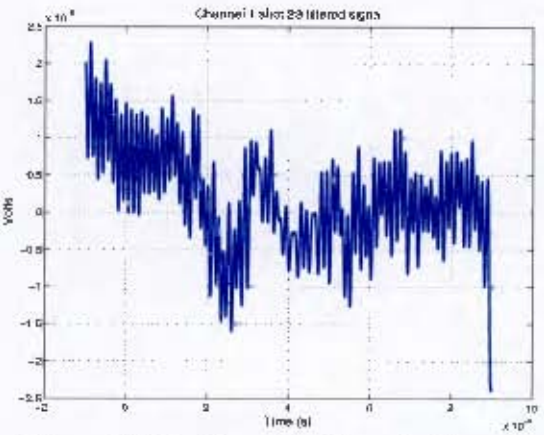

Figure H.36. Channel 1 80g at 4m filtered

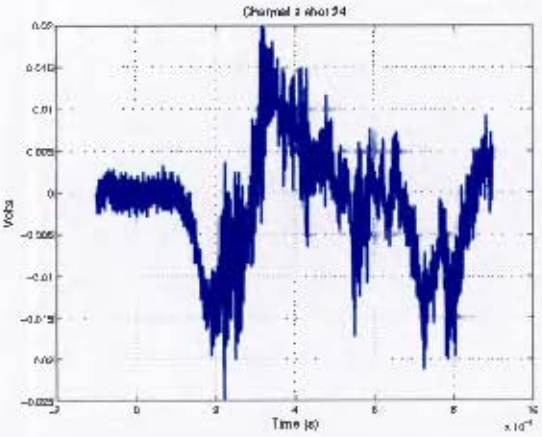

Figure H.37. Channel 1 100g at 4m

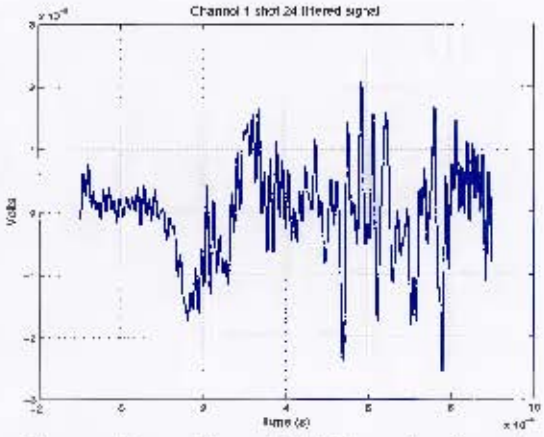

Figure H.38. Channel 1 100g at 4m filtered

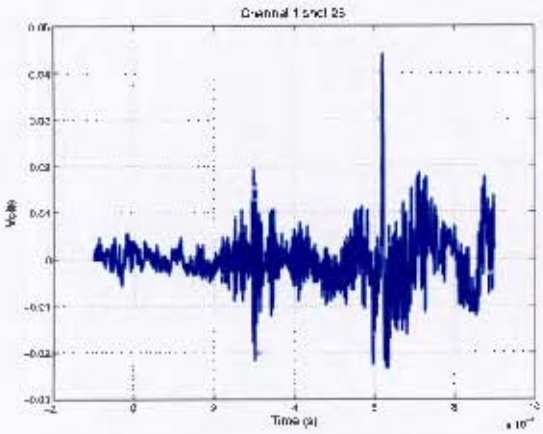

Figure H.39. Channel 1 100g at 4m

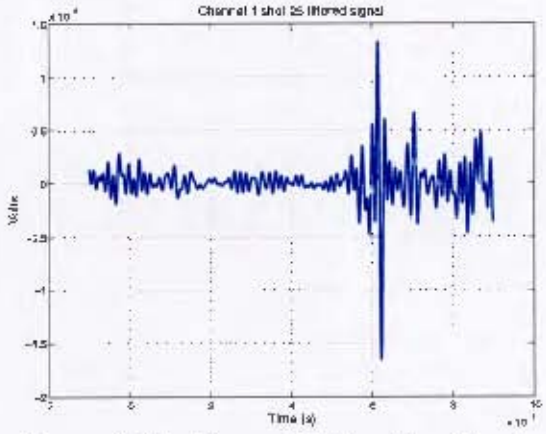

Figure H.40. Channel 1 100g at 4m filtered

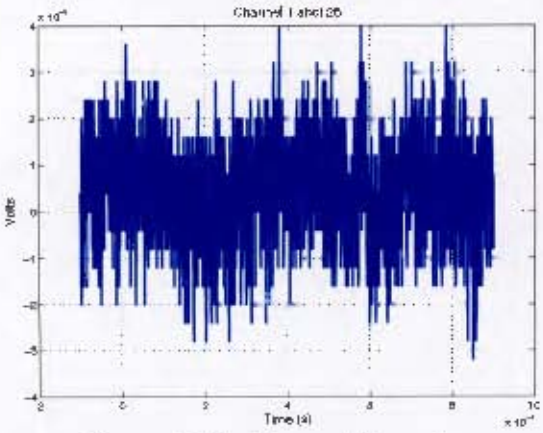

Figure H.41. Channel 40g at 6m

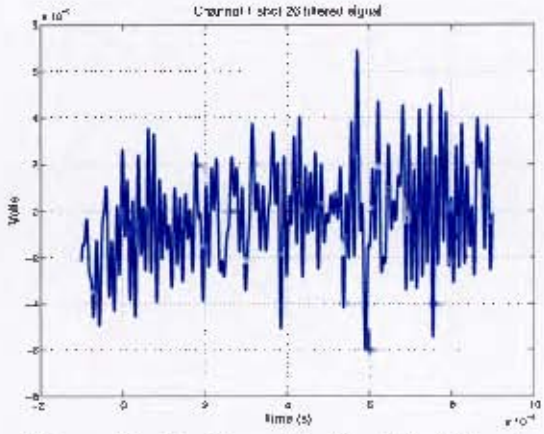

Figure H.42. Channel 1 40g at 6m filtered

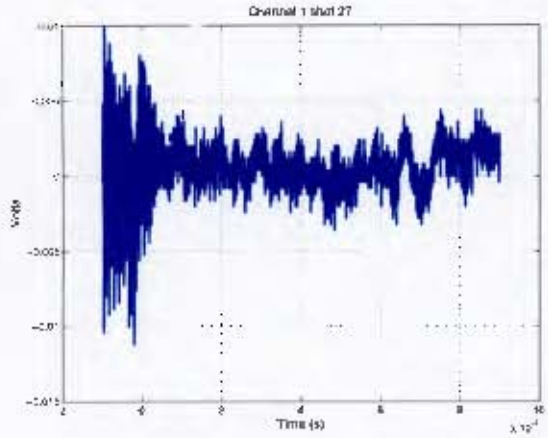

Figure H.43. Channel 1 40g at 6m

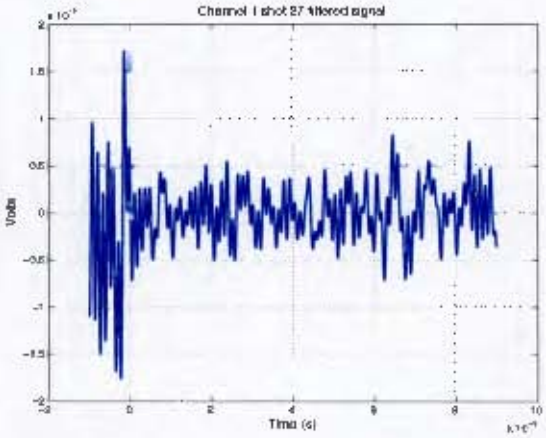

Figure H.44. Channel 1 40g at 6m filtered

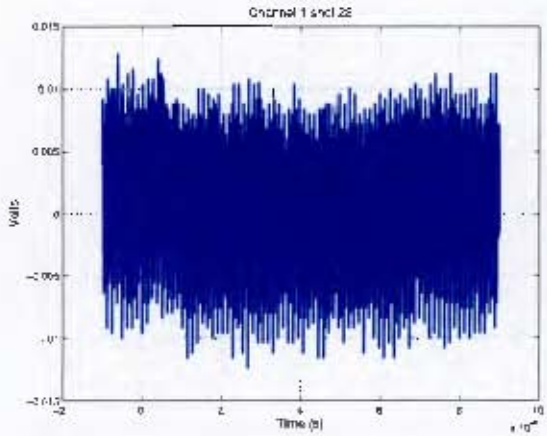

Figure H.45. Channel 1 60g at 6m

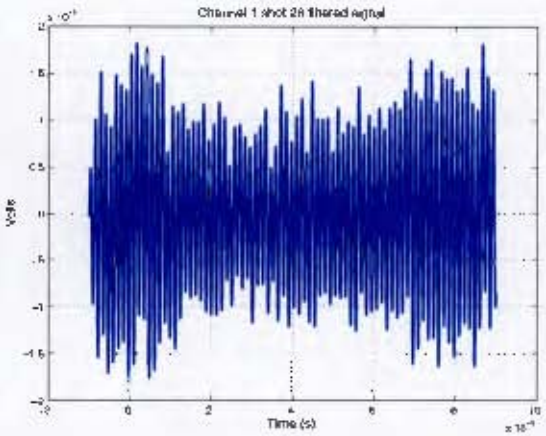

Figure H.46. Channel 1 60g at 6m filtered

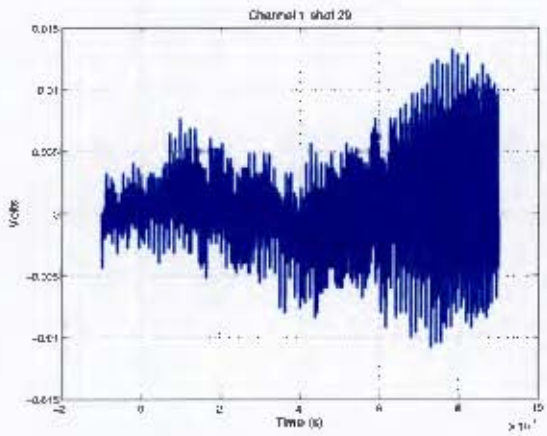

Figure H.47. Channel 1 60g at 6m

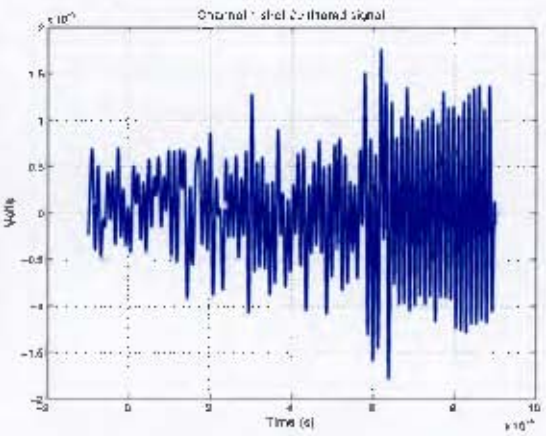

Figure H.48. Channel 1 60g at 6m filtered

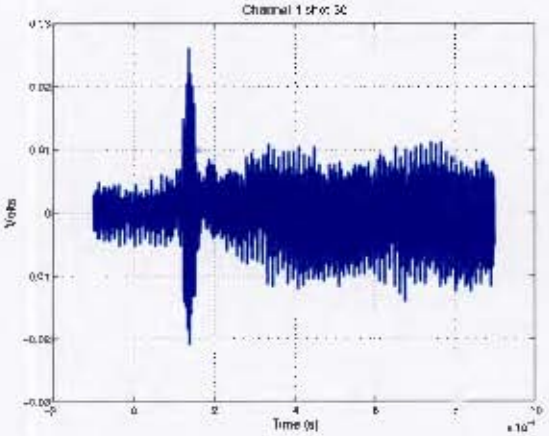

Figure H.49. Channel 1 80g at 6m

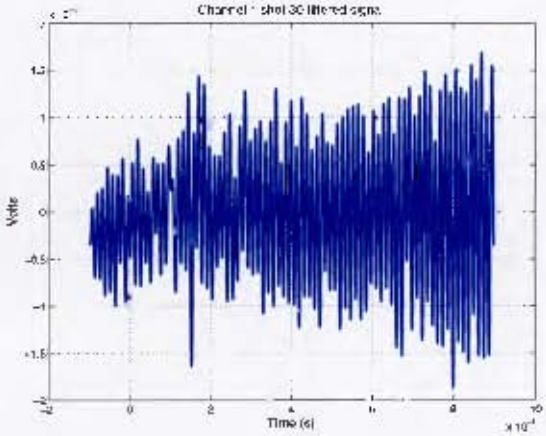

Figure H.50. Channel 1 80g at 6m filtered

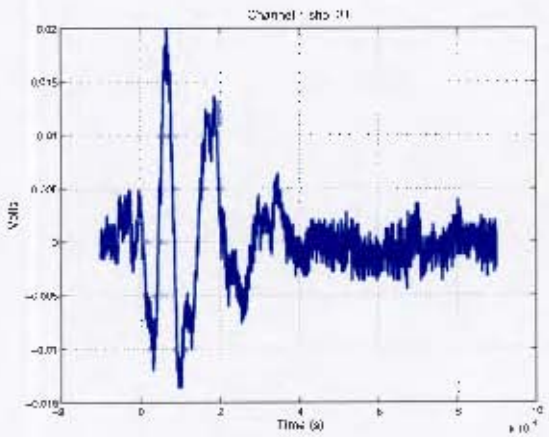

Figure **H.51.** Channel 1 80g at 6m

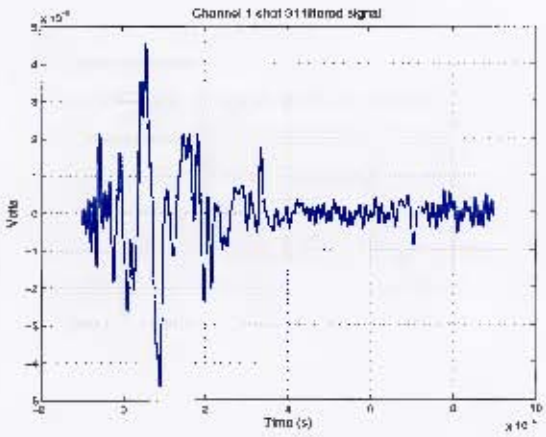

Figure H.52. Channel 1 80g at 6m filtered

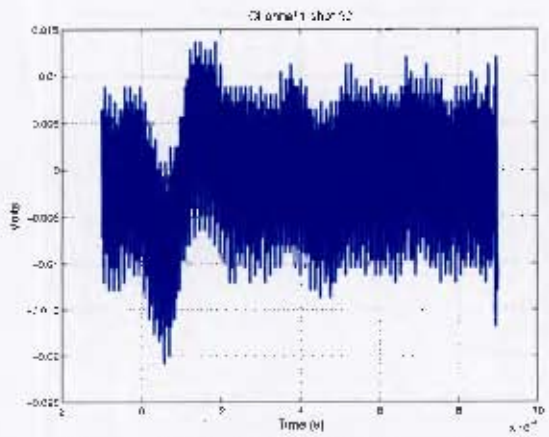

Figure **H.53.** Channel 1 100g at 6m

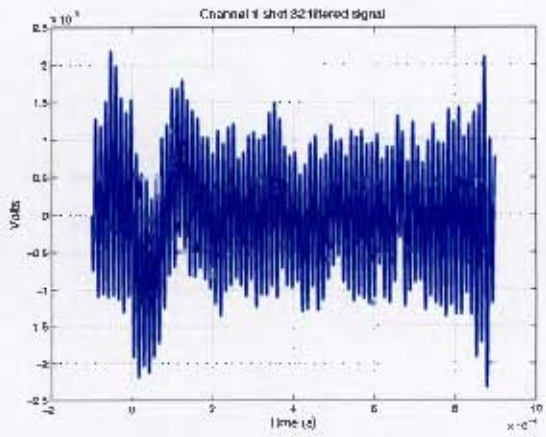

Figure H.54. Channel 1 100g at 6m filtered

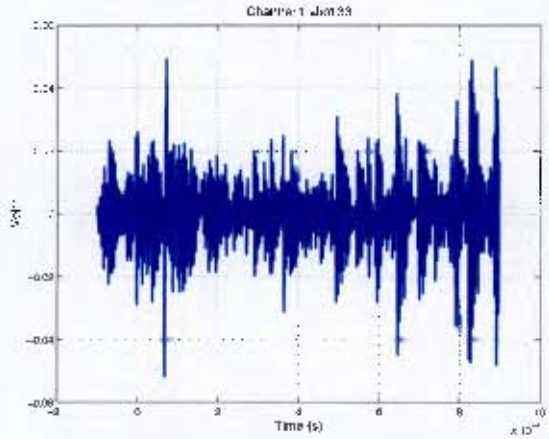

Figure H.55. Channel 1 100g at 6m

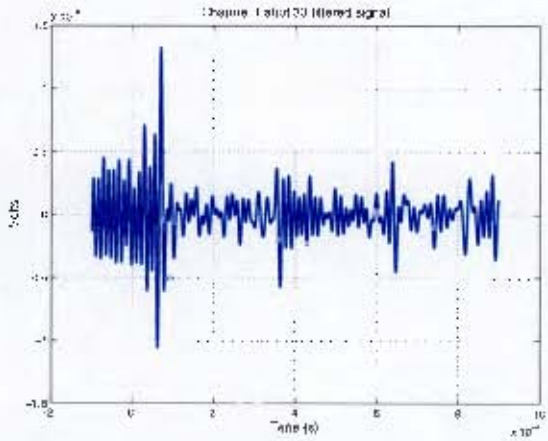

Figure H.56. Channel 1 100g at 6m filtered

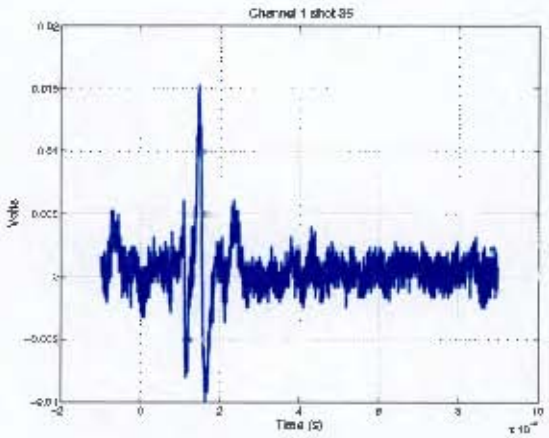

Figure H.57. Channel 1 60g at 8m

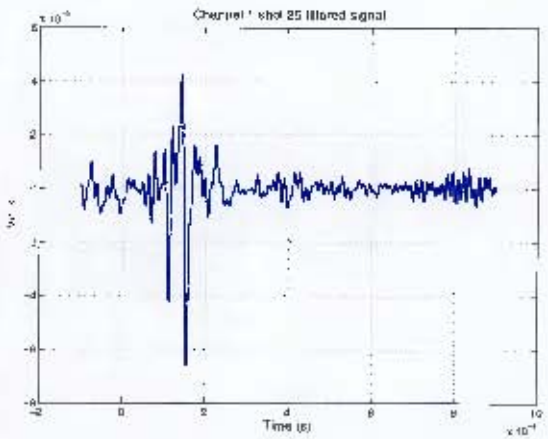

Figure H.58. Channel 1 60g at 8m filtered

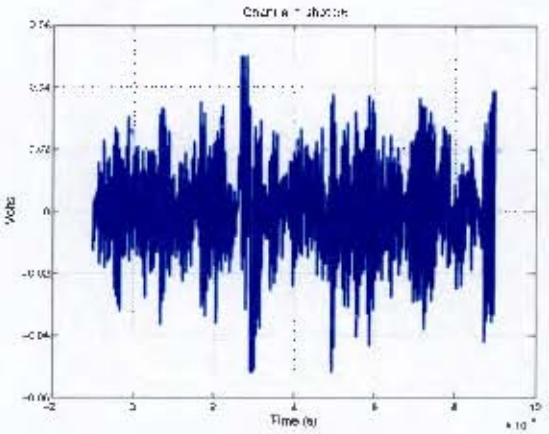

Figure H.59. Channel 1 60g at 8m

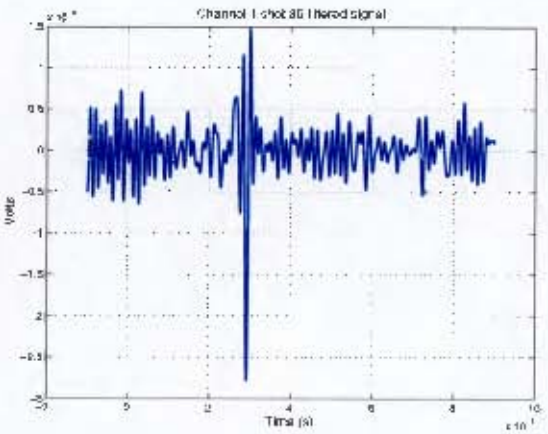

Figure H.60. Channel 1 60g at 8m filtered

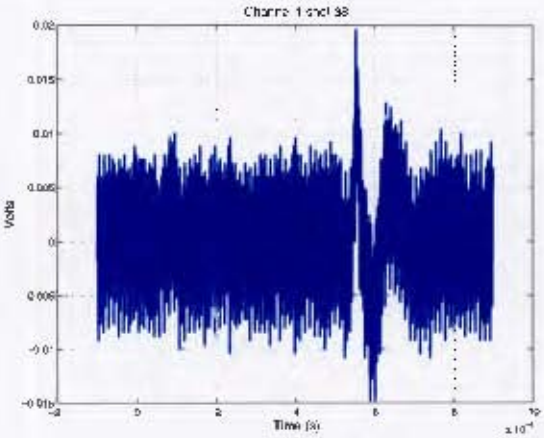

Figure H.61. Channel 1 80g at 8m

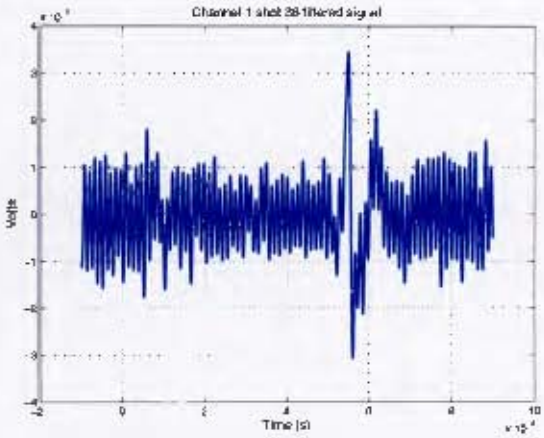

Figure H.62. Channel 1 80g at 8m filtered

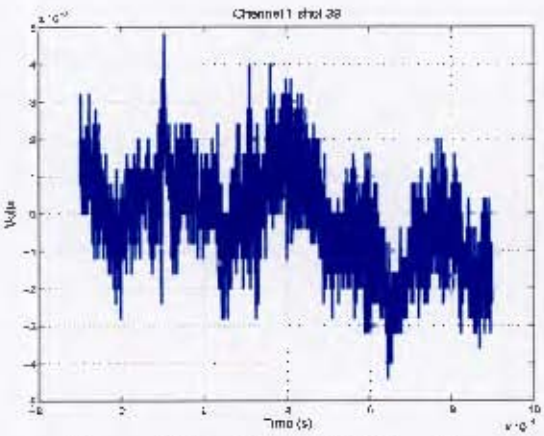

Figure H.63. Channel 1 100g at 8m

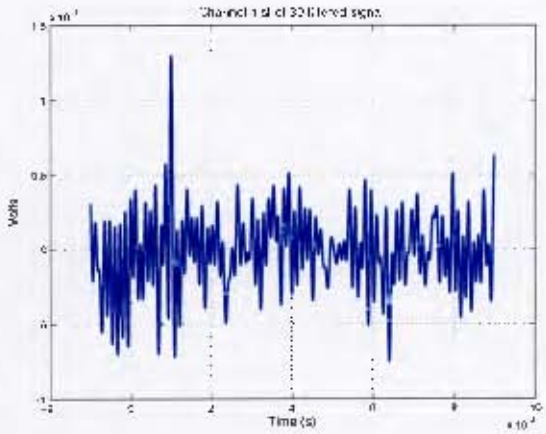

Figure H.64. Channel 1 100g at 8m filtered

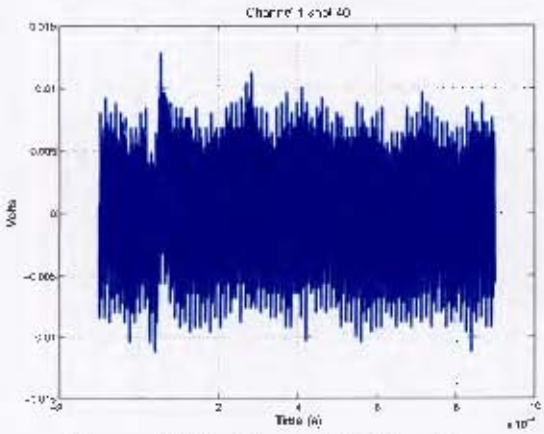

Figure H.65. Channel 1 100g at 8m

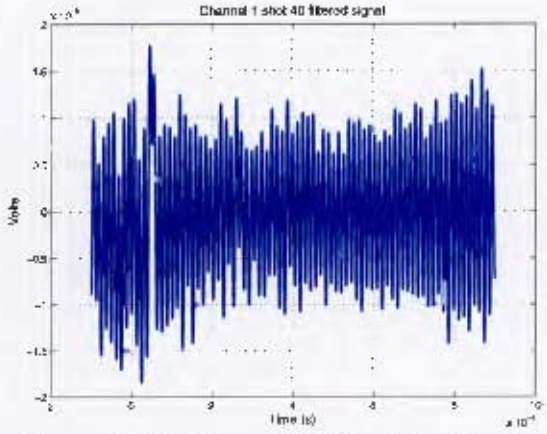

Figure H.66. Channel 1 100g at 8m filtered

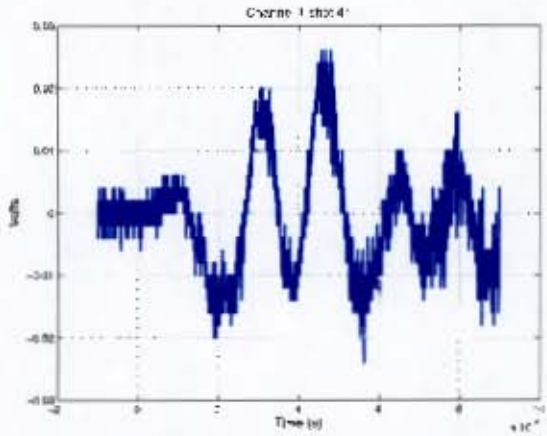

Figure H.67. Channel 1 2.9kg at 10m

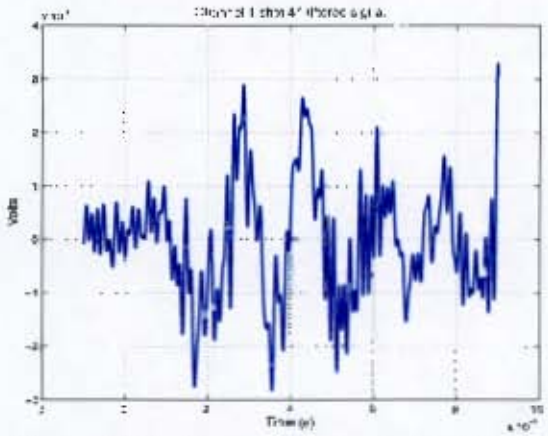

Figure H.68. Channel 1 2.9kg at 10m filtered

II.1.2 Channel 2

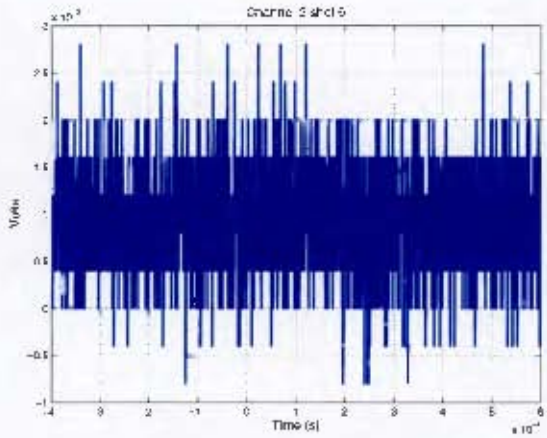

Figure H.69. Channel 2 20g at 2m

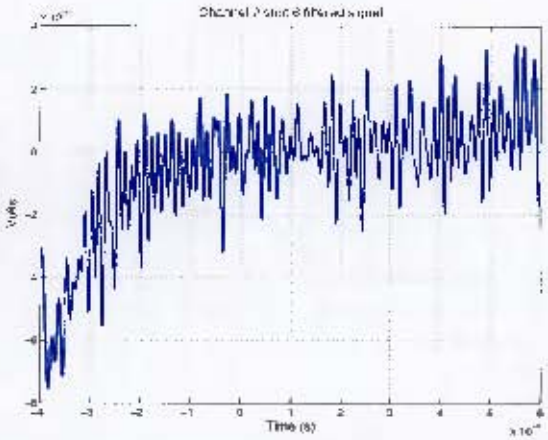

Figure H.70. Channel 2 20g at 2m filtered

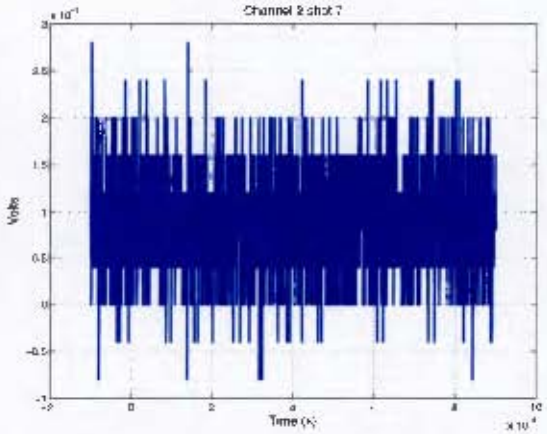

Figure H.71. Channel 2 20g at 2m

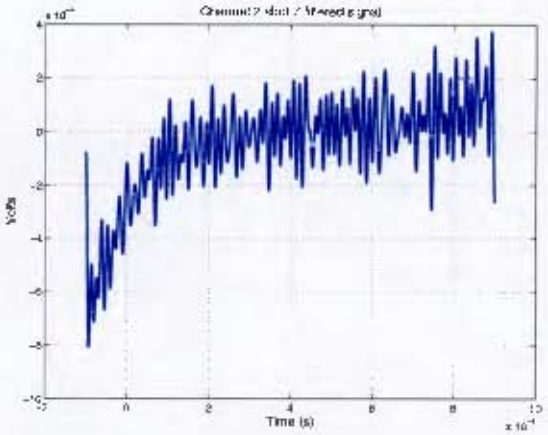

Figure H.72. Channel 2 20g at 2m filtered

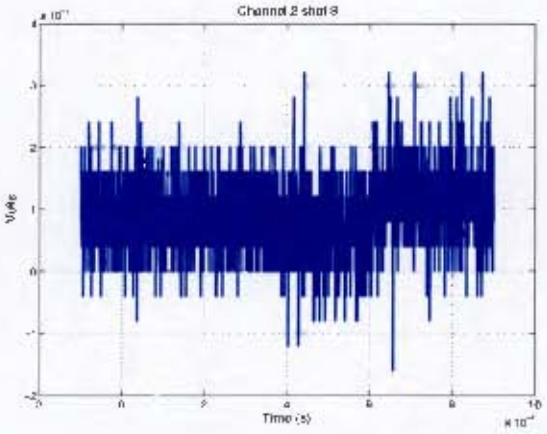

Figure H.73. Channel 2 40g at 2m

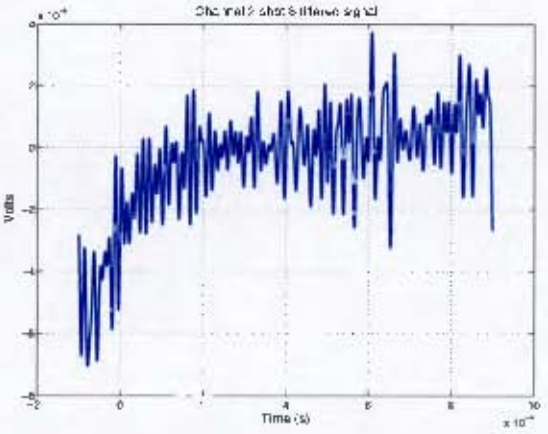

Figure H.74. Channel 2 40g at 2m filtered

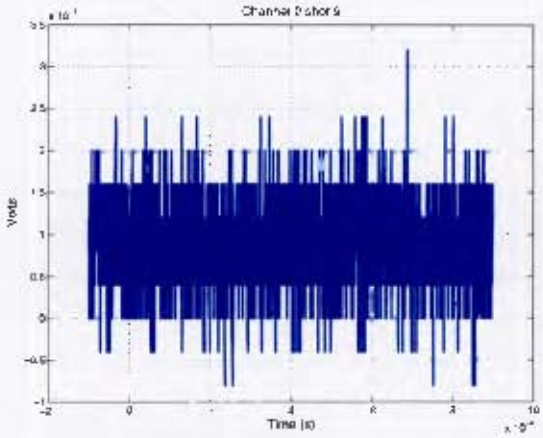

Figure H.75. Channel 2 40g at 2m

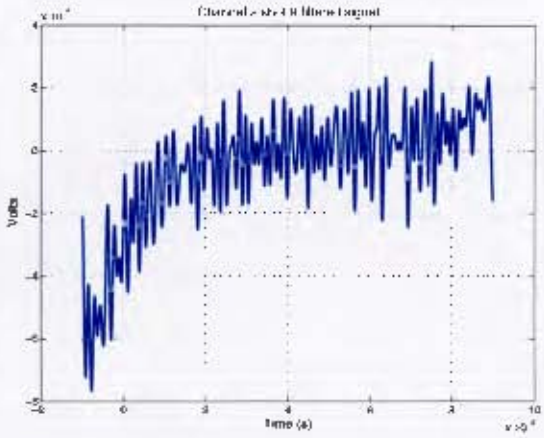

Figure H.76. Channel 2 40g at 2m filtered

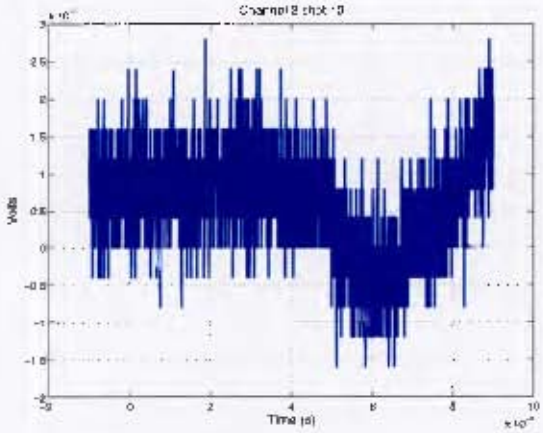

Figure H.77. Channel 2 60g at 2m

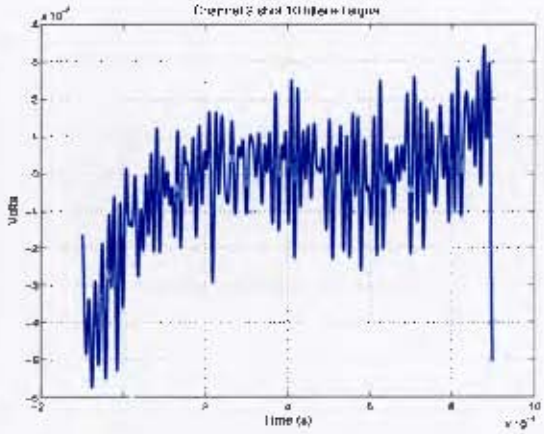

Figure H.78. Channel 2 60g at 2m filtered

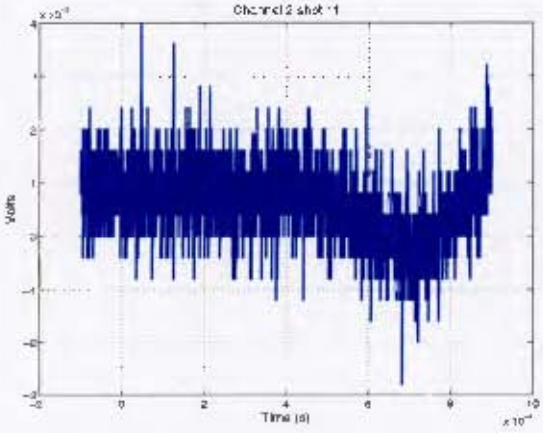

Figure H.79. Channel 2 60g at 2m

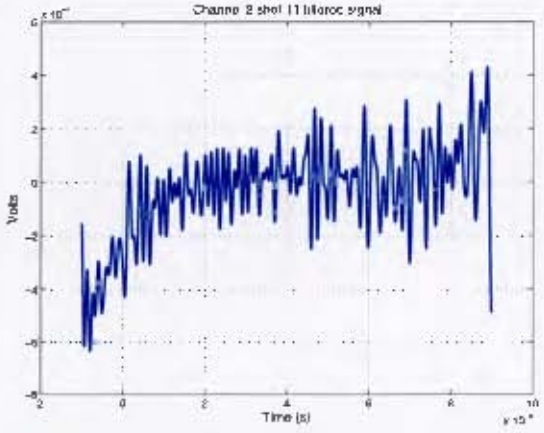

Figure H.80. Channel 2 60g at 2m filtered

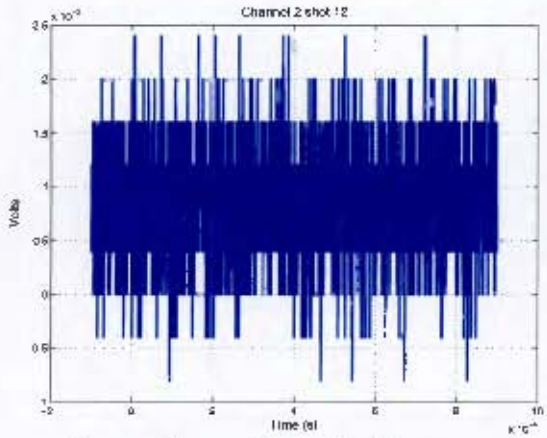

Figure H.81. Channel 2 80g at 2m

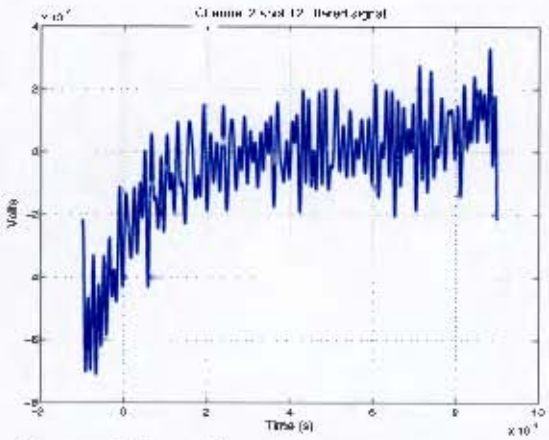

Figure H.82. Channel 2 80g at 2m filtered

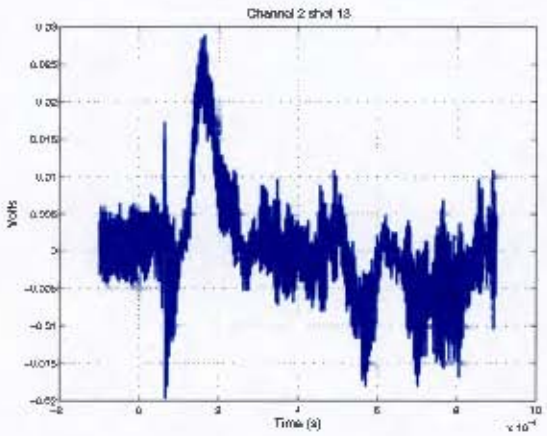

Figure H.83. Channel 2 80g at 2m

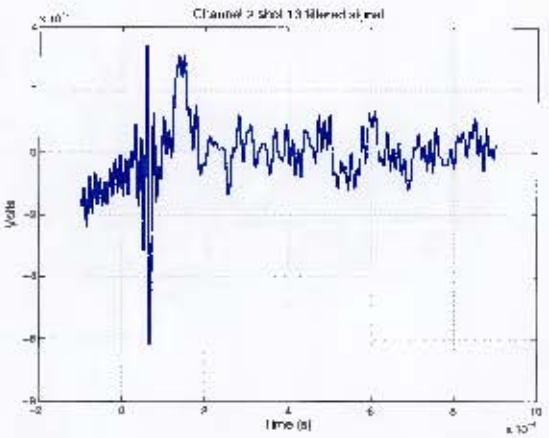

Figure H.84. Channel 2 80g at 2m filtered

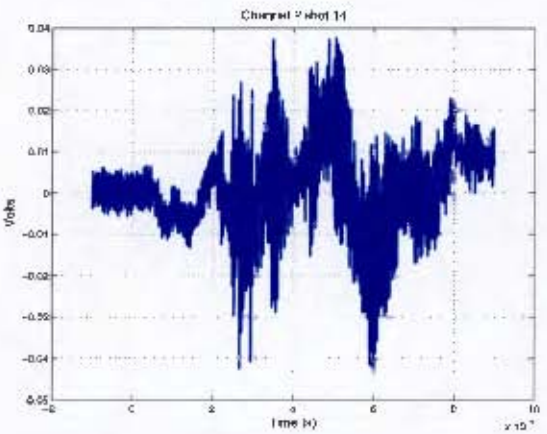

Figure H.85. Channel 2 100g at 2m

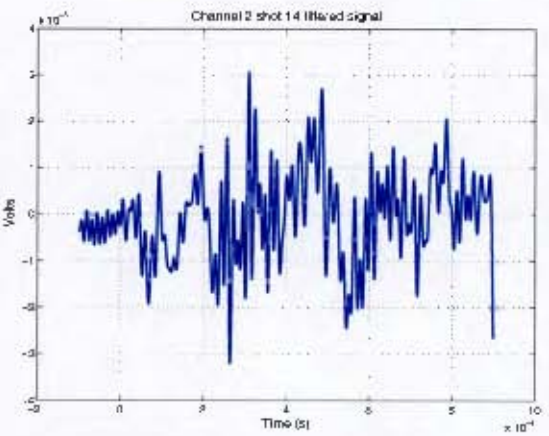

Figure H.86. Channel 2 100g at 2m filtered

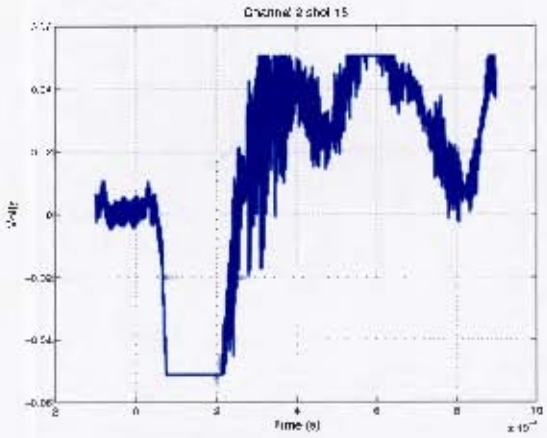

Figure H.87. Channel 2 100g at 2m

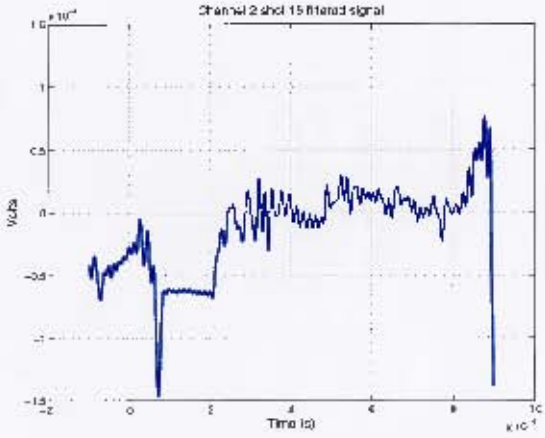

Figure H.88. Channel 2 100g at 2m filtered

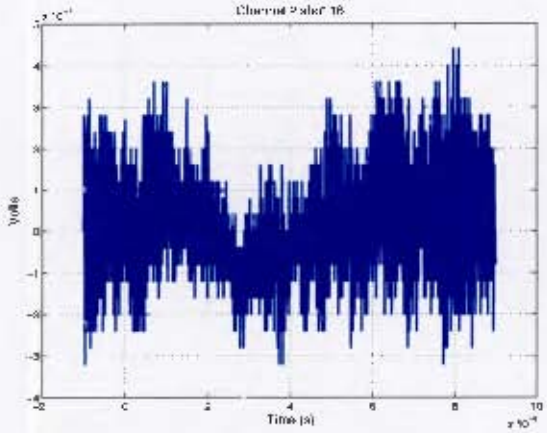

Figure H.89. Channel 2 20g at 4m

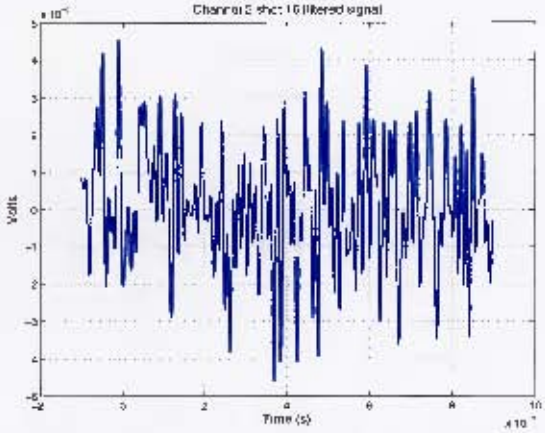

Figure H.90. Channel 2 20g at 4m filtered

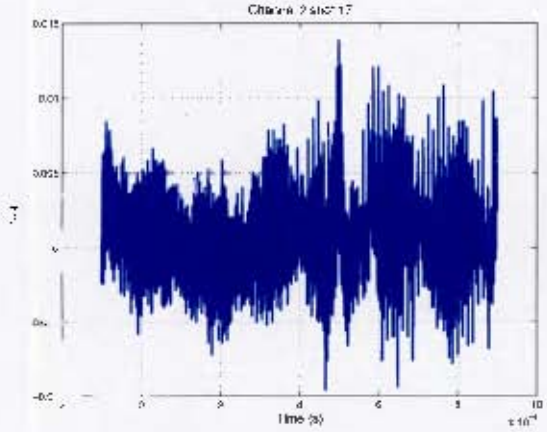

Figure H.91. Channel 2 20g at 4m

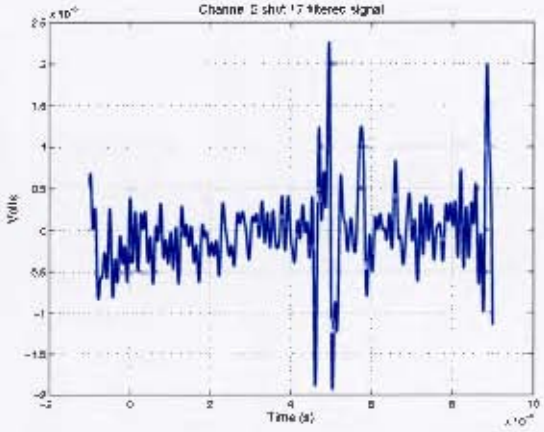

Figure H.92. Channel 2 20g at 4m filtered

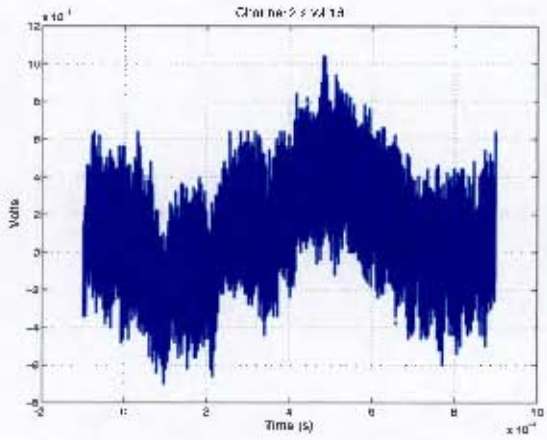

Figure H.93. Channel 2 40g at 4m

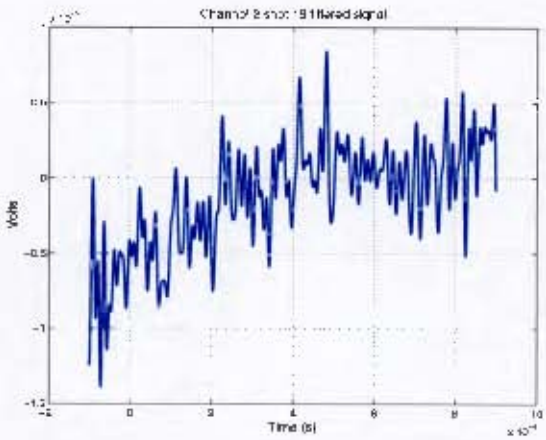

Figure H.94. Channel 2 40g at 4m filtered

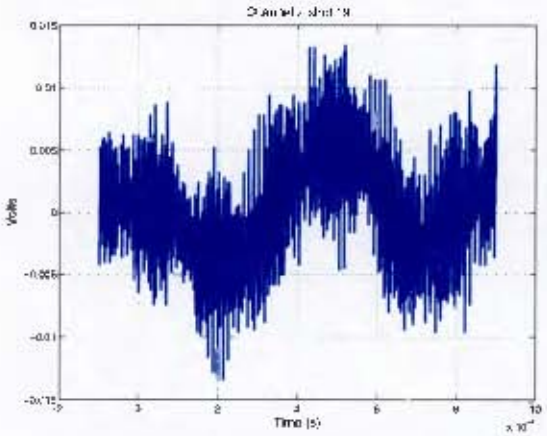

Figure H.95. Channel 2 40g at 4m

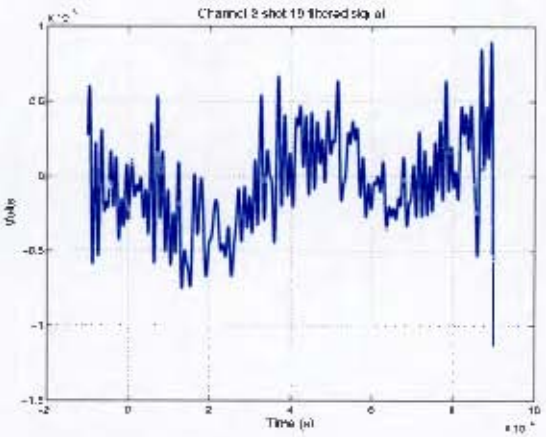

Figure H.96. Channel 2 40g at 4m filtered

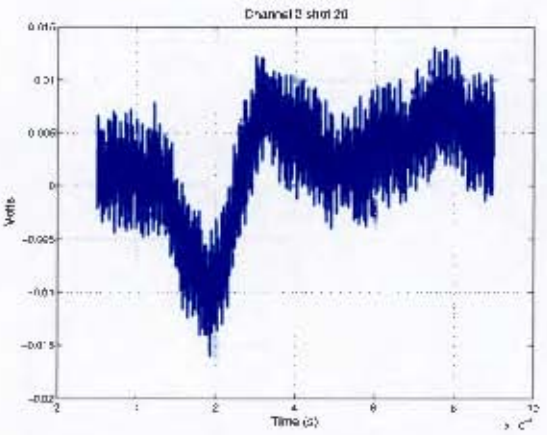

Figure H.97. Channel 2 60g at 4m

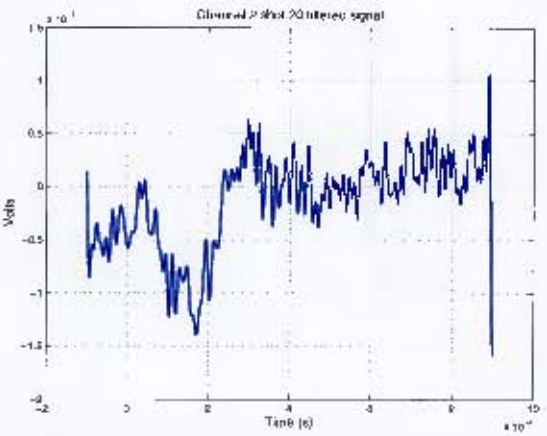

Figure H.98. Channel 2 60g at 4m filtered

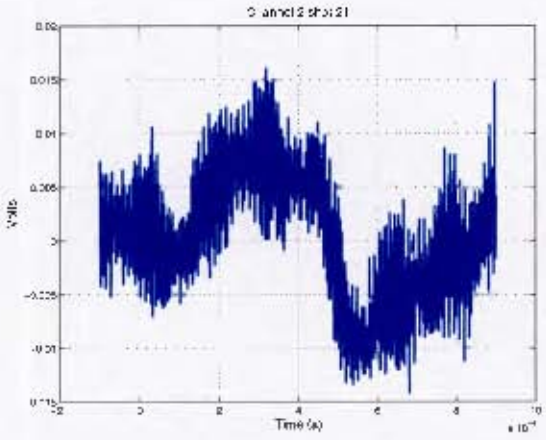

Figure H.99. Channel 2 60g at 4m

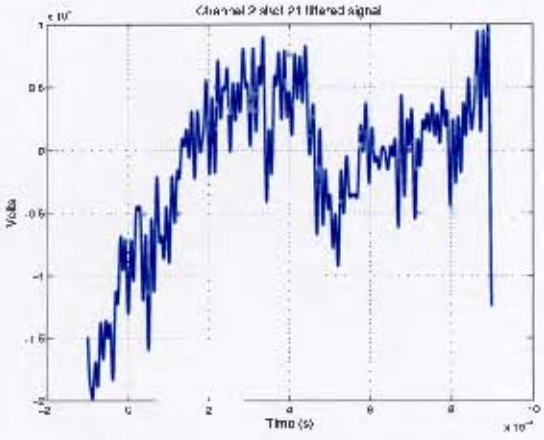

Figure H.100. Channel 2 60g at 4m filtered

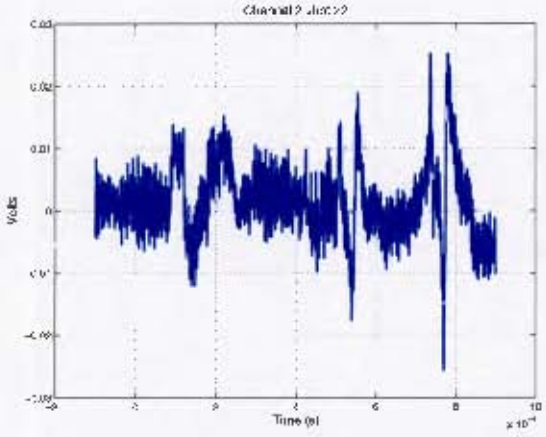

Figure H.101. Channel 2 80g at 4m

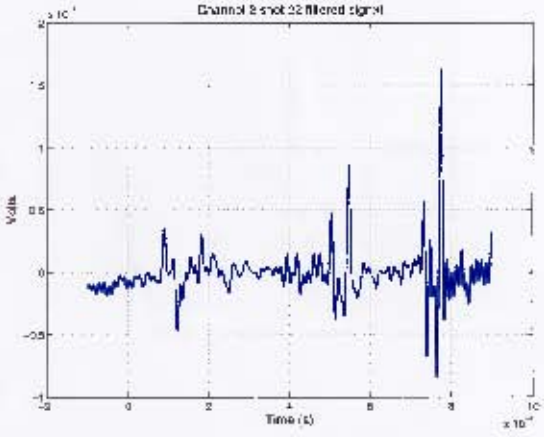

Figure H.102. Channel 2 80g at 4m filtered

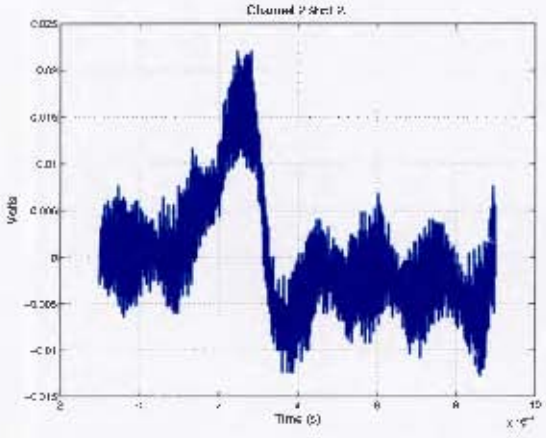

Figure H.103. Channel 2 80g at 4m

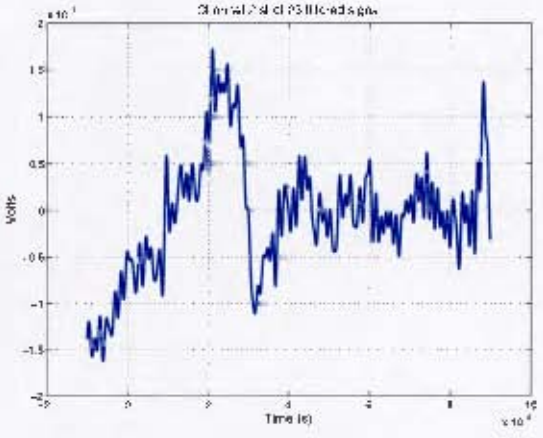

Figure H.104. Channel 2 80g at 4m filtered

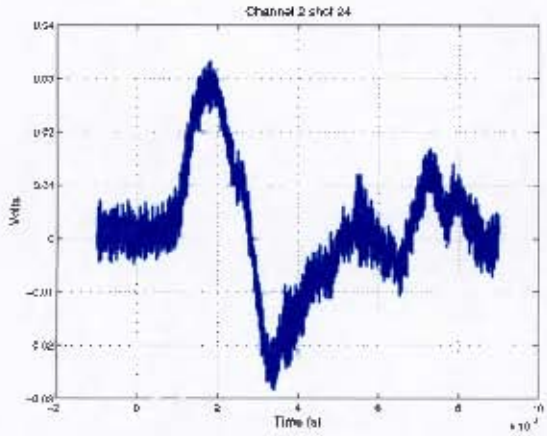

Figure H.105. Channel 2 100g at 4m

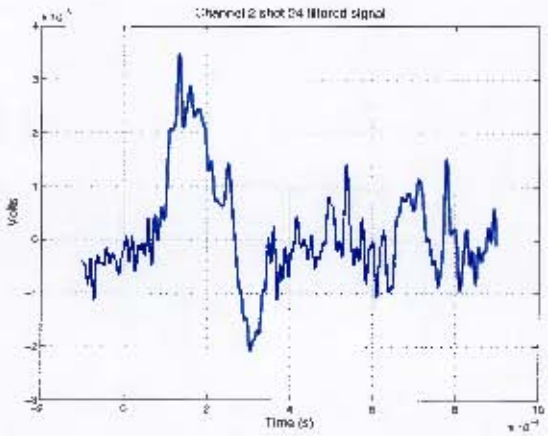

Figure H.106. Channel 2 100g at 4m filtered

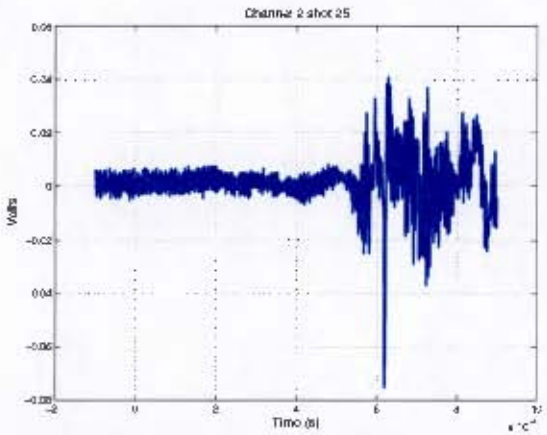

Figure H.107. Channel 2 100g at 4m

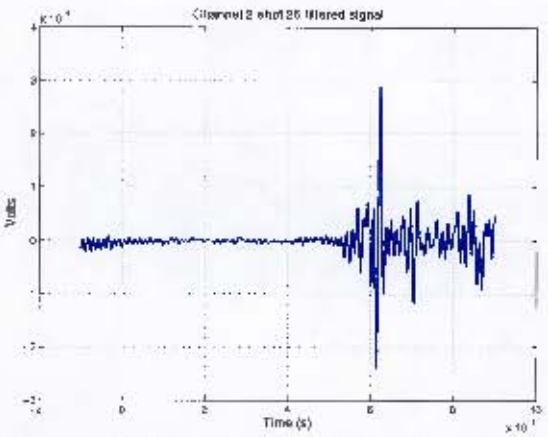

Figure H.108. Channel 2 100g at 4m filtered

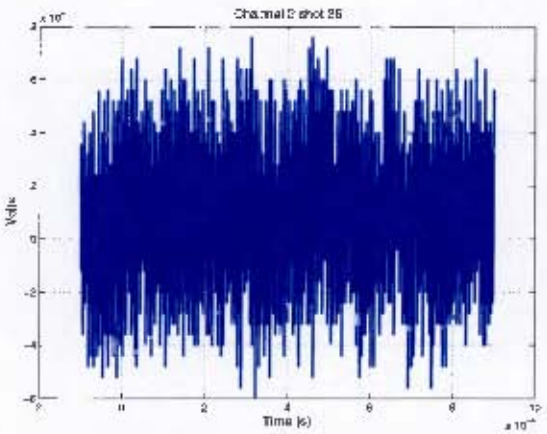

Figure H.109. Channel 40g at 6m

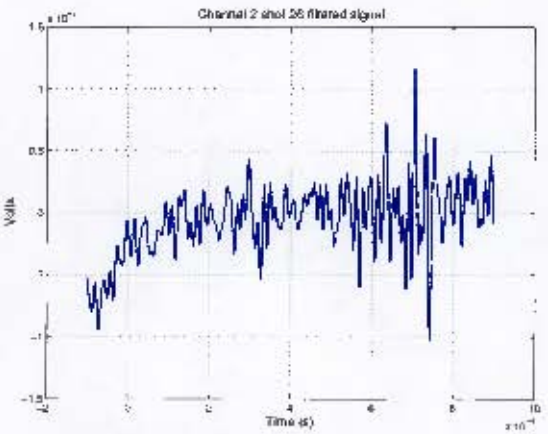

Figure H.110. Channel 2 40g at 6m filtered

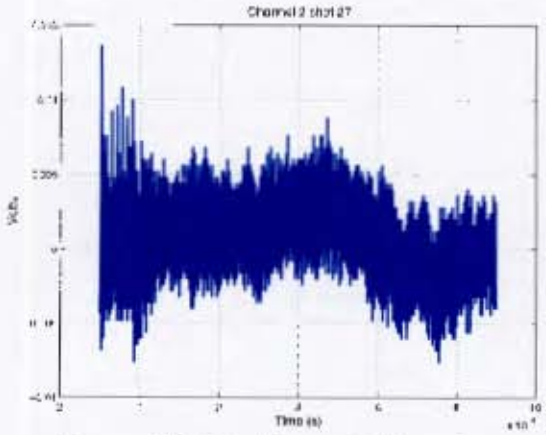

Figure H.111. Channel 2 40g at 6m

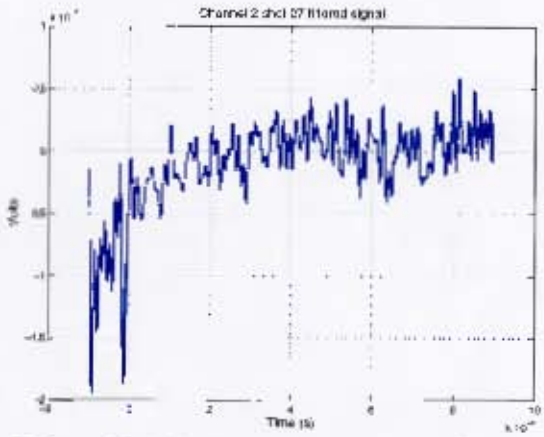

Figure H.112. Channel 2 40g at 6m filtered

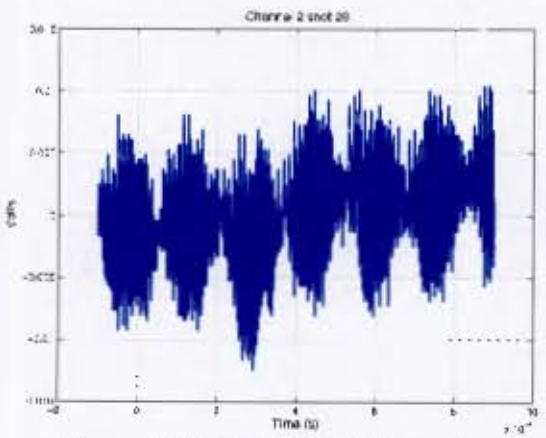

Figure H.113. Channel 2 60g at 6m

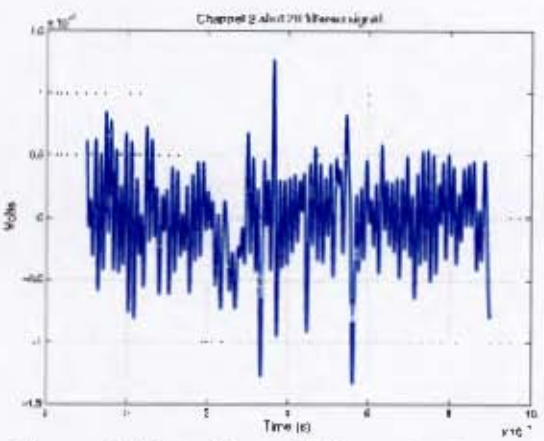

Figure H.114. Channel 2 60g at 6m filtered

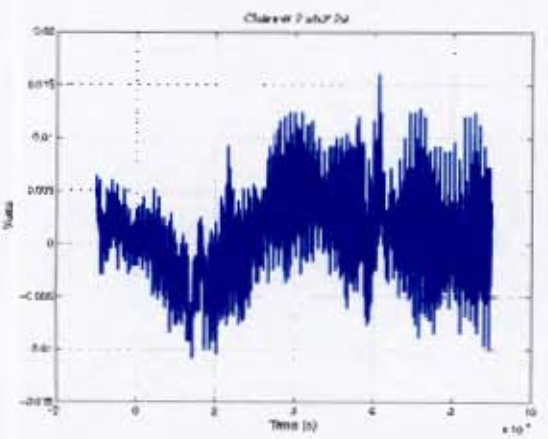

Figure H.115. Channel 2 60g at 6m

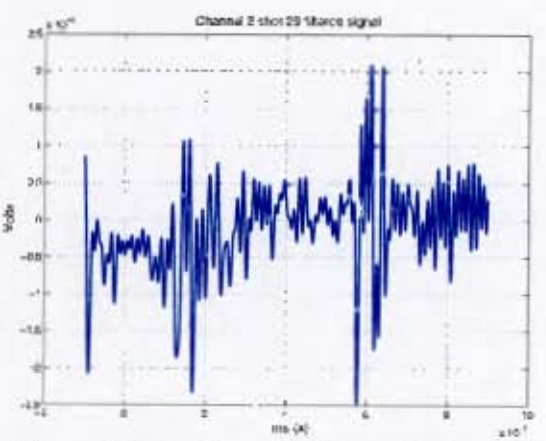

Figure H.116. Channel 2 60g at 6m filtered

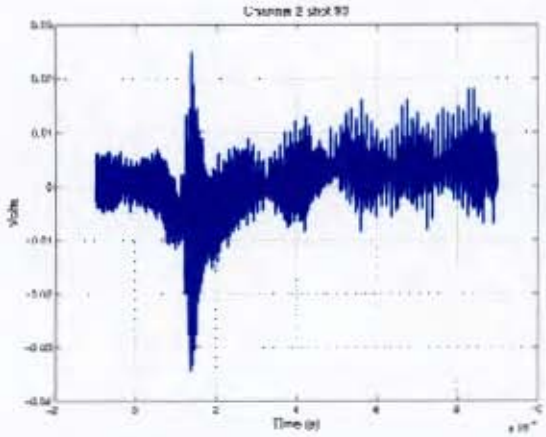

Figure H.117. Channel 2 80g at 6m

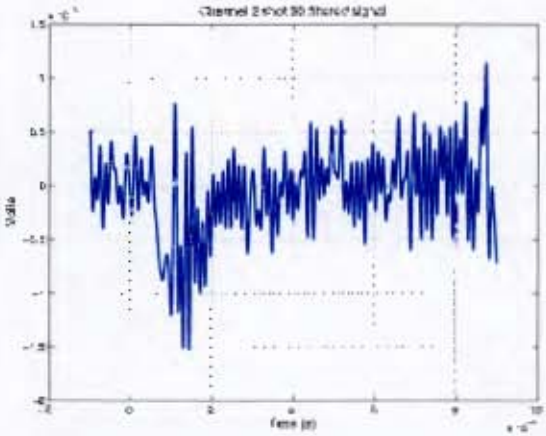

Figure H.118. Channel 2 80g at 6m filtered

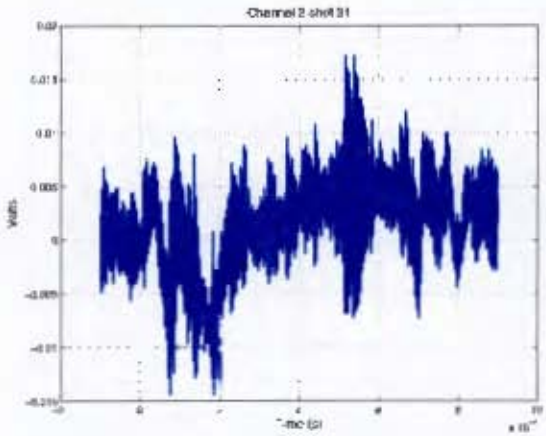

Figure H.119. Channel 2 80g at 6m

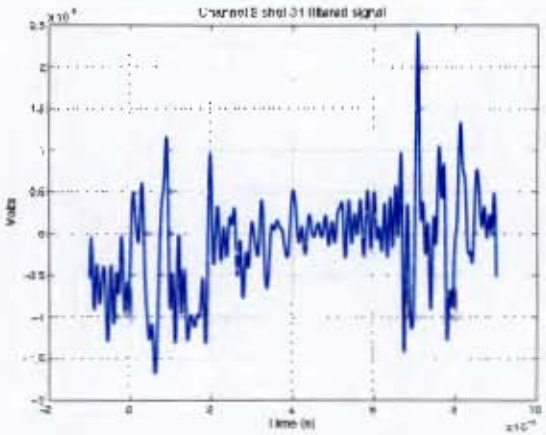

Figure H.120. Channel 2 80g at 6m filtered

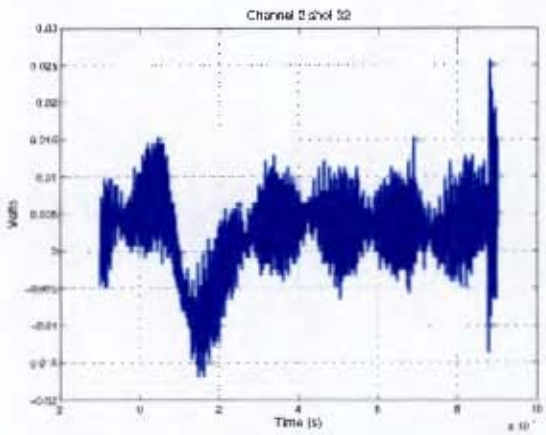

Figure H.121. Channel 2 100g at 6m

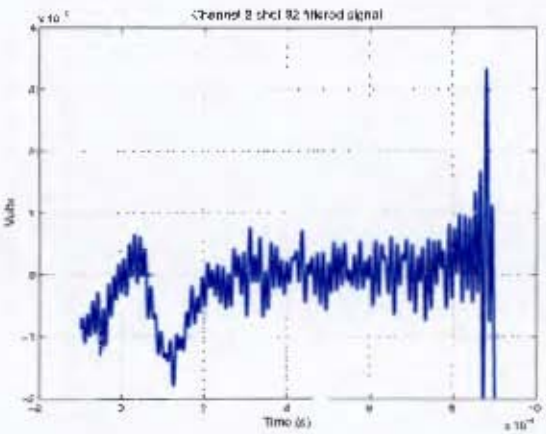

Figure H.122. Channel 2 100g at 6m filtered

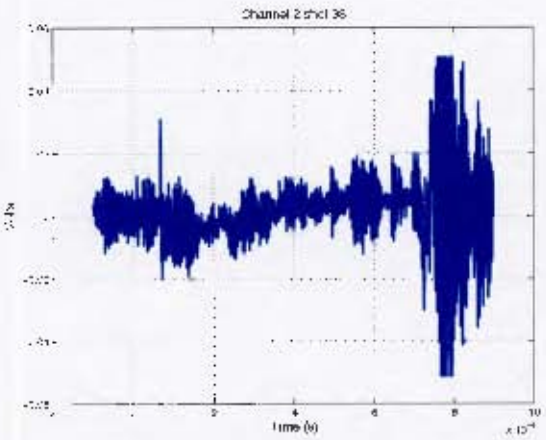

Figure H.123. Channel 2 100g at 6m

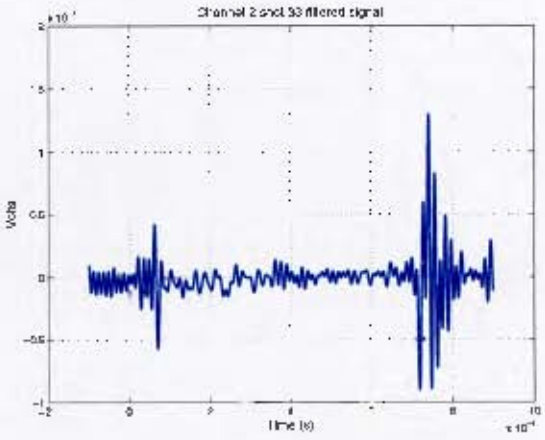

Figure H.124. Channel 2 100g at 6m filtered

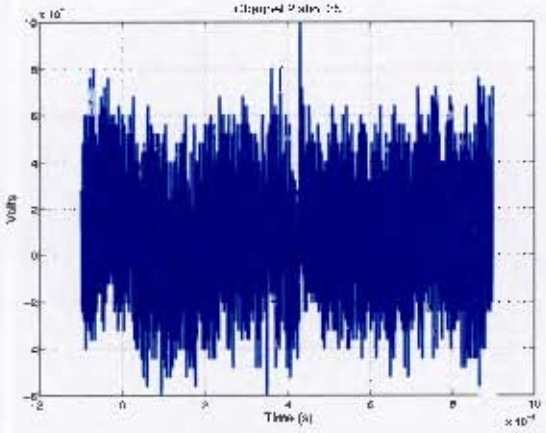

Figure H.125. Channel 2 60g at 8m

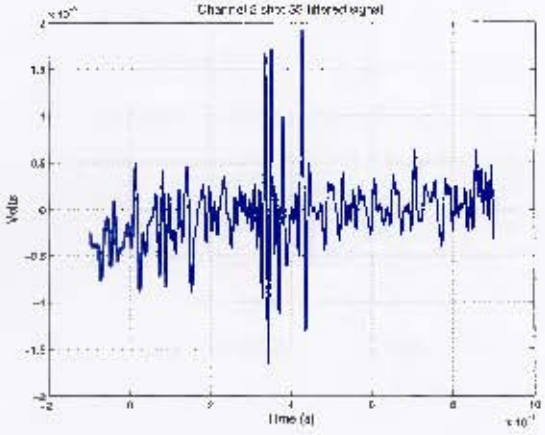

Figure H.126. Channel 2 60g at 8m filtered

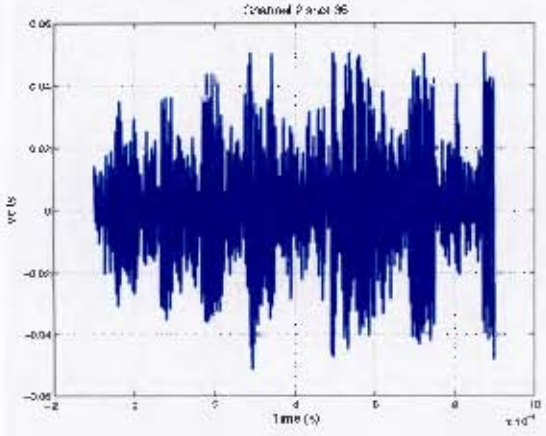

Figure H.127. Channel 2 60g at 8m

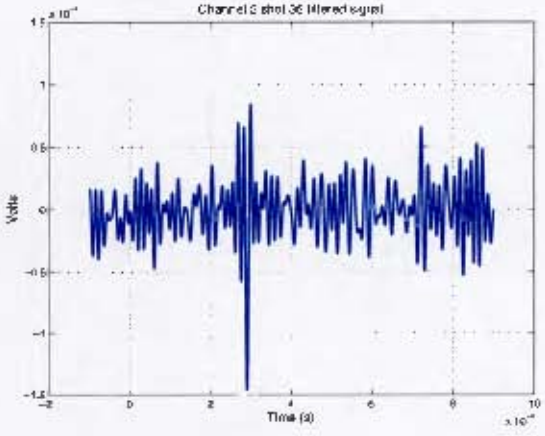

Figure H.128. Channel 2 60g at 8m filtered

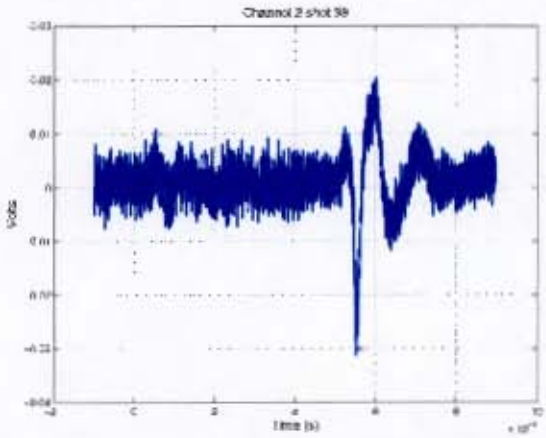

Figure H.129. Channel 2 80g at 8m

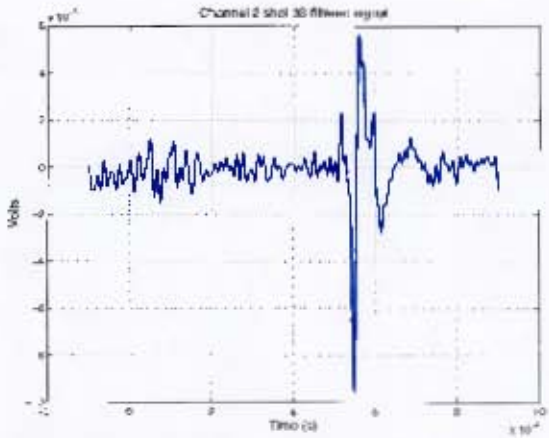

Figure H.130. Channel 2 80g at 8m filtered

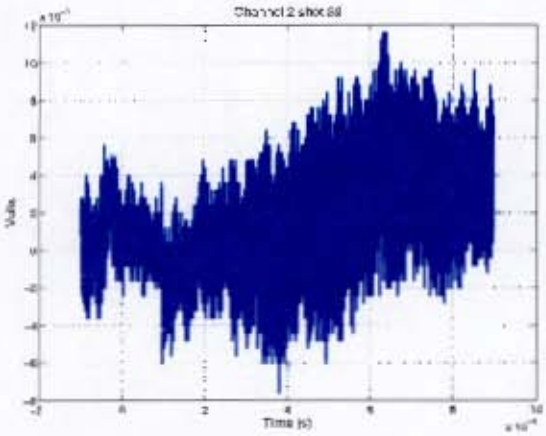

Figure H.131. Channel 2 100g at 8m

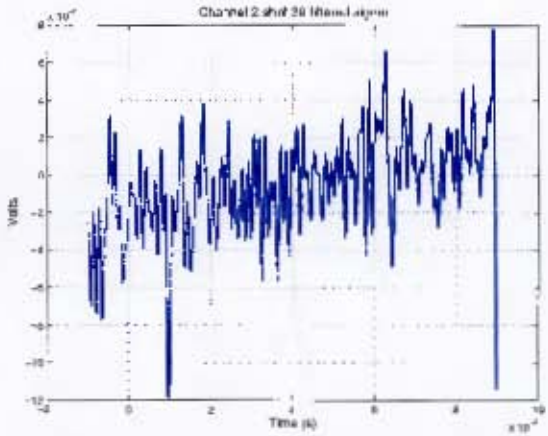

Figure H.132. Channel 2 100g at 8m filtered

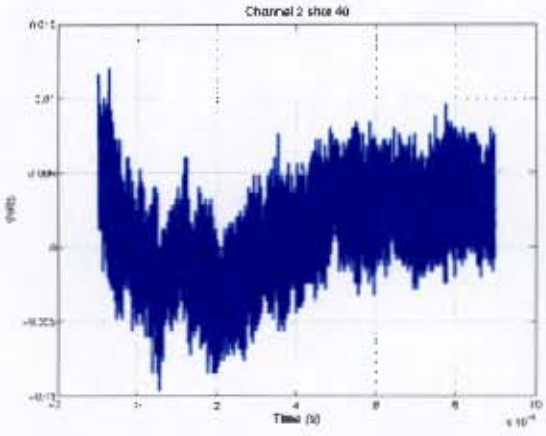

Figure H.133. Channel 2 100g at 8m

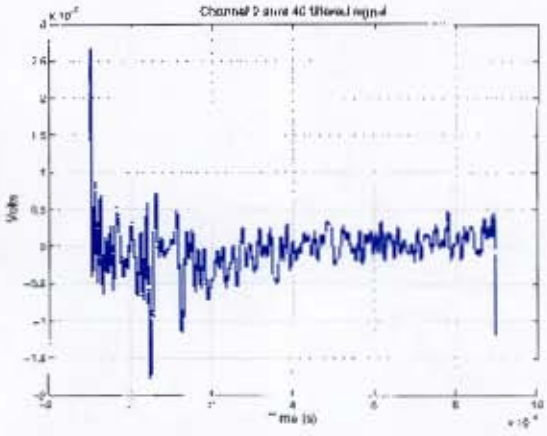

Figure H.134. Channel 2 100g at 8m filtered

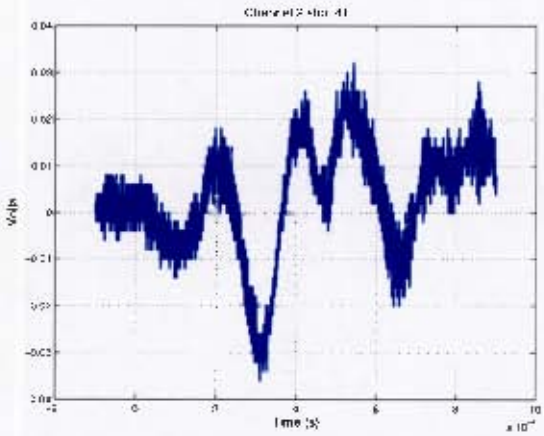

Figure H.135. Channel 2 2.9kg at 10m

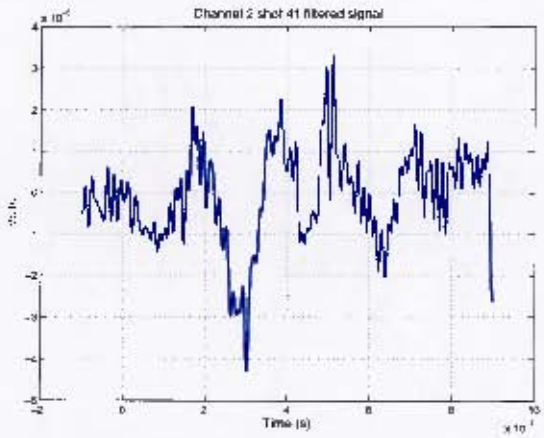

Figure H.136. Channel 2 2.9kg at 10m filtered

H.1.3 Channel 3

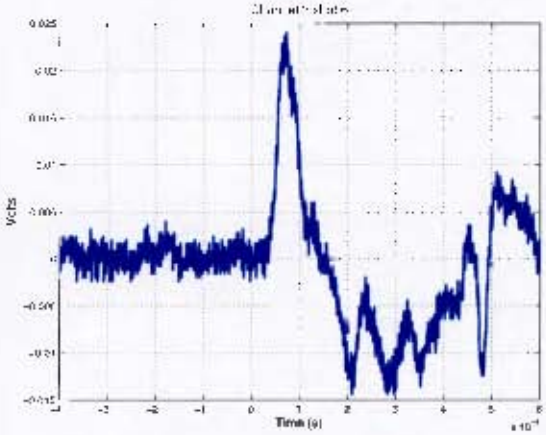

Figure H.137. Channel 3 20g at 2m

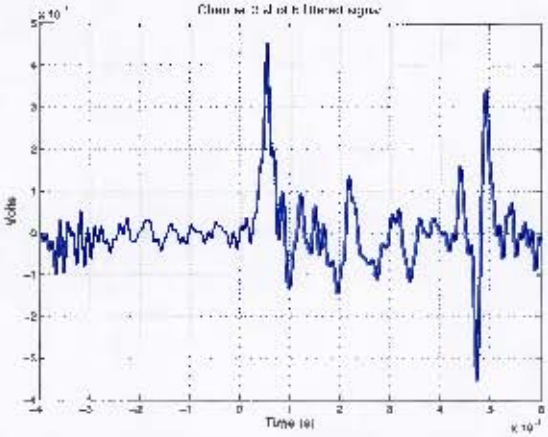

Figure H.138. Channel 3 20g at 2m filtered

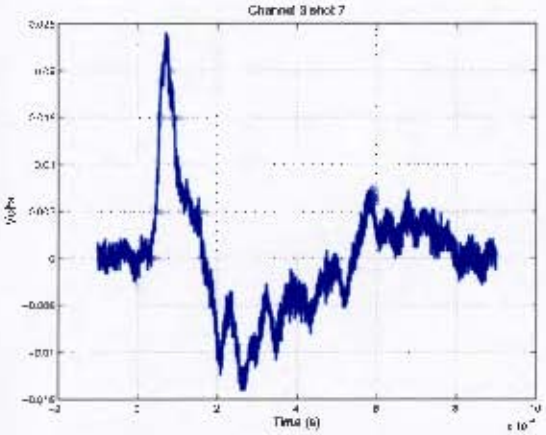

Figure H.139. Channel 3 20g at 2m

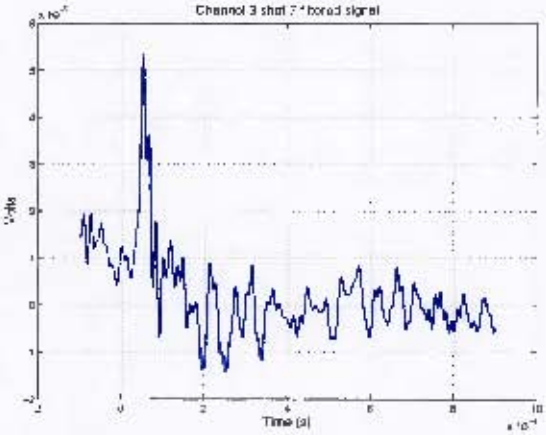

Figure H.140. Channel 3 20g at 2m filtered

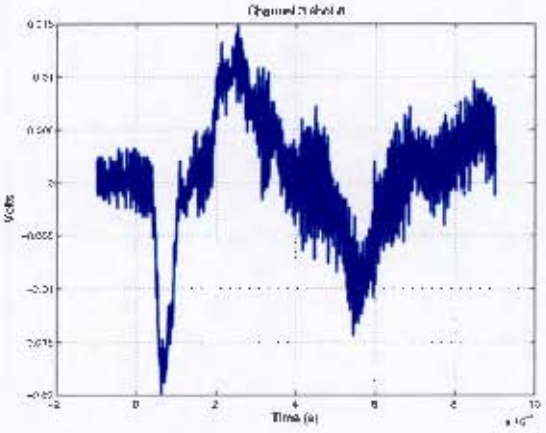

Figure H.141. Channel 3 40g at 2m

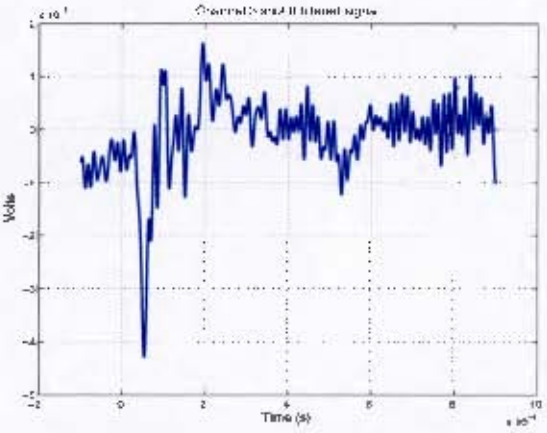

Figure H.142. Channel 3 40g at 2m filtered

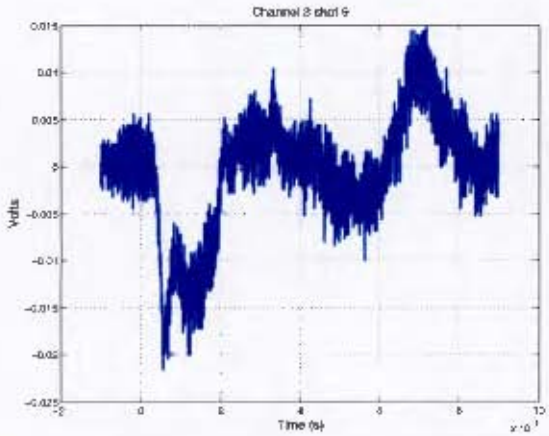

Figure H.143. Channel 3 40g at 2m

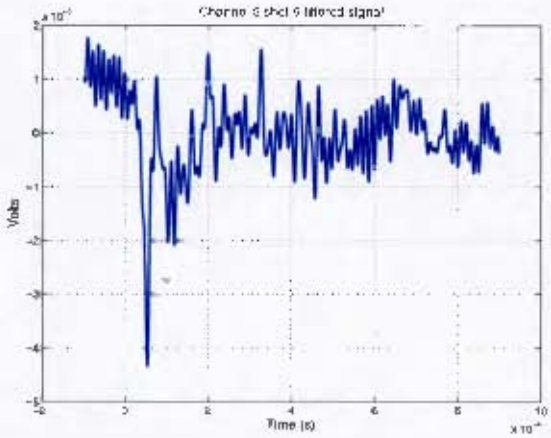

Figure H.144. Channel 3 40g at 2m filtered

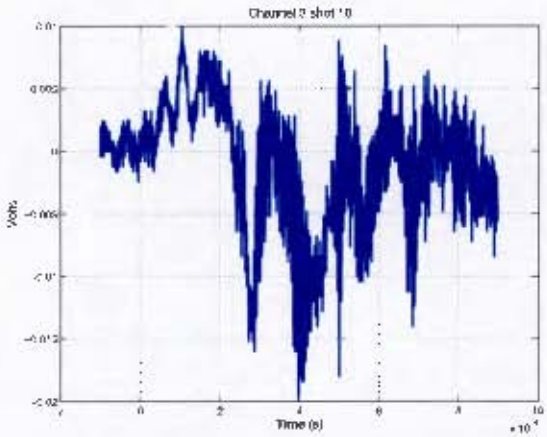

Figure H.145. Channel 3 60g at 2m

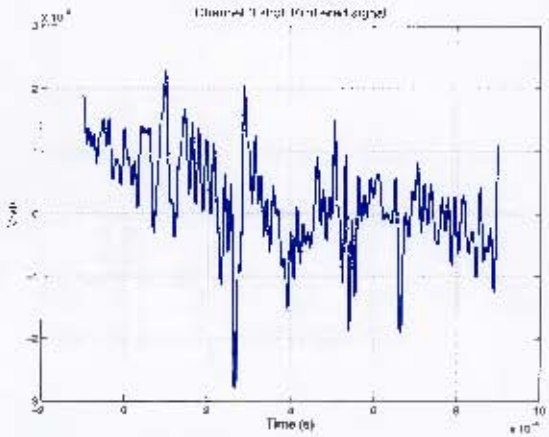

Figure H.146. Channel 3 60g at 2m filtered

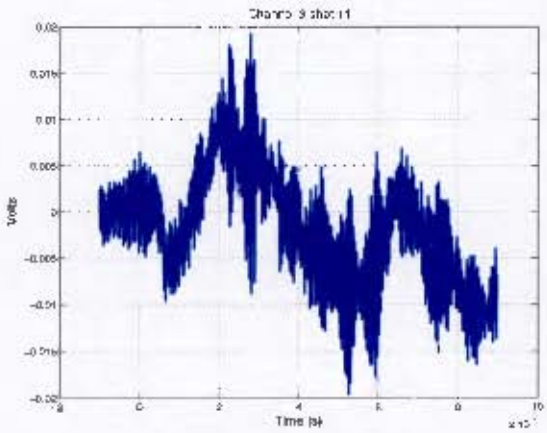

Figure H.147. Channel 3 60g at 2m

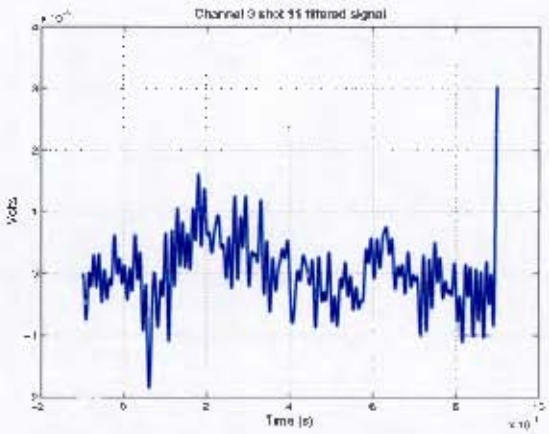

Figure H.148. Channel 3 60g at 2m filtered

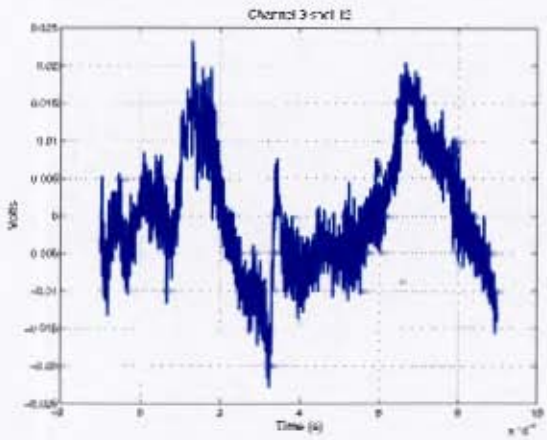

Figure H.149. Channel 3 80g at 2m

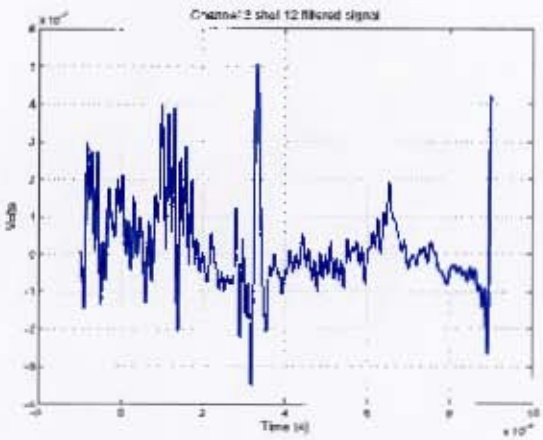

Figure H.150. Channel 3 80g at 2m filtered

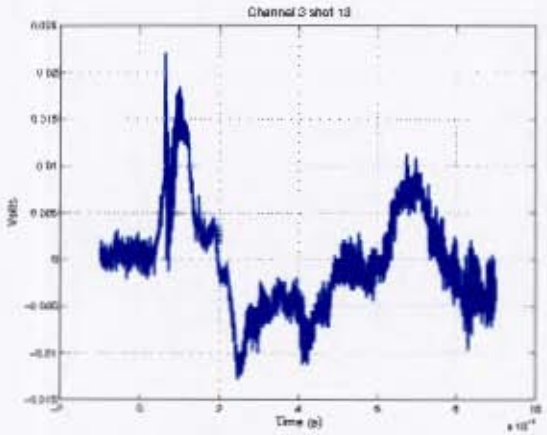

Figure H.151. Channel 3 80g at 2m

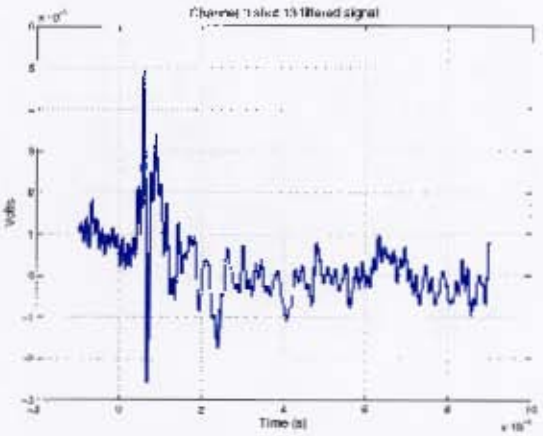

Figure H.152. Channel 3 80g at 2m filtered

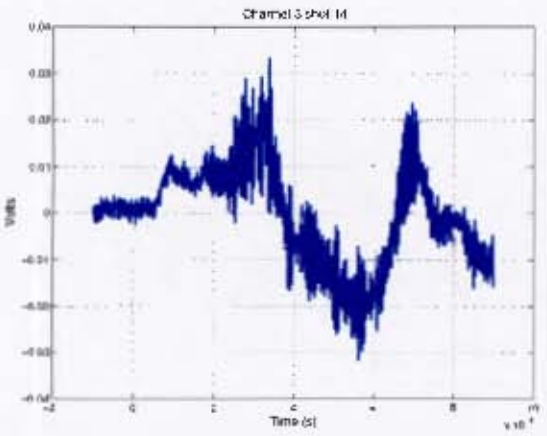

Figure H.153. Channel 3 100g at 2m

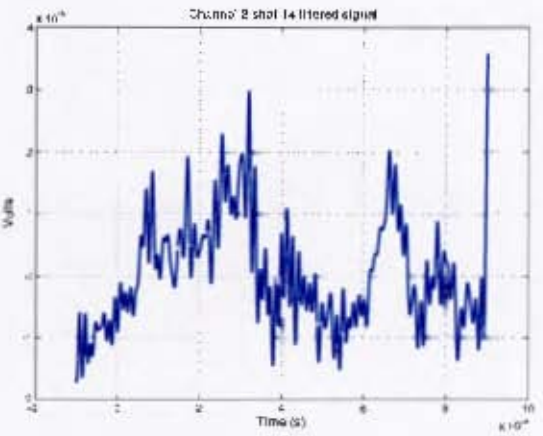

Figure H.154. Channel 3 100g at 2m filtered

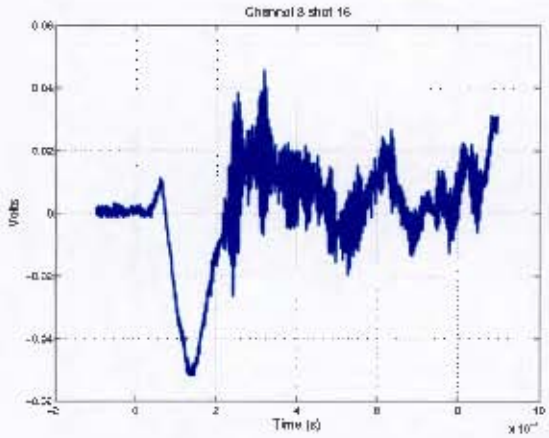

Figure H.155. Channel 3 100g at 2m

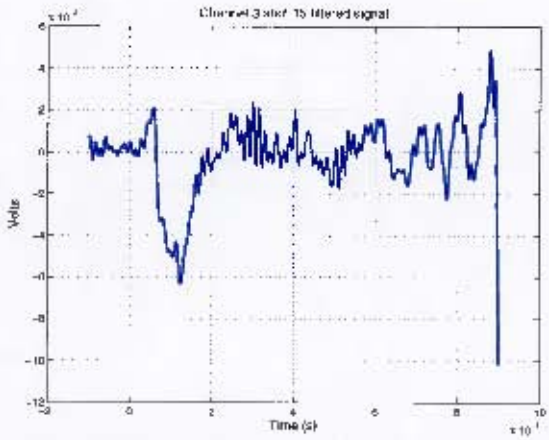

Figure H.156. Channel 3 100g at 2m filtered

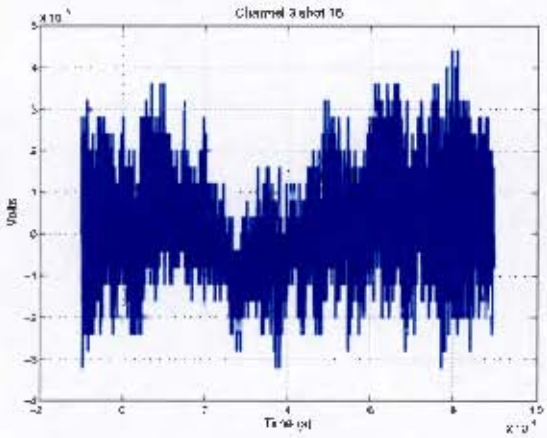

Figure H.157. Channel 3 20g at 4m

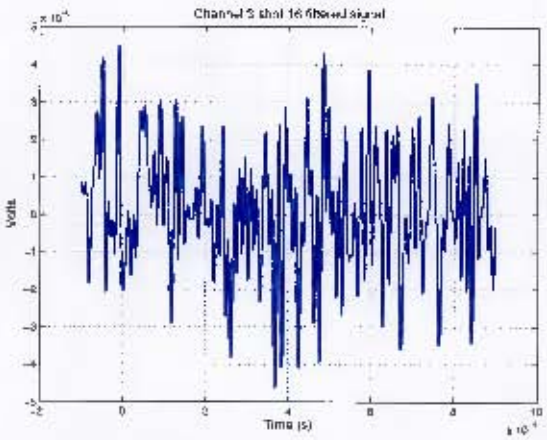

Figure H.158. Channel 3 20g at 4m filtered

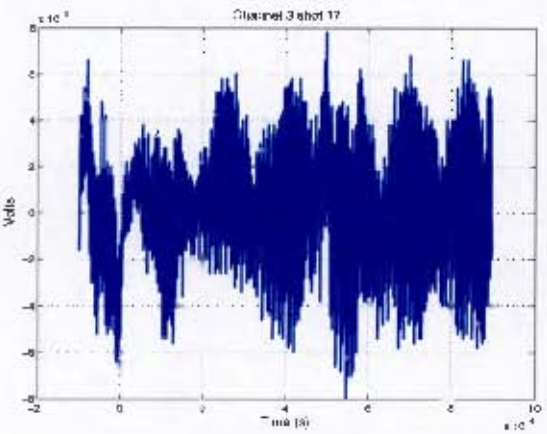

Figure H.159. Channel 3 20g at 4m

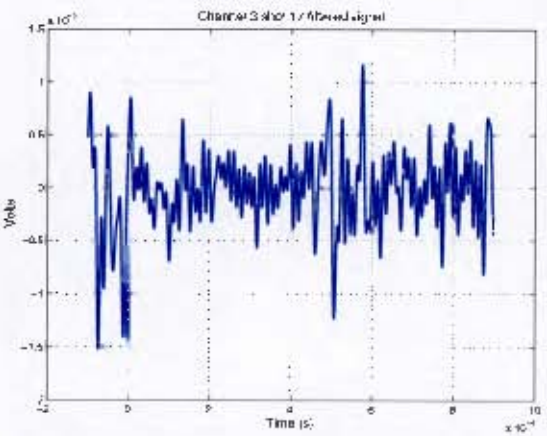

Figure H.160. Channel 3 20g at 4m filtered

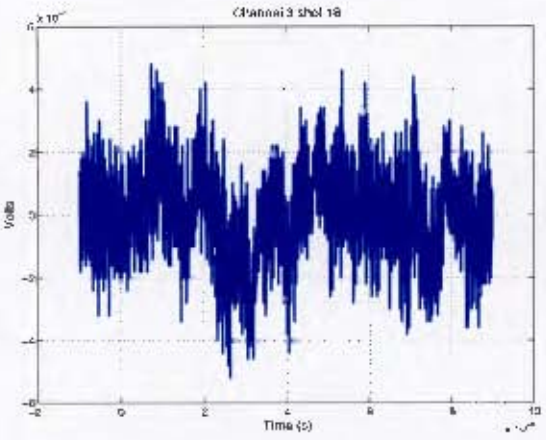

Figure H.161. Channel 3 40g at 4m

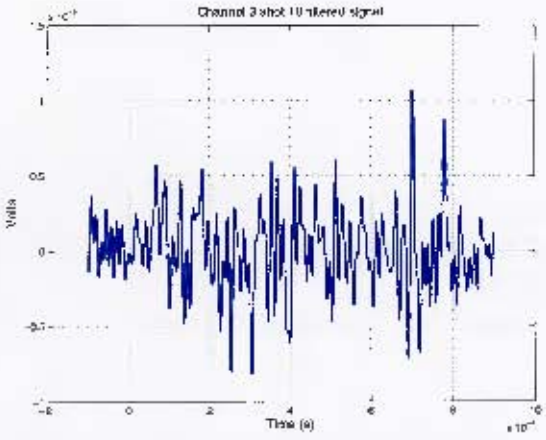

Figure H.162. Channel 3 40g at 4m filtered

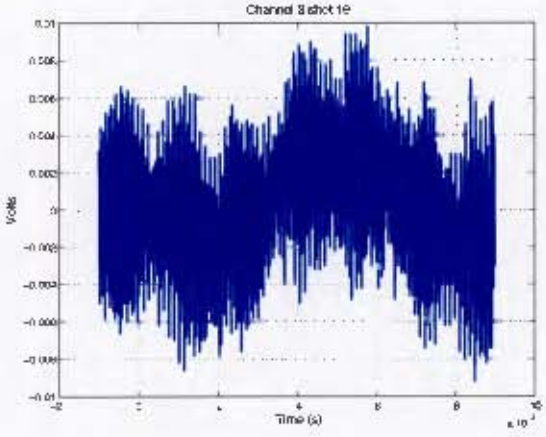

Figure H.163. Channel 3 40g at 4m

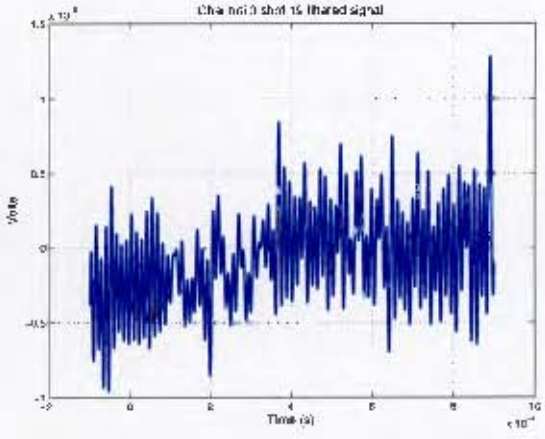

Figure H.164. Channel 3 40g at 4m filtered

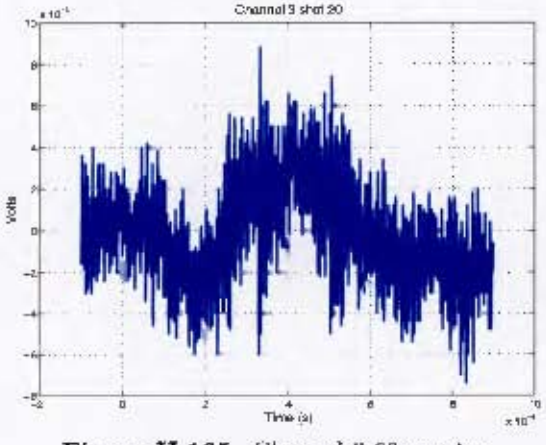

Figure H.165. Channel 3 60g at 4m

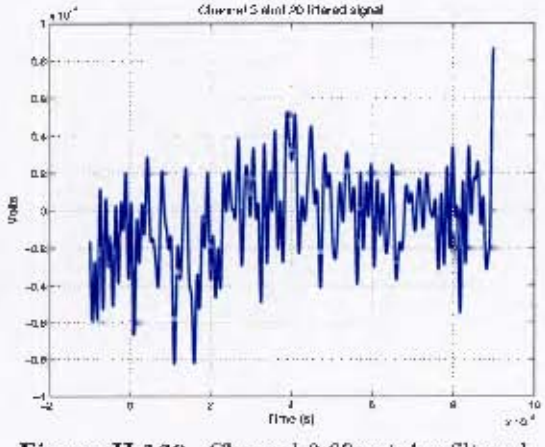

Figure H.166. Channel 3 60g at 4m filtered

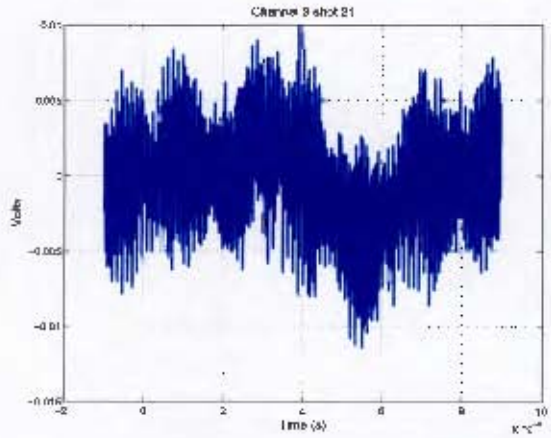

Figure H.167. Channel 3 60g at 4m

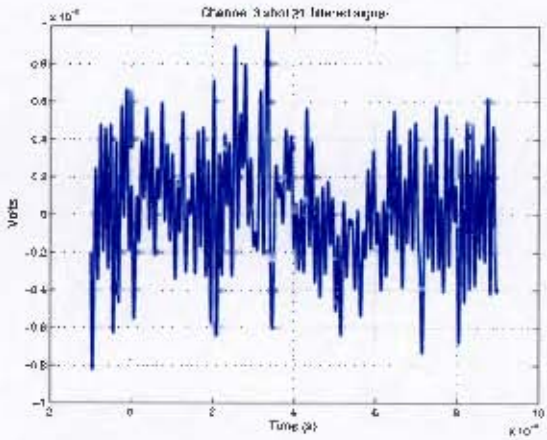

Figure H.168. Channel 3 60g at 4m filtered

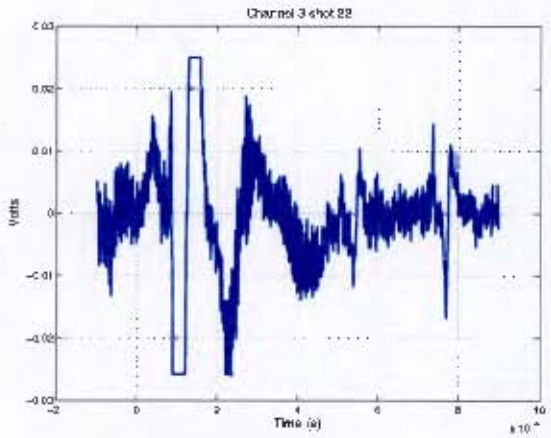

Figure H.169. Channel 3 80g at 4m

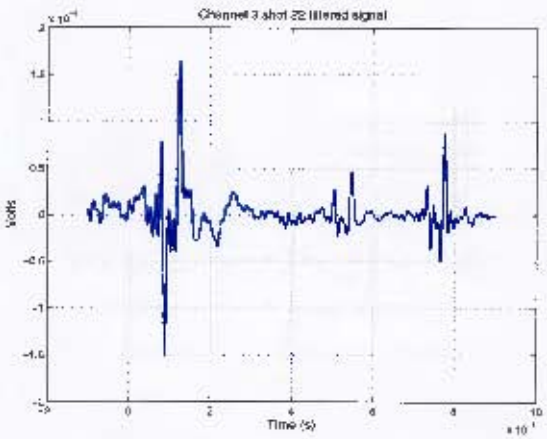

Figure H.170. Channel 3 80g at 4m filtered

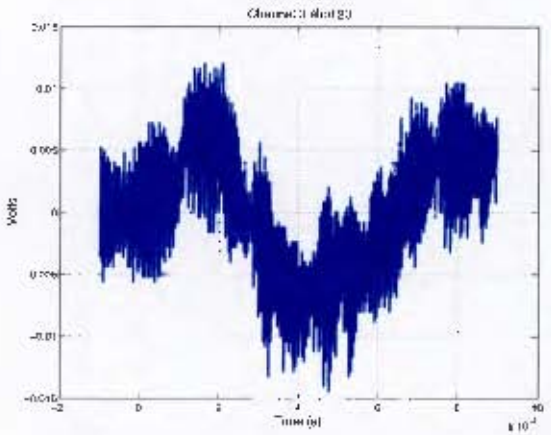

Figure H.171. Channel 3 80g at 4m

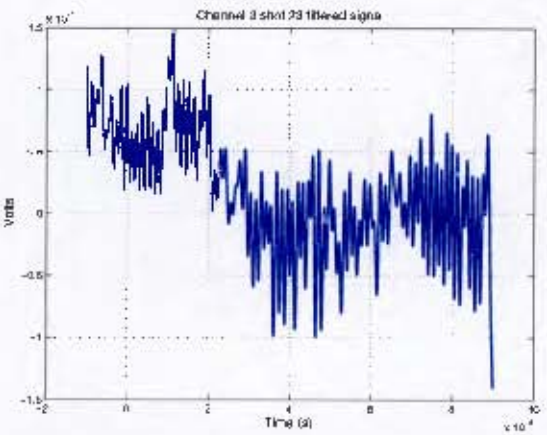

Figure H.172. Channel 3 80g at 4m filtered

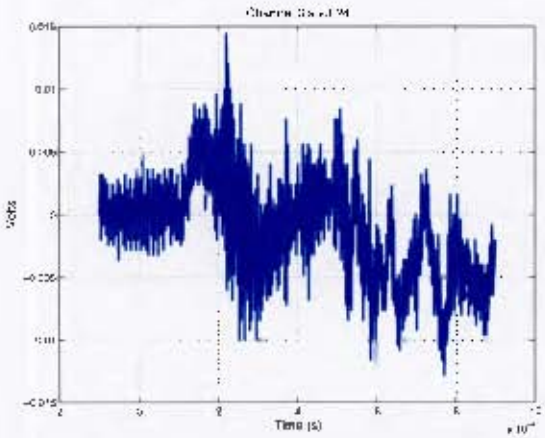

Figure H.173. Channel 3 100g at 4m

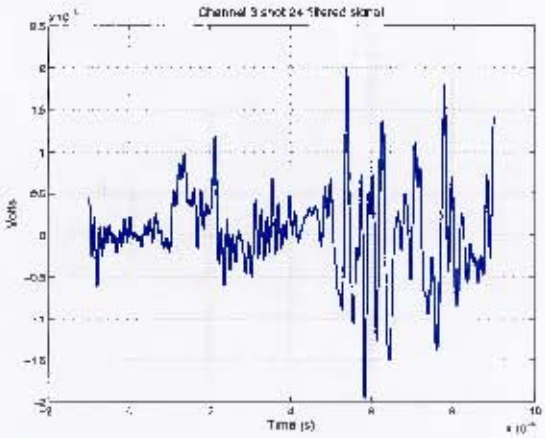

Figure H.174. Channel 3 100g at 4m filtered

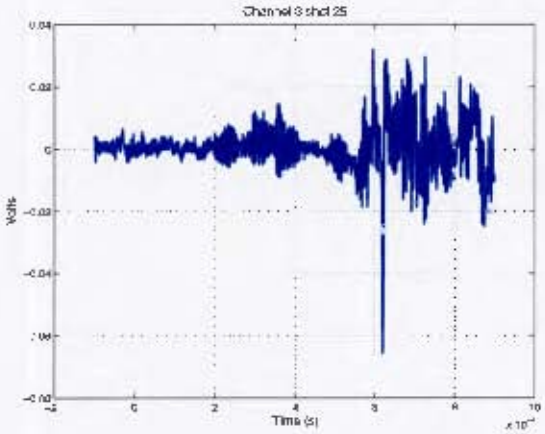

Figure H.175. Channel 3 100g at 4m

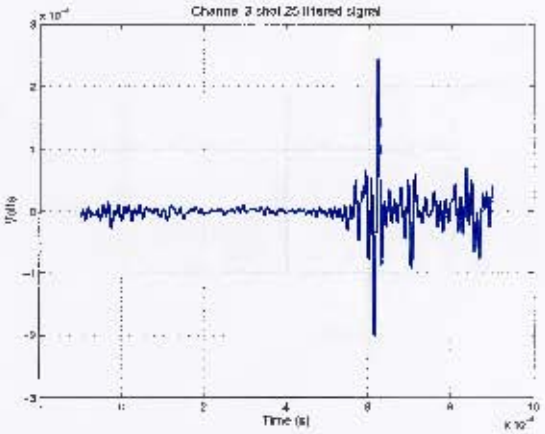

Figure H.176. Channel 3 100g at 4m filtered

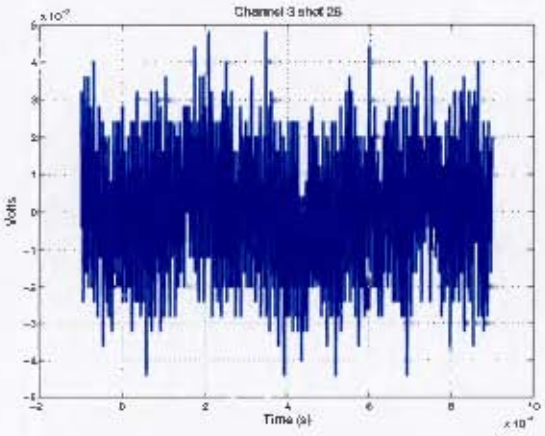

Figure H.177. Channel 40g at 6m

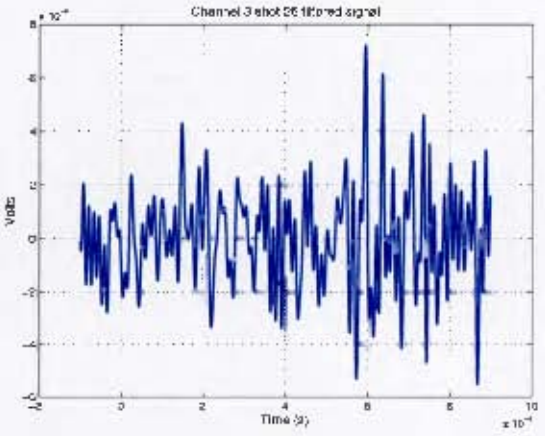

Figure H.178. Channel 3 40g at 6m filtered

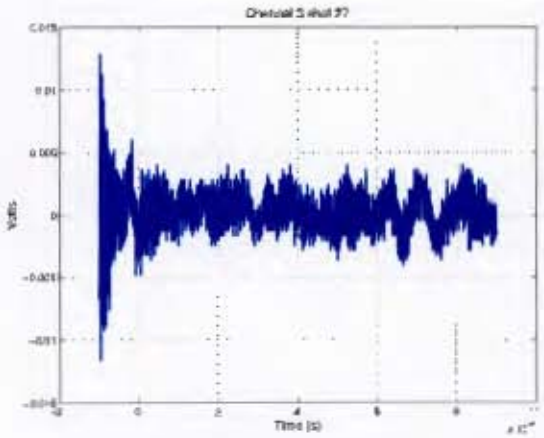

Figure H.179. Channel 3 40g at 6m

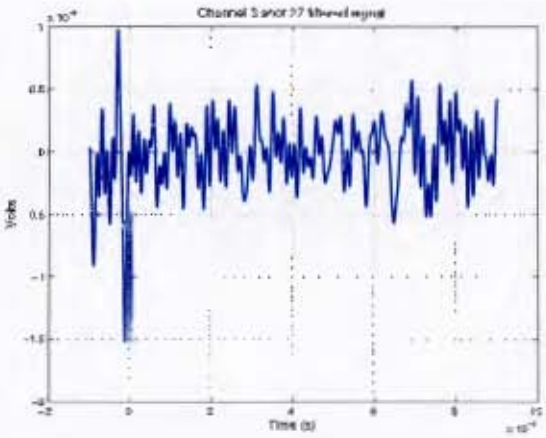

Figure H.180. Channel 3 40g at 6m filtered

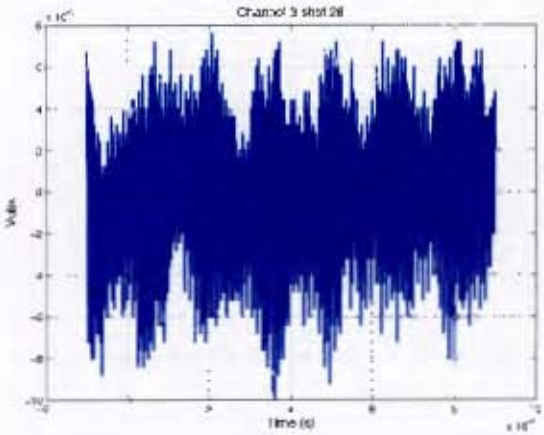

Figure H.181. Channel 3 60g at 6m

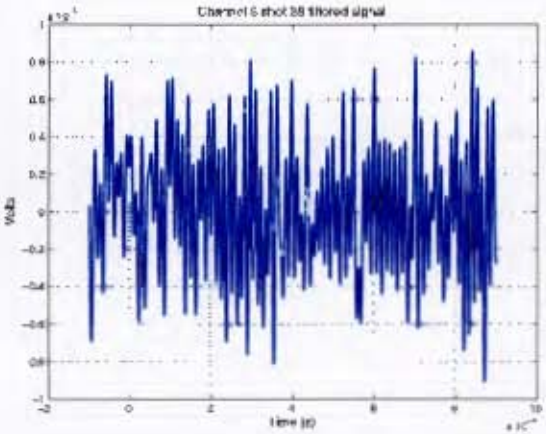

Figure H.182. Channel 3 60g at 6m filtered

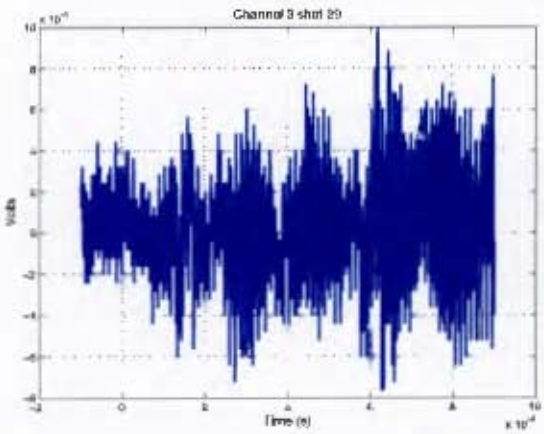

Figure H.183. Channel 3 60g at 6m

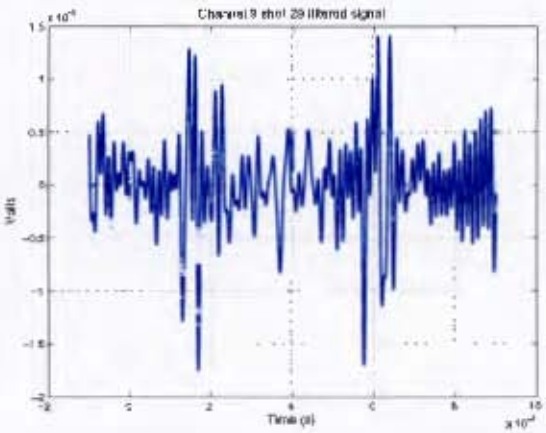

Figure H.184. Channel 3 60g at 6m filtered

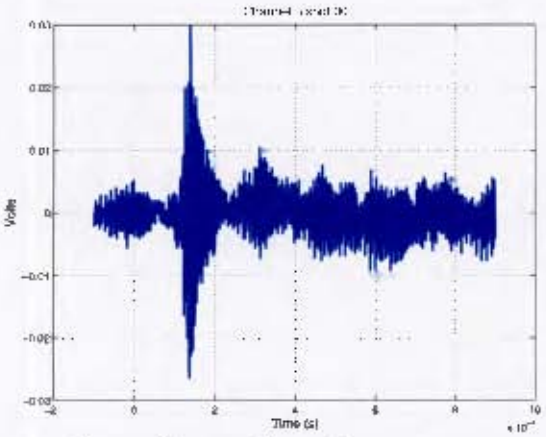

Figure H.185. Channel 3 80g at 6m

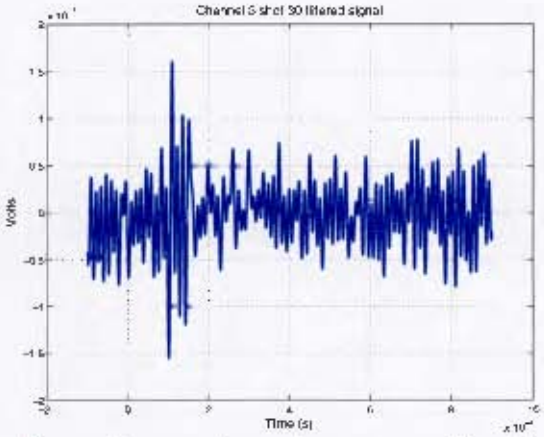

Figure H.186. Channel 3 80g at 6m filtered

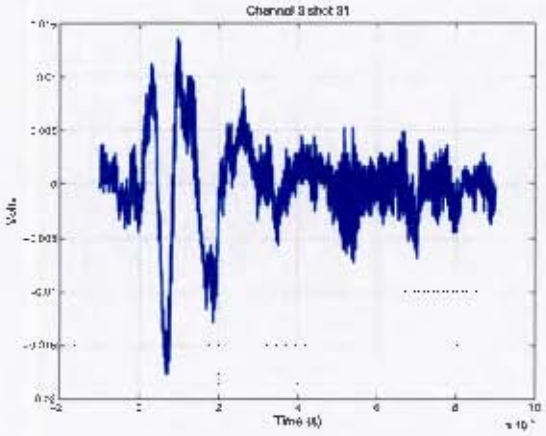

Figure H.187. Channel 3 80g at 6m

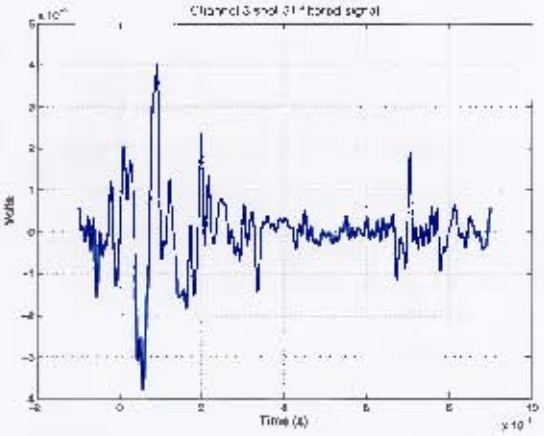

Figure H.188. Channel 3 80g at 6m filtered

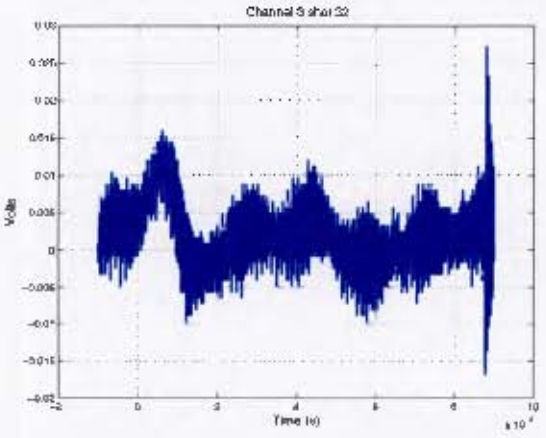

Figure H.189. Channel 3 100g at 6m

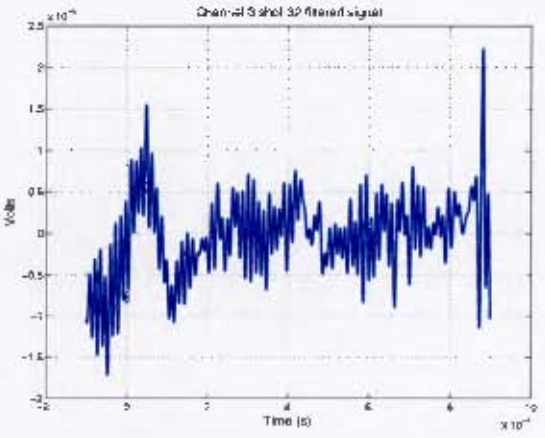

Figure H.190. Channel 3 100g at 6m filtered

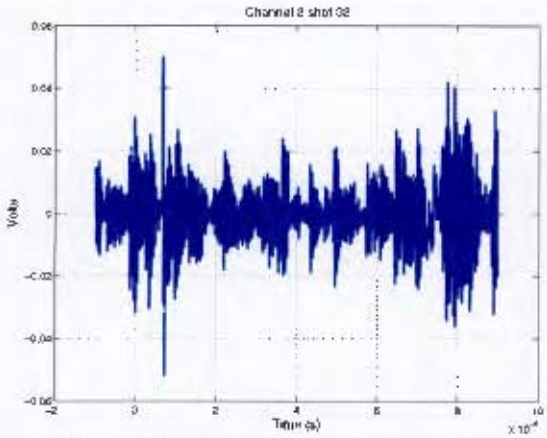

Figure H.191. Channel 3 100g at 6m

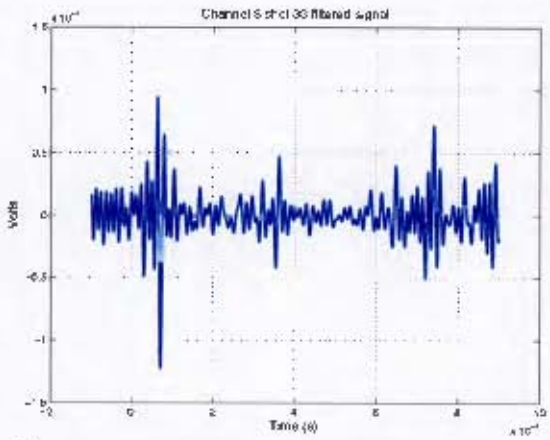

Figure H.192. Channel 3 100g at 6m filtered

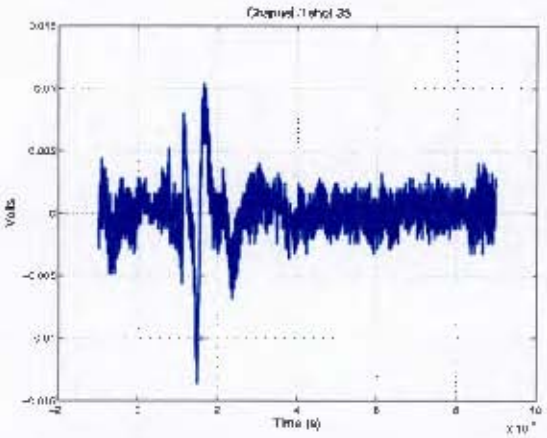

Figure H.193. Channel 3 60g at 8m

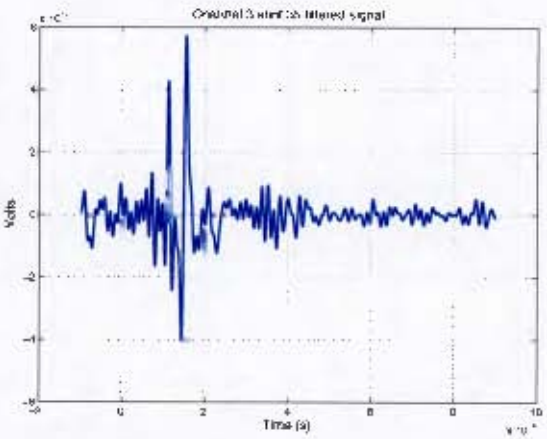

Figure H.194. Channel 3 60g at 8m filtered

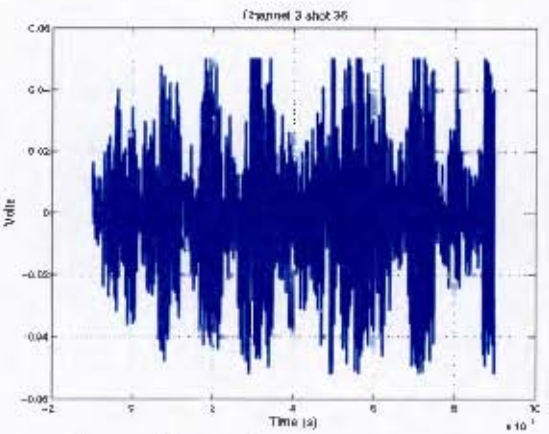

Figure H.195. Channel 3 60g at 8m

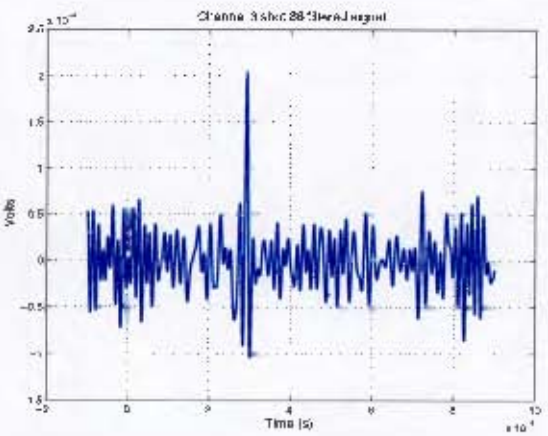

Figure H.196. Channel 3 60g at 8m filtered

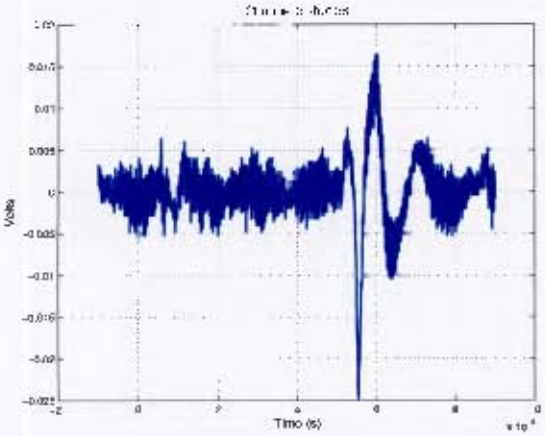

Figure H.197. Channel 3 80g at 8m

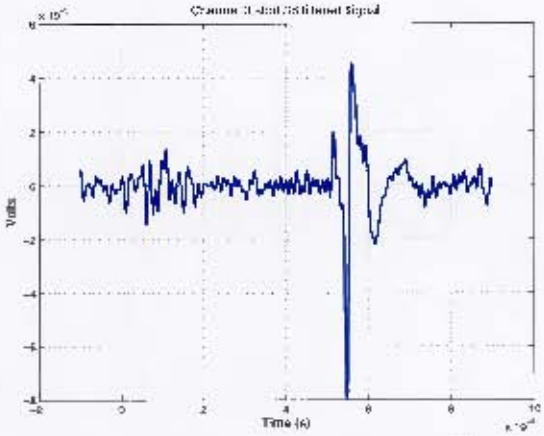

Figure H.198. Channel 3 80g at 8m filtered

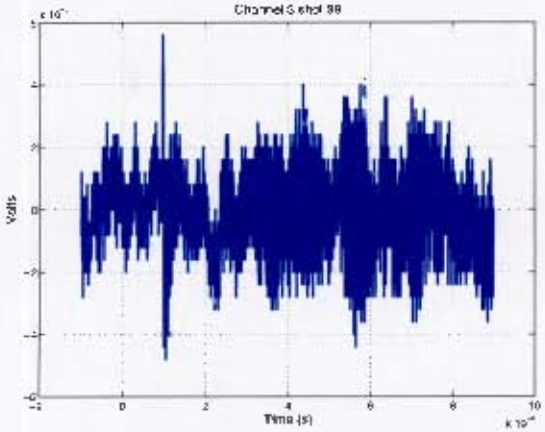

Figure H.199. Channel 3 100g at 8m

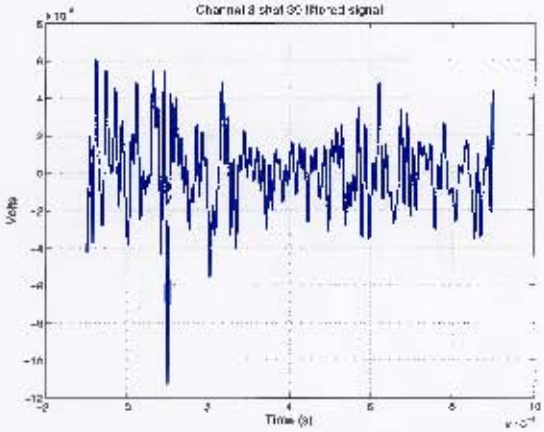

Figure H.200. Channel 3 100g at 8m filtered

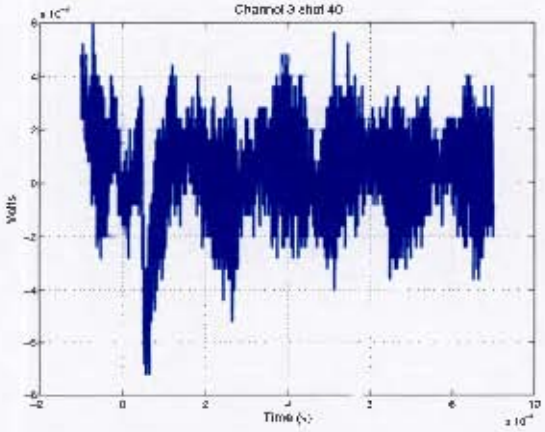

Figure H.201. Channel 3 100g at 8m

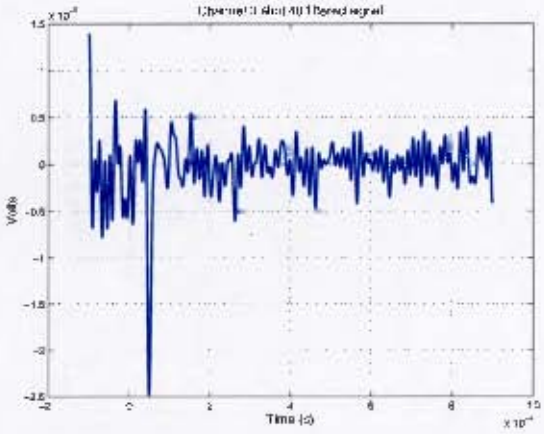

Figure H.202. Channel 3 100g at 8m filtered

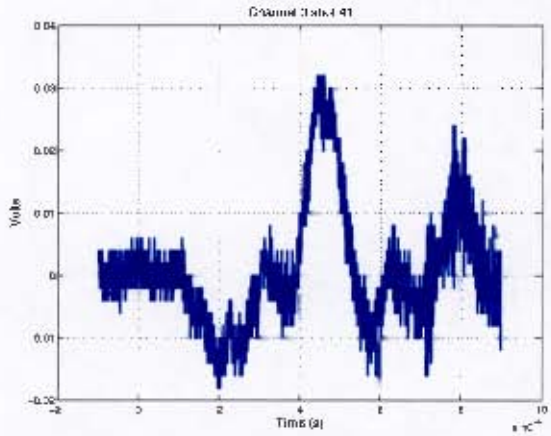

Figure H.203. Channel 3 2.9kg at 10m

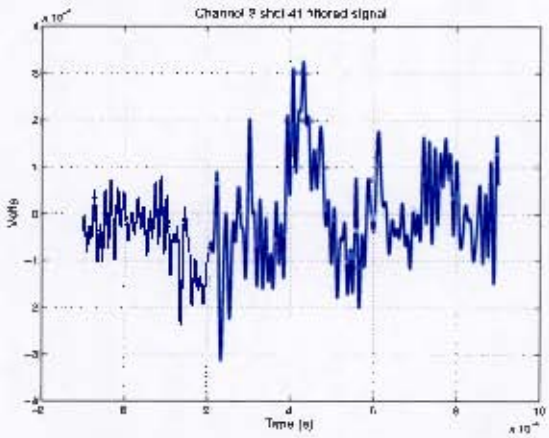

Figure H.204. Channel 3 2.9kg at 10m filtered

H.2 FFT of signals

H.2.1 Channel 1

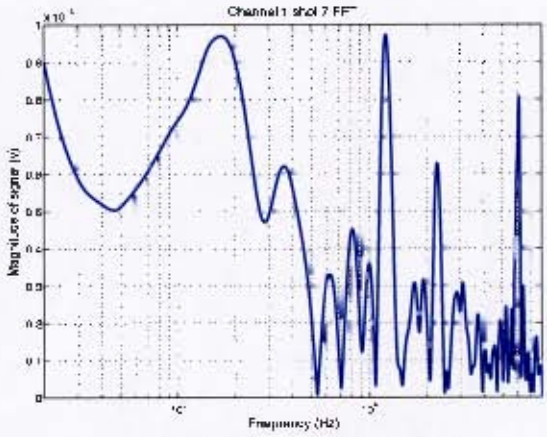

Figure H.205. Channel 1 20g at 2m

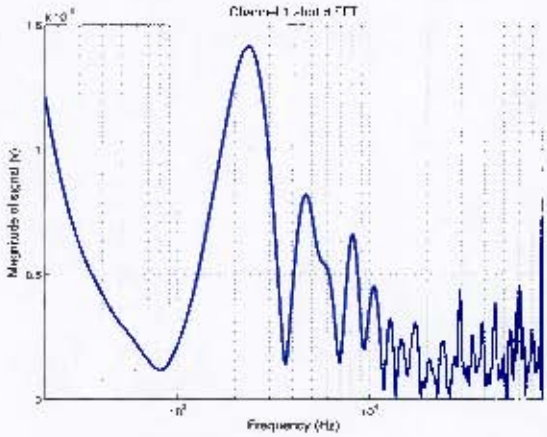

Figure H.206. Channel 1 40g at 2m

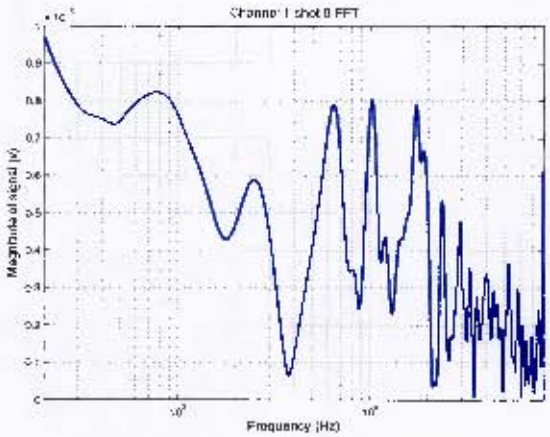

Figure H.207. Channel 1 40g at 2m

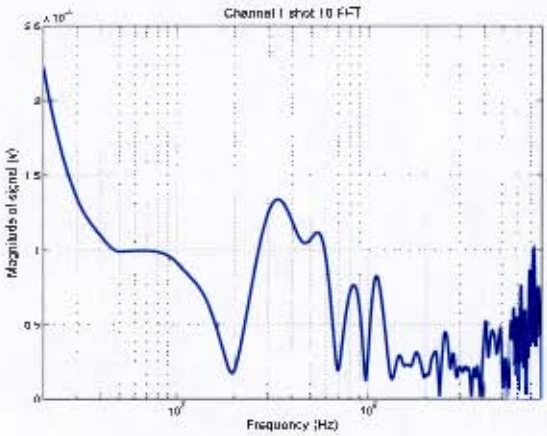

Figure H.208. Channel 1 60g at 2m

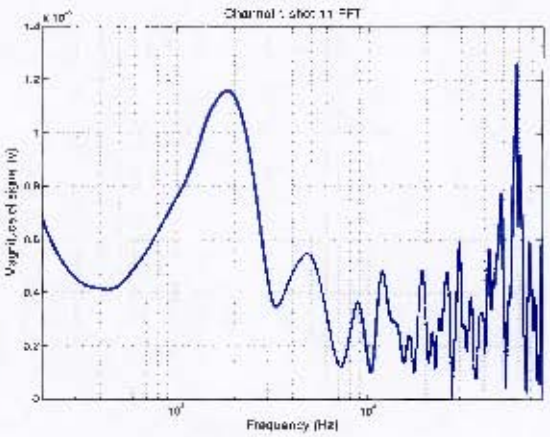

Figure H.209. Channel 1 60g at 2m

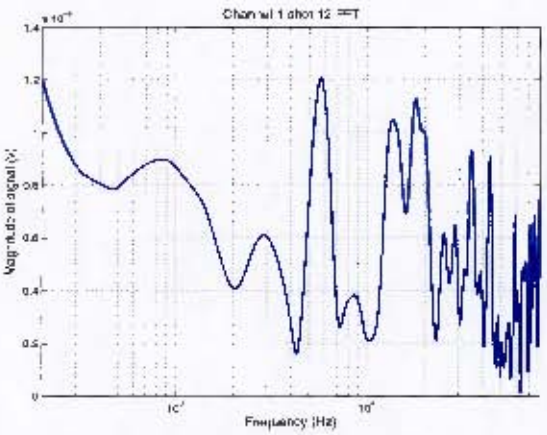

Figure H.210. Channel 1 80g at 2m

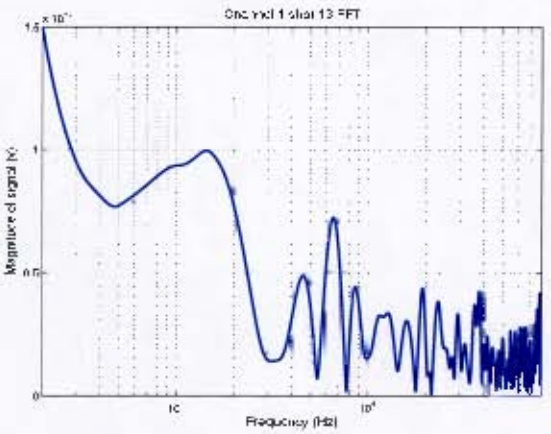

Figure H.211. Channel 1 80g at 2m

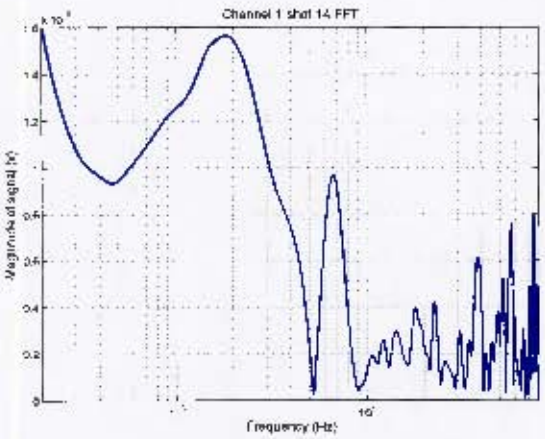

Figure H.212. Channel 1 100g at 2m

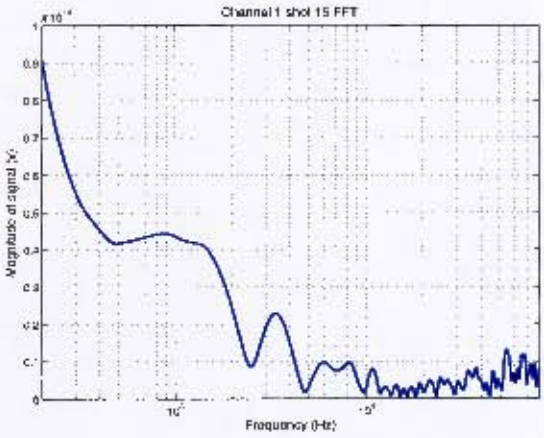

Figure H.213. Channel 1 100g at 2m

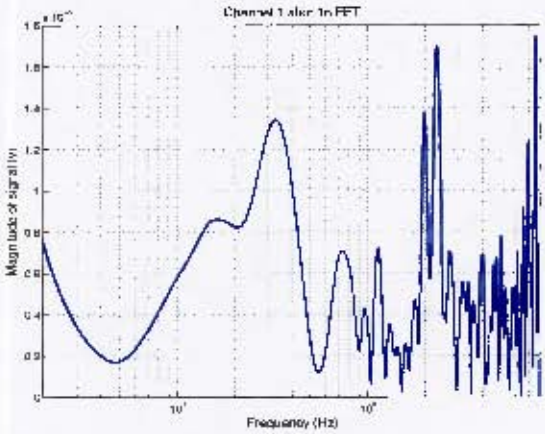

Figure H.214. Channel 1 20g at 4m

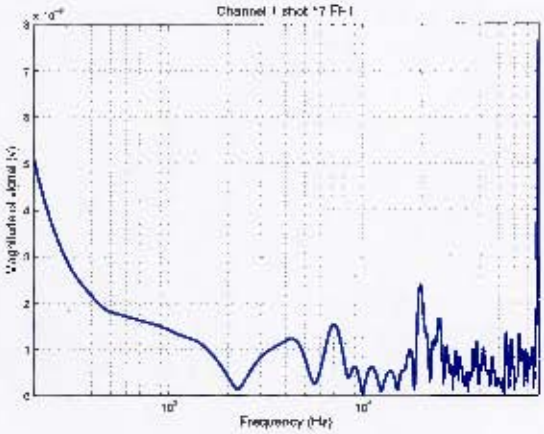

Figure H.215. Channel 1 20g at 4m

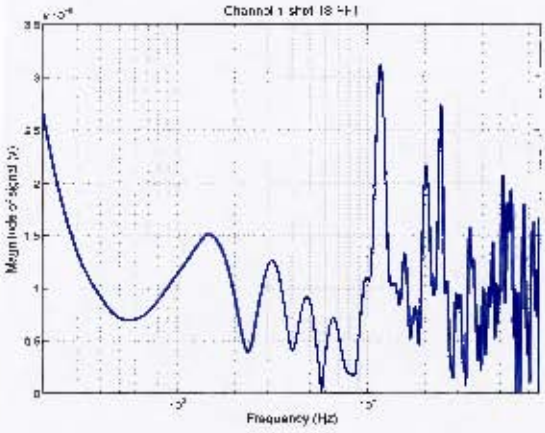

Figure H.216. Channel 1 40g at 4m

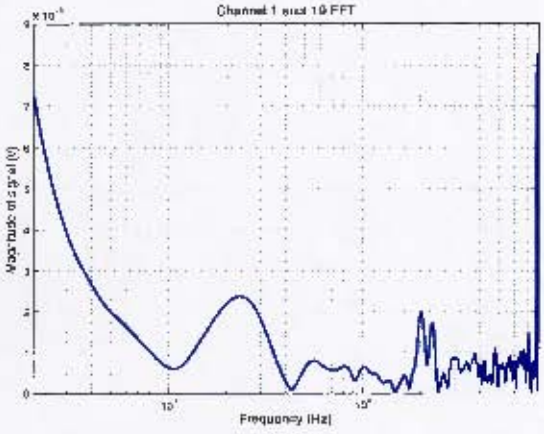

Figure H.217. Channel 1 40g at 4m

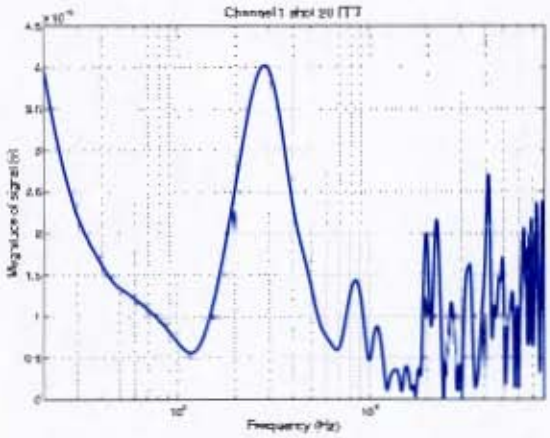

Figure H.218. Channel 1 60g at 4m

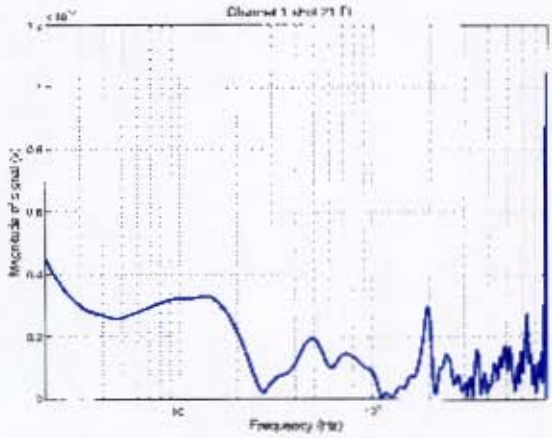

Figure H.219. Channel 1 60g at 4m

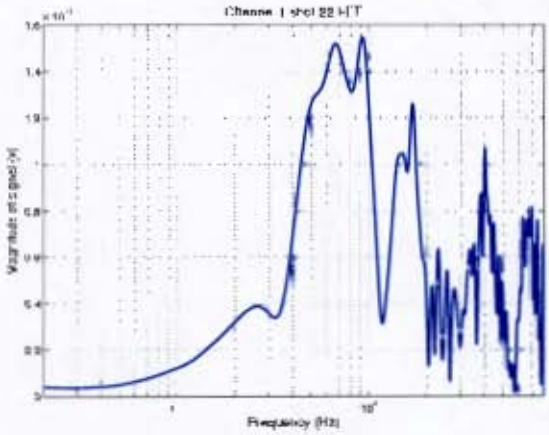

Figure H.220. Channel 1 80g at 4m

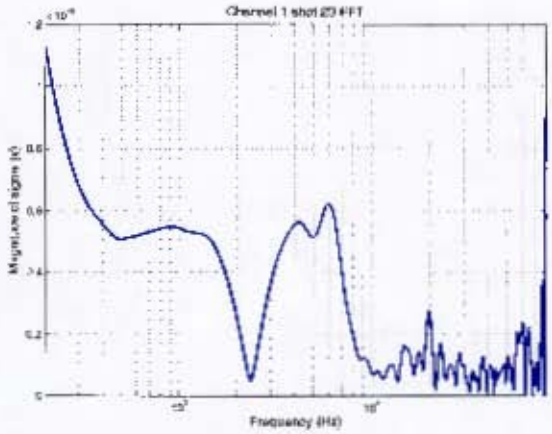

Figure H.221. Channel 1 80g at 4m

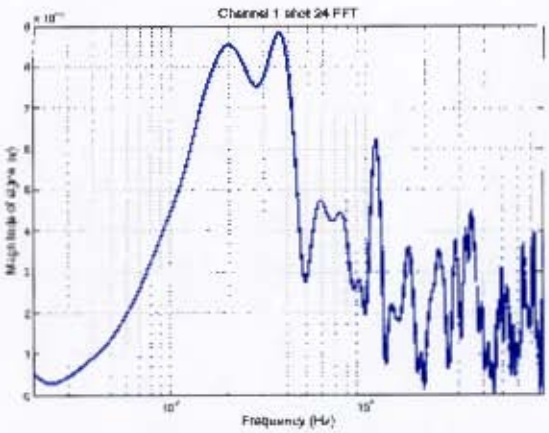

Figure H.222. Channel 1 100g at 4m

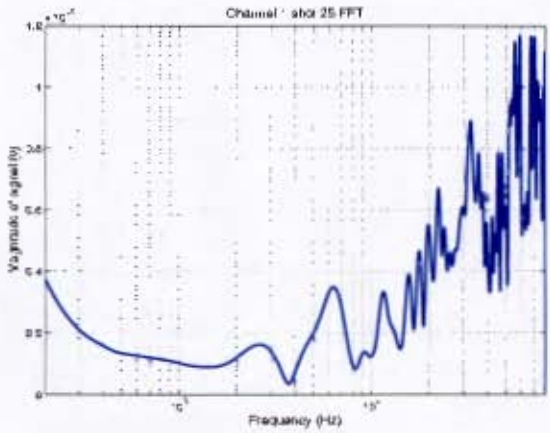

Figure H.223. Channel 1 100g at 4m

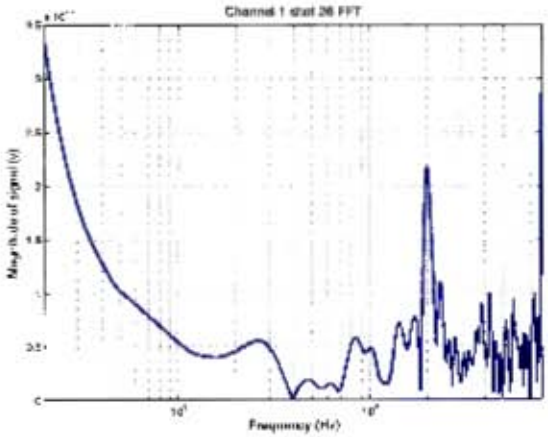

Figure H.224. Channel 1 40g at 6m

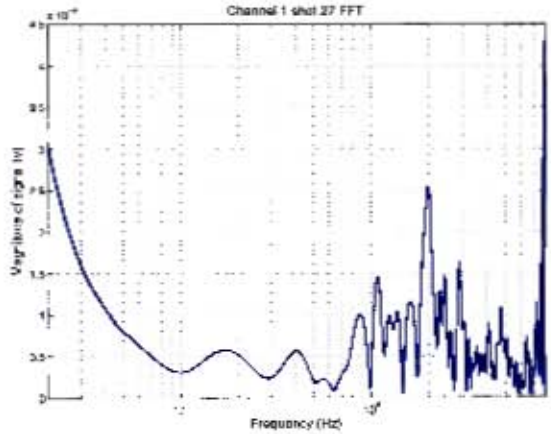

Figure **H.225.** Channel 1 40g at 6m

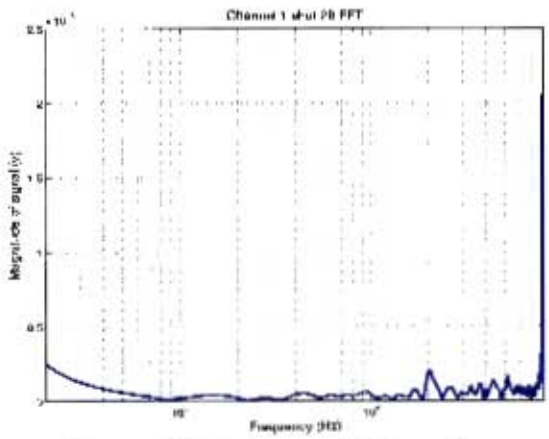

Figure H.226. Channel 1 60g at 6m

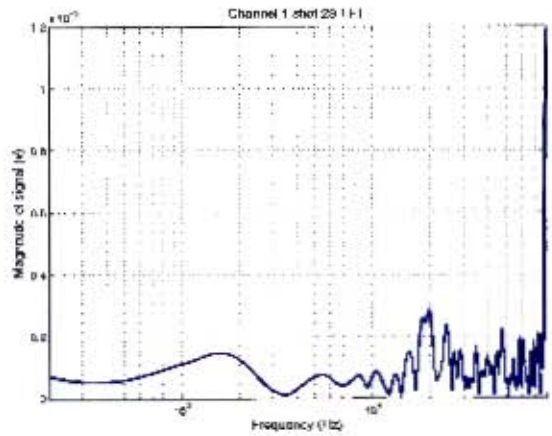

Figure H.227. Channel 1 60g at 6m

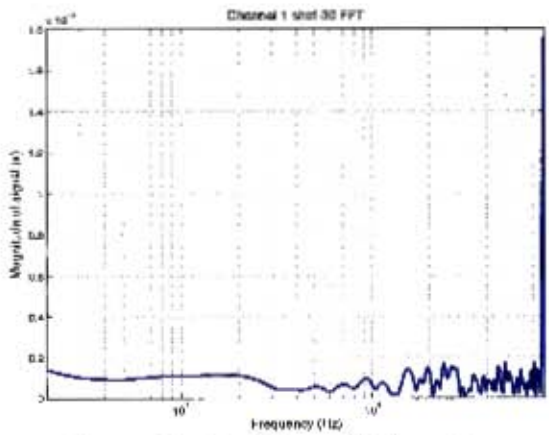

Figure H.228. Channel 1 80g at 6m

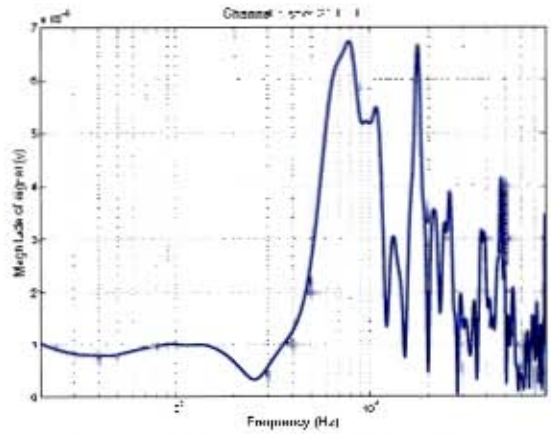

Figure H.229. Channel 1 80g at 6m

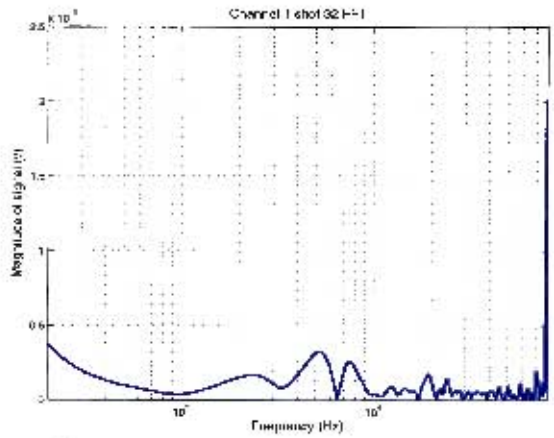

Figure H.230. Channel 1 100g at 6m

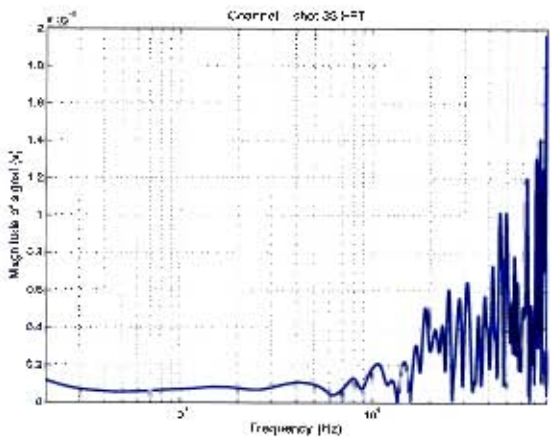

Figure H.231. Channel 1 100g at 6m

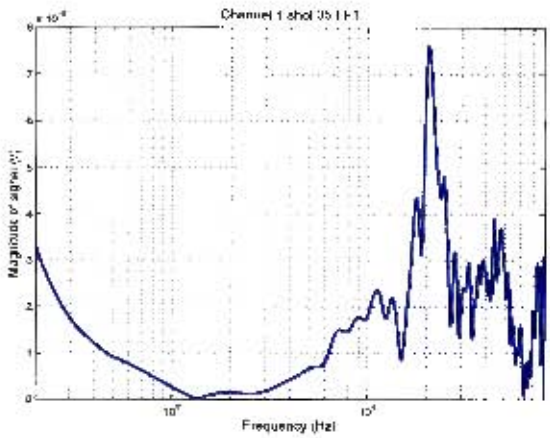

Figure H.232. Channel 1 60g at 8m

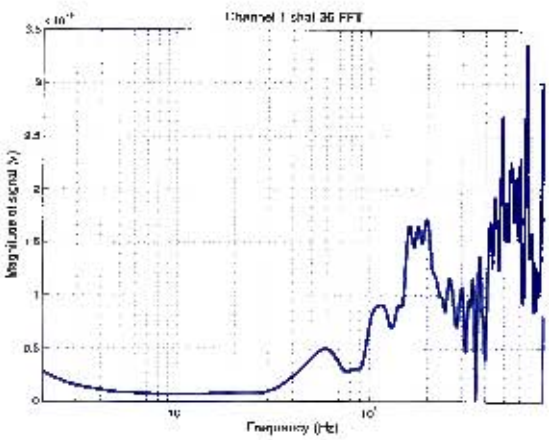

Figure H.233. Channel 1 60g at 8m

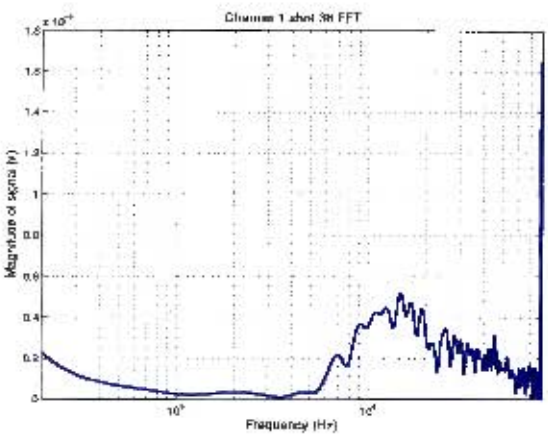

Figure H.234. Channel 1 80g at 8m

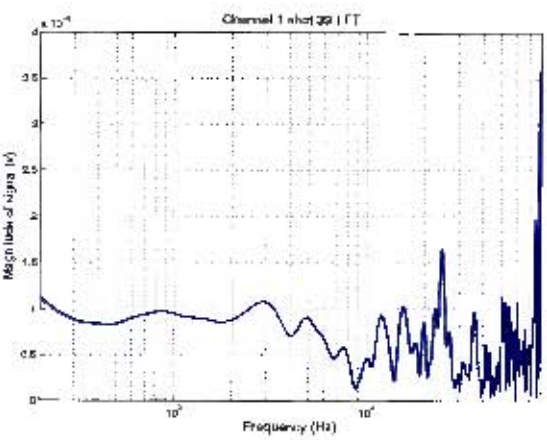

Figure H.235. Channel 1 100g at 8m

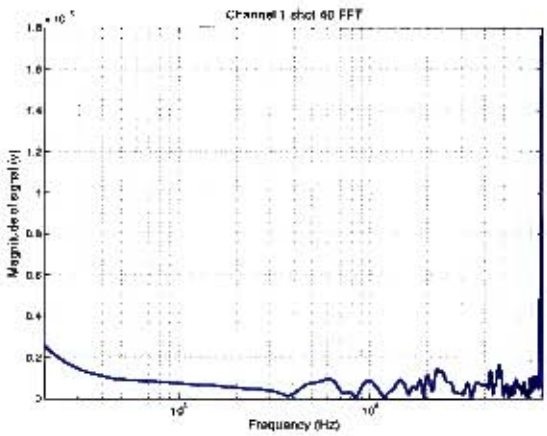

Figure H.236. Channel 1 100g at 8m

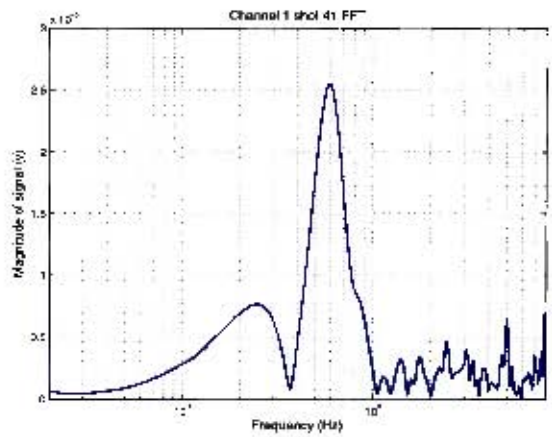

Figure H.237. Channel 1 2.9kg at 10m

H.2.2 Channel 2

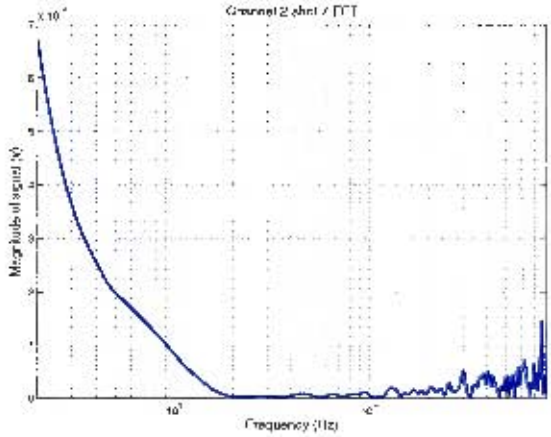

Figure H.238. Channel 2 20g at 2m

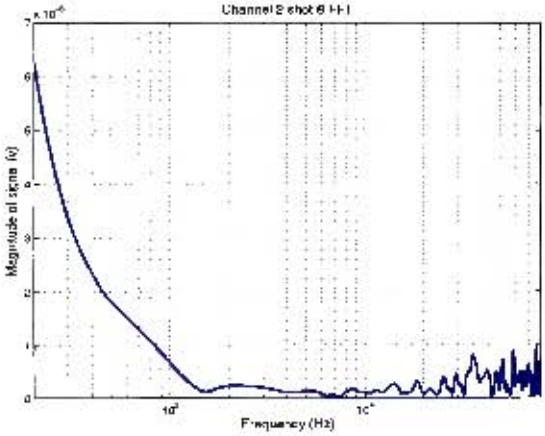

Figure H.239. Channel 2 40g at 2m

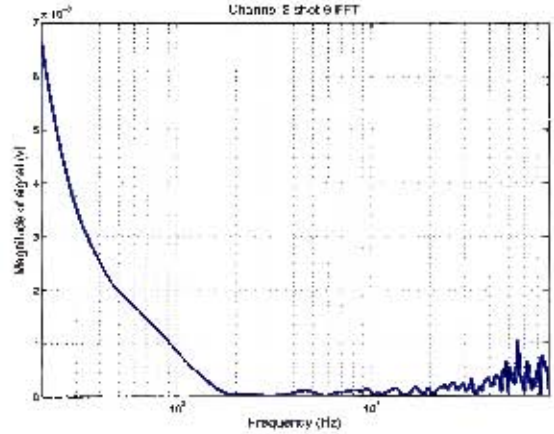

Figure H.240. Channel 2 40g at 2m

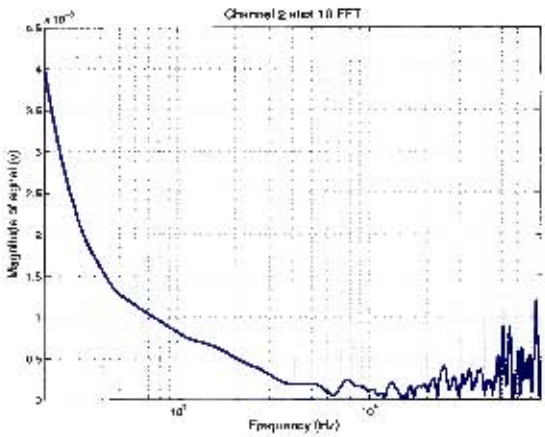

Figure H.241. Channel 2 60g at 2m

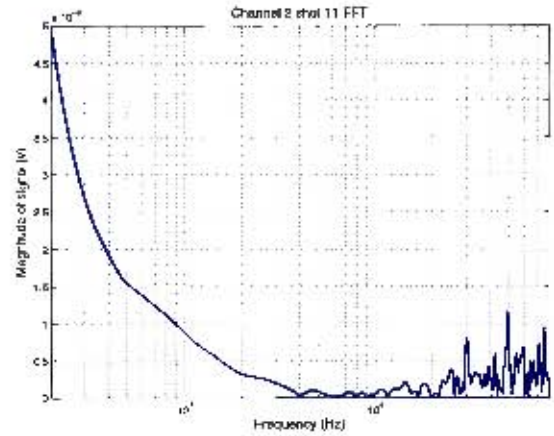

Figure H.242. Channel 2 60g at 2m

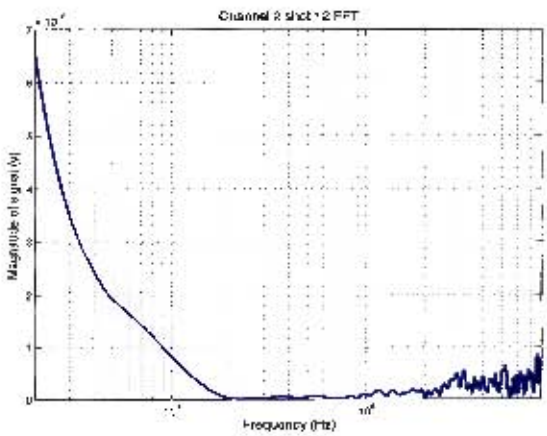

Figure H.243. Channel 2 80g at 2m

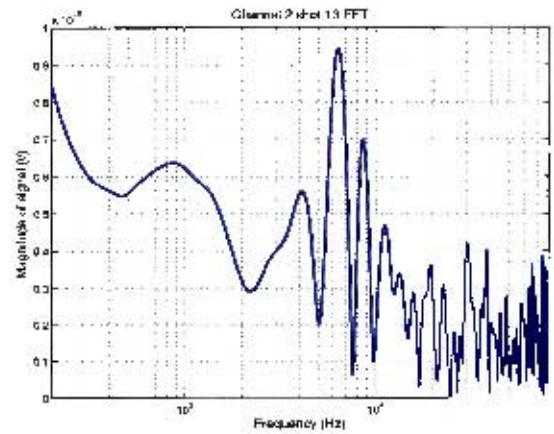

Figure H.244. Channel 2 80g at 2m

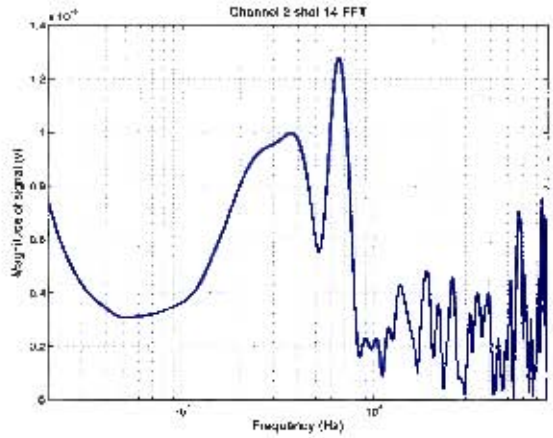

Figure H.245. Channel 2 100g at 2m

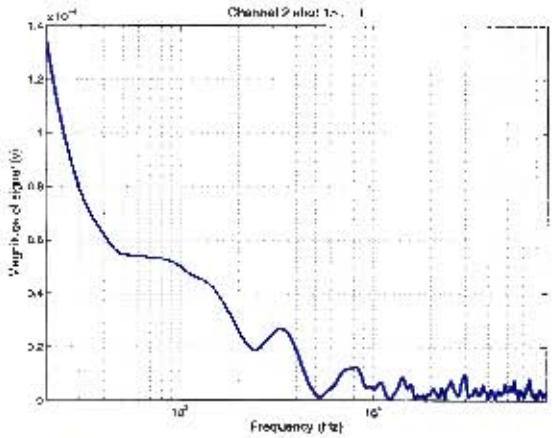

Figure H.246. Channel 2 100g at 2m

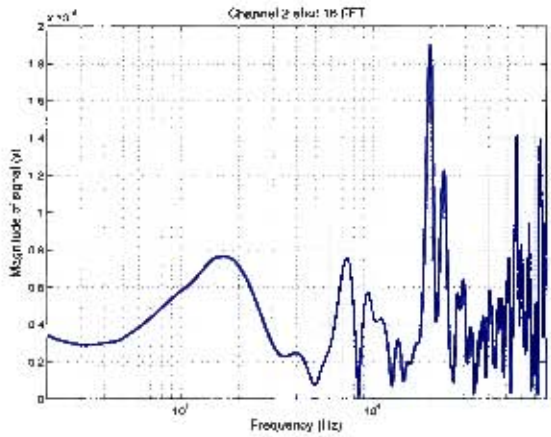

Figure H.247. Channel 2 20g at 4m

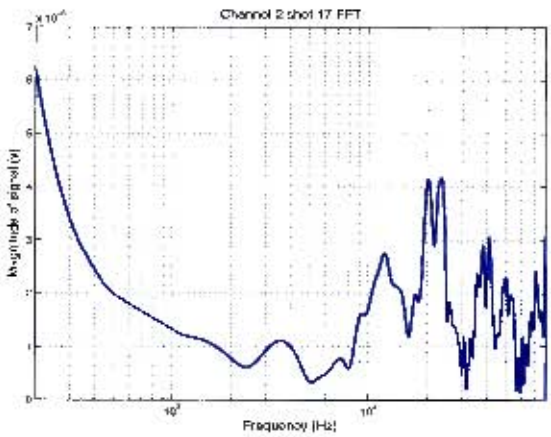

Figure H.248. Channel 2 20g at 4m

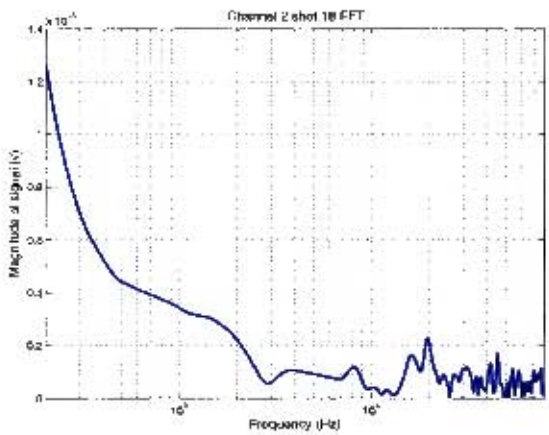

Figure H.249. Channel 2 40g at 4m

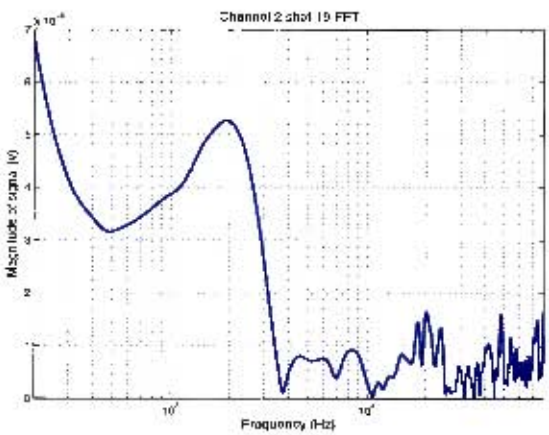

Figure H.250. Channel 2 40g at 4m

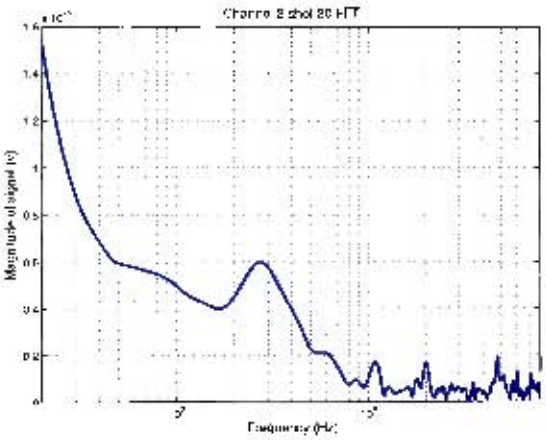

Figure H.251. Channel 2 60g at 4m

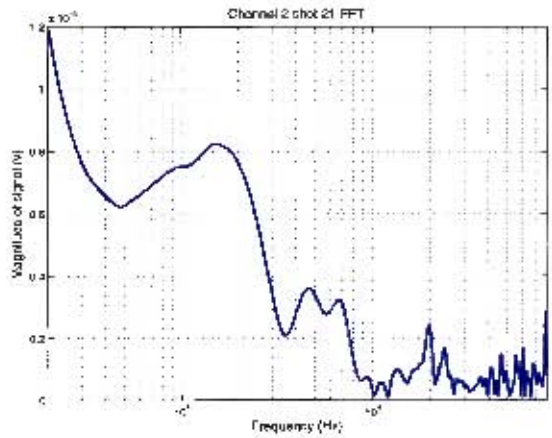

Figure H.252. Channel 2 60g at 4m

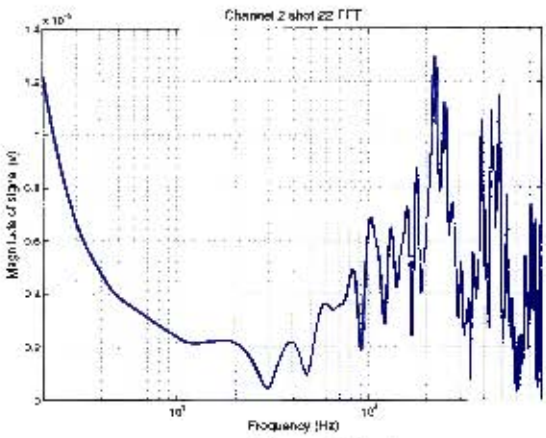

Figure H.253. Channel 2 80g at 4m

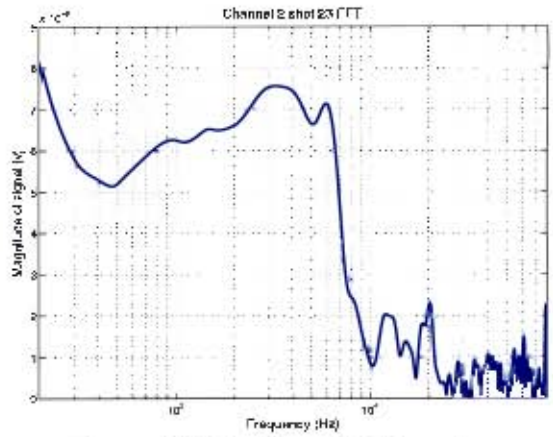

Figure H.254. Channel 2 80g at 4m

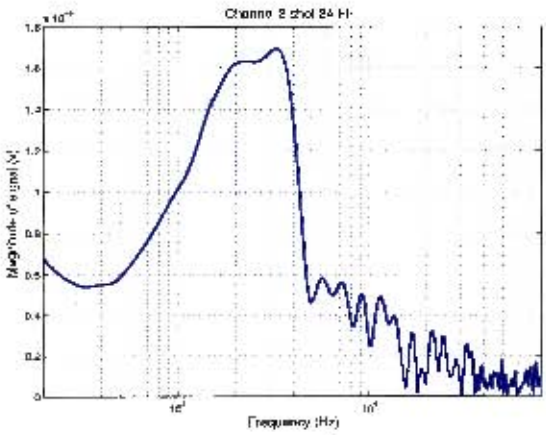

Figure H.255. Channel 2 100g at 4m

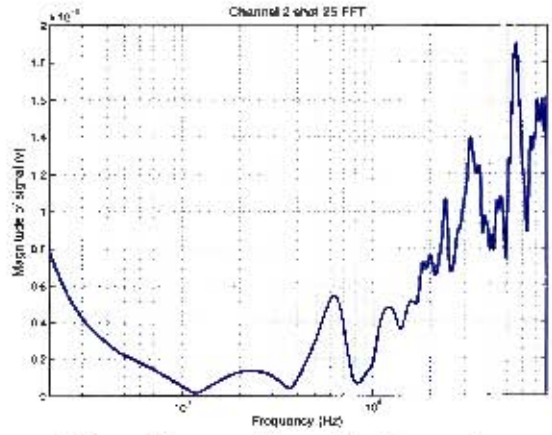

Figure H.256. Channel 2 100g at 4m

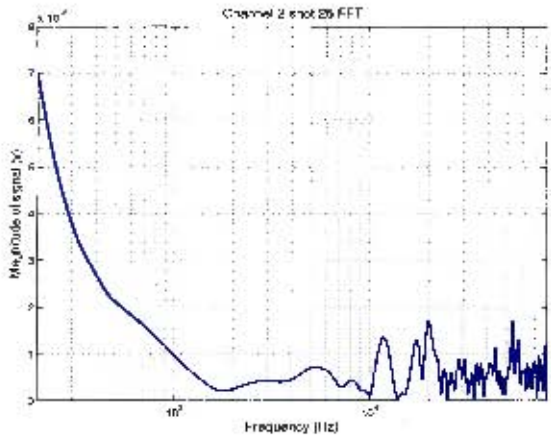

Figure H.257. Channel 2 40g at 6m

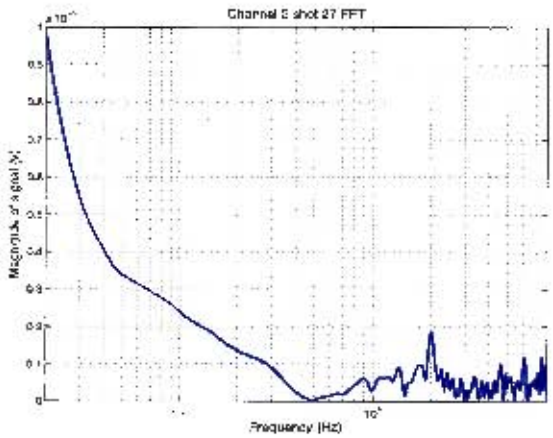

Figure H.258. Channel 2 40g at 6m

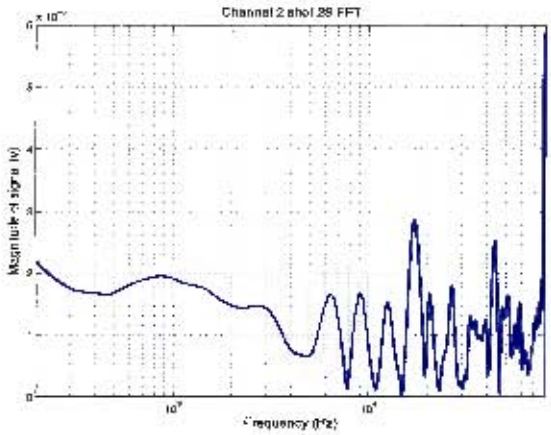

Figure H.259. Channel 2 60g at 6m

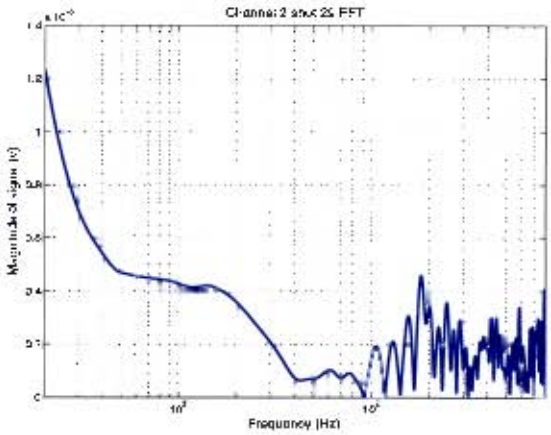

Figure H.260. Channel 2 60g at 6m

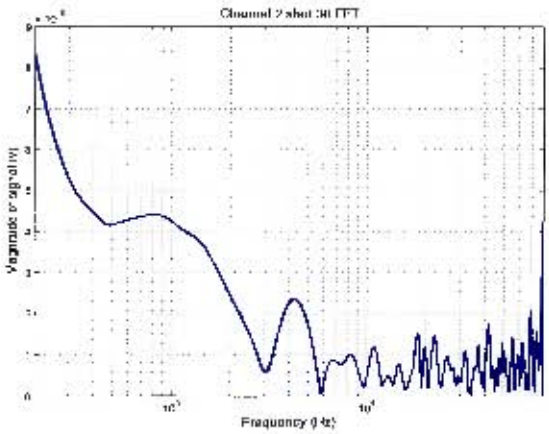

Figure H.261. Channel 2 80g at 6m

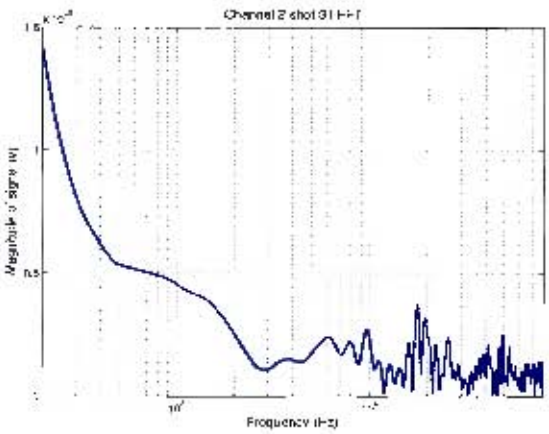

Figure H.262. Channel 2 80g at 6m

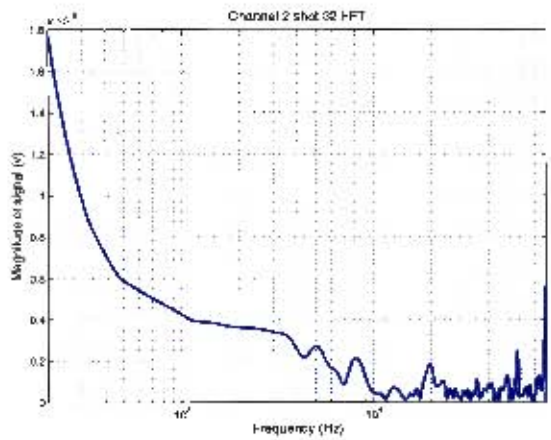

Figure H.263. Channel 2 100g at 6m

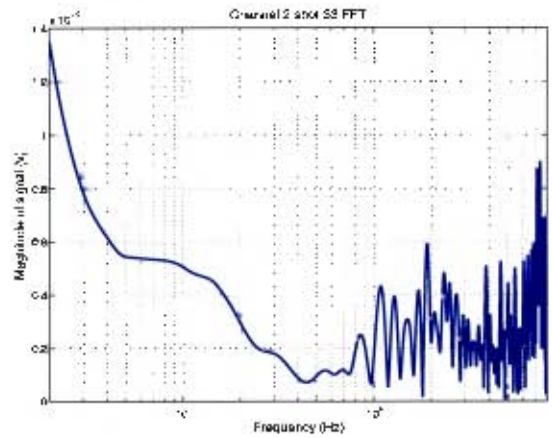

Figure H.264. Channel 2 100g at 6m

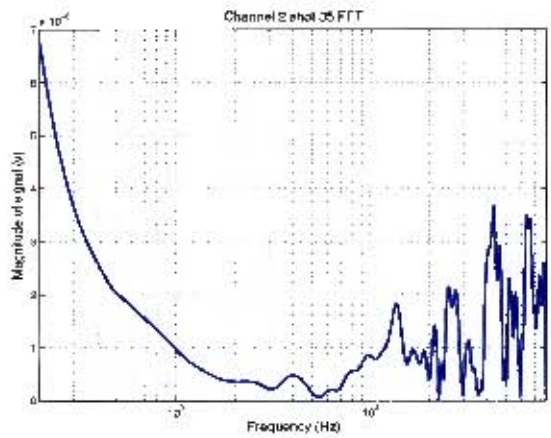

Figure H.265. Channel 2 60g at 8m

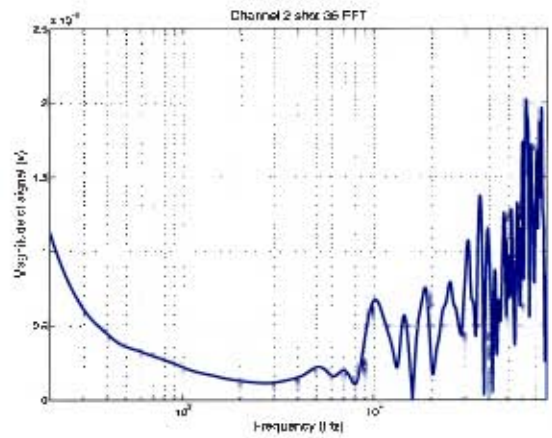

Figure H.266. Channel 2 60g at 8m

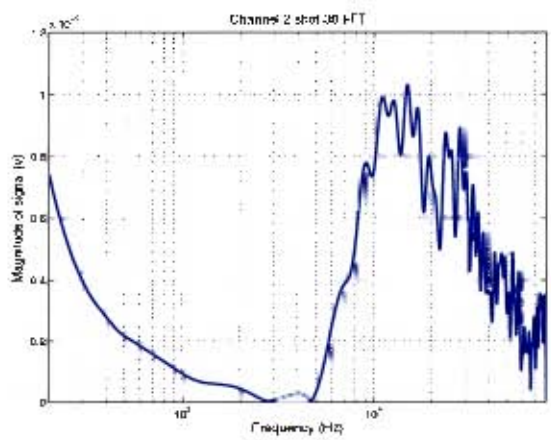

Figure H.267. Channel 2 80g at 8m

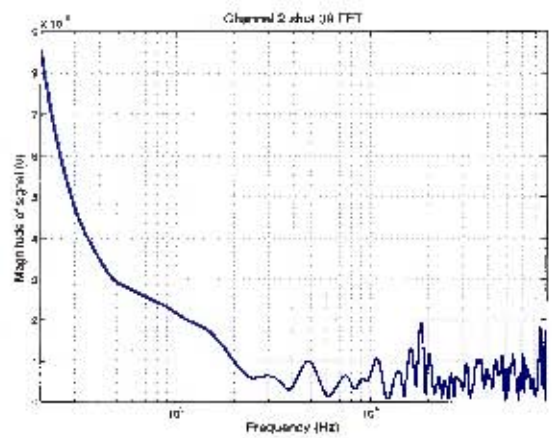

Figure H.268. Channel 2 100g at 8m

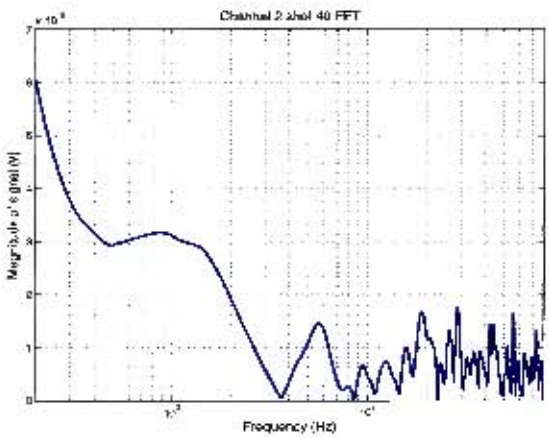

Figure H.269. Channel 2 100g at 8m

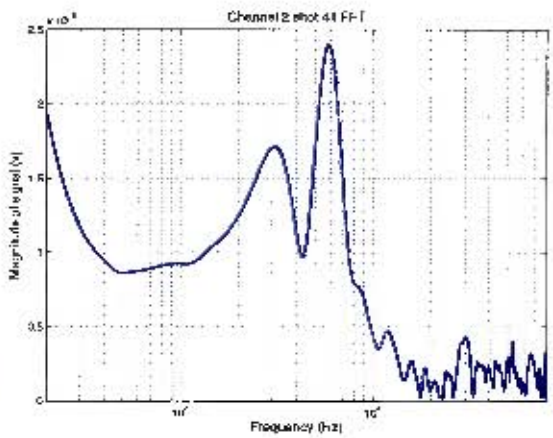

Figure H.270. Channel 2 2.9kg at 10m

H.2.3 Channel 3

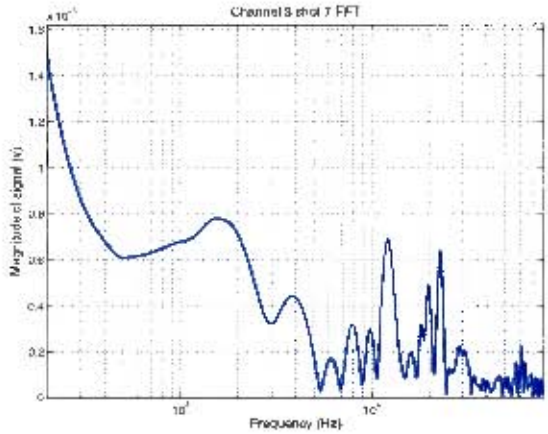

Figure H.271. Channel 3 20g at 2m

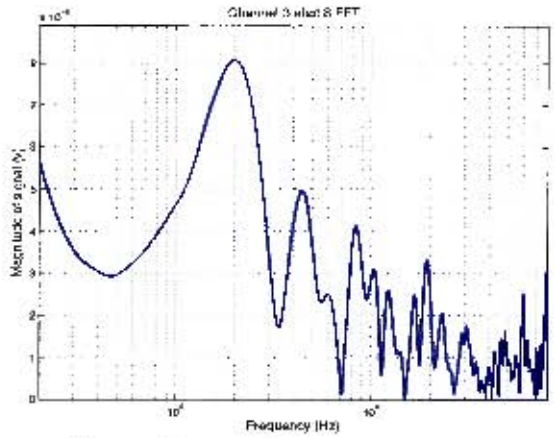

Figure H.272. Channel 3 40g at 2m

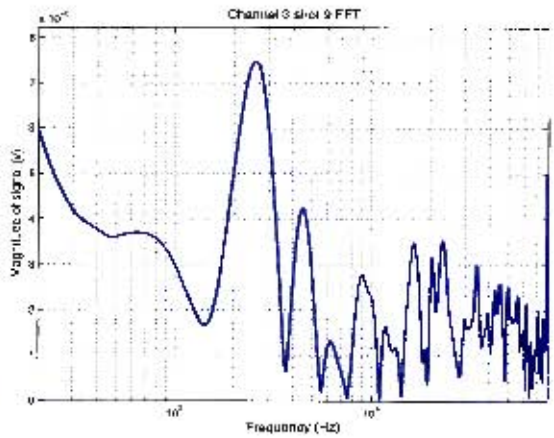

Figure H.273. Channel 3 40g at 2m

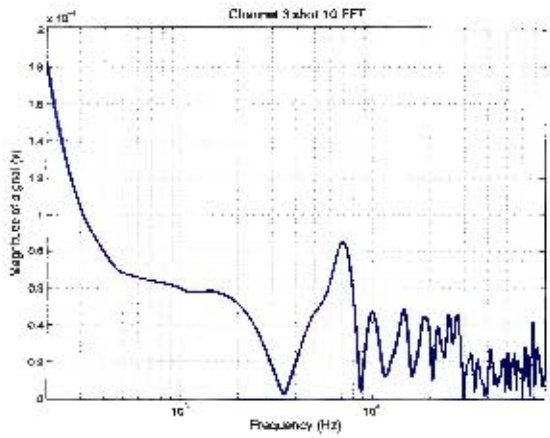

Figure H.274. Channel 3 60g at 2m

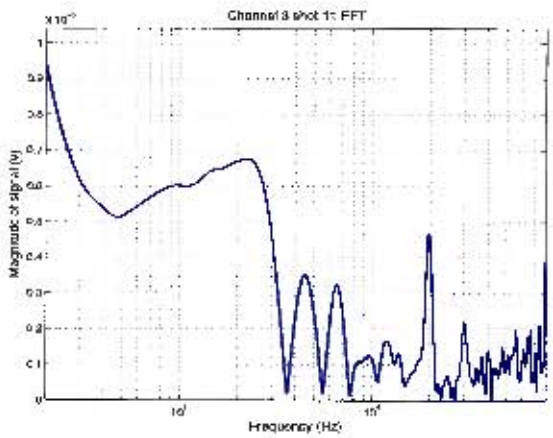

Figure H.275. Channel 3 60g at 2m

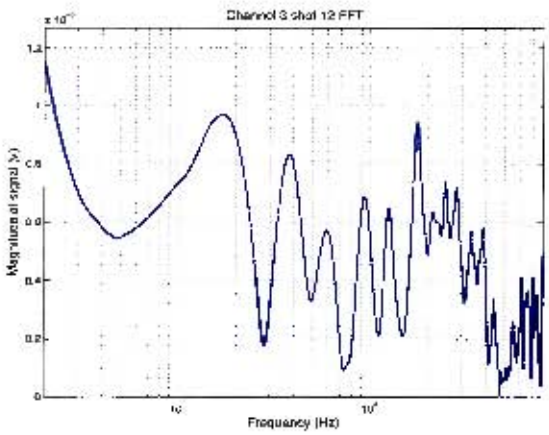

Figure H.276. Channel 3 80g at 2m

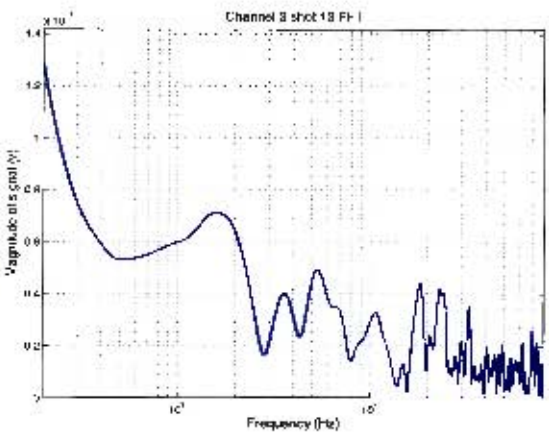

Figure H.277. Channel 3 80g at 2m

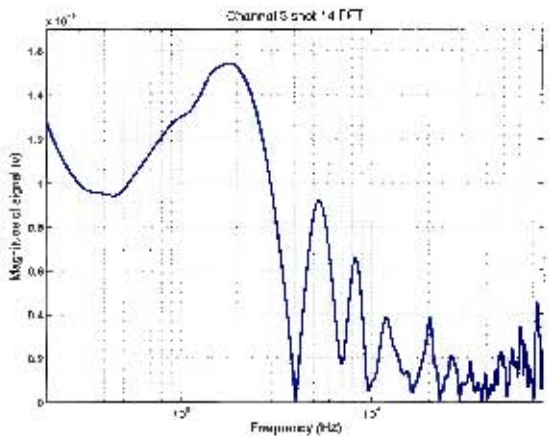

Figure H.278. Channel 3 100g at 2m

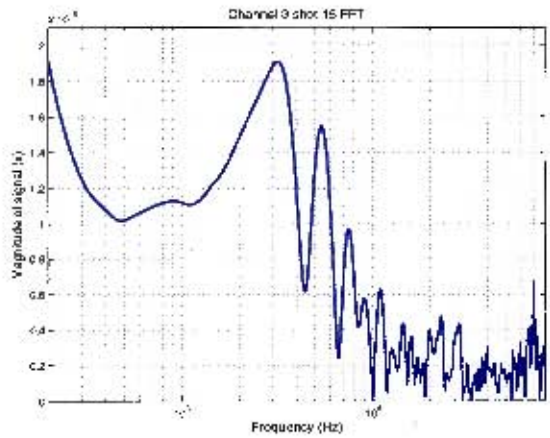

Figure H.279. Channel 3 100g at 2m

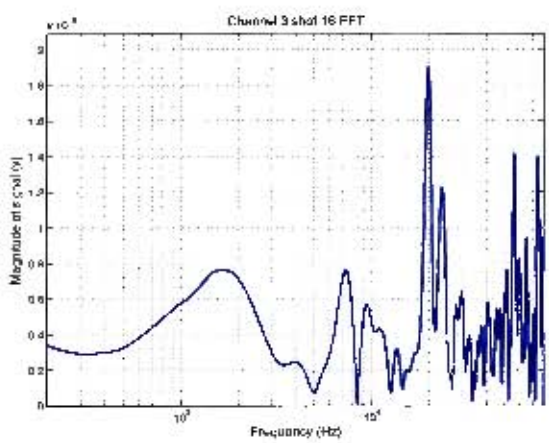

Figure H.280. Channel 3 20g at 4m

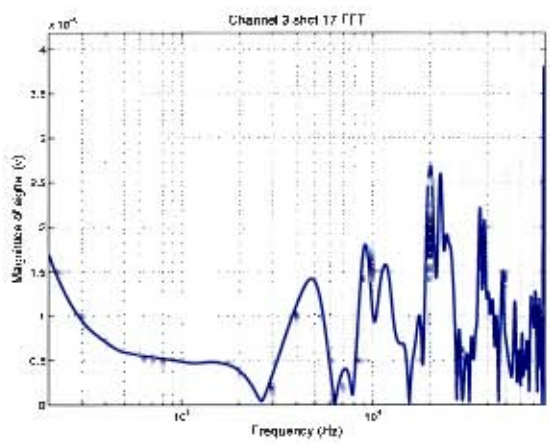

Figure H.281. Channel 3 20g at 4m

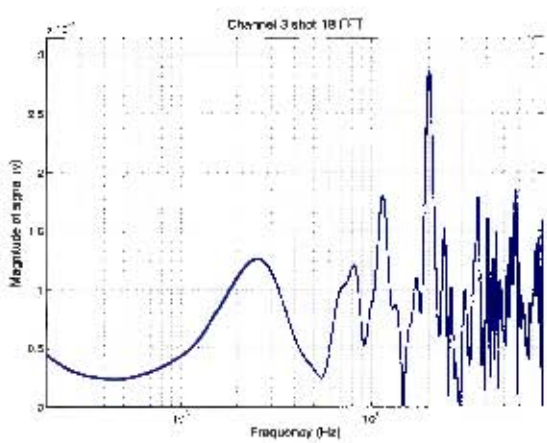

Figure H.282. Channel 3 40g at 4m

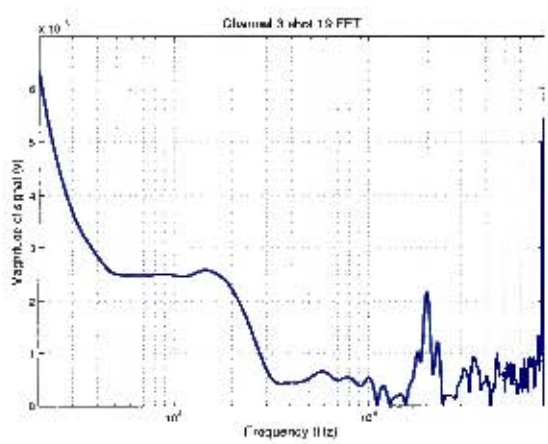

Figure H.283. Channel 3 40g at 4m

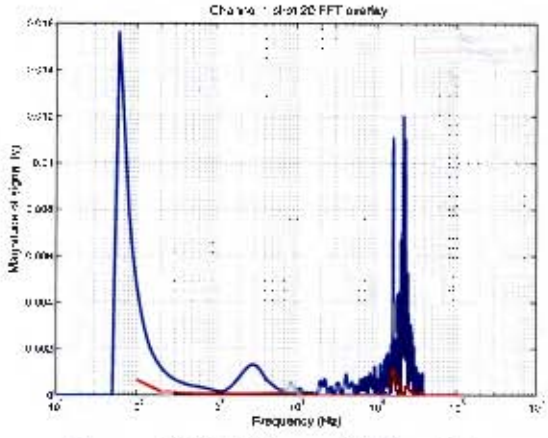

Figure H.317. Channel 1 60g at 4m

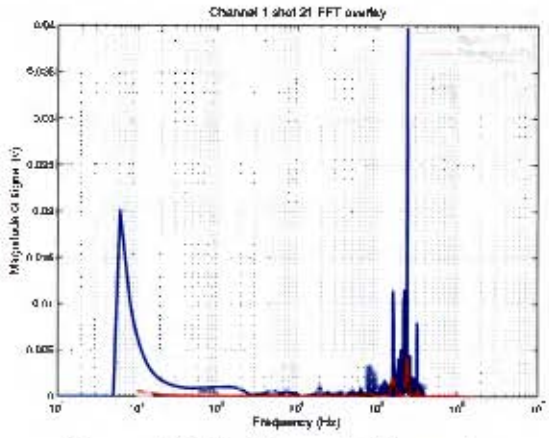

Figure H.318. Channel 1 60g at 4m

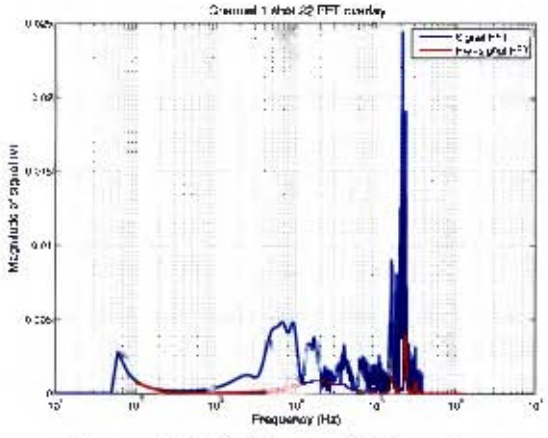

Figure H.319. Channel 1 80g at 4m

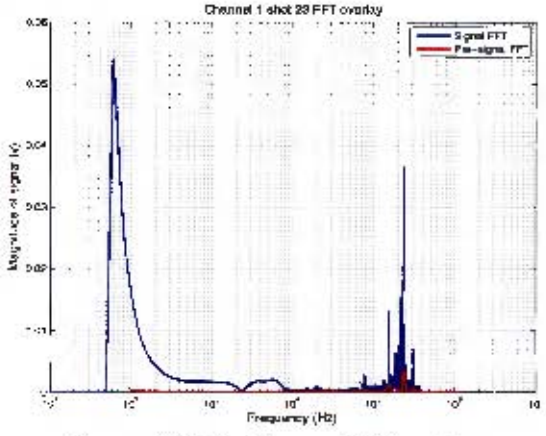

Figure H.320. Channel 1 80g at 4m

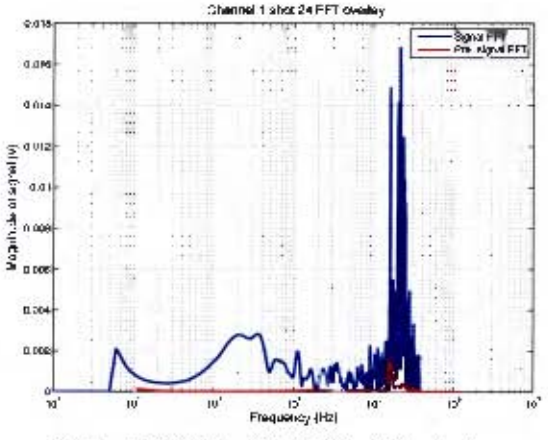

Figure H.321. Channel 1 100g at 4m

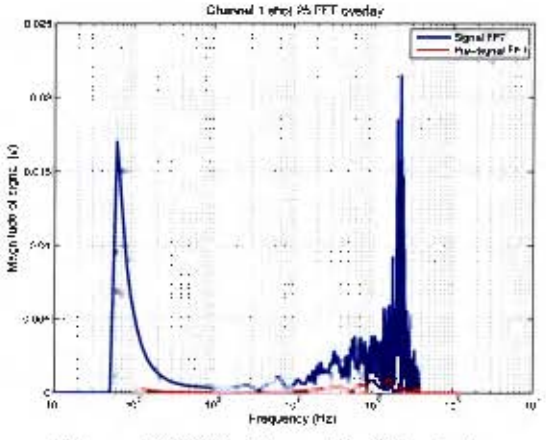

Figure H.322. Channel 1 100g at 4m

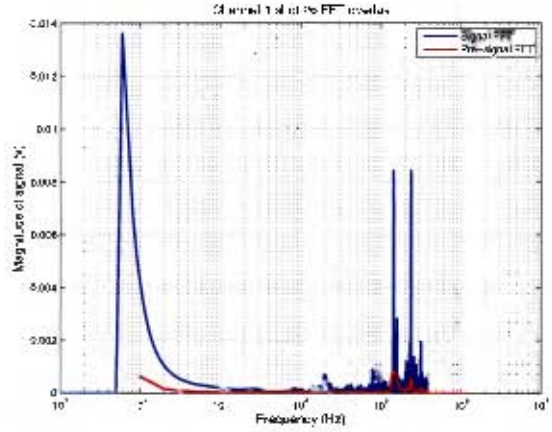

Figure H.323. Channel 1 40g at 6m

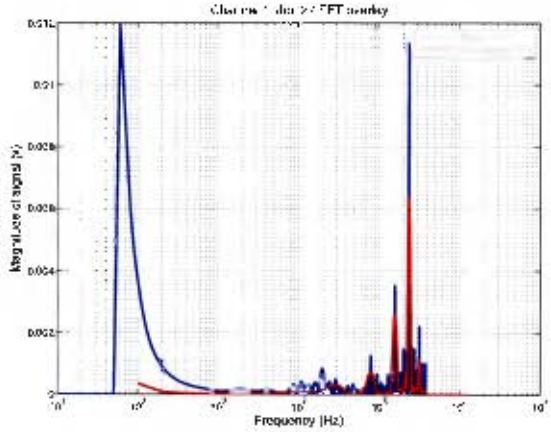

Figure H.324. Channel 1 40g at 6m

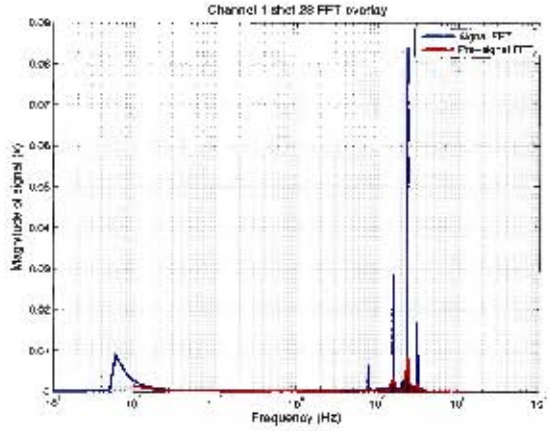

Figure H.325. Channel 1 60g at 6m

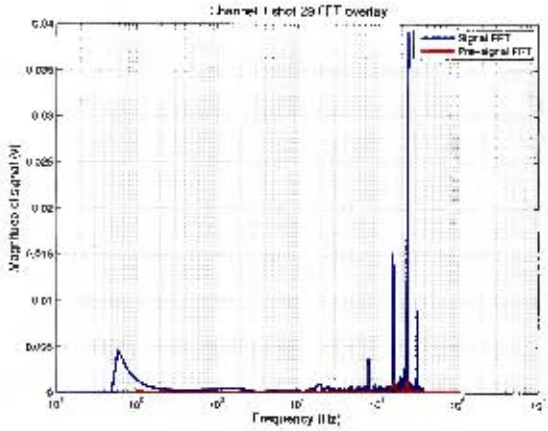

Figure H.326. Channel 1 60g at 6m

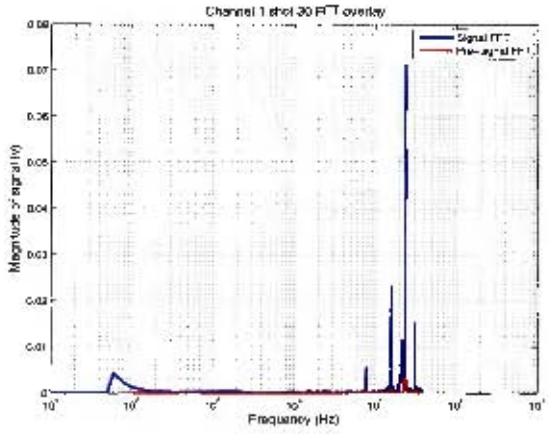

Figure H.327. Channel 1 80g at 6m

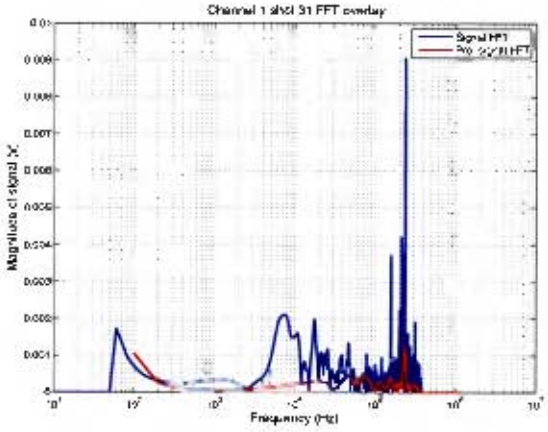

Figure H.328. Channel 1 80g at 6m

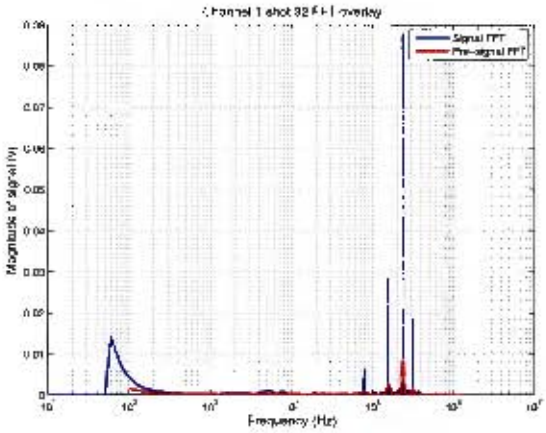

Figure H.329. Channel 1 100g at 6m

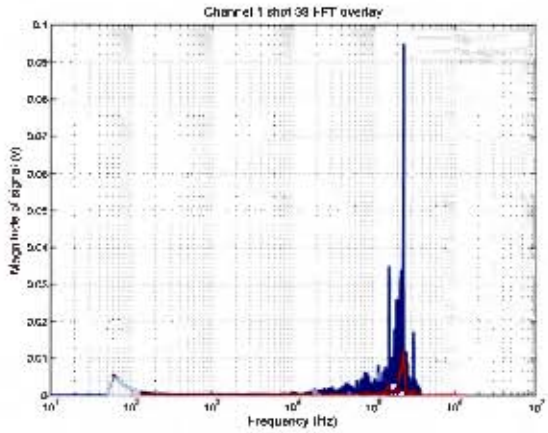

Figure H.330. Channel 1 100g at 6m

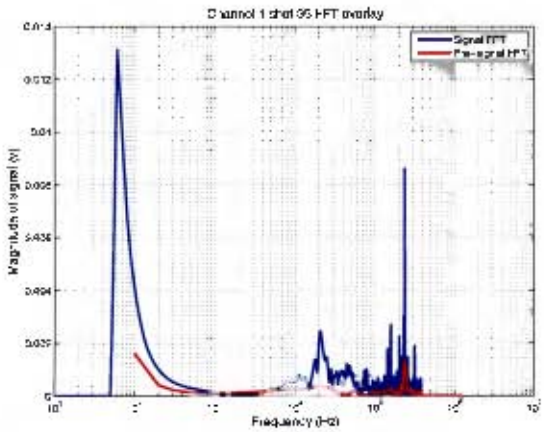

Figure H.331. Channel 1 60g at 8m

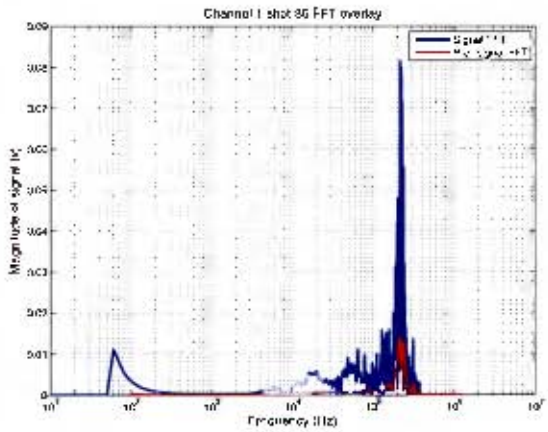

Figure H.332. Channel 1 60g at 8m

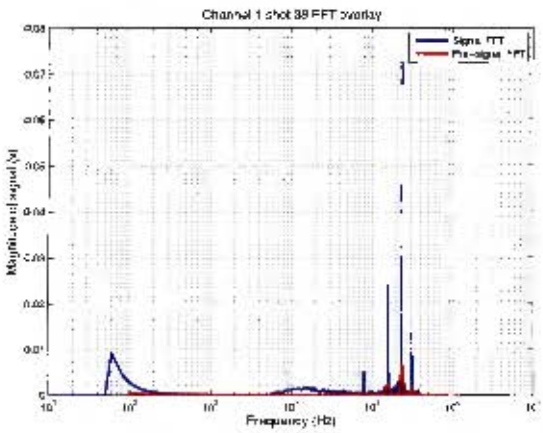

Figure H.333. Channel 1 80g at 8m

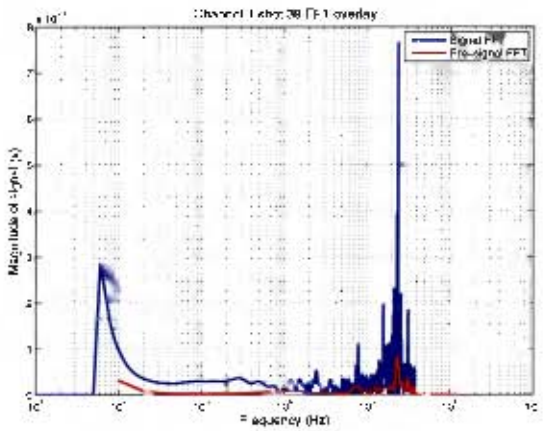

Figure H.334. Channel 1 100g at 8m

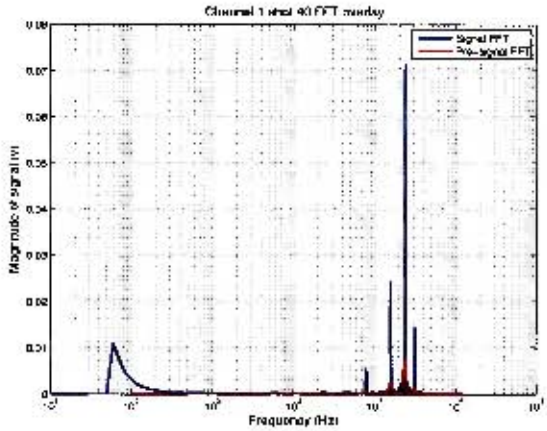

Figure H.335. Channel 1 100g at 8m

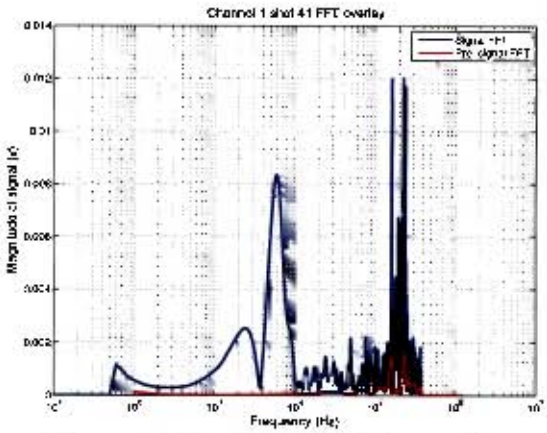

Figure H.336. Channel 1 2.9kg at 10m

H.3.2 Channel 2

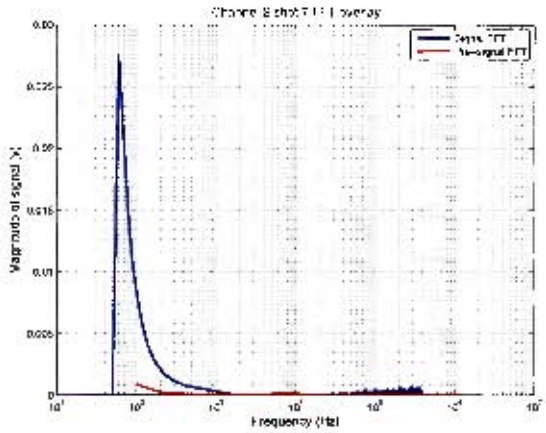

Figure **H.337.** Channel 2 20g at 2m

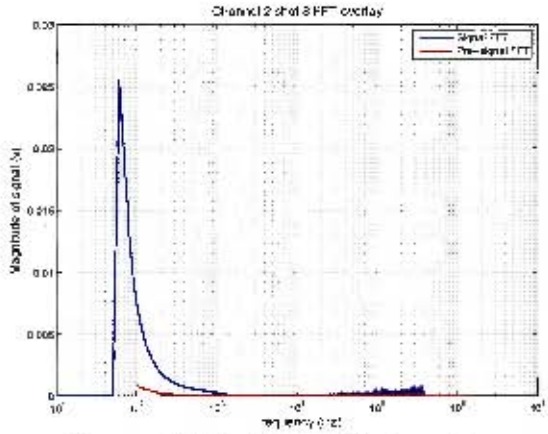

Figure H.338. Channel 2 40g at 2m

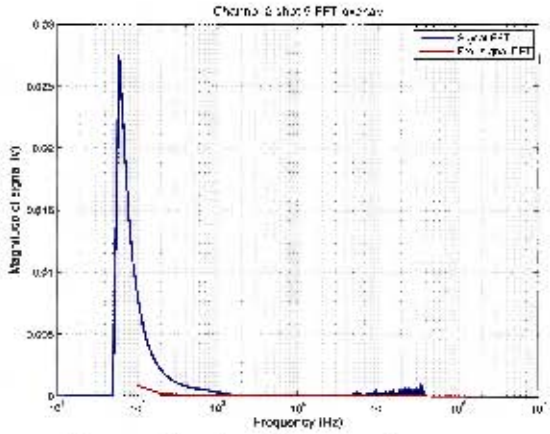

Figure H.339. Channel 2 40g at 2m

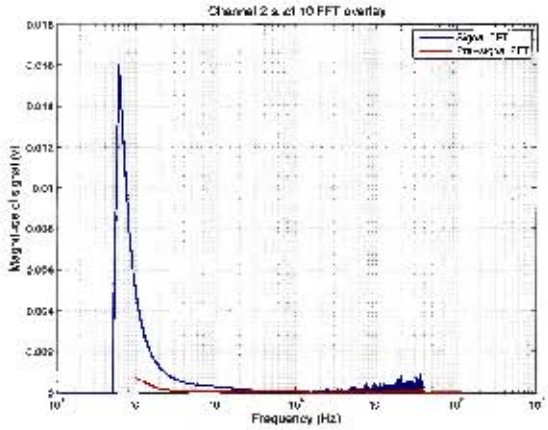

Figure H.340. Channel 2 60g at 2m

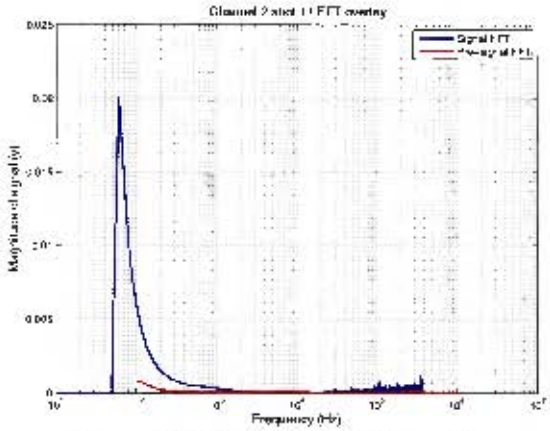

Figure H.341. Channel 2 60g at 2m

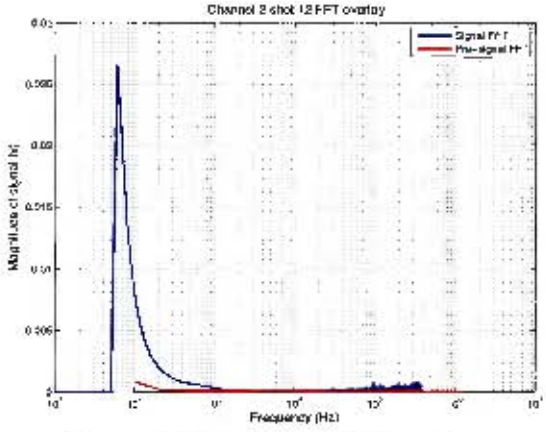

Figure H.342. Channel 2 80g at 2m

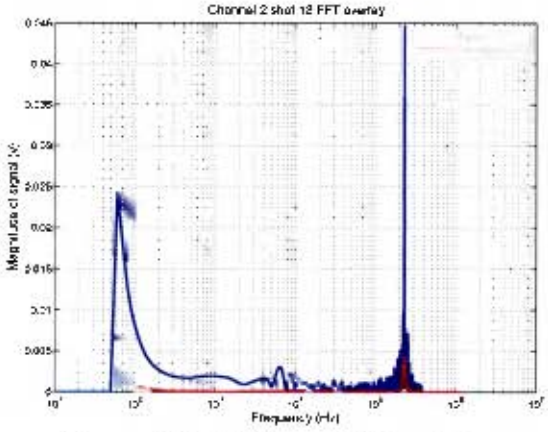

Figure H.343. Channel 2 80g at 2m

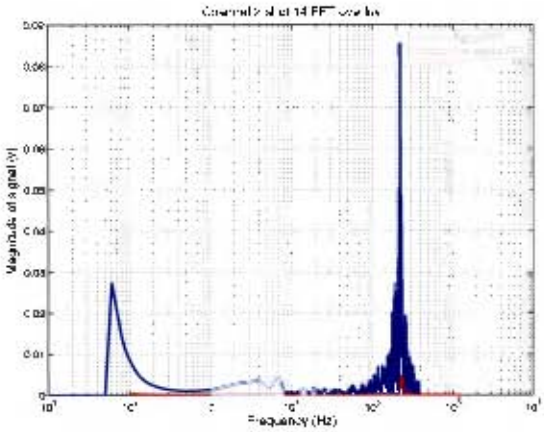

Figure H.344. Channel 2 100g at 2m

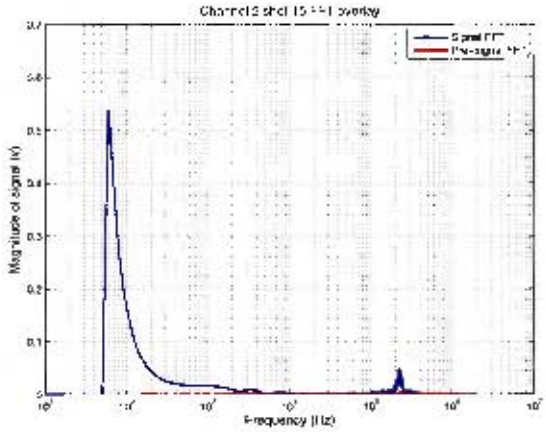

Figure H.345. Channel 2 100g at 2m

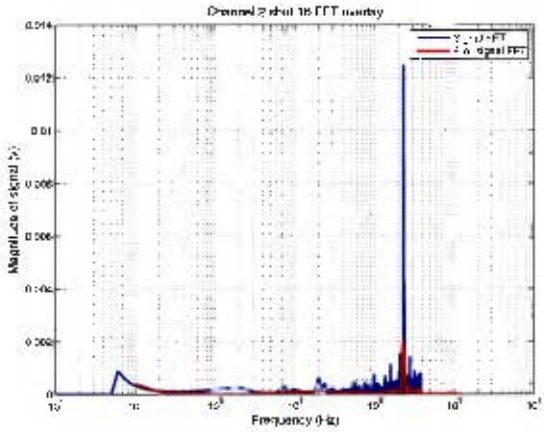

Figure H.346. Channel 2 20g at 4m

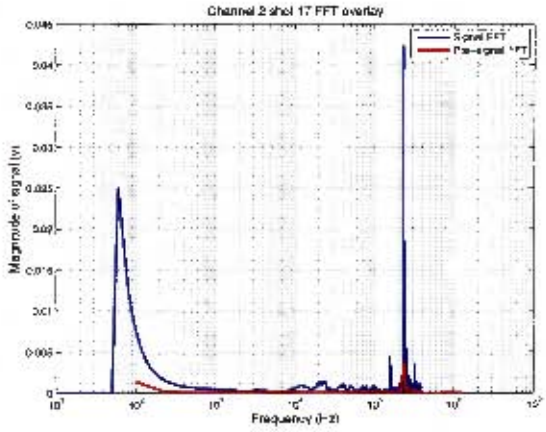

Figure H.347. Channel 2 20g at 4m

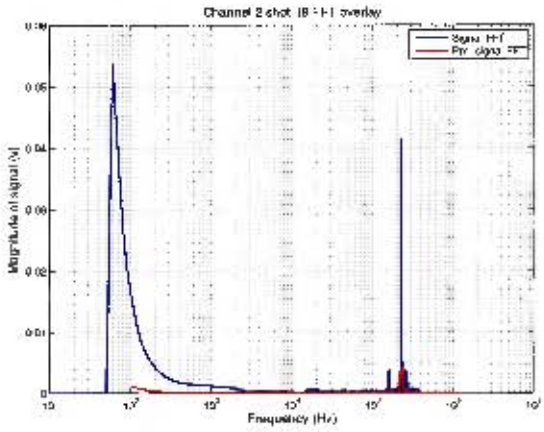

Figure H.348. Channel 2 40g at 4m

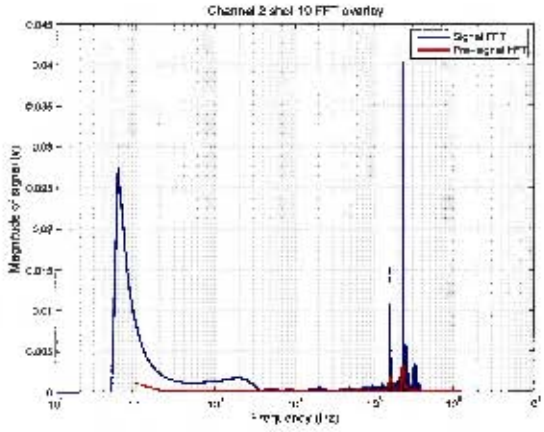

Figure H.349. Channel 2 40g at 4m

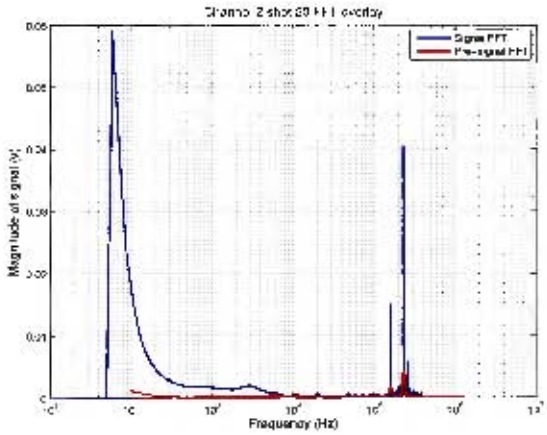

Figure H.350. Channel 2 60g at 4m

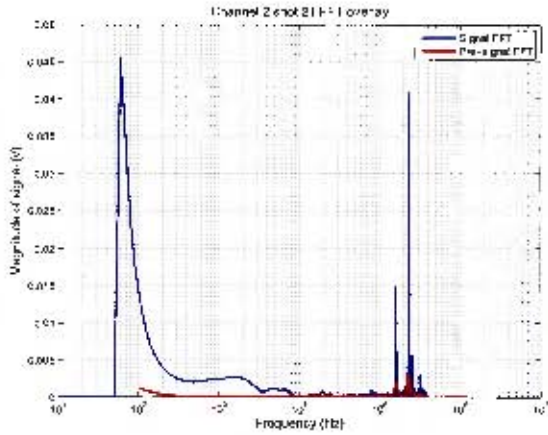

Figure H.351. Channel 2 60g at 4m

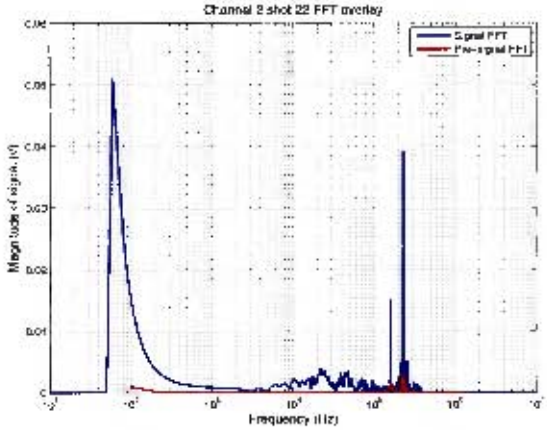

Figure H.352. Channel 2 80g at 4m

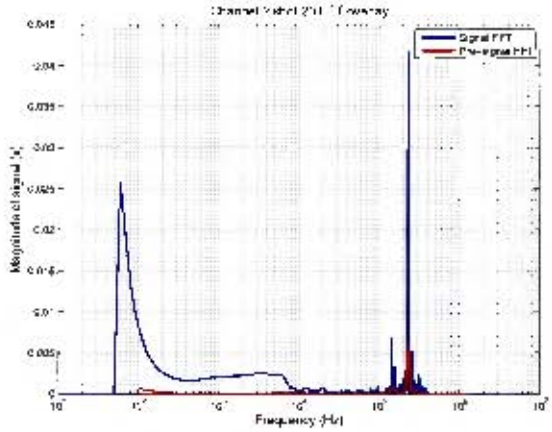

Figure H.353. Channel 2 80g at 4m

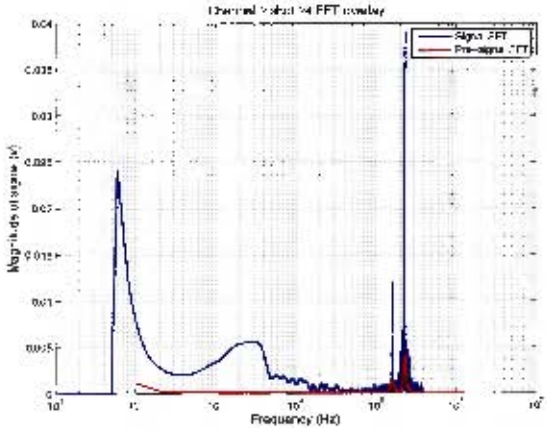

Figure H.354. Channel 2 100g at 4m

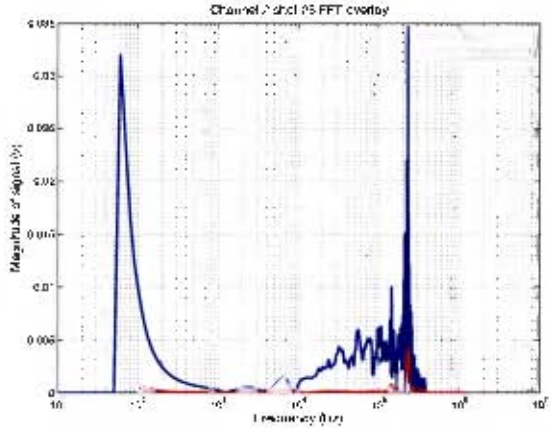

Figure H.355. Channel 2 100g at 4m

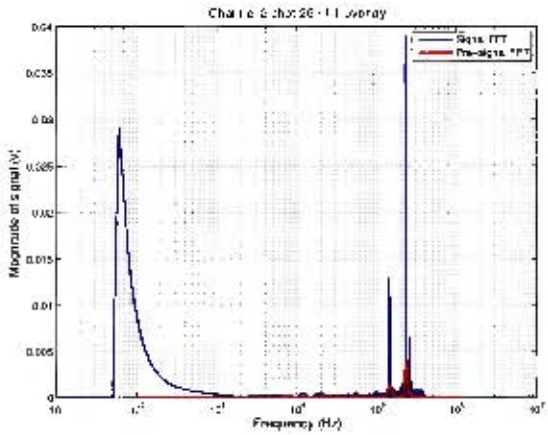

Figure H.356. Channel 2 40g at 6m

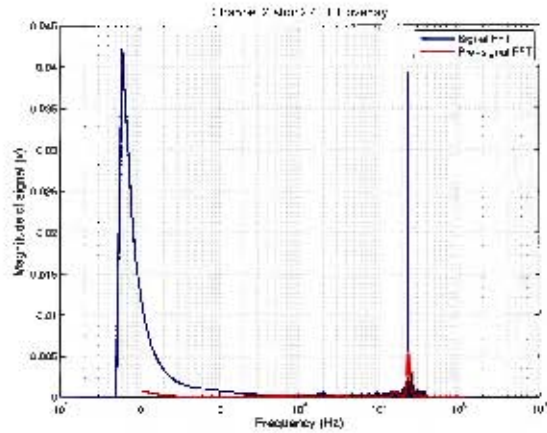

Figure H.357. Channel 2 40g at 6m

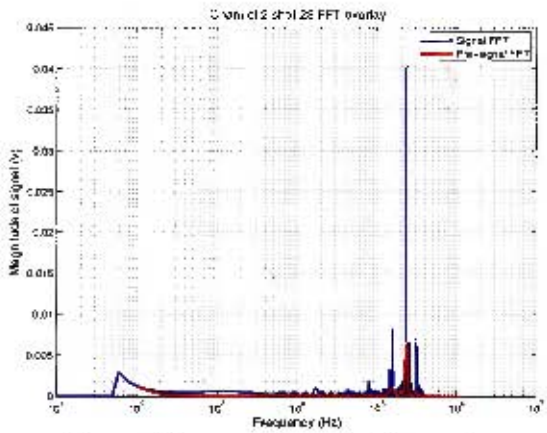

Figure H.358. Channel 2 60g at 6m

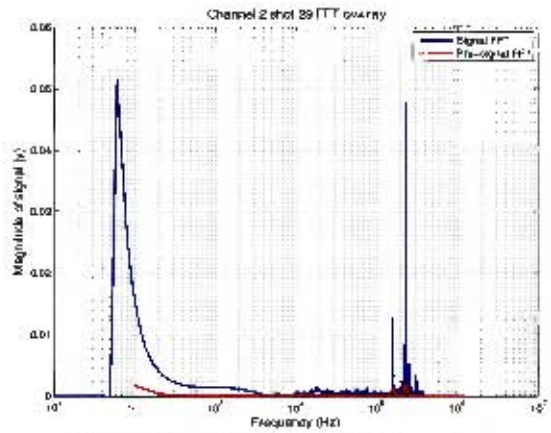

Figure H.359. Channel 2 60g at 6m

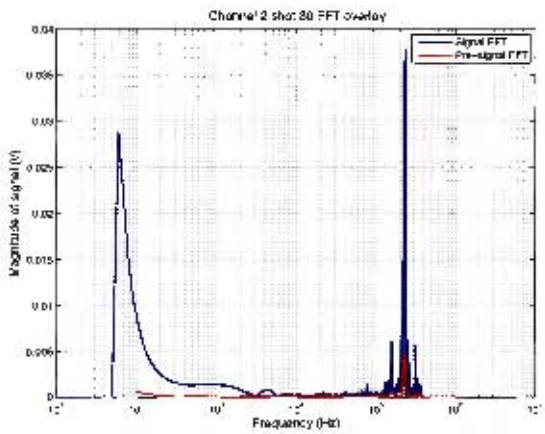

Figure H.360. Channel 2 80g at 6m

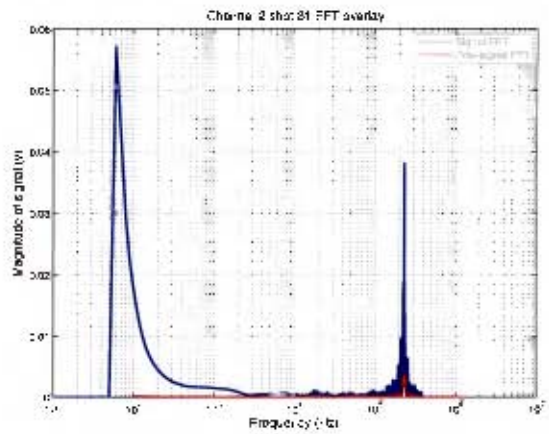

Figure H.361. Channel 2 80g at 6m

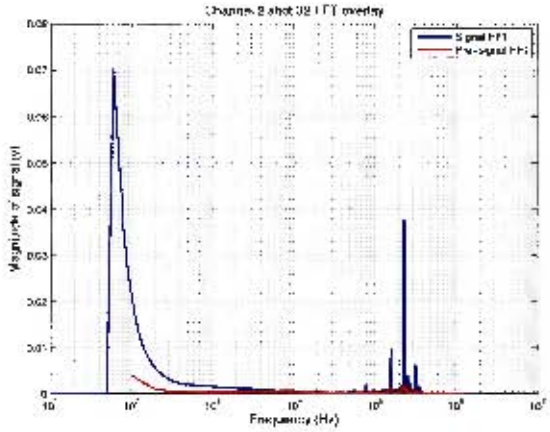

Figure H.362. Channel 2 100g at 6m

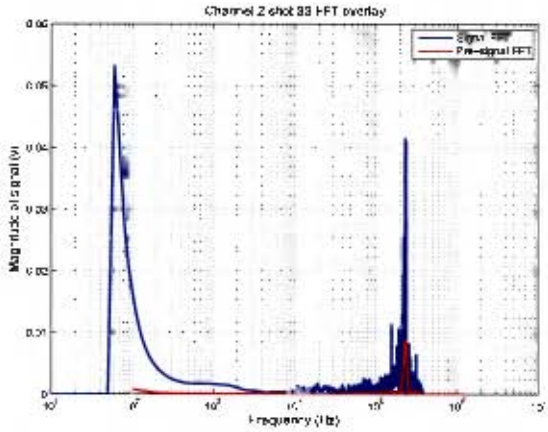

Figure H.363. Channel 2 100g at 6m

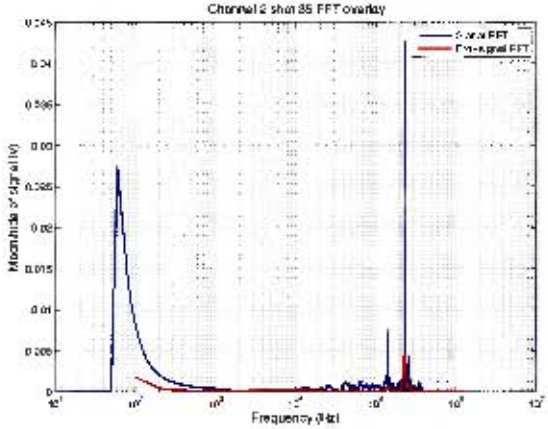

Figure H.364. Channel 2 60g at 8m

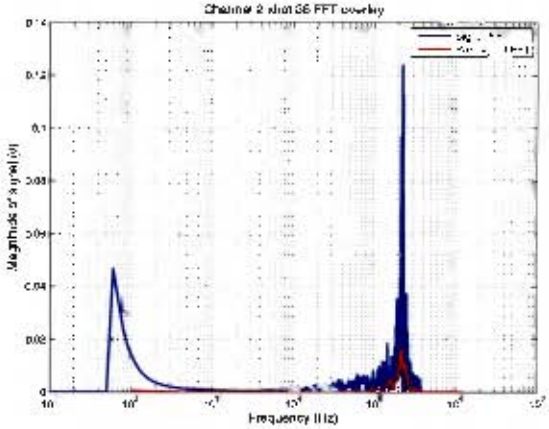

Figure H.365. Channel 2 60g at 8m

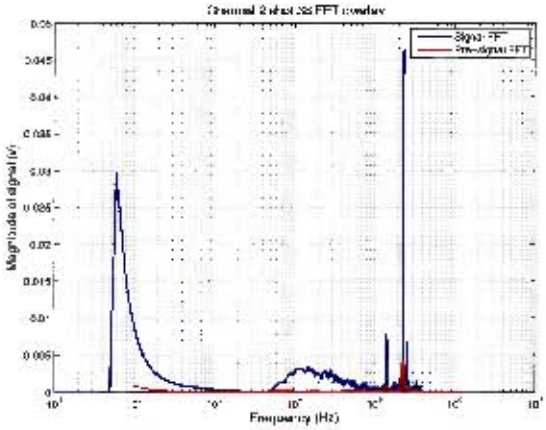

Figure H.366. Channel 2 80g at 8m

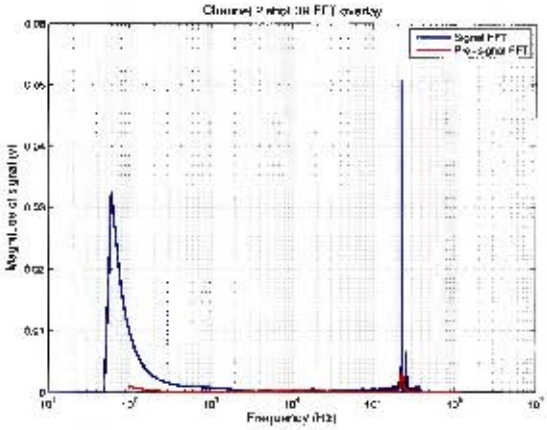

Figure H.367. Channel 2 100g at 8m

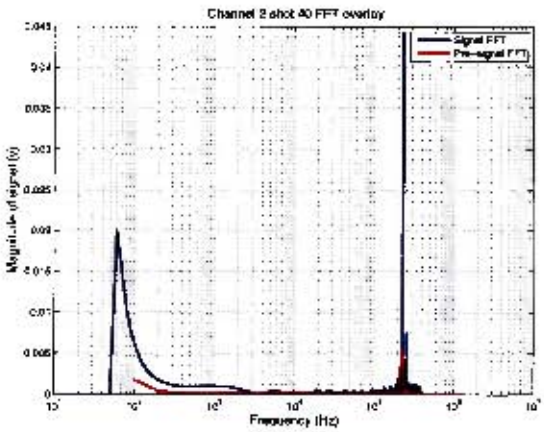

Figure H.368. Channel 2 100g at 8m

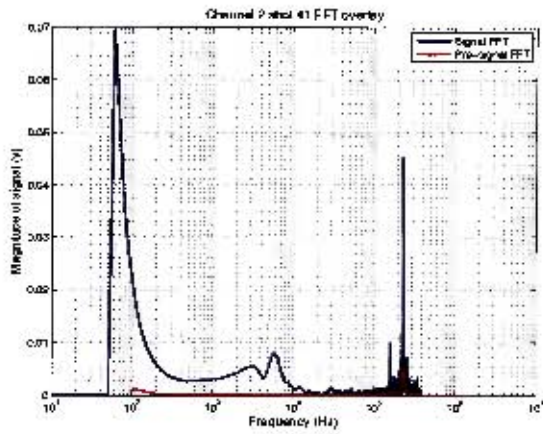

Figure H.369. Channel 2 2.9kg at 10m

H.3.3 Channel 3

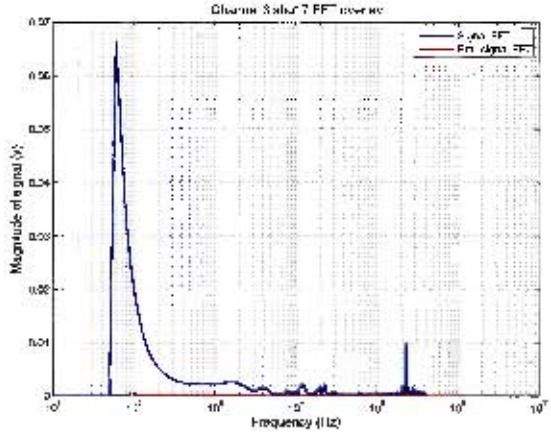

Figure H.370. Channel 3 20g at 2m

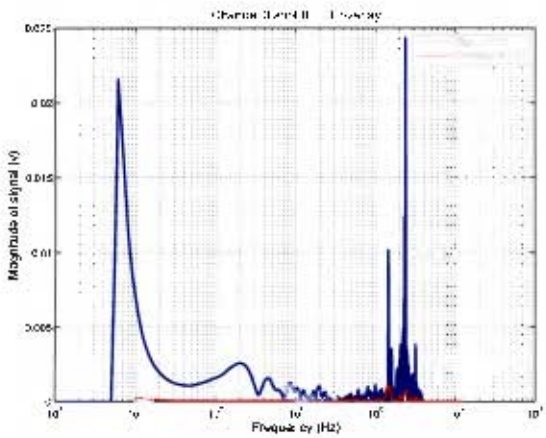

Figure H.371. Channel 3 40g at 2m

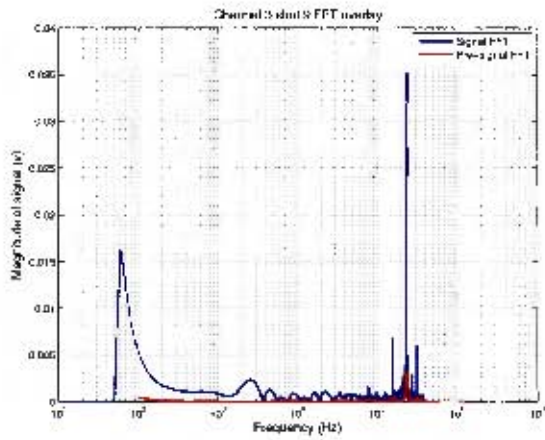

Figure H.372. Channel 3 40g at 2m

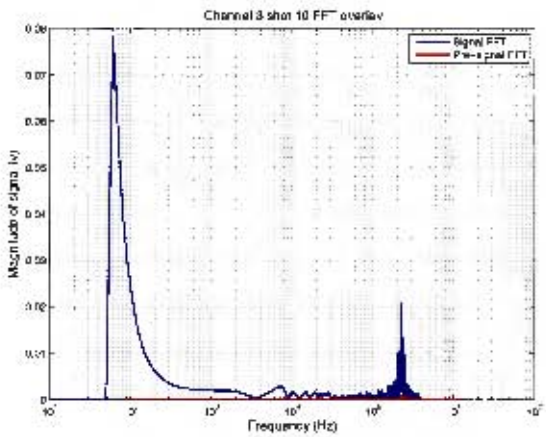

Figure H.373. Channel 3 60g at 2m

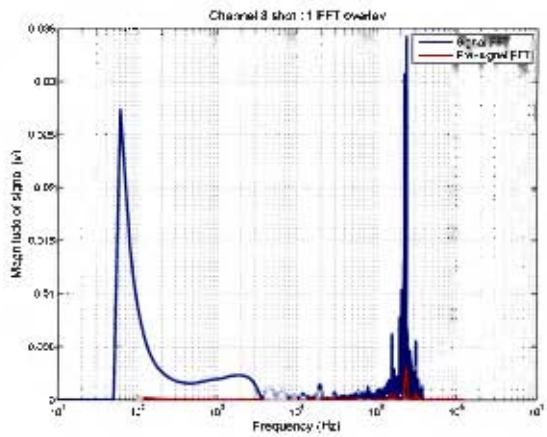

Figure H.374. Channel 3 60g at 2m

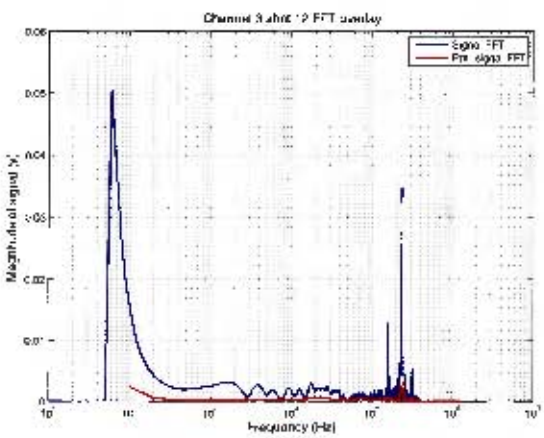

Figure H.375. Channel 3 80g at 2m

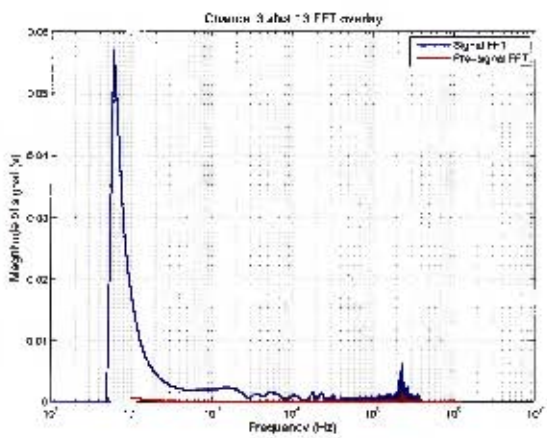

Figure H.376. Channel 3 80g at 2m

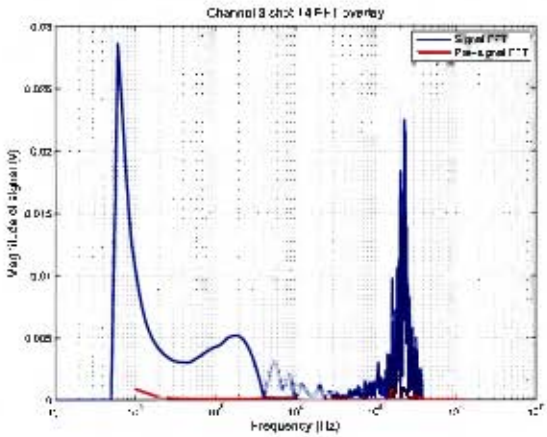

Figure H.377. Channel 3 100g at 2m

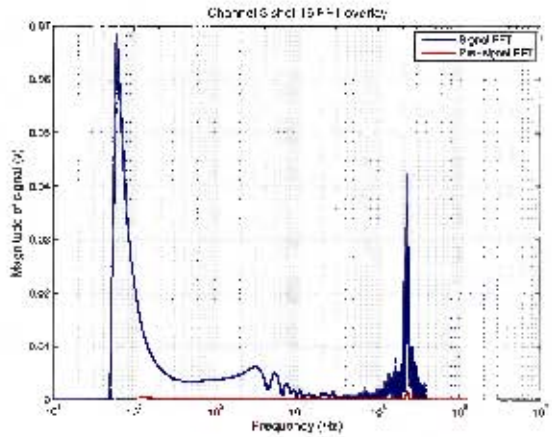

Figure H.378. Channel 3 100g at 2m

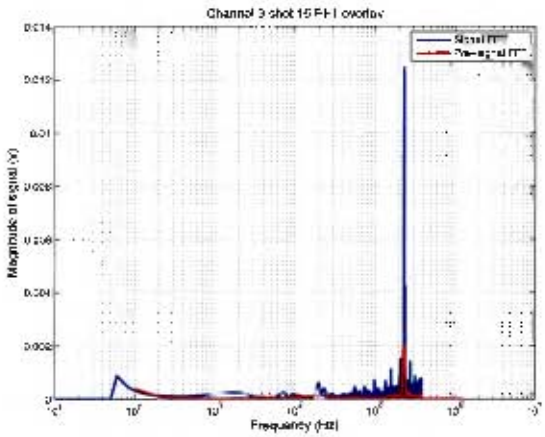

Figure H.379. Channel 3 20g at 4m

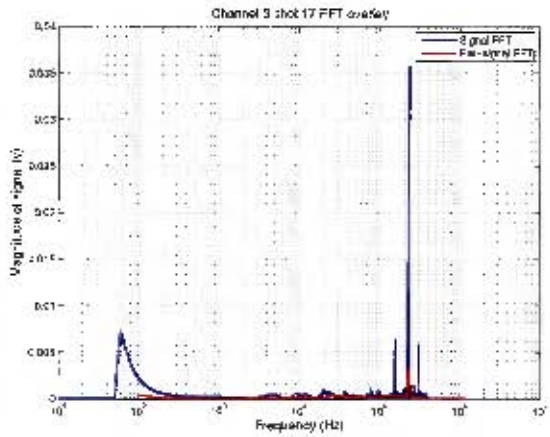

Figure H.380. Channel 3 20g at 4m

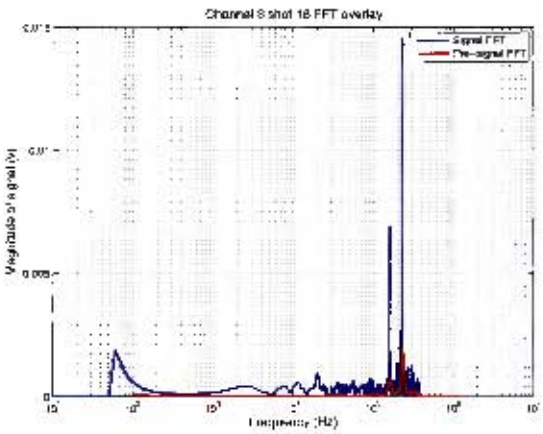

Figure H.381. Channel 3 40g at 4m

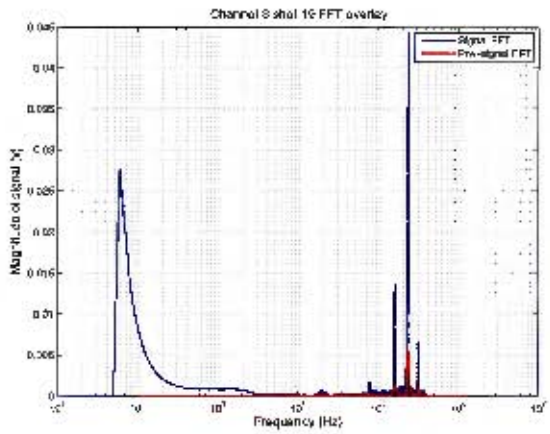

Figure H.382. Channel 3 40g at 4m

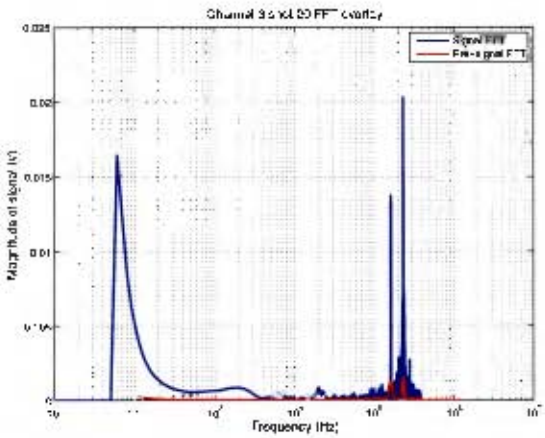

Figure H.383. Channel 3 60g at 4m

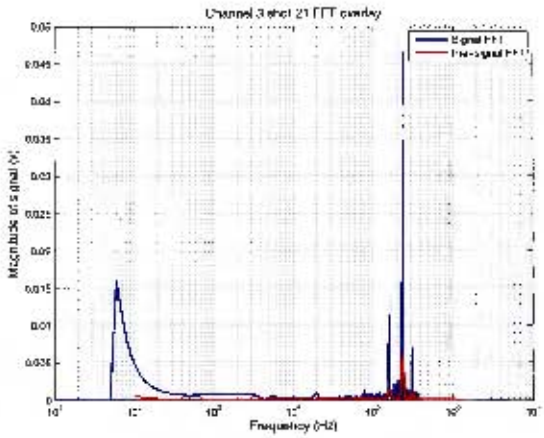

Figure H.384. Channel 3 60g at 4m

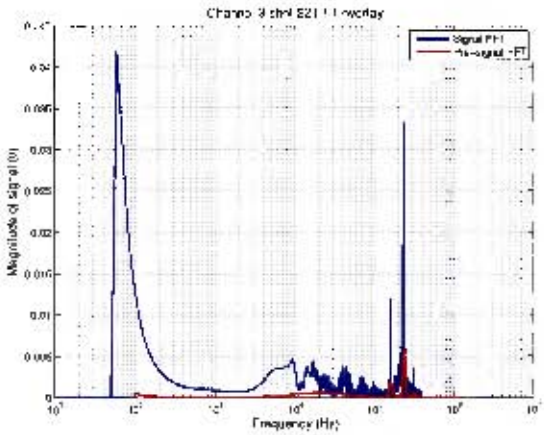

Figure H.385. Channel 3 80g at 4m

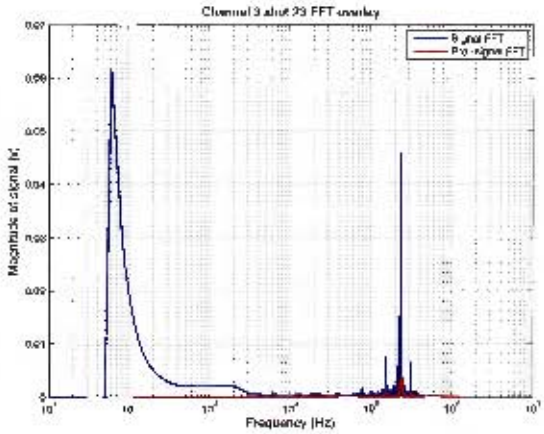

Figure H.386. Channel 3 80g at 4m

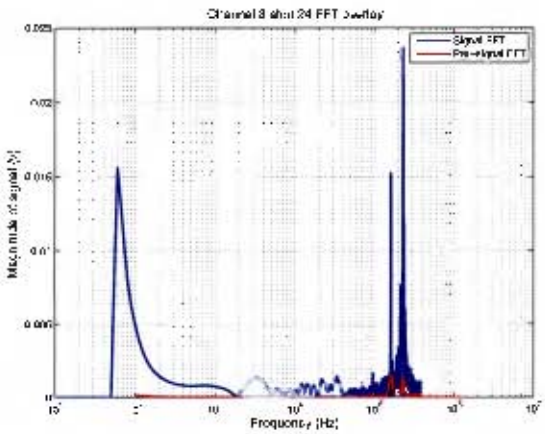

Figure H.387. Channel 3 100g at 4m

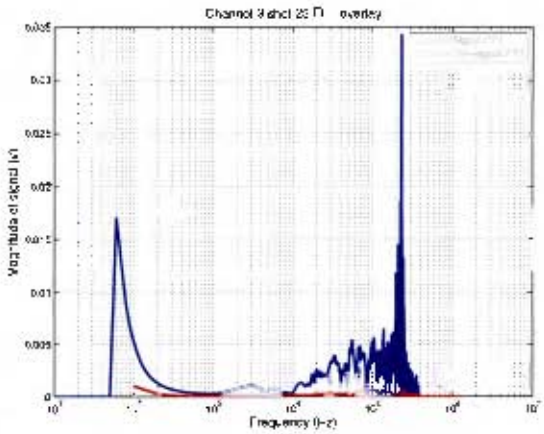

Figure H.388. Channel 3 100g at 4m

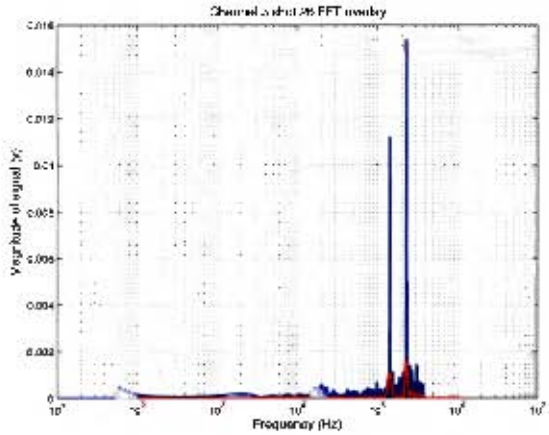

Figure H.389. Channel 3 40g at 6m

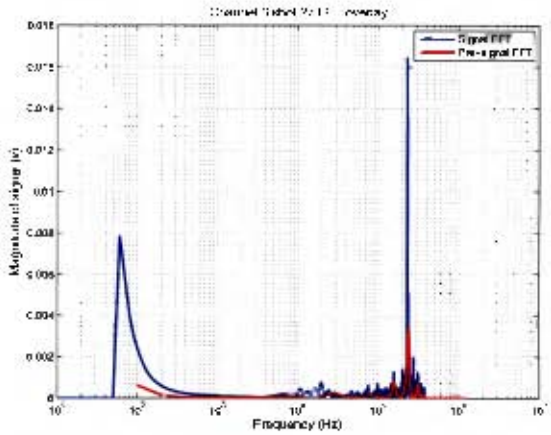

Figure H.390. Channel 3 40g at 6m

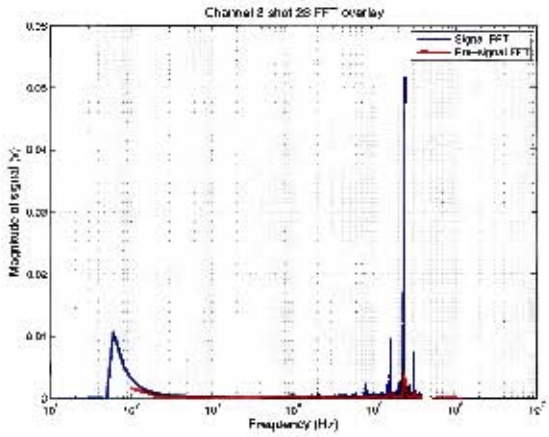

Figure H.391. Channel 3 60g at 6m

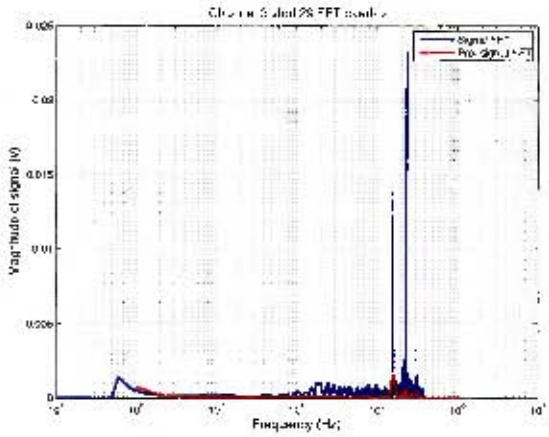

Figure H.392. Channel 3 60g at 6m

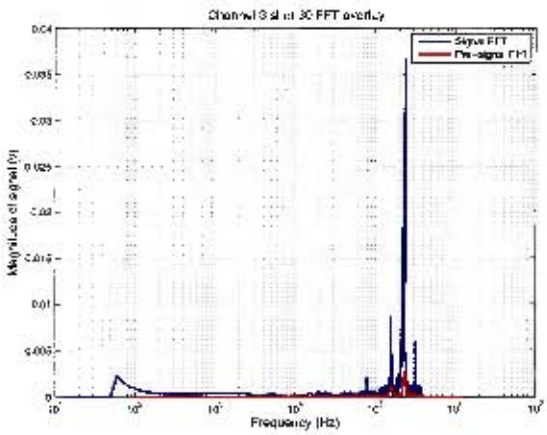

Figure H.393. Channel 3 80g at 6m

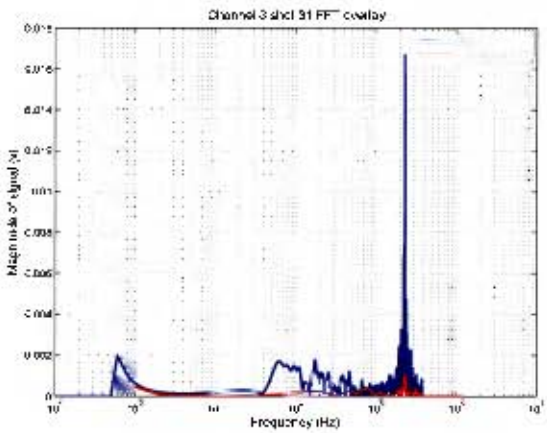

Figure H.394. Channel 3 80g at 6m

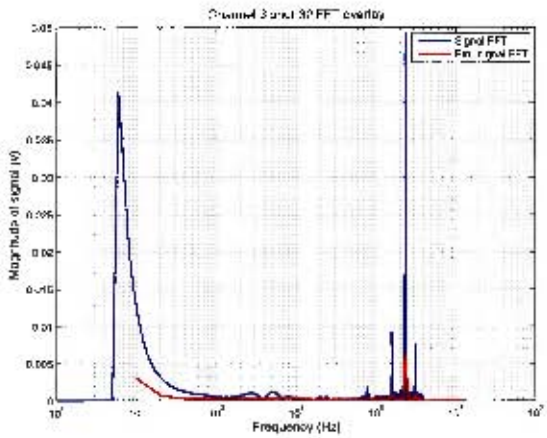

Figure H.395. Channel 3 100g at 6m

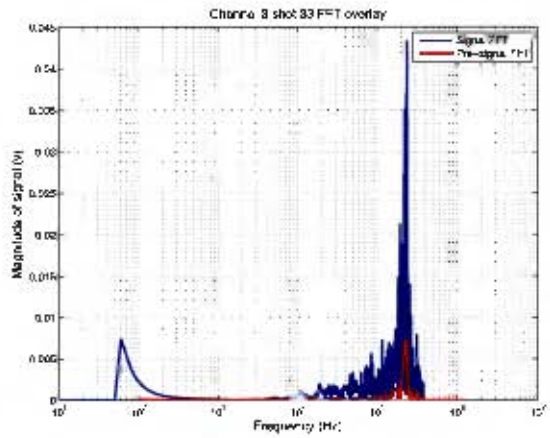

Figure H.396. Channel 3 100g at 6m

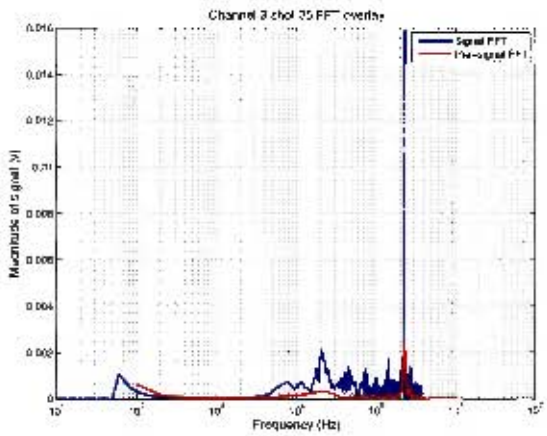

Figure H.397. Channel 3 60g at 8m

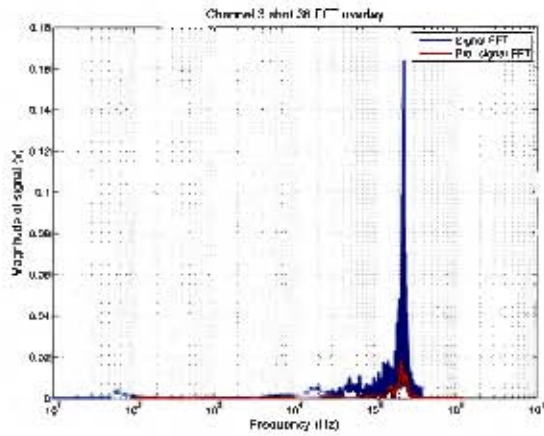

Figure H.398. Channel 3 60g at 8m

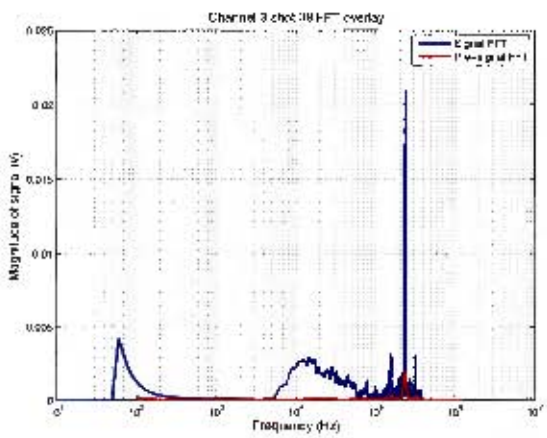

Figure H.399. Channel 3 80g at 8m

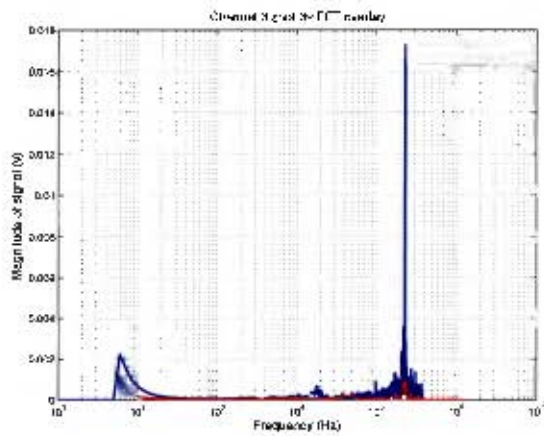

Figure H.400. Channel 3 100g at 8m

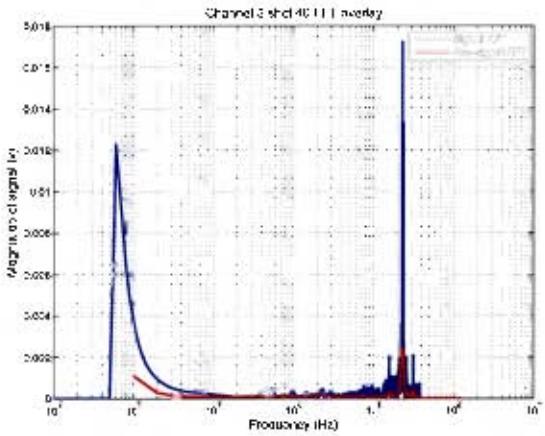

Figure H.401. Channel 3 100g at 8m

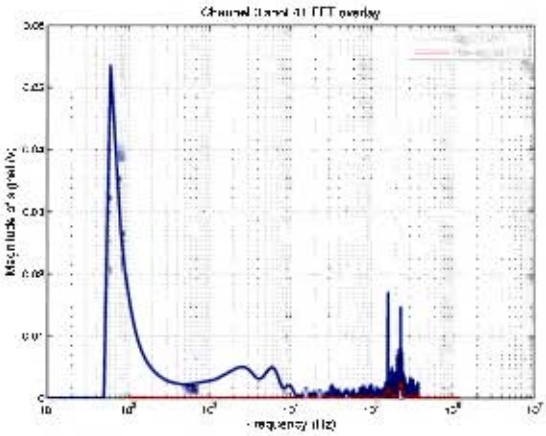

Figure H.402. Channel 3 2.9kg at 10m

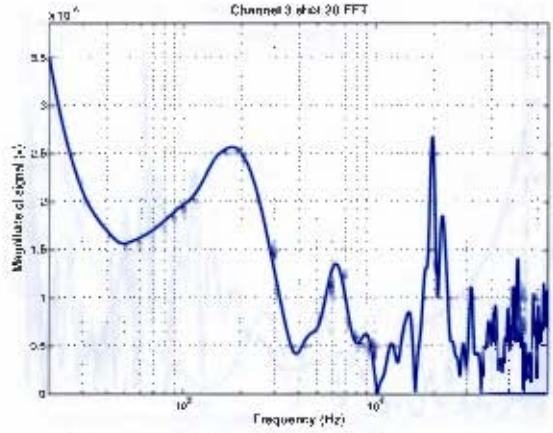

Figure H.284. Channel 3 60g at 4m

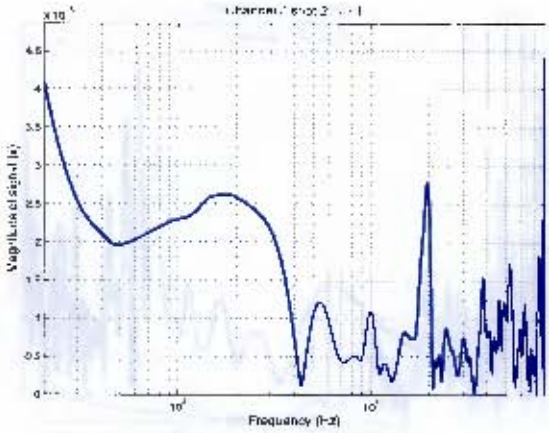

Figure H.285. Channel 3 60g at 4m

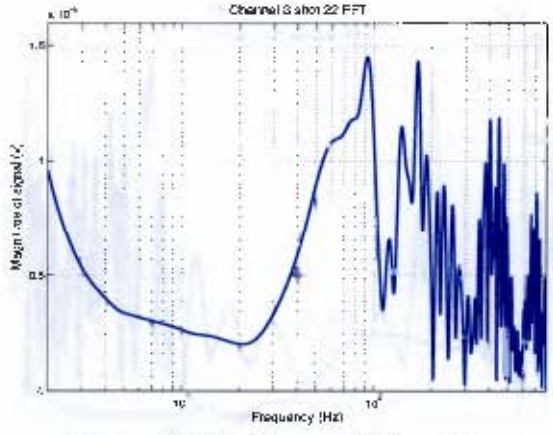

Figure H.286. Channel 3 80g at 4m

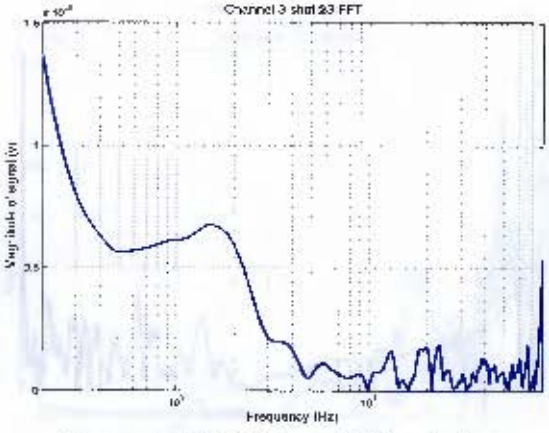

Figure H.287. Channel 3 80g at 4m

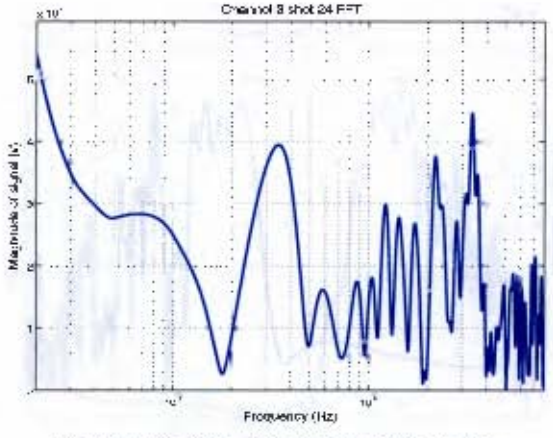

Figure H.288. Channel 3 100g at 4m

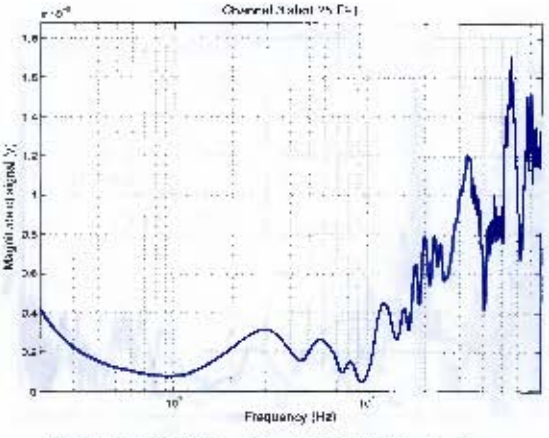

Figure H.289. Channel 3 100g at 4m